

**SPATIAL AND TEMPORAL EVOLUTION OF SNOW-COVERED
SEA ICE, WITH REFERENCE TO POLAR BEAR HABITAT**

by:

John Iacozza

A Thesis submitted to the Faculty of Graduate Studies of

The University of Manitoba

in partial fulfilment of the requirements of the degree of

DOCTOR OF PHILOSOPHY

Department of Environment and Geography

University of Manitoba

Winnipeg, Manitoba

Copyright © 2011 by John Iacozza

ABSTRACT

This dissertation attempts to improve the understanding of spatial distribution and evolution of snow-covered sea ice as related to polar bear habitat. This will be accomplished at both the local (i.e. 1m spatial resolution) and regional scales (i.e. 100 km spatial resolution) for various types of first-year sea ice (FYI) through four primary objectives. The first primary objective (i.e. Chapter 3) examines the observed and modeled temporal evolution of snow over smooth FYI, as well as the estimation of on-ice meteorological conditions. Results suggest that increases in observed snowdrifts and changes to the orientation of the drifts are related to snowfall and drifting events. Modeling these changes over time using a spatially distributed snow model is not able to accurately estimate the snow distribution. As well, only the on-ice temperature and humidity can be estimated from land-based station data, limiting the modeling of snow over sea ice.

The second primary objective (i.e. Chapter 4) extends this research to rough FYI types, more relevant to polar bear habitat. More specifically this objective studies the spatial pattern of snow distribution over rough ice and ridges and the relationship between ice roughness and meteorological conditions. Results suggest that ice roughness influences the magnitude of snow depth, while the wind direction during periods of snow deposition and/or blowing snow events will impact the spatial pattern.

The third primary objective (i.e. Chapter 5) focuses on developing a more feasible method of deriving surface roughness. This objective attempts to use

satellite imagery and texture analysis to derive surface roughness for snow-covered sea ice. Results suggest that a Gamma speckle reduction filter, coupled with a grey-level co-occurrence matrix texture measure (Entropy or Angular Second Moment) is able to account for more than 88% of the variability in the surface roughness.

The final primary objective (i.e. Chapter 6) examines the temporal evolution and factors controlling the changes in sea ice characteristics over regional scale for a period from 1978 to 2002. Observed anomalies in sea ice characteristics within some of the polar bear subpopulations may be explained by thermodynamic and/or dynamic factors. Results suggest that published reduction in polar bear population and condition within the subpopulations co-occur with these observed changes in sea ice characteristics.

ACKNOWLEDGEMENTS

I would like to personally acknowledge my PhD advisory committee for providing me with the necessary guidance in the completion of this dissertation. Namely, I want to thank Dr. David G. Barber, my PhD advisor for all his support through the many years. I will always be indebted to you for all the knowledge you imparted on me and the understanding during the periods of slow productivity. I also would like to thank my advisory committee Dr. Simon Prinsenberg (Bedford Institute for Oceanography, Department of Fisheries and Oceans), Dr. Steve Ferguson (Freshwater Institute, Department of Fisheries and Oceans) and Dr. Rick Riewe (University of Manitoba), as well as my external reviewer Dr. Mike Hammill (Department of Fisheries and Oceans) for providing their assistance during this process.

I would also like to thank the many people in the Department of Environment and Geography and Centre for Earth Observation Science who had provided invaluable support in conducting the research and aiding in the analysis of the data. Namely, Mr. David Mosscrop and Mr. Bob Hodgson for providing logistical support for field activities, Ms. Aggie Roberecki and Ms. Denise Whynot for their administrative support and Mr. Wayne Chan for programming assistance. I would also like to thank Ms. Christina Blouw, Mr. Jens Ehn, Ms. Teresa Fisico and Mr. Alex Langlois (University of Manitoba) and Ms. Carrie Brennan (University of Calgary) for assistance in the field during CASES 2004.

A special acknowledgement is given to Dr. J. Scott Holladay (GeoSensors Inc.) for providing his technical expertise with regards to the helicopter EMI system and Glen Liston (Cooperative Institute for Research in the Atmosphere, Colorado State University) for generously providing *SnowModel*. I wish to acknowledge the Canadian Ice Service (Dr. Roger DeAbreu and Mr. Matt Arkett) for providing the sea ice digital ice charts used in this dissertation. In addition, NCEP Reanalysis 2 data was provided by the NOAA, Boulder, Colorado, and Arctic Oscillation Index data by the National Weather Service Climate Prediction Center, Maryland. Satellite imagery was provided by the European Space Agency, through a CAT-1 proposal.

My research was supported by a number of funding agencies, including the Faculty of Graduate Studies, the Association of Canadian Universities for Northern Studies, Royal Canadian Geographical Society, and the Northern Studies Training Program. The Canadian Arctic Shelf Exchange Studies (CASES) and ArcticNet provided the logistical support required to collect the data in the field. In addition, the Canadian Ice Service provided in-kind support throughout the field program. The crew of CCGS Amundsen also provided invaluable logistical support during the data collection.

Personally, I wish to thank my family and friends who supported me during the many years of working and completing my PhD. My parents and sisters provided me with the emotional support to continue my research during difficult times. As well, my friends both in Winnipeg and in Hamilton provided me the opportunity for a fresh perspective on my research and gave me a sounding board to discuss my research.

DEDICATION

This thesis is dedicated to my father, who taught me that true success comes from hard work and perseverance, no matter how you define 'success'. It is also dedicated to my mother, who showed me that patience is the companion of wisdom (a lesson I am still trying to learn!).

The great book for you is the book that has the most to say to you at the moment when you are reading. I do not mean the book that is most instructive, but the book that feeds your spirit. And that depends on your age, your experience, your psychological and spiritual need.

ROBERTSON DAVIES

TABLE OF CONTENTS

ABSTRACT	i
ACKNOWLEDGEMENTS	III
DEDICATION	IV
LIST OF TABLES	VII
LIST OF FIGURES	VIII
LIST OF COPYRIGHTED MATERIAL	XIV
GLOSSARY OF ABBREVIATIONS	XVII
CHAPTER 1: INTRODUCTION	1
1.1 INTRODUCTION TO DISSERTATION.....	1
1.2 OBJECTIVES OF DISSERTATION.....	5
1.3 STRUCTURE OF DISSERTATION	7
CHAPTER 2: BACKGROUND	8
2.1 DYNAMIC PROCESSES RELATED TO SNOW COVERED SEA ICE	8
2.1.1 <i>First-year sea ice features</i>	8
2.1.2 <i>Dynamic processes</i>	10
2.1.3 <i>Snow catchment</i>	19
2.2 DYNAMIC PROCESSES RELATED TO HABITAT SELECTION	27
2.2.1 <i>Ringed seal habitat</i>	28
2.2.2 <i>Polar bear habitat</i>	33
2.3 ESTIMATING SNOW-COVERED SEA ICE	45
2.3.1 <i>Modeling snow-covered sea ice</i>	45
2.3.2 <i>Remote sensing</i>	46
CHAPTER 3: SNOW REDISTRIBUTION OVER SMOOTH LAND-FAST SEA ICE	48
3.1 METHODS.....	48
3.1.1 <i>Snow redistribution</i>	48
3.1.2 <i>Meteorological variables</i>	53
3.1.3 <i>Spatial continuity</i>	55
3.1.4 <i>SnowModel</i>	57
3.2 CHARACTERIZATION AND FORCING OF OBSERVED SNOW REDISTRIBUTION	60
3.2.1 <i>Meteorological setting on sea ice (2004)</i>	60
3.2.2 <i>Evolution and meteorological forcing of snow distribution</i>	62
3.3 COMPARISON OF LAND-BASED VERSUS ON-ICE METEOROLOGICAL DATA.....	69
3.4 SNOW REDISTRIBUTION MODELING USING SNOWMODEL	75
3.5 CONCLUSION	82

CHAPTER 4: SPATIAL PATTERN OF SNOW DISTRIBUTION VERSUS SEA ICE ROUGHNESS IN THE CANADIAN ARCTIC.....	87
4.1 METHODS.....	87
4.1.1 <i>Snow depth and surface roughness</i>	87
4.1.3 <i>Spatial analysis</i>	93
4.2 ASSOCIATION BETWEEN SNOW DEPTH AND SEA ICE SURFACE ROUGHNESS	97
4.3 SPATIAL PATTERN OF SNOW DEPTH AS A FUNCTION OF SEA ICE ROUGHNESS.....	100
4.4 EVOLUTION OF SPATIAL PATTERN	108
4.5 CONCLUSION	112
CHAPTER 5: DERIVING LAND-FAST SURFACE ROUGHNESS FROM ASAR IMAGES USING SECOND-ORDER TEXTURE MEASURES.....	117
5.1 METHODS.....	117
5.1.1 <i>Helicopter-borne surface roughness</i>	117
5.1.2 <i>Satellite-based remote sensing of sea ice</i>	120
5.1.3 <i>Image processing and texture analysis</i>	121
5.2 INDIVIDUAL PIXEL COMPARISON	126
5.3 BINNED SURFACE ROUGHNESS COMPARISON	128
5.3.1 <i>Effect of ASAR characteristics</i>	128
5.3.2 <i>Optimal GLCM parameters</i>	133
5.3.3 <i>Case Study</i>	135
5.4 CONCLUSION	137
CHAPTER 6: ASSESSMENT OF SUMMER AND AUTUMN ICE CHARACTERISTICS AS RELATED TO POLAR BEAR SUBPOPULATIONS IN THE CANADIAN ARCTIC	139
6.1 METHODS.....	139
6.1.1 <i>Polar bear subpopulation clusters</i>	139
6.1.2 <i>Canadian Ice Service (CIS) ice charts</i>	141
6.1.3 <i>Modeled dynamic and thermodynamic parameters</i>	145
6.1.4 <i>Spectral analysis</i>	147
6.2 SPATIAL AND TEMPORAL TRENDS IN SEA ICE CHARACTERISTICS.....	148
6.2.1 <i>Eastern Canadian Arctic (ECA) cluster</i>	148
6.2.2 <i>Canadian Arctic Archipelago (CAA) cluster</i>	161
6.2.3 <i>Beaufort Sea (BS) cluster</i>	166
6.3 DYNAMIC AND THERMODYNAMIC FORCING	169
6.4 TRENDS IN POLAR BEAR CONDITION RELATED TO SEA ICE TRENDS.....	180
6.5 CONCLUSION	182
CHAPTER 7: CONCLUSION.....	186
7.1 SUMMARY OF RESULTS	186
7.2 CLIMATE CHANGE IMPLICATIONS	189
7.2.1 <i>Projected changes in sea ice and snow</i>	189
7.2.2 <i>Implications for marine mammal habitat</i>	194
REFERENCES.....	201

LIST OF TABLES

Table 4.1: Sampling dates of the rubble and ridge ice sites in 2004. The rubble sites are denoted by the prefix RB-, while the ridge sites have the prefix RD-.....	93
Table 4.2: Kolmogorov-Smirnov (K-S) test and skewness results for the rubble ice and ridge sites sampled in 2004. K-S test and skewness results that are statistically significant (i.e. not normally distributed) at a 0.05 level are shown in bold and italics.	98
Table 4.3: Magnitude and direction of anisotropy for snow depth and sea ice surface roughness derived for the 6 sites sampled on rubble sea ice.	109
Table 5.1: Names, collection date and time, and length (km) of IcePic transects collected during 2004.	120
Table 5.2: Characteristics of the ASAR imagery used in this study. In addition, the IcePic sampling transect(s) corresponding to each image is also listed.	121
Table 6.1: The Canadian polar bear subpopulations (Lunn et al., 2006) comprising the three clusters used in this study.	141
Table 6.2: 31-year trend analysis (r) and associated slopes (β , % per decade) of open water, multiyear and first-year sea ice concentration, large and small floe sizes and fast ice concentration in the polar bear subpopulations within the three clusters. Statistically significant trends ($p < 0.05$) are highlighted in bold and italics. S = Summer season, A = Autumn season, NA = no multiyear sea ice, NS = non-significant slopes. Summer season is between June 11 and September 2, while autumn season is between September 3 to December 2).	151
Table 6.3: Periodicity (in years) of open water, multiyear and first-year sea ice concentration, large and small floe sizes and fast ice concentration in the polar bear subpopulations within the three clusters. Statistically significant results ($p < 0.05$) are presented in the table. S = Summer season, A = Autumn season, NA = no significant periodicity beyond 1 year. Summer season is between June 11 and September 2, while autumn season is between September 3 to December 2). *Note: multiyear sea ice within WH and SH subpopulations was lacking and therefore no periodicity in the trends were calculated.	152

LIST OF FIGURES

Figure 2.1: First-year sea ice features formed in either calm or dynamic/rough conditions..	8
Figure 2.2: Mean geostrophic wind velocity (m/s) fields and annual mean sea level pressure contours for (a) 1979-88 and (b) 1989-96; anomaly fields of geostrophic wind velocity based on the differences (c) between the 1979-88 mean and the 1979-96 mean and (d) between the 1989-96 mean and the 1979-96 mean. The contour interval is 1.0 mbar. (From Zhang <i>et al.</i> , 2000. © American Meteorological Society. Reprinted with permission).....	16
Figure 2.3: Averaged volumes (km ³) of ridged and level ice in (a) winter and (b) summer in the Eurasian (1) and Canadian (2) regions. (From Makshtas <i>et al.</i> , 2003. © American Geophysical Union. Reprinted with permission).....	17
Figure 2.4: Probability distribution functions of snow depth for four separate ice types. The vertical dot-dash line indicates the mean depth at the station. (From Sturm <i>et al.</i> , 2002. © American Geophysical Union. Reprinted with permission.).....	20
Figure 2.5: Standard deviation of snow depth as a function of average depth for the four classes of sea ice. (From Sturm <i>et al.</i> , 2002. © American Geophysical Union. Reprinted with permission).....	21
Figure 2.6: Relative frequency of observed transport threshold wind speed for dry snow and wet snow. (From Li and Pomeroy, 1997. © American Geophysical Union. Reprinted with permission.).....	23
Figure 2.7: Threshold wind speed for fresh snow (open circle) and aged snow (closed circle). (From Li and Pomeroy, 1997 © American Geophysical Union. Reprinted with permission).....	23
Figure 2.8: Snow depth, distance to nearest ice ridge, ice ridge height and ice ridge thickness measured at seal structures (solid bars) and habitat locations in general (open bars) for data collected in 1991-93. (From Furgal <i>et al.</i> , 1996. © National Research Council. Reprinted with permission).....	31
Figure 2.9: Mean density of ringed seals in relation to sea ice cover in western Hudson Bay. (From Lunn <i>et al.</i> , 1997. © National Research Council. Reprinted with permission)..	32
Figure 2.10: Seasonal cycle in selection by female polar bears of four ice type categories found in the (A) Arctic Archipelago and (B) Baffin Bay regions, 1991-1995. (From Ferguson <i>et al.</i> , 2000. © Ecological Society of America. Reprinted with permission)..	36
Figure 2.11: Seasonal cycle in selection by female polar bears of five ice cover categories found in the (A) Arctic Archipelago and (B) Baffin Bay regions, 1991-1995. (From Ferguson <i>et al.</i> , 2000. © Ecological Society of America. Reprinted with permission)..	37

Figure 2.12: Seasonal cycle in selection by female polar bears of four sizes of ice floes found in the (A) Arctic Archipelago and (B) Baffin Bay regions, 1991-1995. (From Ferguson <i>et al.</i> , 2000. © Ecological Society of America. Reprinted with permission).....	39
Figure 2.13: Seasonal changes in movement for female polar bears inhabiting consolidated versus active ice in the Canadian Arctic. (From Ferguson <i>et al.</i> , 2001. © The Arctic Institute of North America. Reprinted with permission).....	41
Figure 2.14: Indices of habitat preference of polar bears by sex and age class. A value greater than one indicates preference, a value less than one indicates avoidance and a value of one indicates no preference. (From Stirling <i>et al.</i> , 1993. © Cambridge University Press. Reprinted with permission).....	44
Figure 3.1: Map of the Canadian Arctic illustrating the general locations of the sampling areas. The two insets show a detailed map of the sampling locations in 2000 (top inset) and 2004 (bottom inset). The stars in the insets indicate the location of the meteorological stations (both on ice and land-based) (From Iacozza and Barber, 2010. © Wiley-Blackwell. Reprinted with permission).....	49
Figure 3.2: Schematic illustrating the orientation of the transect lines established on the sea ice in 2000, as well as the measurements to estimate snow depth at each sampling point along each transect.....	52
Figure 3.3: Time series of daily average temperature (a.), daily average humidity (b.), daily average wind speed (c.), daily average wind direction (d.) and daily precipitation (e.) for January 23 to May 23 2004. Dashed line on the graph of wind speed indicates the threshold wind speed for saltation (7.7 m/s). The open squares on the plot of wind direction (d.) indicate the average daily direction when wind speed was greater than 7.7 m/s. Wind direction is indicated as a degree (on the left axis) and as a qualitative direction on the right axis. N, E, S, and W represent the north, east, south and west direction (respectively). These directions are centred at 0°, 90°, 180° and 270° with a 45° tolerance. (From Iacozza and Barber, 2010. © Wiley-Blackwell. Reprinted with permission).....	61
Figure 3.4: (a.) Plot of the mean (closed circles) and one standard deviation (bars) for snow depth measured at the smooth ice sites between January 24 and May 5 2004. (b.) Three probability density functions representing different snow depth distribution sampled over smooth land-fast sea ice in 2004. The bin size is 2 cm. (From Iacozza and Barber, 2010. © Wiley-Blackwell. Reprinted with permission).....	64
Figure 3.5: Correlation length (a.), anisotropy (b.) and orientation (c.) derived from the variogram analysis for snow depth distributions measured over smooth land-fast sea ice in 2004. Note: For orientation 0° denotes east orientation of snowdrifts, while 90° denotes north orientation. (From Iacozza and Barber, 2010. © Wiley-Blackwell. Reprinted with permission).	66
Figure 3.6: The spatial change in snow depth along the parallel (a.) and perpendicular (b.) transects sampled in 2000. The bottom graphs show the time series of daily wind speed on ice (c.) and precipitation frequency (d.) for 2000. Dashed line on the graph of	

wind speed indicates the threshold wind speed for saltation. (From Iacozza and Barber, 2010. © Wiley-Blackwell. Reprinted with permission).....	68
Figure 3.7: Scatterplots of daily averaged temperature (a. and b.), relative humidity (c. through f.) and wind speed (g. and h.) measured at the ice meteorological station versus the weather station at Tuktoyuktuk and Paulatuk. The dashed lines represent the lines of best fit through the scatterplots. Included are the regression equations and R^2 values. (From Iacozza and Barber, 2010. © Wiley-Blackwell. Reprinted with permission).....	70
Figure 3.8: (a.) Cumulative frequencies in differences in classes of daily wind direction for Tuktoyuktuk (solid line) and Paulatuk (dashed line), compared to the wind direction measured on the sea ice. A difference of 1 would indicate a 45° difference in daily wind direction. (b.) Comparison of cumulative precipitation recorded on the sea ice at the CASES site, and at the Tuktoyuktuk and Paulatuk weather stations. (From Iacozza and Barber, 2010. © Wiley-Blackwell. Reprinted with permission).....	74
Figure 3.9: Comparison between the magnitude of SWE measured at the sampling sites (observed, solid line) and the four model runs using <i>SnowModel</i> (dashed lines). (From Iacozza and Barber, 2010. © Wiley-Blackwell. Reprinted with permission).	76
Figure 3.10: Probability density functions of observed SWE (dashed line) and modeled SWE (solid line) from <i>SnowModel</i> , for run 1 (a.), run 2 (b.), run 3 (c.) and run 4 (d). Only eight sampling days are shown to compare sampled and modeled SWE distributions. Bin size is 0.025 cm. (From Iacozza and Barber, 2010. © Wiley-Blackwell. Reprinted with permission).	78
Figure 3.10 con't: (From Iacozza and Barber, 2010. © Wiley-Blackwell. Reprinted with permission).....	79
Figure 4.1: Schematic of sampling for a. smooth and rubble ice and b. ridge sites. A diagram illustrating the measurements made at each location is provided in c.	89
Figure 4.2: Locations of ridge and rubble ice sites sampled in 2004. The star indicates the location of the meteorological site.....	92
Figure 4.3: Correlation and regression of standardized snow depth versus surface roughness for a. rubble sites and b. ridge sites. The correlation coefficient (r) and coefficient of determination (R^2), as well as the equation of the best-fit line through the scatter of points, for each ice class are included.	99
Figure 4.4: Correlation length and fractal dimension for rubble (a. and b. respectively) and ridge sites (c.). For rubble sites, correlation length and fractal dimensions are presented for the omnidirectional and directional data.....	101
Figure 4.5: Scatterplots of the correlation length of snow depth versus correlation length of surface roughness for rubble sites.....	104

Figure 4.6: Scatterplots of the fractal dimension of snow depth versus fractal dimension of surface roughness for rubble sites..... 105

Figure 4.7: Scatterplots of a. correlation length for snow depth versus correlation length of surface roughness and b. fractal dimension of snow depth versus fractal dimension of surface roughness for ridge sites. Open circles represent the values for ridges aligned in the east-west direction and closed circles represent the values for ridges aligned in the north-south direction. 107

Figure 5.1: Map of the IcePic transects sampled between 20 and 23 April. The star denotes the overwintering location of the icebreaker *CCGS Amundsen*. 119

Figure 5.2: Scatterplot of surface roughness (m) versus HOMO texture statistic based on a window size of 15x15 pixels. The texture measure was calculated for the April 19 VH ASAR image. The correlation coefficient (r) and the coefficient of determination (R^2) are provided. 127

Figure 5.3: Plots of the coefficient of determination (R^2) for the texture measures computed from the original images using four different window sizes. Each line represents the estimated R^2 for each image (different date of acquisition and/or polarization). 129

Figure 5.4: Plots of the coefficients of determination (R^2) for the MEAN (a. through c.) and VAR (d. through f.) texture measures computed from the speckle reduced images (frost - diamond, gamma - circle and lee - square) using four different window sizes. Each plot represents an individual image and texture measure. The lines represent the R^2 calculated for the different speckle reduction technique and/or polarization. 130

Figure 5.5: Same as Figure 5.4, except showing results for the HOMO (a. through c.) and CON (d. through f.) texture measure. 131

Figure 5.6: Same as Figure 5.4, except showing results for the ENT (a. through c.) and ASM (d. through f.) texture measure. 132

Figure 5.7: Scatterplot of surface roughness versus (a.) ENT or (b.) ASM values calculated from the gamma speckle reduced image and a window size of 15 pixels. The dashed line represents the line of best fit through the scatter. 134

Figure 5.8: Scatterplots of surface roughness and texture measures (ENT and ASM) for transect FEM04047 (open circles) and transect FEM04058 (closed circles). Results for transect FEM04047 were based on the VH image on April 19, while for transect FEM04058, the results were based on the HH image on April 22. A gamma speckle reduction technique was used on the original image and a window size of 15 pixels was used to compute each texture measure..... 136

Figure 6.1: Boundaries of the 13 polar bear subpopulations in Canada, and the spatial coverage of the ice charts. The complete names of the subpopulations are listed in Table 6.1..... 140

Figure 6.2: Plot of monthly and 12-month running average of the Arctic Oscillation index (data from the National Weather Service Climate Prediction Center)....	147
Figure 6.3: Summer (a) and autumn (b) open water anomalies calculated for the subpopulations within the Eastern Canadian Arctic (ECA) cluster (top), Canadian Arctic Archipelago (CAA) cluster (middle) and Beaufort Sea (BS) cluster (bottom).....	150
Figure 6.4: Summer (a) and autumn (b) multiyear sea ice anomalies calculated for the subpopulations within the Eastern Canadian Arctic (ECA) cluster (top), Canadian Arctic Archipelago (CAA) cluster (middle) and Beaufort Sea (BS) cluster (bottom).....	153
Figure 6.5: Summer (a) and autumn (b) first-year sea ice anomalies calculated for the subpopulations within the Eastern Canadian Arctic (ECA) cluster (top), Canadian Arctic Archipelago (CAA) cluster (middle) and Beaufort Sea (BS) cluster (bottom).....	155
Figure 6.6: Summer (a) and autumn (b) fast sea ice anomalies calculated for the subpopulations within the Eastern Canadian Arctic (ECA) cluster (top), Canadian Arctic Archipelago (CAA) cluster (middle) and Beaufort Sea (BS) cluster (bottom).....	158
Figure 6.7: Summer (a) and autumn (b) large floe size anomalies calculated for the subpopulations within the Eastern Canadian Arctic (ECA) cluster (top), Canadian Arctic Archipelago (CAA) cluster (middle) and Beaufort Sea (BS) cluster (bottom).....	159
Figure 6.8: Summer (a) and autumn (b) small floe size anomalies calculated for the subpopulations within the Eastern Canadian Arctic (ECA) cluster (top), Canadian Arctic Archipelago (CAA) cluster (middle) and Beaufort Sea (BS) cluster (bottom).....	160
Figure 6.9: Correlation between open water anomalies and temperature anomalies calculated from NCEP (National Centres for Environmental Prediction) data (top graphs) or AO (Arctic Oscillation) seasonal averages (bottom graphs). Statistically significant correlations ($p < 0.05$) are shown for the individual polar bear subpopulations. Negative (positive) correlations are shown in red (blue).	171
Figure 6.10: Correlation between multiyear sea ice anomalies and temperature anomalies calculated from NCEP (National Centres for Environmental Prediction) data (top graphs) or AO (Arctic Oscillation) seasonal averages (bottom graphs). Statistically significant correlations ($p < 0.05$) are shown for the individual polar bear subpopulations. Negative (positive) correlations are shown in red (blue).	172

Figure 6.11: Correlation between first-year sea ice anomalies and temperature anomalies calculated from NCEP (National Centres for Environmental Prediction) data (top graphs) or AO (Arctic Oscillation) seasonal averages (bottom graphs). The correlations are shown for the individual polar bear subpopulations. Negative (positive) correlations are shown in red (blue).174

Figure 6.12: Correlation between fast sea ice anomalies and temperature anomalies calculated from NCEP (National Centres for Environmental Prediction) data (top graphs) or AO (Arctic Oscillation) seasonal averages (bottom graphs). Statistically significant correlations ($p < 0.05$) are shown for the individual polar bear subpopulations. Negative (positive) correlations are shown in red (blue).176

Figure 6.13: Correlation between large floe size anomalies and temperature anomalies calculated from NCEP (National Centres for Environmental Prediction) data (top graphs) or AO (Arctic Oscillation) seasonal averages (bottom graphs). Statistically significant correlations ($p < 0.05$) are shown for the individual polar bear subpopulations. Negative (positive) correlations are shown in red (blue).177

Figure 6.14: Correlation between small floe size anomalies and temperature anomalies calculated from NCEP (National Centres for Environmental Prediction) data (top graphs) or AO (Arctic Oscillation) seasonal averages (bottom graphs). Statistically significant correlations ($p < 0.05$) are shown for the individual polar bear subpopulations. Negative (positive) correlations are shown in red (blue).179

LIST OF COPYRIGHTED MATERIAL

- Figure 2.1: First-year sea ice features formed in either calm or dynamic/rough conditions.. 8
- Figure 2.2: Mean geostrophic wind velocity (m/s) fields and annual mean sea level pressure contours for (a) 1979-88 and (b) 1989-96; anomaly fields of geostrophic wind velocity based on the differences (c) between the 1979-88 mean and the 1979-96 mean and (d) between the 1989-96 mean and the 1979-96 mean. The contour interval is 1.0 mbar. (From Zhang *et al.*, 2000. © American Meteorological Society. Reprinted with permission)..... 16
- Figure 2.3: Averaged volumes (km³) of ridged and level ice in (a) winter and (b) summer in the Eurasian (1) and Canadian (2) regions. (From Makshtas *et al.*, 2003. © American Geophysical Union. Reprinted with permission)..... 17
- Figure 2.4: Probability distribution functions of snow depth for four separate ice types. The vertical dot-dash line indicates the mean depth at the station. (From Sturm *et al.*, 2002. © American Geophysical Union. Reprinted with permission.) 20
- Figure 2.5: Standard deviation of snow depth as a function of average depth for the four classes of sea ice. (From Sturm *et al.*, 2002. © American Geophysical Union. Reprinted with permission) 21
- Figure 2.6: Relative frequency of observed transport threshold wind speed for dry snow and wet snow. (From Li and Pomeroy, 1997. © American Geophysical Union. Reprinted with permission.) 23
- Figure 2.7: Threshold wind speed for fresh snow (open circle) and aged snow (closed circle). (From Li and Pomeroy, 1997 © American Geophysical Union. Reprinted with permission)..... 23
- Figure 2.8: Snow depth, distance to nearest ice ridge, ice ridge height and ice ridge thickness measured at seal structures (solid bars) and habitat locations in general (open bars) for data collected in 1991-93. (From Furgal *et al.*, 1996. © National Research Council. Reprinted with permission) 31
- Figure 2.9: Mean density of ringed seals in relation to sea ice cover in western Hudson Bay. (From Lunn *et al.*, 1997. © National Research Council. Reprinted with permission)..32
- Figure 2.10: Seasonal cycle in selection by female polar bears of four ice type categories found in the (A) Arctic Archipelago and (B) Baffin Bay regions, 1991-1995. (From Ferguson *et al.*, 2000. © Ecological Society of America. Reprinted with permission)..36
- Figure 2.11: Seasonal cycle in selection by female polar bears of five ice cover categories found in the (A) Arctic Archipelago and (B) Baffin Bay regions, 1991-1995. (From Ferguson *et al.*, 2000. © Ecological Society of America. Reprinted with permission)..37

Figure 2.12: Seasonal cycle in selection by female polar bears of four sizes of ice floes found in the (A) Arctic Archipelago and (B) Baffin Bay regions, 1991-1995. (From Ferguson <i>et al.</i> , 2000. © Ecological Society of America. Reprinted with permission).....	39
Figure 2.13: Seasonal changes in movement for female polar bears inhabiting consolidated versus active ice in the Canadian Arctic. (From Ferguson <i>et al.</i> , 2001. © The Arctic Institute of North America. Reprinted with permission).....	41
Figure 2.14: Indices of habitat preference of polar bears by sex and age class. A value greater than one indicates preference, a value less than one indicates avoidance and a value of one indicates no preference. (From Stirling <i>et al.</i> , 1993. © Cambridge University Press. Reprinted with permission).....	44
Figure 3.1: Map of the Canadian Arctic illustrating the general locations of the sampling areas. The two insets show a detailed map of the sampling locations in 2000 (top inset) and 2004 (bottom inset). The stars in the insets indicate the location of the meteorological stations (both on ice and land-based) (From Iacozza and Barber, 2010. © Wiley-Blackwell. Reprinted with permission).....	49
Figure 3.2: Schematic illustrating the orientation of the transect lines established on the sea ice in 2000, as well as the measurements to estimate snow depth at each sampling point along each transect.....	52
Figure 3.3: Time series of daily average temperature (a.), daily average humidity (b.), daily average wind speed (c.), daily average wind direction (d.) and daily precipitation (e.) for January 23 to May 23 2004. Dashed line on the graph of wind speed indicates the threshold wind speed for saltation (7.7 m/s). The open squares on the plot of wind direction (d.) indicate the average daily direction when wind speed was greater than 7.7 m/s. Wind direction is indicated as a degree (on the left axis) and as a qualitative direction on the right axis. N, E, S, and W represent the north, east, south and west direction (respectively). These directions are centred at 0°, 90°, 180° and 270° with a 45° tolerance. (From Iacozza and Barber, 2010. © Wiley-Blackwell. Reprinted with permission).....	61
Figure 3.4: (a.) Plot of the mean (closed circles) and one standard deviation (bars) for snow depth measured at the smooth ice sites between January 24 and May 5 2004. (b.) Three probability density functions representing different snow depth distribution sampled over smooth land-fast sea ice in 2004. The bin size is 2 cm. (From Iacozza and Barber, 2010. © Wiley-Blackwell. Reprinted with permission).....	64
Figure 3.5: Correlation length (a.), anisotropy (b.) and orientation (c.) derived from the variogram analysis for snow depth distributions measured over smooth land-fast sea ice in 2004. Note: For orientation 0° denotes east orientation of snowdrifts, while 90° denotes north orientation. (From Iacozza and Barber, 2010. © Wiley-Blackwell. Reprinted with permission).	66
Figure 3.6: The spatial change in snow depth along the parallel (a.) and perpendicular (b.) transects sampled in 2000. The bottom graphs show the time series of daily wind speed on ice (c.) and precipitation frequency (d.) for 2000. Dashed line on the graph of	

wind speed indicates the threshold wind speed for saltation. (From Iacozza and Barber, 2010. © Wiley-Blackwell. Reprinted with permission).....	68
Figure 3.7: Scatterplots of daily averaged temperature (a. and b.), relative humidity (c. through f.) and wind speed (g. and h.) measured at the ice meteorological station versus the weather station at Tuktoyuktuk and Paulatuk. The dashed lines represent the lines of best fit through the scatterplots. Included are the regression equations and R ² values. (From Iacozza and Barber, 2010. © Wiley-Blackwell. Reprinted with permission).....	70
Figure 3.8: (a.) Cumulative frequencies in differences in classes of daily wind direction for Tuktoyuktuk (solid line) and Paulatuk (dashed line), compared to the wind direction measured on the sea ice. A difference of 1 would indicate a 45° difference in daily wind direction. (b.) Comparison of cumulative precipitation recorded on the sea ice at the CASES site, and at the Tuktoyuktuk and Paulatuk weather stations. (From Iacozza and Barber, 2010. © Wiley-Blackwell. Reprinted with permission).....	74
Figure 3.9: Comparison between the magnitude of SWE measured at the sampling sites (observed, solid line) and the four model runs using <i>SnowModel</i> (dashed lines). (From Iacozza and Barber, 2010. © Wiley-Blackwell. Reprinted with permission).	76
Figure 3.10: Probability density functions of observed SWE (dashed line) and modeled SWE (solid line) from <i>SnowModel</i> , for run 1 (a.), run 2 (b.), run 3 (c.) and run 4 (d). Only eight sampling days are shown to compare sampled and modeled SWE distributions. Bin size is 0.025 cm. (From Iacozza and Barber, 2010. © Wiley-Blackwell. Reprinted with permission).	78
Figure 3.10 con't: (From Iacozza and Barber, 2010. © Wiley-Blackwell. Reprinted with permission).....	79

GLOSSARY OF ABBREVIATIONS

<i>TERM</i>	<i>DEFINITION</i>
α	Orientation
AO	Arctic Oscillation
AP	Alternating polarization
ASAR	Advanced Synthetic Aperture Radar
ASM	Angular Second Moment (texture measure)
BB	Baffin Bay polar bear subpopulation
BS	Beaufort Sea cluster
C_{ij}	Conditional joint probability
CASES	Canadian Arctic Shelf Exchange Study
CAA	Canadian Arctic Archipelago cluster
C-ICE	Collaborative-Interdisciplinary Cryospheric Experiment
CIS	Canadian Ice Service
CL	Correlation length
CON	Contrast (texture measure)
COY	Cub of year
δ	Sampling distance
D	Fractal dimension
d_s	Measured depth of snow
DS	Davis Strait (polar bear subpopulation)
ECA	Eastern Canadian Arctic cluster
EMI	Electromagnetic induction
ENT	Entropy (texture measure)
ϕ	slope of 31-year trend analysis (% per decade)
FB	Foxe Basin (polar bear subpopulation)
F_c	Coriolis force
F_i	Internal ice stress
FS	Concentration of floe size
F_t	Sea surface tilt
FYI	First-year sea ice
$\gamma(h)$	Semivariance
GB	Gulf of Boothia (polar bear subpopulation)
GLCM	Grey-level co-occurrence matrix
h	Lag distance
HH	Horizontal-horizontal co-polarization
HL_c	Height of level at the centre point of the sampling grid
HL_x	Height of level at each <i>in situ</i> sampling point
HOMO	Homogeneity (texture measure)
HV	Horizontal-vertical cross-polarization
IC	Ice concentration
IT	Concentration of ice type
IT_c	Ice thickness at the centre point of sampling grid

IT _x	Ice thickness at each <i>in situ</i> sampling point
IUCN	International Union for the Conservation of Nature and Natural Resources
K-S	Kolmogorov-Smirnov
KB	Kane Basin (polar bear subpopulation)
LS	Lancaster Sound (polar bear subpopulation)
m	Slope of the log of lag distance versus the log of the semivariance
MC	M`Clintock Channel (polar bear subpopulation)
MEAN	Mean (texture measure)
MYI	Multiyear sea ice
N	Sample size
NB	Northern Beaufort Sea (polar bear subpopulation)
NCEP	National Centres for Environmental Prediction
NW	Norwegian Bay (polar bear subpopulation)
PAR	Photosynthetically active radiation
PDF	Probability density function
P _{ij}	Frequency of occurrence of grey levels of pixel i and pixel j
pixel i	Reference pixel for computing conditional joint probability
pixel j	Neighbor pixel for computing conditional joint probability
ρ _s	Density of snow
r	Correlation coefficient
R ²	Coefficient of determination
RB-	Rubble ice site designation
RD-	Ridge site designation
RH _i	Relative humidity measured on ice
SAR	Synthetic aperture radar
SB	Southern Beaufort Sea (polar bear subpopulation)
SD _c	Snow depth at the centre point of sampling grid
SD _x	Snow depth at each <i>in situ</i> sampling point
SH	Southern Hudson Bay (polar bear subpopulation)
SWE	Snow water equivalent
T _i	Air temperature measured on the ice
T _{PS}	Air temperature measured at the Paulatuk weather station
T _{TS}	Air temperature measured at the Tuktoyuktuk weather station
τ _a	Drag on the top of the sea ice by atmospheric processes
τ _w	Drag on the bottom of the sea ice by water or ocean currents
U winds	East-west component of wind
V winds	North-south component of wind
VAR	Variance (texture measure)
VH	Vertical-horizontal cross-polarization
VM	Viscount Melville Sound (polar bear subpopulation)
VV	Vertical-vertical co-polarization
WH	Western Hudson Bay (polar bear subpopulation)
WMO	World Meteorological Organization

x_i	Measured sample value at point i
x_{i+h}	Measured sample value at point $i+h$

CHAPTER 1: INTRODUCTION

1.1 INTRODUCTION TO DISSERTATION

The marine cryosphere plays a fundamental role in Arctic dynamics, and in particular, in the habitat selection of ringed seals and polar bears. The cryosphere can be defined as the atmosphere, snow/sea ice and ocean, and the interactions between these strata. Snow-covered sea ice in the Arctic regions is a significant part of this system varying in space and time. On average, sea ice covers a maximum area of approximately 15.7×10^6 km² during the winter (peak extent in late March; Parkinson, 2000). At the end of the melt season (occurring in early September), approximately half of the sea ice area has ablated, leaving the remaining sea ice confined to the central Arctic Ocean. In terms of the snow cover, accumulation begins in the autumn season when sea ice is beginning to form. The maximum snowfall is reached during the autumn and early winter season (December and January), with limited accumulation occurring in the spring and summer seasons (Warren *et al.*, 1999; Sturm *et al.*, 2002). Not only is the amount of meteoric snowfall on the sea ice an important component of the cryosphere, but also the spatial distribution of snow as a function of location and ice type. Due to a limited number of weather reporting stations in the Arctic and because of our inability to estimate snow thickness over space using remote sensing techniques, limited research has focused on the snow catchment hydrology as it relates to first-year sea ice (FYI) evolution.

The snow-covered sea ice plays an important role in the meteorological and

oceanic processes operating within the Arctic system. This layer acts as a barrier between the ocean and atmosphere, limiting matter and energy flow between these two strata. Owing to its low thermal conductivity (0.1 to 0.4 W/m² for snow and 1 to 4 W/m² for sea ice) and high albedo (0.5 for bare ice to 0.9 for freshly deposited snow), snow-covered sea ice controls the conductive fluxes from the underlying warmer ocean to the overlying colder atmosphere during the winter season, while also reducing the amount of solar radiation absorbed at the surface (Kotlyakov and Grosswald, 1990; Moritz and Perovich, 1996). For instance, during the winter period, heat flux through an opening or lead in the sea ice is two orders of magnitude greater than that through the surrounding snow-covered sea ice (Maykut, 1986). The snow cover layer regulates the growth and decay of sea ice by impeding ice growth through the reduction of conductive heat flux and moderation of shortwave radiation entering into the ice layer (Maykut, 1986; Eicken *et al.*, 1995; Eicken, 2003). Snow cover accumulating on sea ice will also have a general net cooling effect on the global climate (Ledley, 1991). Ocean circulation is also impacted by the formation and melting of the snow-covered sea ice. During the freeze-up period, sea ice expunges brine and this flux controls the formation of deep and bottom waters and drives convection within the water column (Lemke *et al.*, 2000). During the melt period, fresh water from the ablation of the overlying snow layer is introduced into the water column through leads or holes in the sea ice, causing the stabilization and retreat of the mixed layer from the surface (Lemke *et al.*, 2000).

The economical and social culture of the Canadian Inuit is also dependent on the

snow/sea ice component of the cryosphere. The Inuit have been utilizing sea ice for over 5000 years (Riewe, 1991). Snow-covered sea ice characteristics as related to the habitat and hunting of ringed seal and polar bear has been qualitatively documented for over six decades (Stefansson, 1945; Nelson, 1969). Currently, traditional Inuit and Eskimo peoples depend on the snow-covered sea ice and associated habitat of various Arctic mammals (i.e. polar bears and ringed seals) as an important food source and support for local economy, through commercial harvesting. As well, these relationships form the basis for their cultural and social identity, by strengthening social relationships (Berkes, 1998). In the past, the Inuit would construct igloo villages, essentially snow houses, on the sea ice close to their hunting grounds (Cooke, 1984).

Snow-covered sea ice is also a major controlling factor in the ecology of the Arctic system. During the spring period, snow-covered sea ice controls the amount of photosynthetically active radiation (PAR) reaching the underlying ocean (Welch and Bergmann, 1989; Iacozza and Barber, 1999; Mundy *et al.*, 2005). PAR plays an important role in algal production and provides nutrients for copepods, which is an important food source for Arctic cod and other Arctic fish species, and ultimately for other mammals in the Arctic food web that rely on these fish species. The habitat selection by apex predators of the Arctic ecosystem is also controlled by snow-covered sea ice and its associated spatial distribution. Preferentially thick snow drifting associated with rough first-year sea ice (i.e. sea ice with considerable ice surface topography created by large ridges) is preferred by ringed seals for the construction of their birthing and resting lairs (Hammill and Smith, 1989; Furgal *et*

al., 1996; Ferguson *et al.*, 2005). Predator/prey dynamics mean that the preferred habitat of polar bears closely coincides with the distribution of deformation catchments (Welch, 1991; Stirling and Derocher, 1993). Polar bears, as with ringed seals, generally select thick first-year sea ice in areas with complete or almost complete ice cover (Ferguson *et al.*, 2000; Ferguson *et al.*, 2001). However spatial and temporal variability exists in the relationship between snow-covered sea ice conditions and polar bear habitat selection (Ferguson *et al.*, 2000; Durner *et al.*, 2004). A more complete discussion of the linkages between the environmental conditions and ringed seal/polar bear habitat are provided in Chapter 2.

Conservation of polar bears in the Canadian Arctic has been an issue for several decades and has received considerable attention in the recent popular media and scientific community. In the early 1970s, the Agreement on Conservation of Polar Bears was signed by the circumpolar countries partly in response to increased hunting and concern of polar bear populations. This agreement outlined the delineation and management of polar bear populations throughout the circumpolar Arctic. As part of its agreement, the contracting parties approved the protection of the ecological systems of which polar bears are a part (Article II; Prestrud and Stirling, 1994). While this agreement has had significant influence on stabilizing and securing polar bear populations, some shortcomings exist. To protect the ecosystems of polar bears, the physical factors controlling the habitat of polar bears (as well as other Arctic species such as the ringed seal) needs to be established. The study of habitat relationships between Arctic marine mammals and dynamic processes in the marine cryosphere is limited by (i) the remoteness of the area and

the associated high logistic costs; (ii) the low densities of the marine mammals in the Arctic, requiring a large sampling area and (iii) the semi-permanent nature of the system - icescape features deemed important for polar bear and ringed seal habitat (i.e. sea ice ridging and snow distribution) exhibit considerable spatial and interannual variability. A better understanding of the relationship between snow catchment and sea ice topography, along with the use of remote sensing technologies will allow a more complete understanding of the habitat relationships for ringed seals and polar bears, as well as climate change implications to the habitat relationships.

1.2 OBJECTIVES OF DISSERTATION

The overarching aim of this dissertation is to examine the spatial distribution and temporal evolution of snow and sea ice characteristics related to polar bear habitat over a variety of scales. Within this aim, there are four primary objectives:

- i. The first objective (i.e. Chapter 3) is to examine and characterize the evolution of snow depth over smooth first-year sea ice and to determine if land-based meteorological observations can be used to estimate the meteorological conditions over sea ice. This objective will also assess the ability of a snow evolution model (*SnowModel*) to estimate the temporal change in snow cover over smooth land-fast sea ice.
- ii. The second objective (i.e. Chapter 4) is to investigate snow depth distribution and evolution over rough sea ice. This will be accomplished by describing the spatial pattern of snow distribution as a function of sea ice roughness and how

the observed spatial pattern evolves over rubble sea ice and ridges as a consequence of meteorological forcing. The first two objectives of this dissertation rely on *in situ* measurements of snow-covered sea ice, generally not a logistically practical method of snow data collection in the Arctic.

- iii. The third objective (i.e. Chapter 5) is to determine if surface roughness of snow-covered sea ice can be estimated using remote sensing imagery, a more convenient method for studying Arctic processes. In addition the effects of various satellite processing techniques (i.e. speckle reduction techniques) and image characteristics (i.e. polarization, incidence angle and path) on the estimation of surface roughness using a grey-level co-occurrence matrix (GLCM) texture technique will be investigated. The first three objectives of this dissertation examine various aspects of snow-covered sea ice over local spatial and daily temporal scales.
- iv. The final objective (i.e. Chapter 6) examines the evolution of sea ice characteristics related to polar bear habitat at regional spatial scales over decadal temporal scales. The spatial and temporal patterns of sea ice characteristics within the polar bear subpopulations in the Canadian Arctic between 1978 and 2008 will be described, and discussed in the context of published variation in polar bear population condition. The dynamic and thermodynamic factors that may influence these changes will also be studied.

1.3 STRUCTURE OF DISSERTATION

This dissertation is divided into seven chapters. An introduction for this dissertation, which provides the context for this research and the objectives are presented in Chapter 1. Chapter 2 provides a background into the dynamic processes which govern the formation of sea ice topography and associated snow catchment as related to polar bear habitat. A discussion of snow covered sea ice as related to ringed seal habitat is also provided in this chapter, since ringed seal and polar bear habitat are intricately related. Chapters 3 through 6 present the methods utilized and results from each of the four objectives of this dissertation defined above. Chapter 7 presents a conclusion to this dissertation by discussing the potential climate change implications of snow covered sea ice on polar bear habitat.

CHAPTER 2: BACKGROUND

2.1 DYNAMIC PROCESSES RELATED TO SNOW COVERED SEA ICE

2.1.1 First-year sea ice features

During the evolution of first-year sea ice (FYI), dynamic processes play a critical role in the formation of specific iceforms and influencing the ice thickness over an area. In calm conditions, the evolution of FYI creates smooth ice (Figure 2.1).

Thermodynamic processes are the principal processes responsible of the formation of this ice type. The formation and growth of this ice type will be dependent on the temperature of the atmosphere and ocean, the thickness of the sea ice and the presence of a snow cover (Haas, 2003). At the macroscale, no noticeable surface features are created on this ice type and it can be considered non-deformed, level ice. The thickness of smooth FYI over an area is known as the thermodynamic thickness.

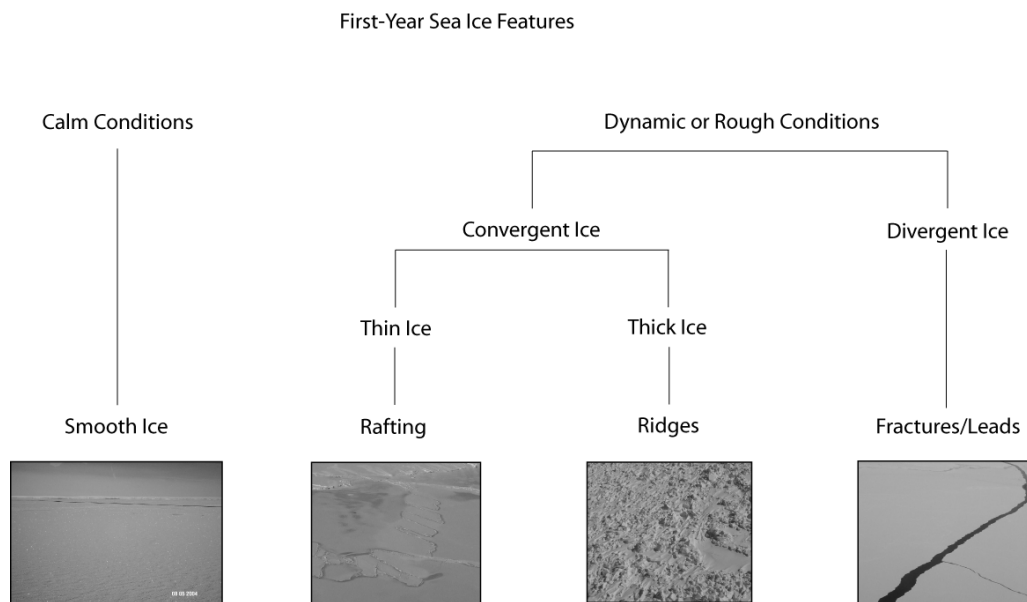


Figure 2.1: First-year sea ice features formed in either calm or dynamic/rough conditions.

Dynamic or rough conditions in the atmosphere and/or ocean form a number of ice types and will influence the ice thickness within an area. Sea ice can be described as large floes that move and interact (i.e. converge or diverge) under the influence of wind and ocean currents. Since ice does not have great strength under tension (Wadhams, 2000), the diverging ice will create fractures or leads in the sea ice (Figure 2.1). During the winter period, these leads may refreeze because of the significant temperature difference between the atmosphere and the ocean, forming thin ice and thus producing ice thicknesses less than the thermodynamic thickness. This thin ice will be generally be weaker than the surrounding ice and may crack again under divergent forces or be sites of convergence.

Drifting ice may also converge, resulting in rafting or ridging depending on ice thickness (Figure 2.1), leading to an increase in the ice thickness (relative to the thermodynamic thickness). Rafting is a pressure process where one ice floe overrides another floe (Parmeter, 1975). This process is common in new or young ice with ice thickness less than 0.6 m. Surface features are less pronounced in this type of deformation, compared to ridging. Ridging occurs when thicker ice floes (greater than 1 m) converge or collide due to dynamic forces. The continual pressure created by the collision may exceed the internal strength of the sea ice, resulting in the failure of the ice and formation of ice blocks (Parmeter and Coon, 1972). If the dynamic forces continue, these ice blocks will pile onto one another forming long linear features (i.e. pressure ridges) or a mass of randomly dispersed block structures (i.e. rubble or hummock field; Figure 2.1), which have a greater thickness relative to the surrounding non-deformed ice. Shear ridging occurs when

there is shearing and grinding between two ice floes, with more lateral movement compared to convergent movement. This feature is common in locations where ice drifts against a coast or landfast sea ice. In the Arctic, ridges can obtain thickness of tens of meters (Lubin and Massom, 2006); an important contribution to the mass of the sea ice. It has been estimated that ridging of the sea ice accounts for on average 50% of the ice volume in the central Arctic Basin and increases to 65% in the coastal regions (Flato and Hibler, 1995; Wadhams, 2000). Regional variability in the amount of ridging exists with more ridging in the Canadian Basin, compared to the Eurasian Basin. This greater ridging results in ice thicknesses 2-3 times greater north of the Canadian Arctic Archipelago than for the sea ice north of Siberia (Flato and Hibler, 1995; Wadhams, 2000).

2.1.2 Dynamic processes

The divergent iceforms defined in Section 2.1 are created by a combination of dynamic forces. These forces describe the movement of the ice floe and can be defined by [2.1]:

$$M = \tau_a + \tau_w + F_c + F_i + F_t \quad [2.1]$$

where M is the momentum associated with the movement of the sea ice floe, τ_a is the drag on the top of the sea ice by atmospheric processes (i.e. wind stress), τ_w is the drag on the bottom of the sea ice by water or ocean currents, F_c is the Coriolis force, F_i internal ice stress and F_t is the sea surface tilt. Of the five forces, water stress and wind stress are greater than the other three forces by an order of magnitude (Haas,

2003) and therefore considered the most important forces acting on the sea ice to form deformation structures.

Wind Stress

Once the ice has formed, surface winds will act on the surface of the sea ice and cause divergence or convergence. Wind forcing of the sea ice is the primary stress acting on the sea ice to cause movement during the winter season (Steele *et al.*, 1997; Richter-Menge *et al.*, 2002). This factor dominates the short-term movements of sea ice on the scale of a few days and may explain up to 70% of sea ice motion at that time scale (Thorndike and Colony, 1982; Heil *et al.*, 1998; McNutt and Overland, 2003). These processes can operate at the local scale, with localized winds influencing convergence or divergence of floes or at larger scales (i.e. atmospheric circulation patterns at the regional or hemispheric scales).

Wind stress exhibited onto a snow-covered ice surface can be estimated as a product of the air density, wind velocity and air-ice drag coefficient. Assuming consistent air density and air-ice drag coefficient, as the wind velocity increases, the wind stress and hence the movement of sea ice will also increase. One environmental condition that influences the wind velocity is the atmospheric pressure gradient, which varies locally and over short time scales (i.e. hours to days). A steeper pressure gradient will result in stronger wind velocities and thus greater potential for ice drift. In the Baltic Sea, wind velocity explains 80% of the variability in the sea ice drift (Uotila, 2001). The rate of ice movement caused by wind stress is generally estimated to be 2% of the wind speed (Richter-Menge *et al.*,

2002), but may be higher in areas with low ice concentrations (and thus less obstacles for drifting).

The air-ice drag coefficient component of the wind stress is dependent on the characteristics of the sea ice including sea ice type and amount of surface roughness at the local-scale. Surface ice roughness will impact the air-ice drag coefficient. Smooth sea ice has a lower air-ice drag coefficient compared to rough or deformed sea ice (2.0×10^{-3} vs. 3.1×10^{-3} for smooth and rough first-year sea ice respectively; Wadhams, 2000), suggesting that differences in surface geometry may change the drag coefficient by up to a factor of two (Banke *et al.*, 1980). The ice deformation features will act as a sail, propelling the ice along with the wind. Therefore, the density and height of the ridges will control the air-ice drag coefficient.

Water Stress

Stress exerted on the sea ice by ocean currents is also an important factor in sea ice dynamics. The motion of water will exert a force onto the bottom of the ice causing movement. The amount of force that will be exerted onto the ice is affected by parameters similar to those controlling the wind stress, including water density, velocity of the water and ice-water drag coefficients. A strong current will, in combination with the wind stress, act to accelerate a floe, while the surface water or still water will act to counter the wind stress and the floe may slow down (Wadhams, 2000).

The ice-water drag coefficient, like the air-ice drag coefficient, is a function of the characteristics of the sea ice. The underside of MYI is generally rougher than first-

year sea ice, thus it will have a greater ice-water drag coefficient and cause greater movement of the sea ice (Wadhams, 2000). Smooth first-year sea ice will have a lower ice-water drag coefficient, compared to rough first-year sea ice due to the presence of the keels under ridges. For rough FYI, the keels of the ridges will act like the sails above the surface of the ice to move the sea ice with the water currents. The density and depths of the keels are positively correlated with the ice-water drag coefficient (Wadhams, 2000). Sea ice thickness will also impact the movement of sea ice due to water stress. This difference in ice thickness constitutes a greater component of the ice-water drag coefficient compared to air-ice drag coefficient because the boundary layer under ice is much smaller than that over the sea ice (Wadhams, 2000). The water stress in an area (determined by the permanent ocean currents) dominates the long-term movement of sea ice. Combined, the wind and water stresses act to significantly influence the dynamic processes operating in the Canadian Arctic to produce the deformation structures defined in Section 2.1.

Large-scale Arctic Ocean circulation patterns influence the water stress component of the sea ice dynamics. The Beaufort Gyre is characterized as anticyclonic circulation (i.e. clockwise) in the Canadian Basin and is caused by the strong winds produced by a quasi-permanent high atmospheric pressure in the area (Haas, 2003). It takes approximately four (4) years for the gyre to make one complete rotation. The majority of deformation of sea ice in the Arctic is attributed to the motion of the gyre (Melling and Riedel, 1995). Sea ice within the gyre will be in motion, constantly diverging and converging relative to other ice floes. This movement will result in rafting/ridging, increasing the ice thickness in the Canadian

Basin. The circulation will also result in ice being pushed up against the coast of the Canadian Arctic Archipelago. In addition, the Transpolar Drift or Current, which is driven by cyclonic systems, is the other Arctic Ocean circulation pattern that transports ice from the Eurasian Basin into Fram Strait. Sea ice thickness is thinner in the Eurasian Basin where the Transpolar Drift continually transports ice out of the area. A smaller circulation pattern is located in the waters of the Barents Sea. The Barents Gyre rotates in a counterclockwise fashion due to the counterclockwise wind system that dominates the area, creating sea ice conditions similar to those experienced in the Canadian Basin.

On the larger scale, the sea ice dynamics in the Arctic are controlled by the combined efforts of atmospheric and oceanic circulation patterns at the synoptic-scale. The Arctic Oscillation (AO) and the North Atlantic Oscillation (NAO) are part of the North Annular Mode (NAM). The NAM describes the variability in the atmospheric flow that is not associated with the seasonal cycle. The NAO is a dipole in sea level pressure between temperate (i.e. Azores High) and high latitudes (i.e. Icelandic Low) over the Atlantic region, and is dominant in the winter months (Hurrell et al., 2003). During the positive (negative) phase, the Azores High and Icelandic Low are enhanced (diminished). This oscillation is a regional pattern controlled by Atlantic sector processes. The AO characterizes the contrasting atmospheric pressure patterns in the northern middle latitudes and high latitudes. During the 'negative' phase, a high pressure system forms over the polar regions, while a low pressure occurs at middle latitudes, while the opposite pattern in pressure is observed during the 'positive' phase. While similar to the NAO, this

oscillation is a hemispheric scale pattern of atmospheric pressure differences that is strongest in the Atlantic sector, however it influences circulation throughout the northern hemisphere.

The AO is a dominant decadal variation in sea-level pressure that forms over the Arctic region. Between 1950 and 1988, the AO index was low or negative (Yu *et al.*, 2004) due to higher than normal Arctic sea level pressure, causing a strengthening of the Beaufort high-pressure system. This strengthening of the Beaufort high produced anticyclonic circulation of the wind anomaly over the Arctic (Figure 2.2; Zhang *et al.*, 2000). As a consequence, the Beaufort Gyre strengthened, causing sea ice to be circulated longer within the Arctic Basin. Sea ice was pushed from the Canadian Basin into the Eurasian Basin with less ice advected out of the Arctic through the Transpolar Drift. This corresponded to greater ice convergence and thus greater deformation/ridging and ice volume in the Arctic (Figure 2.3; Zhang *et al.*, 2000; Rigor *et al.*, 2002; Makshtas *et al.*, 2003; Yu *et al.*, 2004). Ridged ice volume was generally greater in the winter season, compared to the summer period for the Canadian Basin between 1950 and 1988 (Figure 2.3). In the period between 1989 and 1996, the Beaufort high weakened causing a cyclonic wind anomaly to form over the Arctic Ocean (Figure 2.2; Zhang *et al.*, 2000), pushing relatively thinner ice from the Eurasian Basin into the Canadian Basin. This weakening corresponded to a change in phase of the AO, with the AO in a positive phase (or AO index higher than normal). This resulted in more ice advected through Fram Strait via the Transpolar Drift, causing ice divergence and a decrease in ice volume (Figure 2.3; Zhang *et al.*, 2000; Rigor *et al.*, 2002; Makshtas *et al.*, 2003; Yu *et al.*, 2004). In

addition, less ridging was occurring within the Canadian Basin due to the weakening of the gyre. Barber and Hanesiak (2004) found that AO modes could account for 25% of the variance in sea ice concentration anomalies in the Southern Beaufort Sea.

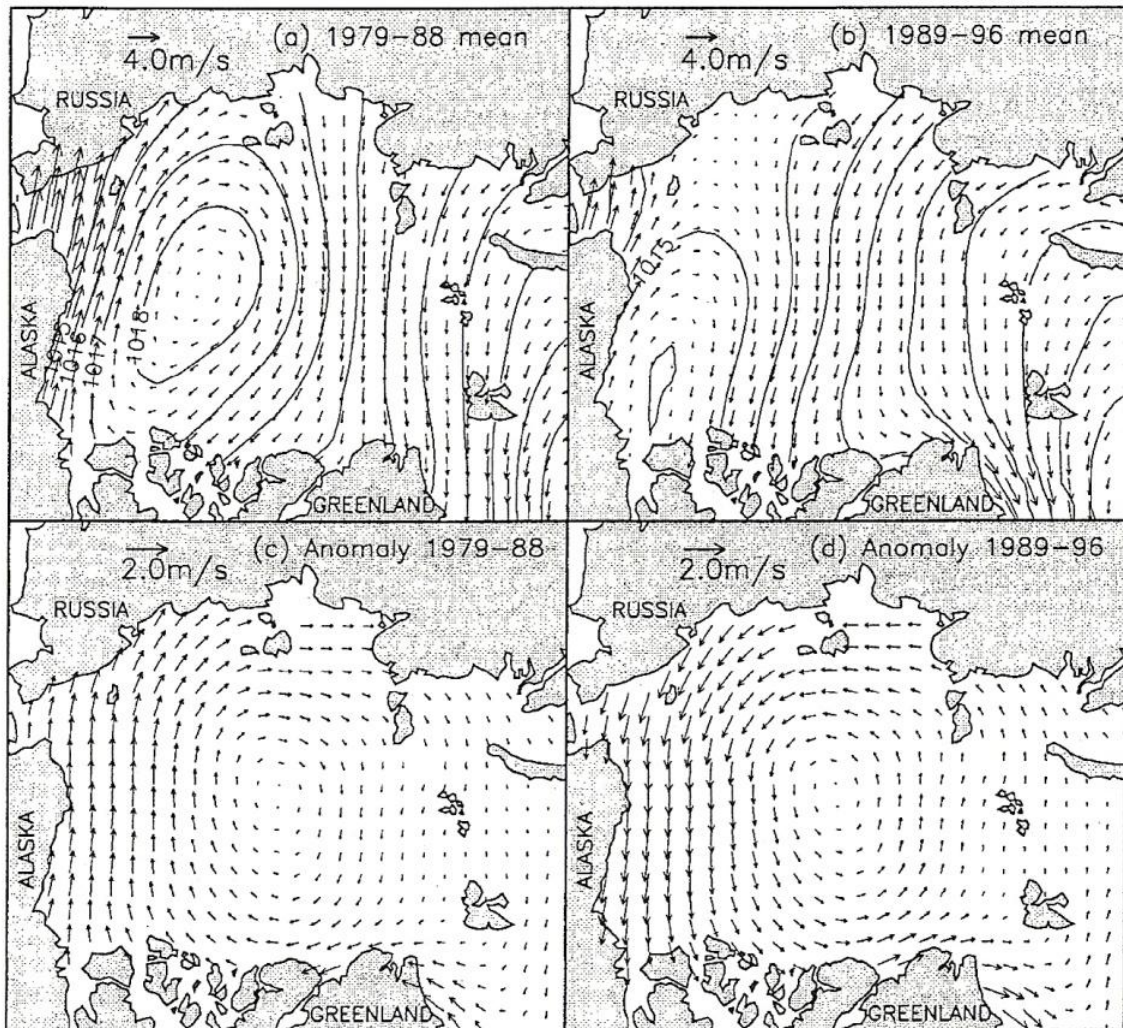


Figure 2.2: Mean geostrophic wind velocity (m/s) fields and annual mean sea level pressure contours for (a) 1979-88 and (b) 1989-96; anomaly fields of geostrophic wind velocity based on the differences (c) between the 1979-88 mean and the 1989-96 mean and (d) between the 1989-96 mean and the 1979-88 mean. The contour interval is 1.0 mbar. (From Zhang *et al.*, 2000. © American Meteorological Society. Reprinted with permission)

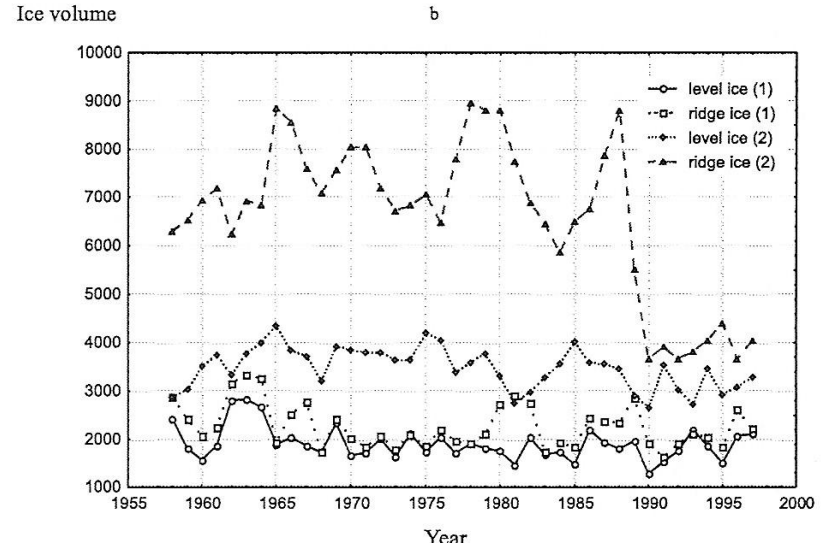
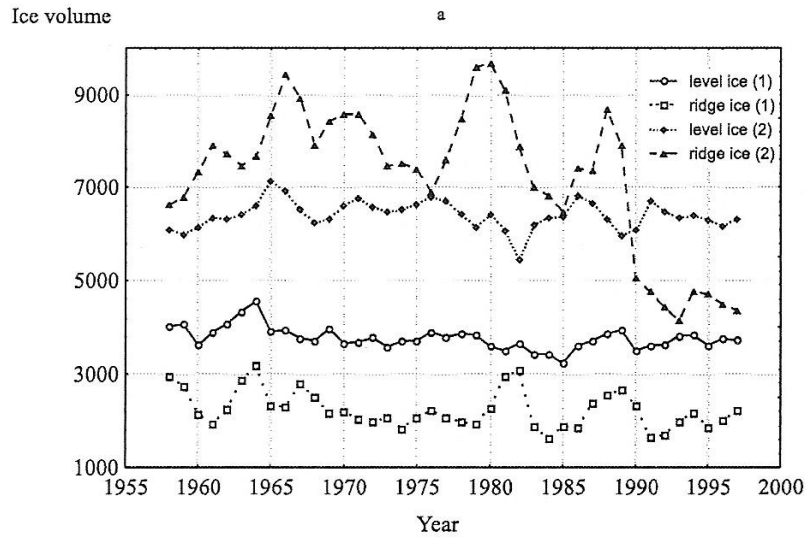


Figure 2.3: Averaged volumes (km³) of ridged and level ice in (a) winter and (b) summer in the Eurasian (1) and Canadian (2) regions. (From Makshtas *et al.*, 2003. © American Geophysical Union. Reprinted with permission)

Other Factors

Dynamic processes related to sea ice are also influenced by the Coriolis force, internal ice stress and sea surface tilt, but to a much lesser degree than wind and water stresses. Due to the rotation of the Earth, the Coriolis force will accelerate the movement of sea ice, as well as deflecting ice to the right of the intended path. The amount of force and the deflection is proportional to the mass of the sea ice, with thicker ice having a greater Coriolis force, compared to thin sea ice (Wadhams, 2000). In terms of dynamic processes on the sea ice, this force is more significant at the global and hemispheric scales, compared to local or regional scales (Wadhams, 2000). Internal ice stress is related to the compactness of the sea ice and acts to counter the wind stress. In areas with a high concentration of ice cover, the internal stress will be high and the movement of the sea ice may be minimal (i.e. the sea ice will have no place to move). In an environment with open water and leads, the compaction of the sea ice and thus the internal stress will be low, allowing more movement due to wind stress. Internal stress also increases when the sea ice converges and the ice will fail when the strength of the ice exceeds the internal stress (Wadhams, 2000). This will result in the formation of leads or deformed sea ice. Sea surface tilt corresponds to differences in the ocean surface level. On a large scale, the ocean surface is not flat, rather it consists of high and low areas caused by gravity differences, as well as uneven heating, salinity variations and ocean currents. This force is more important over longer time periods (i.e. years) and is negligible over a period of hours or days, accounting for only a few percent of ice motion (Wadhams, 2000).

2.1.3 Snow catchment

Snow catchment hydrology over first-year sea ice is determined by characteristics of the sea ice (age of sea ice and surface topography), as well as meteorological conditions (namely wind speed and precipitation amounts). Deeper snow will generally be found on older first-year and multiyear sea ice, compared to newly formed sea ice or refrozen leads since a greater temporal period has elapsed to catch any meteoric snowfall in the area (Massom *et al.*, 2001). With regards to precipitation, sea ice in areas with higher snowfall amounts will be expected to have greater median snow depth, compared to areas with lower snowfall. In addition, if sea ice forms in the late winter after the peak in snowfall, one would expect a lower median snowfall over the sea ice.

The dynamic processes responsible for sea ice topography discussed in Section 2.2 also play a key role in the snow catchment hydrology over first-year sea ice. The pattern of snow distribution is primarily controlled by the sea ice surface topography formed by the dynamic processes operating in the environment (Eicken *et al.*, 1994; Jeffries *et al.*, 1995; Adolphs, 1999; Iacozza and Barber, 1999; Sturm *et al.*, 2002; 2006). As the surface roughness increases, the snow holding capacity of the sea ice also increases. Therefore sea ice with large ridges or hummocks tends to have a deeper snow cover, resulting in greater median snow depths (Figure 2.4; Iacozza and Barber, 1999; Sturm *et al.*, 2002). For first-year sea ice with small topographic features (i.e. smooth first-year sea ice), the snow-holding capacity is lowest among different ice types and thus exhibits the thinnest snow depths. In the Antarctic, it has been estimated that snow depth over deformed sea ice is four (4)

times greater than that over adjacent smooth ice (Eicken *et al.*, 1994). The same relationship is true with regards to the variability of the snow depth over different surface topographic features (Figure 2.5; Sturm *et al.*, 2002; 2006). The median snow depth increases as the variability in surface roughness increases (i.e. due to larger density of ridges), assuming no difference in snowfall or age of sea ice. This suggests that the snow cover over smooth first-year sea ice is relatively uniform, while greater variations in snow depth observed over ridged and rubble sea ice (Iacozza and Barber 1999; Sturm *et al.*, 2002).

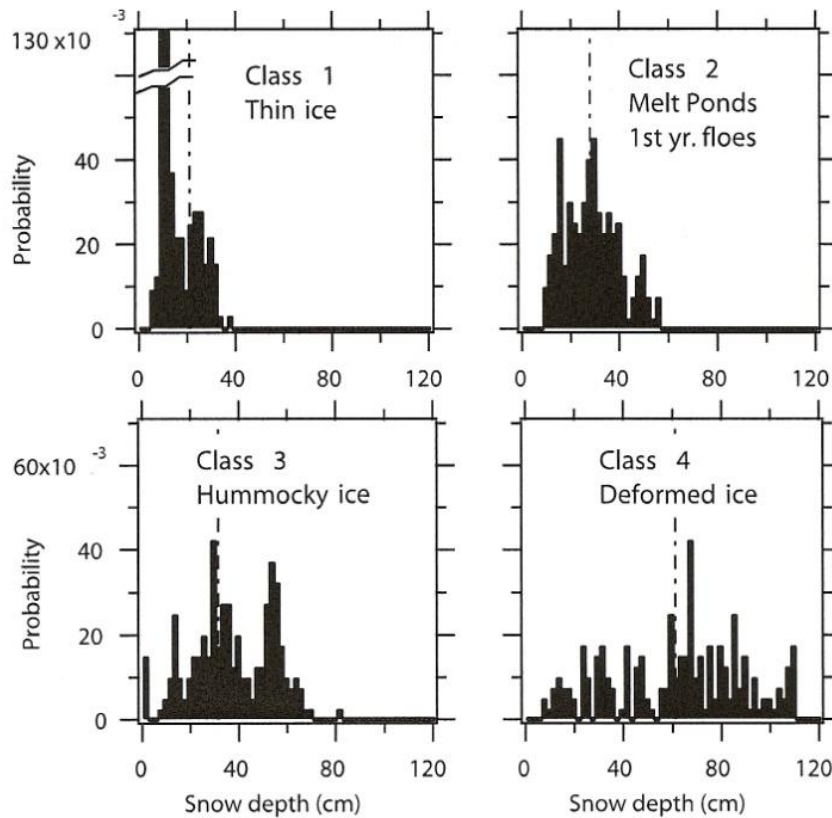


Figure 2.4: Probability distribution functions of snow depth for four separate ice types. The vertical dot-dash line indicates the mean depth at the station. (From Sturm *et al.*, 2002. © American Geophysical Union. Reprinted with permission.)

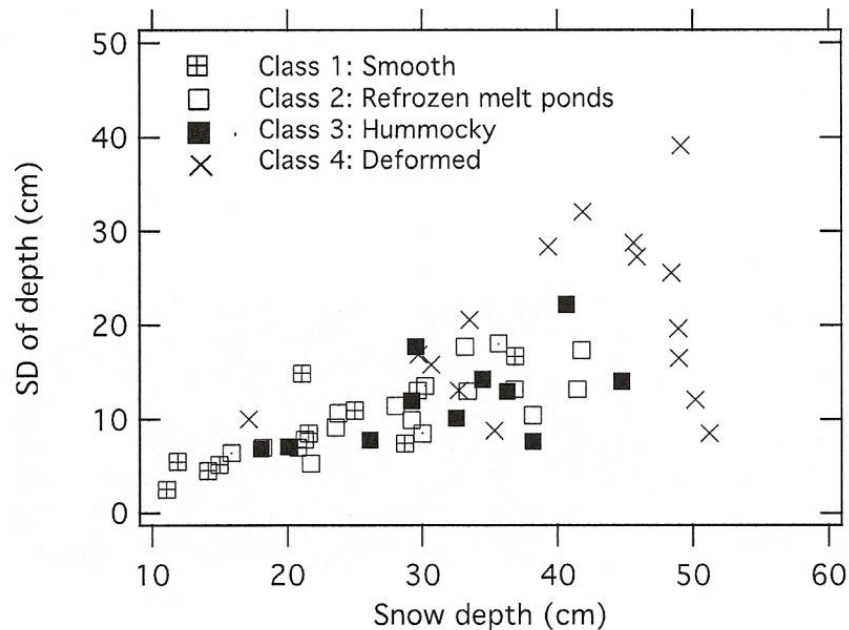


Figure 2.5: Standard deviation of snow depth as a function of average depth for the four classes of sea ice. (From Sturm *et al.*, 2002. © American Geophysical Union. Reprinted with permission)

Snow transport also plays a critical role in the development of snow distribution over sea ice. Snow can redistribute over the surface through three transport processes: surface creep, suspension and saltation. The bulk of the mass transport of snow over sea ice (approximately 75%) is accomplished through saltation (Bagnold, 1941). Saltation is the bouncing of snow particles along the surface of the snow. An individual snow particle will be influenced by a number of forces including aerodynamic lift and drag, cohesion and gravity. Aerodynamic lift and drag are created by the wind over the surface and act as a drag force. Gravity and cohesion (or intercrystal bond strength) are considered resisting forces since they act to keep the snow particle on the surface. Of the two forces, cohesion is

considered the more dominant resisting force (Schmidt, 1980). Erosion through saltation occurs when the atmospheric drag force or shear velocity exceeds the resisting forces or threshold velocity. The threshold velocity for snow drifting (recorded at 10 m) through saltation is dependent on the cohesion of the snow particles, i.e. whether the snowpack is considered to be in a loose (less cohesion) or wind-hardened state (more cohesion). Empirical studies of threshold velocities suggest that typical values recorded at 10 m ranged from 6-9 m/s for wind-hardened snow (Pomeroy and Gray, 1990) to approximately 4.5 m/s for loose snow (Budd *et al.*, 1966; Schmidt, 1982). The cohesion between snow particles will be greater for wind-hardened snow, especially at the surface where particles are exposed to the atmospheric conditions and wind. Therefore a lower wind speed will be required to move snow in a loose state (i.e. during or right after snowfall). The threshold velocity is also related to whether the snow surface is in a wet state (with a wet cohesive regime and thus more cohesion between snow crystals) or in a dry state (warm or cold cohesive regime and less cohesion between snow crystals). Li and Pomeroy (1997) found average threshold velocities to be 9.9 m/s for wet snow and 7.7 m/s for dry snow (Figure 2.6). The age of the snow pack will also influence the threshold velocity (Schmidt, 1980). Older snow generally requires a higher threshold wind speed to initiate saltation (8.0 m/s), compared to fresh snow (7.5 m/s) (Li and Pomeroy, 1997; Figure 2.7). After deposition, snow will undergo metamorphism, thus increasing the bonding between individual particles and the cohesion of the top of the snowpack. The threshold wind speed increases

progressively when drifting continues without an additional snowfall due to the compaction and hardening of the surface that occurs (Kind, 1981).

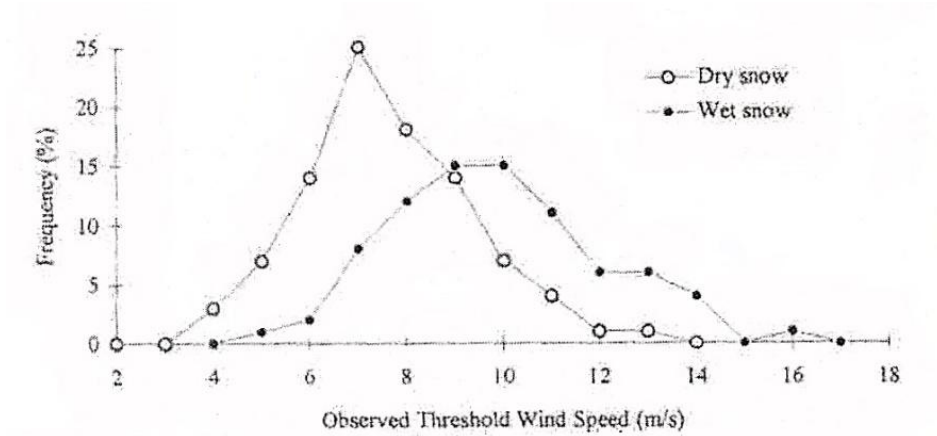


Figure 2.6: Relative frequency of observed transport threshold wind speed for dry snow and wet snow. (From Li and Pomeroy, 1997. © American Geophysical Union. Reprinted with permission.)

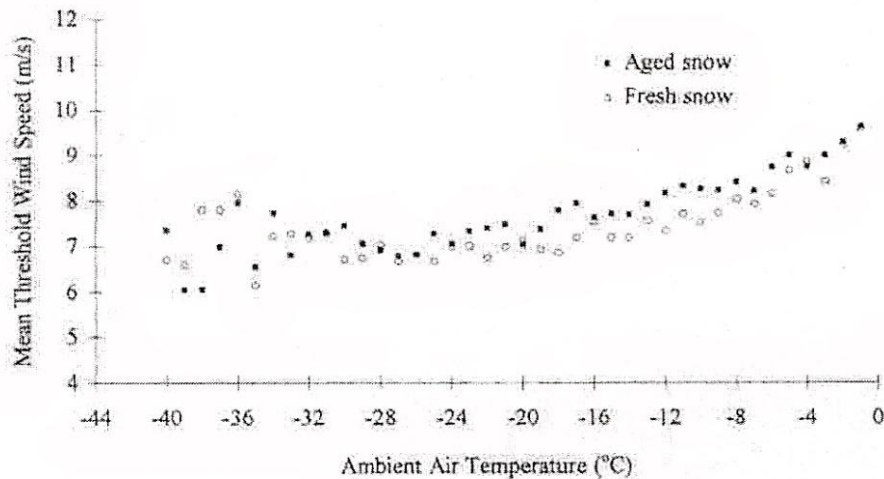


Figure 2.7: Threshold wind speed for fresh snow (open circle) and aged snow (closed circle). (From Li and Pomeroy, 1997 © American Geophysical Union. Reprinted with permission)

Once the threshold velocity is exceeded, a snow particle will be lifted into the atmosphere directly above the snow surface and move through the process of saltation. The height of the bounce is usually only a few centimeters above the surface, depending on the size of the particle and the wind velocity (Kobayashi, 1972; Kikuchi, 1981; Maeno *et al.*, 1985). The trajectory of the particle follows a nearly vertical ascent with a very horizontal descent back towards the surface. The maximum horizontal trajectory of the particle will be a few millimeters to 5 cm (Pomeroy and Gray, 1995). Upon impact with the surface, the saltating particle may eject one or two new particles, perpetuating the saltation process. To be ejected from the “splash” of the original particle, the energy of the impact must be greater than the cohesion between particles. Thus the shear stress available for saltation is equal to the shear stress by the wind minus the shear strength at the surface. The shear stress by the wind is estimated from the friction velocity of the wind. The velocity of the saltating particle is proportional to the threshold velocity (Pomeroy and Gray, 1990).

The transport rate for saltation is dependent on a number of atmospheric and physical factors including distribution of wind and the fetch distance, as well as the hardness of snow surface (Pomeroy and Gray, 1995). The saltation transport rate increases with increase wind speed in a linear fashion beyond the threshold velocity for both stubble and non-stubble terrestrial environments. The non-stubble environments would transport snow similar to a smooth first-year sea ice icescape with no or few obstacles that would penetrate the surface and thus act to influence the snow transport and deposition. A rubble or ridge icescape would be analogous

to a stubble environment. Beyond the threshold velocity, the snow transport rate does not increase due to the trapping of snow along or between the roughness elements. The transport rate also increases with an increase in fetch, or the uninterrupted distance over the surface, until a saturated state is achieved (Takeuchi, 1979). This saturated state is dependent on the roughness and hardness of the snow surface. For instance, when the snow surface is wind-packed, less snow particles will be available for saltation at a given wind speed and thus the saturated state will be lower.

For smooth first-year sea ice, snow depth distribution is independent of the surface conditions, and the observed pattern is primarily controlled by snow transportation. Snow distribution over smooth first-year sea ice resembles barchan dunes found in terrestrial desert environments. In the Antarctic, these dunes may cover approximately 50% of the surface of larger flatter floes (Massom *et al.*, 1997). Dune formation begins with a small-scale roughness feature found on the ice surface (such as a clump of hoarfrost crystals or frost flowers), which generally act as loci for trapping snow (Lang *et al.*, 1984; Massom *et al.*, 1997). When local wind speed is greater than a threshold velocity, the snow will move downwind through the process of saltation and the dunes will grow in size and migrate. This migration is accomplished by deposition on the lee side of the dune and erosion on the windward side. These features are important from a catchment hydrology perspective because they may increase the snow thickness estimation over smooth FYI by a factor of 1.5 to 3 (Massom *et al.*, 2001). Over time, the surface may become wind-hardened and the dune becomes semi-permanent with a reduction in the

migration of the dune (Massom et al, 2001). Due to any slight variations in surface hardness, the erosion on the windward side of the dune may become spatially non-uniform (Granberg, 1998). This will eventually lead to the development of sharp-edged surface snow forms known as sastrugi. These features are more irregularly shaped and longitudinal, compared to dunes.

Wind direction will also influence the distribution of snow. Surface features, such as dunes and sastrugi will be oriented parallel to the direction of the latest snow-drifting event. A new snow-drifting event with winds oriented in a different direction will first fill in the troughs formed on the snow surface by the mature features (Granberg, 1998), changing the spatial pattern of snow distribution and shape of the surface features. The snow surface features over smooth first-year sea ice have an average length of between 10 and 15 cm (Iacozza and Barber, 1999). Since the ice surface roughness features (i.e. clumps of hoarfrost crystals or frost flowers) would have a smaller structure length, the snow cover will 'smooth out' the ice surface and reduce the surface drag on the sea ice (Andreas *et al.*, 1993). Similar results were also found for other ice types in the Arctic (i.e. Sturm *et al.*, 2002) and for the Antarctic (i.e. Andreas *et al.*, 1993; Massom *et al.*, 2001).

The presence of deformation features on the surface such as ridges and rubble ice will create different snowdrift patterns, compared to those on smooth FYI. These patterns are created by changes in the wind field above the surface. Wind will be accelerated in certain areas and decelerate at other locations. These velocity changes will impact the occurrence of exceeding the threshold velocity, thus

resulting in either deposition or erosion of snow particles in the air. When the wind speed is less than the threshold wind speed, deposition of the snow will occur, and when the opposite is true, erosion will move snow particles from one area to another. As the wind approaches a ridge (windward side), there is a reduction in the wind stress at the surface causing a reduction in erosion and cessation of saltation, thus creating a net accumulation of snow (Granberg, 1998). As time progresses, the accumulation of snow on the upwind side of the ridge will cause the feature to be more aerodynamic. As this occurs, the wind stress is not reduced until the lee side of the ridge, where snow deposition and accumulation will then occur. The drift on the lee side will then build up and outward from the crest of the ridge. The horizontal extent of the snowdrift on either side of the ridge is greater than the height of the ridge. Research based on snow fences indicates that the drift can be 10 to 15 times greater than the height of the ridge (Granberg, 1998). This process will also occur in a rubble area; however the small separation distances between deformed ice areas complicate the accumulation process.

2.2 DYNAMIC PROCESSES RELATED TO HABITAT SELECTION

Ringed seals (*Phoca hispida*) and polar bears (*Ursus maritimus*) are both considered ice-obligate species (Moore and Huntington, 2008) since they rely on sea ice as a platform for most of life's activities, including hunting, breeding and resting. The ringed seal has been characterized as the smallest and most abundant of the northern seals (Frost and Lowry, 1981; Smith *et al.*, 1991). The exact population of this species is unknown, however it has been estimated that there are a few million ringed seals in the Arctic (Reeves, 1996). Polar bears are found throughout the

circumpolar world with population estimates of between 21,500 and 25,000 bears in 19 relatively distinct populations (IUCN/SSC Polar Bear Specialist Group, 2002). Ringed seals and polar bears are at the top of the Arctic marine ecosystem, thus they can be used to monitor the environmental state of the Arctic (Stirling *et al.*, 1982). This section will examine how snow-covered sea ice in the Arctic and dynamic processes creating specific iceforms controls the habitat selection of these two species.

2.2.1 Ringed seal habitat

Snow-covered sea ice forms an integral part of the marine ecosystem at high latitudes, including habitat for ringed seals and polar bears. At the large scale, ringed seals preferentially select different sea ice types. Multiyear sea ice areas have lower densities of ringed seals compared to first-year sea ice (Kingsley *et al.*, 1985). The reason for the avoidance of multiyear sea ice by ringed seals is two-fold. Firstly, there is most probably lower biological productivity in the areas of multiyear sea ice due to the thicker sea ice and less penetration of sunlight or PAR (Stirling *et al.*, 1982). As well, ringed seals would have more difficulty in maintaining breathing holes in the thicker multiyear ice, compared to the thinner sea ice found in the first-year sea ice areas. Densities of ringed seals are highest in areas where first-year sea ice exhibits interannual and seasonal motion with greater opportunity for the influence of dynamic processes, such as within Hudson Bay and Baffin Bay/Davis Strait (Lunn *et al.*, 1997). For instance, the density of ringed seals on landfast ice in Hudson Bay is estimated to be between 1.48 and 1.69 seals/km² (Smith, 1975; Lunn *et al.*, 1997), while similar densities (1.31 to 1.72 seals/km²) were found in Baffin

Bay (Finley *et al.*, 1983). Greater biological productivity would be found along an ice edge and therefore greater seal densities would be found in Baffin Bay/Davis Strait where there are a greater number of ice edges due to the active nature of the ice (Ferguson *et al.*, 2000). The lowest densities are found in areas where there is less interannual and seasonal variability of first-year sea ice (i.e. High Arctic and southern Beaufort Sea) with values between 0.31 and 0.97 seals/km² (Stirling *et al.*, 1982; Kingsley *et al.*, 1985).

The ringed seal has one of the largest ranges of all Arctic seals, using landfast sea ice as their primary breeding habitat (Smith and Hammill, 1981), as well as the pack ice for other activities including birthing lairs, resting lairs and breathing holes (Finley *et al.*, 1983; Smith, 1987, Wiig *et al.*, 1999). The seals maintain breathing holes in the sea ice, allowing them to use the ice-covered waters as a habitat between sea ice break-up and freeze up. Breathing holes are usually created on newly forming sea ice during the freeze-up period (Smith and Hammill, 1981). In addition, sea ice divergence created by wind and water stresses can also be used as sites for breathing holes. Ice convergence creates holes in the sea ice surface around uplifted ice blocks that may also be used as breathing holes by ringed seals.

In late spring, the snow-covered sea ice around the breathing holes will also be used as a platform to give birth and nurse pups (Smith and Stirling, 1975). A physical requirement for the construction of birthing lairs is areas with sufficient sea ice deformation (less than 40% of the area covered by ridges; Frost *et al.*, 1988), producing thick first-year sea ice (Figure 2.8). Most selected habitats will be in close

proximity to large sea ice ridges or deformation structures, compared to the area available for habitat selection (Figure 2.8; Furgal et al, 1996). In two separate studies for different regions in the Arctic, Lukin and Potelov (1978) and Hammill and Smith (1989) found that ringed seals preferred areas with ridges and hummocks with ice pieces 15 to 25 cm thick and 80 to 150 cm high. Ringed seals may have more difficulty excavating through the ice with thicker ice pieces, however thinner or shorter ice will not catch enough snow to form a sufficient snow drift. Some instances of birthing lair construction on drift ice have been recorded (Wiig *et al.*, 1999); however these are considered rare instances. The dynamic processes, especially wind and ocean currents, may produce significant ridges that will catch significant snow and thus provide an environment for the construction of subnivean birthing lairs.

Research suggests that snow depth, related to sea ice surface topography, is more important than ice coverage in the construction of seal lairs (Furgal *et al.*, 1996). Seal lairs are found in areas with greater snow depth compared to the available habitat of the area (Figure 2.8; Frost *et al.*, 1988; Furgal *et al.*, 1996). Up to 1 m or more of hard wind-packed snow (depending on snowfall amount and wind speed/direction) will accumulate on top of the breathing holes located along ridges. The ringed seals will excavate birthing lairs between the sea ice and the snow cover over the breathing holes. Within the Canadian Arctic, lairs were constructed in areas with average snow depths between 65 and 79 cm (Smith and Stirling, 1975; Hammill and Smith, 1989). In Admiralty Inlet and Strathcona Sound, seal pup lairs were found in smooth ice areas with snow depths as little as 32 cm (Furgal *et al.*,

1996), while in Amundsen Gulf and Prince Albert Sound areas lairs were constructed in areas with 25 cm of consolidated wind packed snow (Smith and Stirling, 1975). After birth, these lairs and the overlying snow depths will further provide protection to the seal pups from predation by polar bears and from the colder atmosphere above the lair (Smith *et al.*, 1991). As discussed in Section 2.3, the snow depth over an area is dependent on the sea ice surface topography, thus these two factors are related in creating ringed seal habitats.

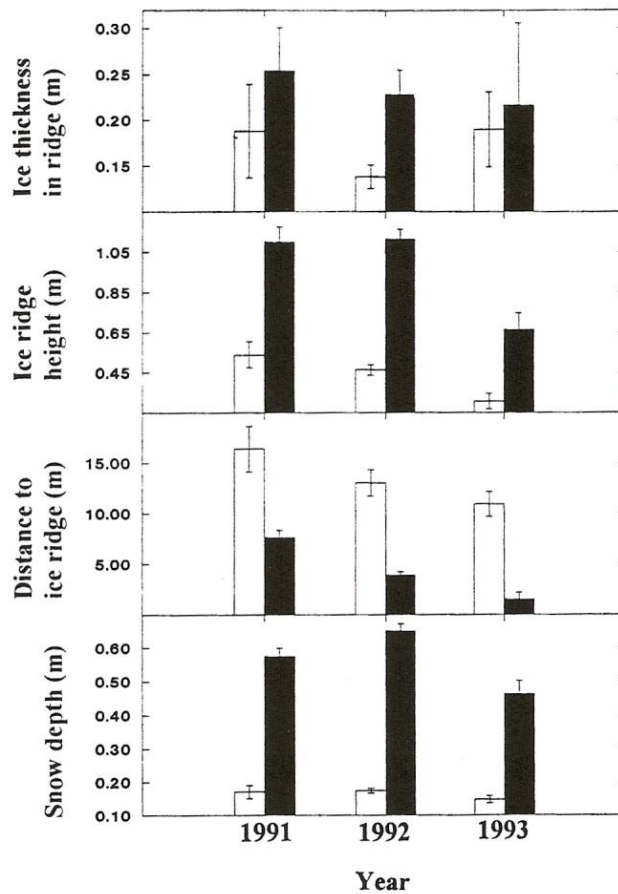


Figure 2.8: Snow depth, distance to nearest ice ridge, ice ridge height and ice ridge thickness measured at seal structures (solid bars) and habitat locations in general (open bars) for data collected in 1991-93. (From Furgal *et al.*, 1996. © National Research Council. Reprinted with permission)

Most of these birthing lairs are found on landfast sea ice (McLaren, 1958; Kingsley *et al.*, 1985; Furgal *et al.*, 1996) or in environments with almost complete ice cover, i.e. 6+⁺/₈ or 75% coverage (Figure 2.9; Stirling *et al.*, 1982; Kingsley *et al.*, 1985; Lunn *et al.*, 1997) such as large stable ice floes in Baffin Bay and Barents Sea (Finley *et al.*, 1983; Wiig *et al.*, 1999). The reason for this habitat preference is due to the stability of these areas through the birthing and nursing periods.

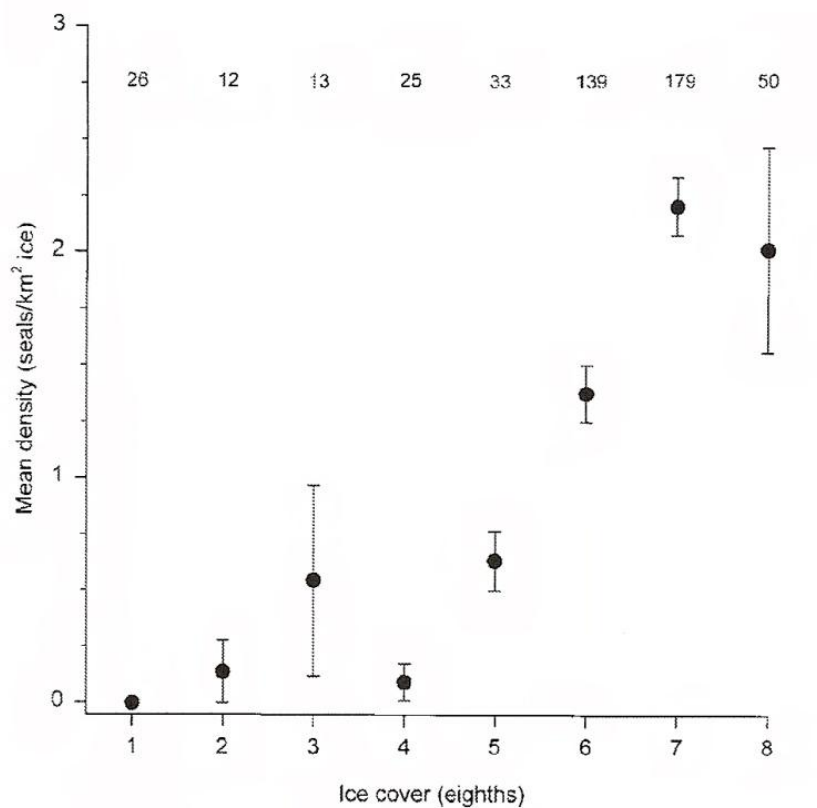


Figure 2.9: Mean density of ringed seals in relation to sea ice cover in western Hudson Bay. (From Lunn *et al.*, 1997. © National Research Council. Reprinted with permission)

Date of ice consolidation is also an important factor when examining the habitat of ringed seals. Ringed seals tend to abandon structures found in ice that has consolidated early in the season more often than in late consolidating ice (Kingsley *et al.*, 1985; Hammill and Smith, 1989). As well, lairs and breathing holes were also found not immediately at the ice edge, rather they were located between 0.5 and 1.0 km from the edge that had consolidated months earlier and which was thicker and more stable (Hammill and Smith, 1989). The reasons for these patterns may be due to increased food availability and mobility (Hammill and Smith, 1989). Productivity and food availability may be lower under ice that has consolidated earlier due to the deeper snow cover and thus less penetration of photosynthetically active radiation. Other factors that influence the construction of seal structures (but not related to the dynamic processes that influence first-year sea ice) include distance to open water and bathymetry (McLaren, 1958; Smith and Stirling, 1975; Kingsley *et al.*, 1985).

2.2.2 Polar bear habitat

Polar bears are considered non-territorial animals because they do not defend any home range, rather select habitat based on physical factors (Ramsay and Stirling, 1988; Stirling *et al.*, 1993; Stirling and Øritsland, 1995). The habitat selected by polar bears is controlled by three factors: (i) the seasonal variability in the snow-covered sea ice characteristics, (ii) the distribution and availability of the key prey species (ringed seals) and (iii) age and sex class of the polar bears. In the Canadian Arctic, regional differences in the preference of habitat selection by polar bears exist. These regional differences are based on dissimilar sea ice

characteristics relative to polar bear habitat selection. Consolidated ice areas (i.e. areas in the Canadian Archipelago) have ice present year-round (multiyear sea ice will be present within the area) and once the first-year sea ice forms it will remain in place with little dynamic movement. In the mobile or active ice regions, found in the periphery areas of the Canadian Arctic (namely the Beaufort Sea, Baffin Bay/Davis Strait and Hudson Bay areas) sea ice will be in constant motion allowing dynamic process to act on the ice, constantly changing the characteristics of the ice. In addition, this region will be ice-free for a period of time. Prior to the discussion on habitat selection, it is important to indicate that most of the information known about polar bear habitat selection is based on female polar bears. Due to the shape of the head relative to their neck, satellite-based collars used to track polar bears do not adequately stay on the male bear and thus are not an option to track this sex class. However, polar bear tracks and sightings have been used to estimate habitat selection for all age and sex classes, and will be discussed below.

A number of sea ice characteristics, including sea ice type, ice concentration, floe size and presence of ice edges have been shown to influence habitat selection by polar bears in mobile ice areas and consolidated ice areas. In the spring and summer periods, polar bears in both mobile ice areas (i.e. Baffin Bay and Beaufort Sea) and consolidated ice areas (i.e. Canadian Archipelago) select habitats with thick first-year sea ice (Figure 2.10; Stirling *et al.*, 1993; Ferguson *et al.*, 2000; Durner *et al.*, 2004). This selection is probably related to the presence of deformation structures on the sea ice (i.e. ridges) and the associated snow drifting, as related to habitat selection by ringed seals (see Section 2.2.1). During the same season, polar

bears in the Archipelago also selected multiyear sea ice more often than bears in the Baffin Bay region (Figure 2.10). This ice will still be present in the Archipelago during this period and may also be used as a hunting area for seals that may utilize this ice type in the absence of first-year sea ice. In the Beaufort Sea, polar bears also selected area of multiyear sea ice during summer (Durner *et al.*, 2004), again due to the presence of this ice type and the hunting availability. In the autumn season, bears in all regions selected multiyear sea ice (Figure 2.10; Ferguson *et al.*, 2000; Durner *et al.*, 2004), again due in part by the absence of first-year and new sea ice. Polar bears in the Archipelago prefer thick first-year sea ice in the winter season (Figure 2.10; Ferguson *et al.*, 2000). Baffin Bay and Beaufort Sea polar bears selected areas with either new ice, first-year or thick first-year sea ice during the winter season (Ferguson *et al.*, 2000; Durner *et al.*, 2004). The preference of thick first-year sea ice is again related to the presence of deformation structures and snow drifts utilized by ringed seals for the creation of lairs. In the winter period, young ringed seals move into the Baffin Bay region (Ferguson *et al.*, 2001), and hence polar bears may be using the new ice and thinner first-year sea ice to reach these populations of ringed seals. As well, thick first-year sea ice in Baffin Bay will have a deeper wind-packed snow drifts, reducing the ability of polar bears to catch ringed seals and thus forcing them into the new ice and thinner first-year sea ice areas (Ferguson *et al.*, 2001).

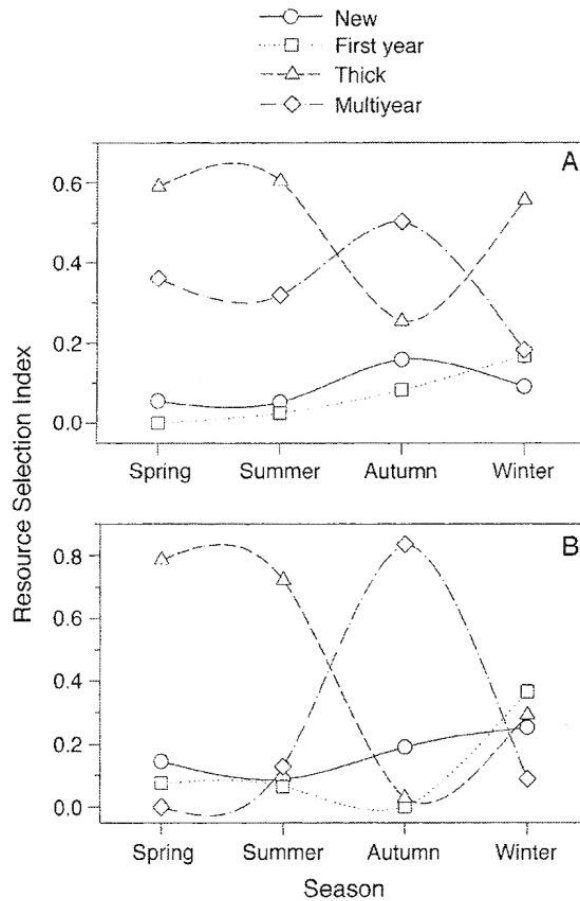


Figure 2.10: Seasonal cycle in selection by female polar bears of four ice type categories found in the (A) Arctic Archipelago and (B) Baffin Bay regions, 1991-1995. (From Ferguson *et al.*, 2000. © Ecological Society of America. Reprinted with permission)

Sea ice concentration is another sea ice characteristic that influences habitat selection by polar bears and is related to the dynamic processes operating in the marine cryosphere. Female polar bears in both consolidated and mobile ice regions selected habitat with complete (10/10 coverage) or almost complete (9+/10 coverage) sea ice more often than other ice concentrations (Figure 2.11). This finding is consistent with result from other regions in the Arctic (i.e. Hansen, 2004). During early summer, seal breeding takes place on completely covered sea ice (Mauritzen *et al.*, 2003), which increases the availability of prey for polar bears. The

timing of peak use of almost complete ice coverage varied between regions. The use of areas with almost complete ice coverage peaked in the autumn for polar bears in the Canadian Archipelago, compared to a peak in the winter for the Baffin Bay polar bears (Figure 2.11; Ferguson *et al.*, 2000). This difference was attributed to later freeze-up in the Baffin Bay area. Another difference between the two regions is that polar bears in Baffin Bay also used areas with between 7/10 and 9/10 ice coverage more often than bears in the Canadian Archipelago (Ferguson *et al.*, 2000). This may be due to the greater availability of this ice type in the Baffin Bay region.

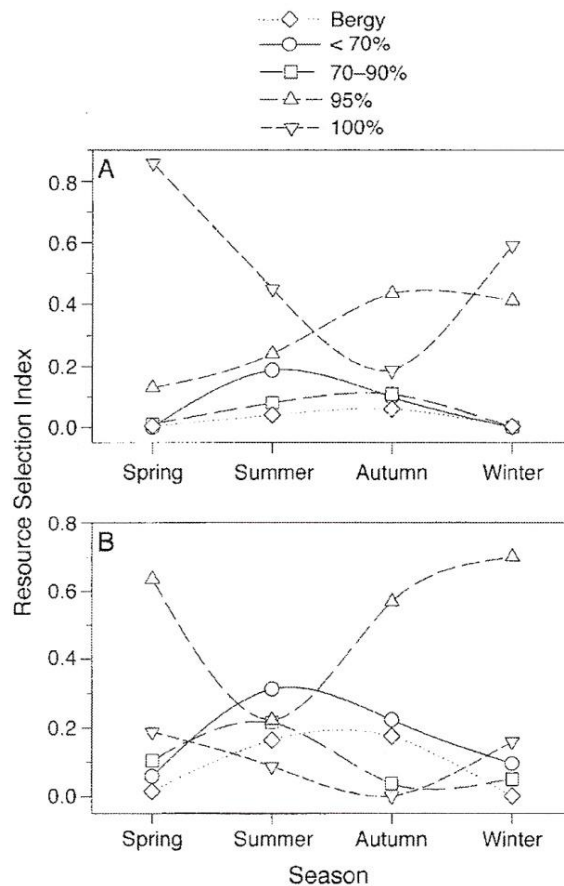


Figure 2.11: Seasonal cycle in selection by female polar bears of five ice cover categories found in the (A) Arctic Archipelago and (B) Baffin Bay regions, 1991-1995. (From Ferguson *et al.*, 2000. © Ecological Society of America. Reprinted with permission)

Habitat selection by polar bears is also defined based on the size of ice floes and distance to ice edge. Polar bears in the Canadian Archipelago are found on landfast ice in winter and spring, while bears in Baffin Bay are found in areas dominated by large ice floes during the same period, as well as summer (Figure 2.12; Ferguson *et al.*, 2000). Similar results are also found for polar bears in the Beaufort Sea (Durner *et al.*, 2004). The selection of landfast sea ice in the Canadian Archipelago is due to the establishment of breathing holes by ringed seals in this environment (Smith and Hammill, 1981). The selection of large ice floes may be related to polar bears attempting to stay on stable ice during the sea ice ablation season (Mauritzen *et al.*, 2003). Another reason for this difference is the availability and occurrence of landfast sea ice in the Canadian Archipelago due to the distribution of land and water in the area. Preference in ice floes for Canadian Archipelago polar bears changes to large floes in summer and autumn (Figure 2.12; Ferguson *et al.*, 2000). During the summer season, polar bears in Baffin Bay and Beaufort Sea selected habitat close to an ice edge (Stirling *et al.*, 1993; Ferguson *et al.*, 2000; Durner *et al.*, 2004). The location close to the ice edge during this season may be used by polar bears to locate seals that may still be available. The habitat selection was similar in autumn, with habitat close to an ice edge with high total ice coverage selected more often than expected. During the winter season, the location of the ice edge is also an important habitat characteristic. This again may be due to the fact that accessibility to prey is highest in those regions (Ferguson *et al.*, 2001). Similar trends in distance to ice edge were not evident for polar bears in the Canadian Archipelago (Ferguson *et al.*, 2000).

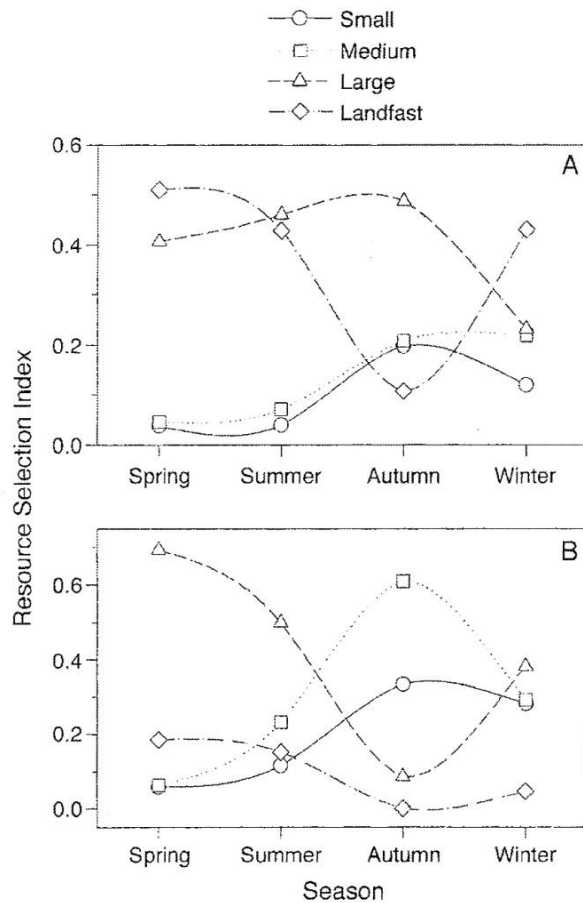


Figure 2.12: Seasonal cycle in selection by female polar bears of four sizes of ice floes found in the (A) Arctic Archipelago and (B) Baffin Bay regions, 1991-1995. (From Ferguson *et al.*, 2000. © Ecological Society of America. Reprinted with permission)

As indicated above, polar bears will select different habitats based on season.

This shift in preference of habitat type may be due in part to changes in polar bear behavior. For instance, in early summer, adult female polar bears may spend more time trying to hunt for prey and therefore select habitats with increased seal densities and accessibility to seals, such as areas with the formation of leads or open water (Stirling and Øritsland, 1995). In the early winter season, due to reduced seal availability and accessibility, more time may be spent on energy conservation or on

risk aversion, thus selecting areas with greater ice concentration and away from an ice edge (Mauritzen *et al.*, 2003). Sea ice with the formation of significant snowdrifts is also used as denning habitat by polar bears of all family groups, age and sex classes except those in Hudson Bay (Ferguson *et al.*, 2000; Parks *et al.*, 2006) to escape inclement weather or severe cold temperature (Derocher and Stirling, 1990; Messier *et al.*, 1994; Ferguson *et al.*, 2000). Therefore habitats with deformation structures (i.e. ridging) produced by dynamic processes, and the associated thicker snow drifts may be selected at a greater frequency. Most female polar bears will produce maternity denning on land, however some will utilize fast ice or drifting multiyear sea ice for dens (Lentfer, 1975; Amstrup and Gardner, 1994), again requiring ice deformation (i.e. hummocks) and the snow drifts produced by wind velocity and surface topography.

Movement of polar bears is correlated with the seasonality in the condition of the sea ice, namely the break-up and freeze-up cycle. The active ice areas in the Beaufort Sea and Baffin Bay zones generates greater mobility and seasonal movement of polar bears (Figure 2.13) due to the changes in the location of the prey species or greater hunting opportunities (Wiig, 1995; Ferguson *et al.*, 2000; Ferguson *et al.*, 2001). In these areas, polar bears move north into the MYI pack ice as FYI retreats in June, while in September, the movement is in a southerly direction following the formation of FYI (Wiig, 1995; Amstrup *et al.*, 2000). The rate of movement is also influenced by the seasonality of sea ice retreat and advancement. The movement of polar bears is greatest when the sea ice is consolidating and thawing during early winter and summer periods in the Beaufort Sea zone (Amstrup *et al.*, 2000). This is

probably a consequence of polar bears moving into habitats with high densities of ringed seals, as well as the unpredictability of hunting opportunities. In the autumn season, polar bear movement is low, due to the absence of ice prior to annual ice freeze-up, decreasing ringed seal densities and reducing movement of polar bears. As well, polar bear hunting will be concentrated in smaller areas causing smaller rates of movement (Amstrup *et al.*, 2000).

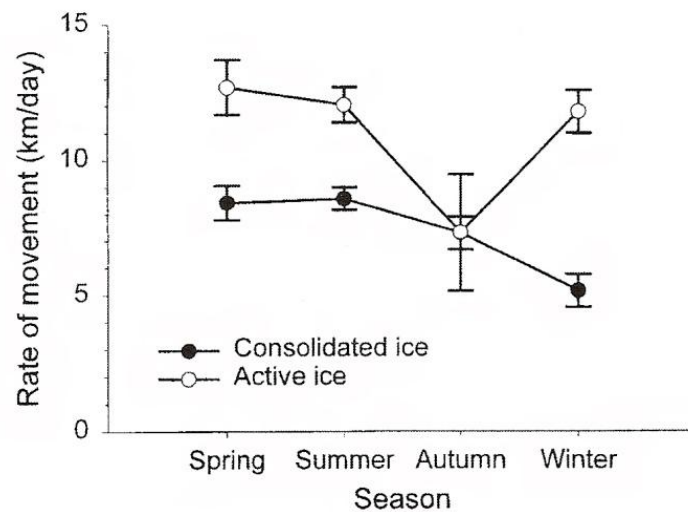


Figure 2.13: Seasonal changes in movement for female polar bears inhabiting consolidated versus active ice in the Canadian Arctic. (From Ferguson *et al.*, 2001. © The Arctic Institute of North America. Reprinted with permission)

For consolidated sea ice in the Canadian Archipelago (i.e. Viscount Melville Sound –VMS population), lower rates of movement were determined for polar bears (Figure 2.13; Messier *et al.*, 1992; Ferguson *et al.*, 1998; 2001). These low rates were probably due to high amounts of multiyear sea ice in that area which

establishes low densities of ringed seals, however concentrates ringed seals along cracks and pressure regions in that zone (Kingsley *et al.*, 1985) and thus limiting the movement required by polar bears to find suitable hunting habitat. In addition, during the winter season there are large numbers of juvenile seals, which are more difficult for the polar bear to catch (Ferguson *et al.*, 2001). During the autumn season, sea ice concentration will undergo less change in the Canadian Archipelago due to the presence of MYI in the area. This sea ice will still provide polar bears with a hunting platform and thus the rate of movement for polar bears will be low (Figure 2.13; Ferguson *et al.*, 2001). The change in sea ice characteristics will also impact the movement rates. In areas of consolidated sea ice, the ice condition (i.e. deformation) does not change significantly after freeze-up (i.e. autumn and winter) and thus polar bears do not have to significantly travel once hunting areas were found (Amstrup *et al.*, 2000). Polar bear mobility is greatest during the spring and summer seasons, irrespective of ice type (Figure 2.13; Ferguson *et al.*, 2001) due to the greater accessibility and availability of seals (Stirling and Øristland, 1995). Home ranges of polar bears are smaller in areas of consolidated sea ice, compared to active areas due to the stability in the extent of the sea ice and greater access to seals throughout the year (lower densities but more consistent on a monthly basis) (Ferguson *et al.*, 2001).

The selection of habitat types is also dependent on sex and age class of the polar bear. Female polar bears with cubs of one year (COY) prefer habitat that consists of stable landfast ice with snowdrifts (habitat that is suitable for seal birthing lairs) (Figure 2.14; Stirling *et al.*, 1993). Selection of this habitat class may be due to the

female polar bear wanting to keep the COY away from areas where they would have to swim and get chilled (Stirling *et al.*, 1993). Females with COY also prefer the pressure ridges to be less visible to other bears in the area To avoid predation of the COY by other polar bears. Polar bears of other sex and age classes (i.e. adult males, subadult males, lone adult females and females with two year old cubs) avoid stable landfast ice with drifts and show a preference for ice edges (Figure 2.14; Stirling *et al.*, 1993). One reason for this selection of habitat is that there is generally a high density of seals along the edges of ice floes and greater access to seals because of the thinner snow cover, therefore the more dominant classes of polar bears would be located in this habitat (Stirling *et al.*, 1993). Another possible reason for the selection of this type of habitat by adult or subadult males is that it may be easier for these bears to find a potential mate. Bears of all age and sex classes use moving or drifting ice habitat, suggesting that ringed seals are abundant and accessibility to all classes (Figure 2.14; Stirling *et al.*, 1993). Areas with large deformation features and large ice roughness values (i.e. coastal pressure ridges) are also considered good habitat for polar bears, with large number of animals and tracks sighted in these areas (Stirling *et al.*, 1993). A potential reason for this is due to the ability of these areas to catch and retain significant amounts of snow, creating large drifts and the potential for birthing lairs for ringed seals.

Snow conditions on the sea ice will also influence habitat selection by polar bears. Areas with hard wind-packed snowdrifts will result in lower hunting success (Ferguson et al, 2001). In addition, polar bears do not utilize stable landfast sea ice that lacks any snowdrifts (Stirling *et al.*, 1993), suggesting the importance of this

characteristic in habitat selection. This may be due to the fact that ringed seal densities are low in that type of ice environment (Smith and Stirling, 1975). In heavily deformed sea ice, polar bears may have difficulty to transverse the sea ice due to the large snow drifts and thus limited access to ringed seals in the subnivean lairs.

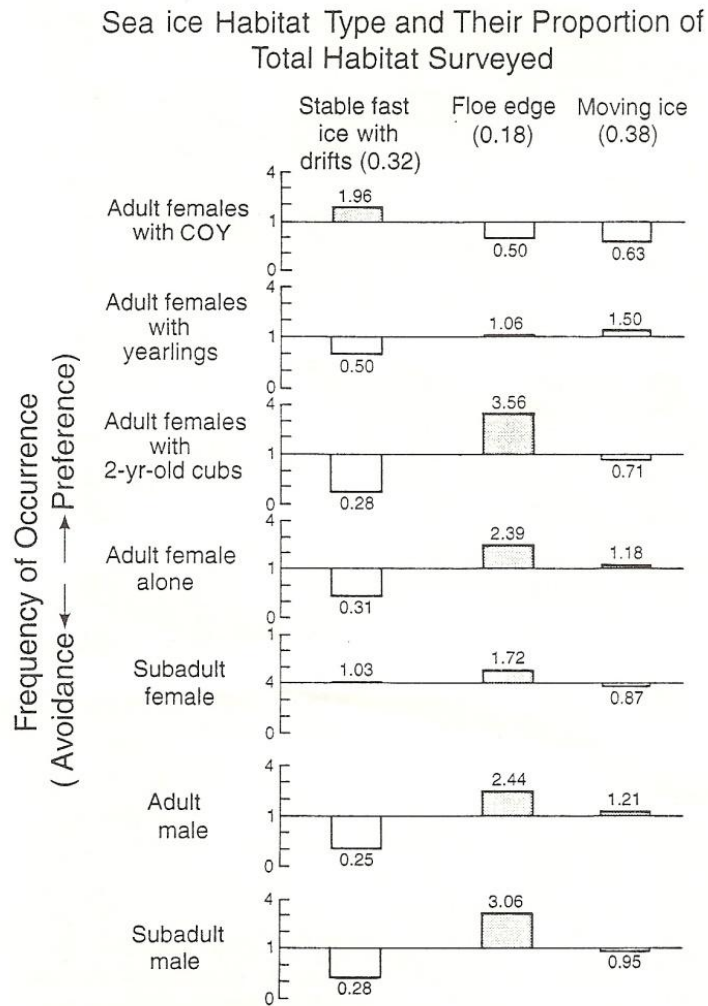


Figure 2.14: Indices of habitat preference of polar bears by sex and age class. A value greater than one indicates preference, a value less than one indicates avoidance and a value of one indicates no preference. (From Stirling *et al.*, 1993. © Cambridge University Press. Reprinted with permission)

2.3 ESTIMATING SNOW-COVERED SEA ICE

2.3.1 Modeling snow-covered sea ice

Measurement of snow distribution and redistribution over sea ice has been primarily conducted using a point sampling approach. Blowing snow particle counters have been set up on the sea ice to investigate blowing snow events and the relationship to meteorological parameters (Savelyev *et al.*, 2006). These studies are limited in space to a few points and may not accurately represent the spatial variability in the snow redistribution once it has been deposited on the sea ice. It is not feasible to locate a substantial number of these sensors to obtain the necessary spatial scale to examine changes in snow distribution over sea ice. Other studies have attempted to examine the spatial redistribution using transects over similar ice conditions that were not resampled, instead compared the evolution of snow distribution based on surface conditions (Massom *et al.*, 1997; Sturm *et al.*, 1998). These methods are useful for examining small areas (or large spatial scales) for a short duration, but due to the time required to complete, are not feasible for a large area over an extended duration (i.e. entire snowfall season).

Due to the limitations of acquiring reliable measurements of snow distribution from *in situ* sampling techniques, physical models are essential to estimate redistribution of snow cover on sea ice. To study the temporal redistribution of snow cover, the meteorological conditions (including snowfall and wind events) need to be incorporated into such models. Previous research over Arctic terrestrial surfaces have been able to estimate the redistribution of snow cover over land using the meteorological variables measured at permanent or semi-permanent land-based

weather stations (Liston and Sturm, 2002; Dery and Yau, 2002). For instance, *SnowModel*, a spatially distributed high-resolution snow evolution model, is able to simulate the snow evolution over forested and non-forested landscapes using the vegetation cover and meteorological state within the study area (Liston and Elder, 2006). One issue with producing a snow redistribution model over sea ice is the lack of meteorological data over sea ice at the scale necessary to force the model. Meteorological measurements are not routinely collected over sea ice due to logistical and practical issues. Future modeling will have to be able to use meteorological measurements made at land-based weather stations throughout the Arctic as a proxy for the on-ice conditions.

2.3.2 Remote sensing

Electromagnetic induction (EMI) techniques have been shown to be effective at estimating both snow-plus-ice thickness and surface roughness (Karvonen *et al.*, 2004; Peterson *et al.*, 2008; Haas *et al.*, 2006; 2010). This technique allows for greater spatial resolution and areal sampling of the sea ice characteristics, however as with in situ sampling, requires field participation and is limited by logistical constraints (i.e. daylight and fair weather sampling). Airborne- and satellite-based laser altimeters and lidar systems have also been used to measure sea ice elevation and roughness (Hvidegaard and Forsberg, 2002; Giles *et al.*, 2007; Kwok and Cunningham, 2008, Kurtz *et al.*, 2008, Zwally *et al.*, 2008). As with EMI, the advantage of the satellite systems are that large spatial areas can be studied, however information from these systems are not available for the entire Arctic for a long temporal period, and still requires extensive validation. In addition, reliability

of altimetry measurements of sea ice is affected by snow depth uncertainties over sea ice.

Satellite radar remote sensing is a more practical technique for sampling sea ice characteristics throughout the year, as well as providing a longer temporal period compared to laser altimeters. However, surface roughness is not a direct measurement from radar imagery. A direct comparison between surface roughness measurements of first-year sea ice from EMI system and backscatter from synthetic aperture radar imagery suggests that high surface roughness is associated with high radar backscatter (Peterson *et al.*, 2008). The association increases as the spatial averaging of the measurements increase, however there is only a moderate association, with the variability in radar backscattering only accounting for approximately 60% of the variability in surface roughness (Peterson *et al.*, 2006; 2008). Image processing techniques, such as second-order texture measures, have been shown to be successful in the discrimination of sea ice types within synthetic aperture radar imagery (Barber and LeDrew, 1991; Shokr, 1991; Soh and Tsatsoulis, 1999; Clausi, 2002). Snow and sea ice surface roughness can be defined as the texture within satellite imagery, thus texture measures may improve the estimation of surface roughness. Grey level co-occurrence matrix (GLCM), a type of texture measure, has been an effective technique for evaluating surface roughness of various features at different spatial scales (i.e. Wang and Georganas, 2009; Liu *et al.*, 2010).

CHAPTER 3: SNOW REDISTRIBUTION OVER SMOOTH LAND-FAST SEA ICE

This chapter attempts to describe and model the evolution of winter snow depth distribution over smooth land-fast first year sea ice. This will be accomplished by examining three specific objectives: (i) characterize the observed snow redistribution over smooth sea ice and establish the meteorological forcing influencing the redistribution, (ii) determine if land-based meteorological measurements can be used to estimate the meteorological conditions over sea ice during ice covered periods, and (iii) test the ability of *SnowModel* to estimate the spatial and temporal evolution of snow over smooth land-fast sea ice. This research has been published in *Hydrological Processes* (Iacozza J. and D.G. Barber. 2010. An examination of snow redistribution over smooth land-fast sea ice. *Hydrological Processes*, 24:850–865, doi: 10.1002/hyp.7526).

3.1 METHODS

3.1.1 Snow redistribution

Snow depth distribution and meteorological measurements were collected in the winter and spring of 2004 as part of the Canadian Arctic Shelf Exchange Study (CASES). Between January and May 2004, the icebreaker *CCGS Amundsen* was frozen into the ice within Franklin Bay, Northwest Territories (Figure 3.1). Snow distribution data were collected on smooth land-fast first year sea ice. For the purposes of this study, smooth land-fast sea ice was defined as ice that had been formed at the same time in a relatively stable environment with little dynamic

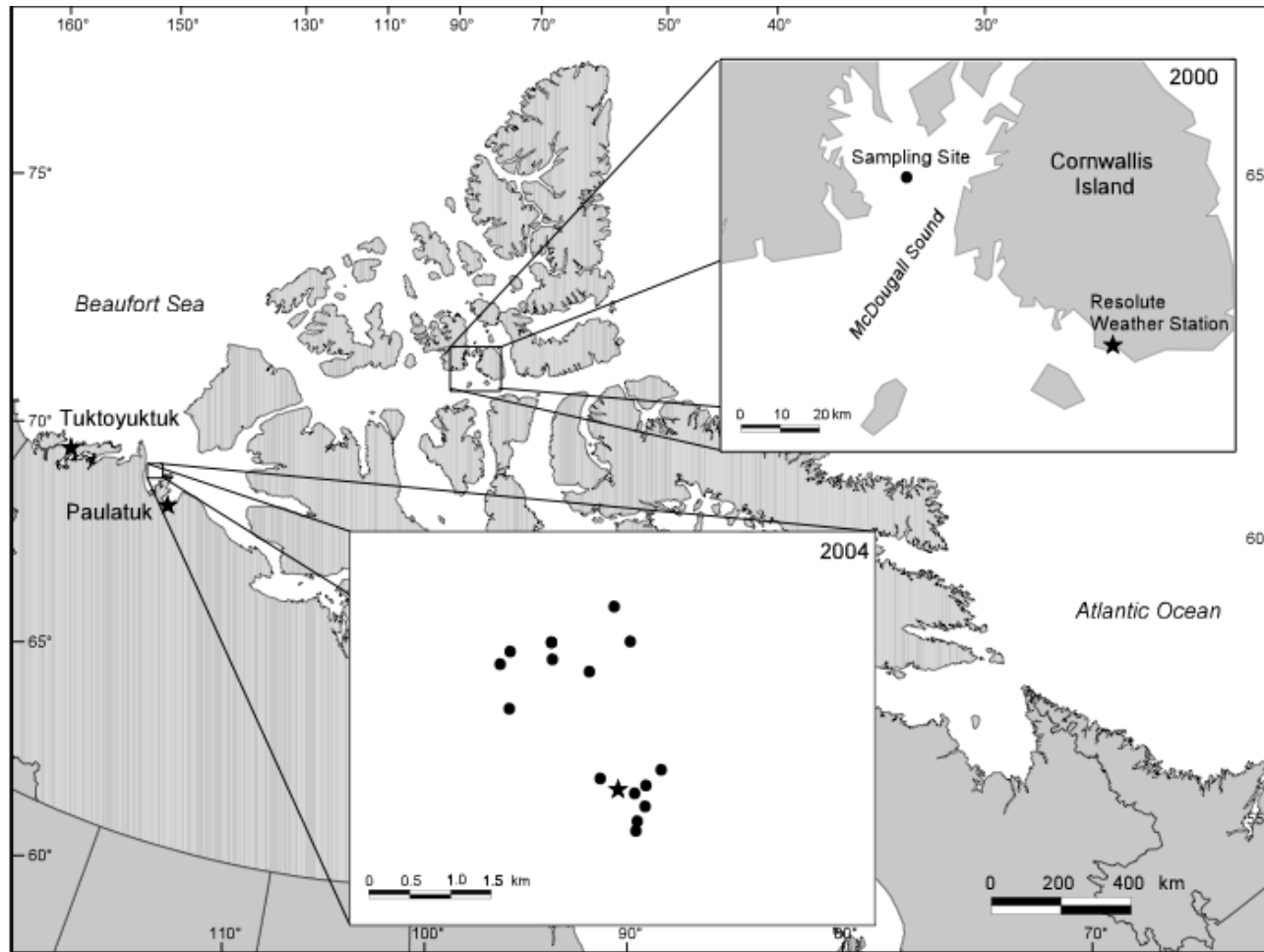


Figure 3.1: Map of the Canadian Arctic illustrating the general locations of the sampling areas. The two insets show a detailed map of the sampling locations in 2000 (top inset) and 2004 (bottom inset). The stars in the insets indicate the location of the meteorological stations (both on ice and land-based) (From Iacoza and Barber, 2010. © Wiley-Blackwell. Reprinted with permission).

deformation. Due to the nature of the close proximity of sampling sites, snow depth did not vary as a function of age of the sea ice.

Within the smooth ice class, sampling sites were selected randomly. The only requirement for the selection of sites was that each site be located at least 150 m from another ice type to reduce the influence of the adjacent ice type on the snow distribution patterns within the sampling site. Snow depth sampling involved systematic measurements taken at 1 m sampling intervals along eight straight transects radiating from a central point. In the four cardinal directions, sampling was conducted for a distance of 50 m from the central point, while for the other 4 transects, sampling was conducted at a distance of 71 m from the central point. This was done to maintain a square sampling area. Previous research showed that sampling lengths of 50 m and 71 m at an interval of 1 m are sufficient to capture the majority of the statistical variability in snow distribution (Iacozza and Barber, 1999). Snow depth measurements were collected using an automated snow probe (Magnaprobe©, produced by Snow-Hydro) with a precision of 2 millimeters. Each site was destroyed due to the manual sampling technique employed, and thus was only visited once during the sampling period (i.e. sampling was done without replacement).

During the winter and spring of 2004, 17 sites were sampled on smooth land-fast sea ice (Figure 3.1). These sites were in close proximity to the location of the ship in Franklin Bay due to logistics of transportation to the sites and the time required to complete the surveys. The sampling commenced on January 24 and

concluded on May 5, 2004.

Small-scale snow depth distribution measurements (0.1 m intervals) were collected in the spring of 2000 as part of the Collaborative-Interdisciplinary Cryospheric Experiment (C-ICE). This study was a multi-year field experiment in the Canadian Archipelago, focusing on sea ice energy balance and the physical controls on the Arctic ecosystem. In 2000, this project was based on smooth land-fast first year sea ice in McDougall Sound, northwest of Resolute Bay, Nunavut (Figure 3.1).

In 2000, two snow depth lines, each approximately 7.4 m in length, were installed in the sea ice on May 16. One line was aligned parallel to the predominant snowdrift direction (referred to as parallel transect), while the other line was orthogonal to the first (referred to as perpendicular transect; Figure 3.2). Each transect was located approximately 4.8 m from the other transect in order to eliminate the effect one line would have on the snow distribution under the other line. Further details are available in Iacozza and Barber (2001).

On a daily basis, the height of the line above the snow surface was measured using a metre stick (to the nearest 0.25 cm) at a sampling interval of 0.10 m. The depth of the snow under each sampling point was computed by subtracting the height of the line above the snow surface from the height of the line from the sea ice surface (Figure 3.2). Measurements were not taken on either side of the centre post due to the influence the post would have on catching snow during depositional or redistribution events. To maintain consistency between sampling days, all

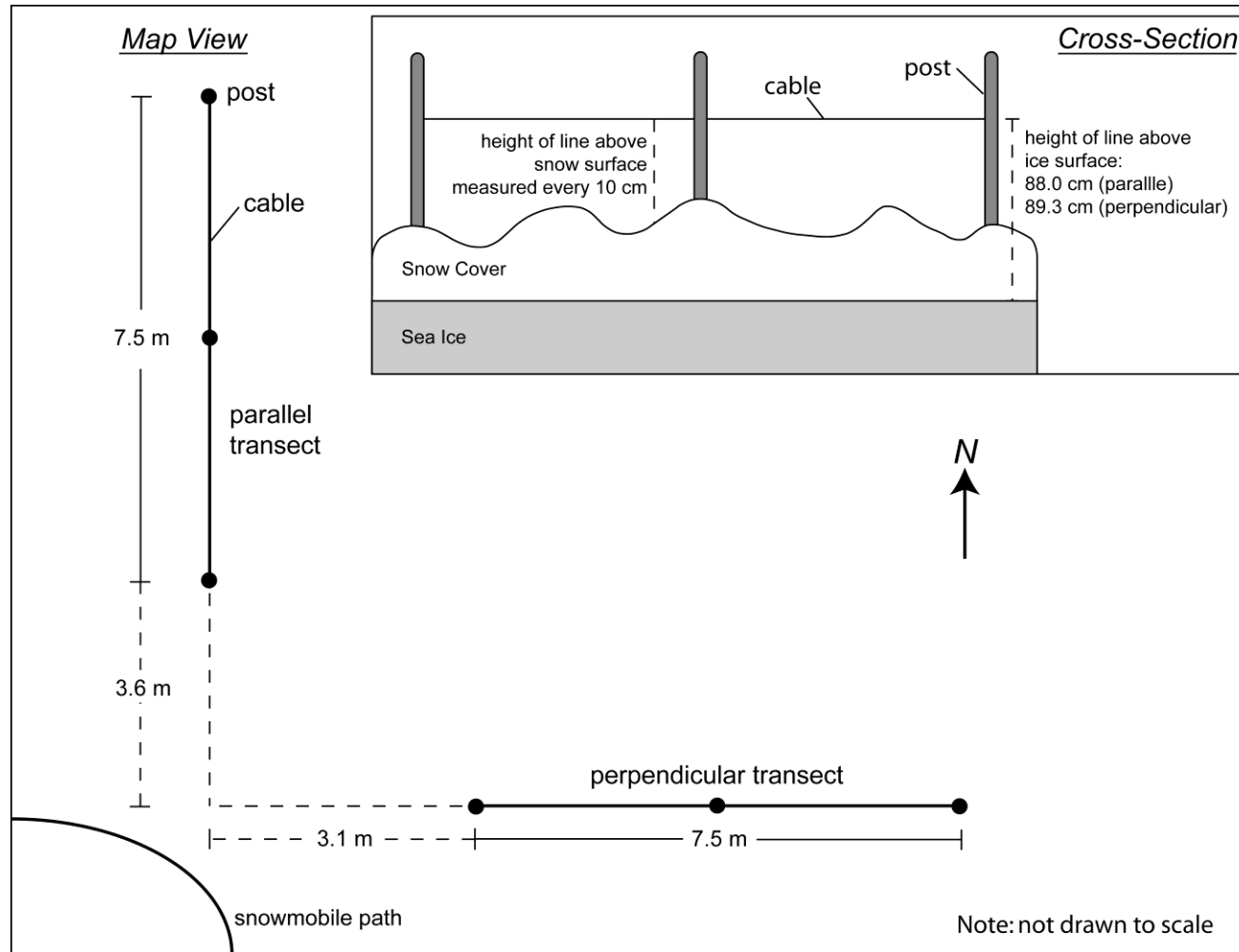


Figure 3.2: Schematic illustrating the orientation of the transect lines established on the sea ice in 2000, as well as the measurements to estimate snow depth at each sampling point along each transect.

measurements were made within an hour of local solar noon. Measurements were made daily between May 16 and June 8, 2000. Data were not collected on May 22 due to logistical problems with the field experiment, and on May 26 to 27 due to inclement weather.

3.1.2 Meteorological variables

Meteorological variables were collected on the sea ice using towers established during the sampling periods. In 2004, the meteorological towers were established on smooth land-fast first year sea ice at 70°02.5'N and 126°15.9'W (Figure 3.1). This site was in close proximity (less than 5 km) to the snow sampling locations. Air temperature and relative humidity were sampled using a Vaisala humidity and temperature probe (model HMP45C) housed in a radiation shield. This instrument has an accuracy of $\pm 3\%$ for relative humidity and air temperature. Wind speed and direction were acquired using a RM Young wind monitor with an accuracy of 0.3 m/s for wind speed and 3° for wind direction. Instrumentation on the towers recorded the values for the meteorological variables as 15-minute averages with a scan rate of 3 seconds throughout a 24-hour period. For this study, the 15-minute values were averaged into daily values. A shielded Nipher precipitation gauge was placed on the ship and daily-corrected measurements of snowfall were recorded. During the CASES field program, meteorological data were missing for March 17, 18 and April 30, 2004. This gap in data acquisition was due to instrument maintenance and/or malfunction. We are confident that, because of the short duration of the gap, the missing data do not significantly influence our analysis.

Similar meteorological variables were also acquired from long-term weather stations located on land. Data from the land-based weather station were acquired from the Tuktoyuktuk (69°25.8'N, 133°01.8'W) and Paulatuk (69°21.6'N, 124°04.8'W) weather stations operated by Environment Canada (Figure 3.1). These two stations were the closest meteorological stations to the on-ice sampling location, and had the longest recorded observations for the meteorological variables. The meteorological variables were reported on an hourly basis and downloaded from the National Climate Data and Information Archive operated by Environment Canada (climate.weatheroffice.ec.gc.ca/Welcome_e.html). Data were acquired from October 31, 2003 to May 25, 2004, which incorporated the timing of the field sampling. Hourly data for Tuktoyuktuk were available from 6:00 to 22:00 daily. Data from this location were missing for 7 days during the study period. For the Paulatuk weather station, hourly data were available from 6:00 to 16:00 daily. Data were missing for only one day from this weather station.

In 2000, meteorological towers were established on smooth land-fast first year sea ice at 75°14.6'N and 97°04.4'W (Figure 3.1). Air temperature and relative humidity were measured using a Campbell Scientific probe (model CS500) housed in a ventilated housing. This instrument has an accuracy of $\pm 2\%$ for temperature and $\pm 3\%$ for relative humidity. Wind speed and direction were acquired using a RM Young wind monitor. As in 2004, meteorological variables were recorded as 15-minute averages, and daily averages were computed for this study. During C-ICE 2000, meteorological data were missing during the second half of June 7 to June 8 due to instrument problems. Since precipitation on the sea ice was not collected,

data from the Resolute Bay weather station (74°43.2'N, 94°59'W; Figure 3.1), operated by Environment Canada, was used to estimate the snowfall over sea ice during the sampling period.

3.1.3 Spatial continuity

The spatial continuity of the snow depth was computed using a geostatistical technique known as the variogram. This method examines the spatial continuity of a regionalized variable and how this continuity changes as a function of distance and direction. The spatial continuity is estimated by examining the relationship between the semivariance ($\gamma(h)$) and lag distance (h) (Isaaks and Srivastava, 1989). The semivariance is defined by equation [3.1]:

$$\gamma(h) = \frac{1}{2N} \sum_{i=1}^N (x_i - x_{i+h})^2 \quad [3.1]$$

where $\gamma(h)$ is the semivariance, x_i is the measured sample value at point i , x_{i+h} is the measured sample value at point $i+h$ (where h is the lag distance) and N is the number of observations for a particular separation or lag distance. The lag distance is defined as the distance separating two points within a dataset. This method has been utilized to characterize the spatial pattern of snow over both terrestrial surfaces (Herzfeld, 2002; Molotch *et al.*, 2005) and sea ice (Iacoza and Barber, 1999; Sturm *et al.*, 2002).

The nugget variance (or effect) is an important variogram parameter that can be used to describe the spatial continuity of the snow distribution. A nugget effect is

the discontinuity of the variogram at the origin, suggesting that as the sampling distance approaches zero, the semivariance is greater than zero (Isaaks and Srivastava, 1989). This parameter can be interpreted as sampling error or autocorrelation occurring at intervals less than the sampling interval (i.e. snow distribution smaller than the sampling interval of 1 m).

The correlation length is another variogram parameter that examines the spatial continuity. This parameter quantifies the distance in which points are autocorrelated. The basic principle behind correlation length is that measurements made at a smaller interval tend to be more similar compared to those made further apart. The entire range of the sample variability is encountered within a distance equivalent to the correlation length. Beyond the value, the samples are no longer correlated and thus are considered statistically independent.

Geometric anisotropy and orientation, derived from the variogram analysis, can be used to investigate the directional component of the snow depth distribution. The geometric anisotropy for each site was measured using an anisotropy ratio, which is equal to the correlation length of the variogram in the direction of the shortest axis divided by the correlation length in the direction of the longest axis. The more dissimilar the ratio is from 1, the greater the geometric anisotropy and therefore snowdrifts are more elongated. Orientation is defined as the direction with the longest correlation length and would suggest the orientation of the snowdrifts. Due to the analysis procedure, orientation is offset by 90° in comparison to the meteorological variables. For instance, a wind direction of 0°

would indicate a north wind, while for the geostatistical analysis an orientation of 0° would indicate the east-west alignment of snowdrifts. Additional information on the variogram technique is provided in Isaaks and Srivastava (1989) and Pannatier (1996).

3.1.4 *SnowModel*

To examine the snow accumulation and redistribution over smooth land-fast first year sea ice, a spatially distributed snow-evolution model (*SnowModel*) was used. This model incorporates drifting snow processes and has been used to successfully model the spatial snow redistribution over terrestrial surfaces (Liston and Elder, 2006). *SnowModel* incorporates four sub-models, including MicroMet (a meteorological distribution model), EnBal (a surface energy balance estimation), SnowPack (a snowpack evolution model) and SnowTran-3D (a three-dimensional snow depth evolution model from wind-blown snow). The spatial resolution of *SnowModel* is designed to operate at between 1 and 200 m (which is user defined), while the temporal resolution operates on scales of 10 minutes to 1 day (Liston and Elder, 2006). The required inputs into the model include temporally varied meteorological variables (including temperature, humidity, wind speed and direction) and spatially varied topography. *SnowModel* outputs the spatial distribution of snow water equivalent (SWE) over the study area. This model has been successful at simulating the evolution of snow accumulation, blowing snow, snowmelt and runoff for the Mittivakkat Glacier (Mernild *et al.*, 2008) and

Zachenberg river drainage basin (Mernild *et al.*, 2007), however it has not been applied to sea ice.

Four model runs were completed using *SnowModel*. The first (run 1) was performed using daily meteorological measurements taken on the sea ice beginning on January 21, 2004. The model was initialized with the observed surface topography of the snow-covered sea ice collected on January 21. Each daily output was then added to the snow distribution on that day in order to obtain a realistic measure of snow depth. The advantage of this run is that it was able to include meteorological inputs directly measured on the sea ice. A potential limitation is that the snow evolution commenced in the middle of the snow accumulation season, and may not accurately represent the complete snow redistribution.

The second model run (run 2) used daily meteorological data from Paulatuk weather station and precipitation data measured at the field site. This station was selected because it was the closest land-based meteorological weather station to the modeling site. This model run commenced on October 31, 2003, the approximate date of ice consolidation (100% coverage) for the study area, estimated from weekly regional ice charts provided by the Canadian Ice Service. For this run, level bare ice was the initial surface topography used since the focus was on smooth land-fast sea ice. The advantage of this run is that a full season of snow evolution was modeled using a more realistic surface topography. However the greatest potential limitation is that this model run was required to use meteorological data from a land-based weather station.

For the third model run (run 3) on-ice temperature and relative humidity were modeled using relationships estimated from air temperature recorded at the Paulatuk weather station. Wind speed and direction recorded at the Paulatuk weather station was also used for this model run. Since the relationship between land-based weather station temperature and on-ice temperature and relative humidity are limited to the winter season (beginning in late January), this model run covered the same temporal period as run 1. In addition, it also used the snow cover estimated for January 21 as the initial cover. The purpose of this model run is to determine if using the relationship to estimate the meteorological parameters on the sea ice would improve the ability of the model to replicate snow redistribution over smooth land-fast sea ice.

Due to the scarcity of land-based meteorological stations in the Arctic, *SnowModel* was also run using atmospheric modeled products (run 4). Daily temperature, relative humidity, wind speed and direction (estimated from u and v winds) were obtained for the period October 31, 2003 to May 25, 2004 from NCEP model reanalysis. The initial topography for this run was estimated to be level bare smooth sea ice. For all the model runs, *SnowModel* was run on a daily time step over a 100 m x 100 m study area at a cell resolution of 2 m.

To compare the model outputs to the sampled data at each site, measured snow depths were converted to SWE estimates. This was done using the equation [3.2]:

$$\text{SWE} = 0.01 * d_s \rho_s \quad [3.2]$$

where d_s is the measured depth of snow (cm) and ρ_s is the density of snow (kg/m^3). The daily densities of snow used in this calculation were measured on the sea ice at a relatively short distance from the snow sampling sites and reported in Langlois *et al.* (2007).

3.2 CHARACTERIZATION AND FORCING OF OBSERVED SNOW REDISTRIBUTION

3.2.1 Meteorological setting on sea ice (2004)

Two environmental factors are important when examining the spatial and temporal evolution of snow distribution: the amount of snowfall and occurrence of drifting snow. A number of meteorological variables are related to these two factors, including daily air temperature, relative humidity, wind speed and direction, and precipitation. With regards to daily air temperature and relative humidity, two different regimes were evident. During the winter period between January 23 and March 27, the air temperature was relatively cold, with a daily average temperature of approximately -31°C (Figure 3.3a) and relative humidity was comparatively low (Figure 3.3b). After March 27, the daily average air temperature showed a general warming trend and the relative humidity increased to 80%. The area north of the study area consisted of mobile ice with areas of open water that opened and closed with the dynamic movement of the sea ice. These open water areas and the increase in daily average air temperature during these periods may account for the observed increases in relative humidity.

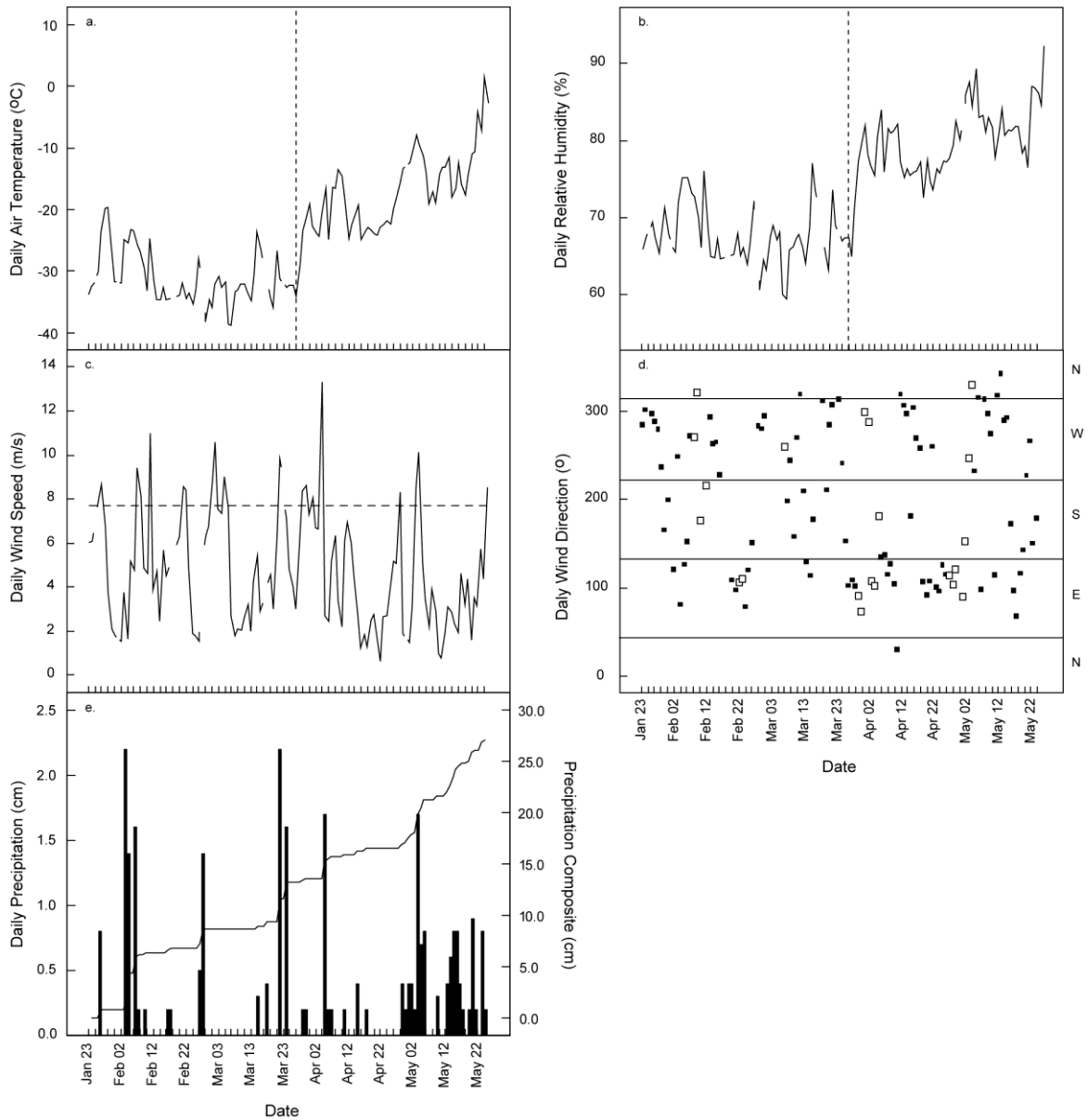


Figure 3.3: Time series of daily average temperature (a.), daily average humidity (b.), daily average wind speed (c.), daily average wind direction (d.) and daily precipitation (e.) for January 23 to May 23 2004. Dashed line on the graph of wind speed indicates the threshold wind speed for saltation (7.7 m/s). The open squares on the plot of wind direction (d.) indicate the average daily direction when wind speed was greater than 7.7 m/s. Wind direction is indicated as a degree (on the left axis) and as a qualitative direction on the right axis. N, E, S, and W represent the north, east, south and west direction (respectively). These directions are centred at 0°, 90°, 180° and 270° with a 45° tolerance. (From Iacozza and Barber, 2010. © Wiley-Blackwell. Reprinted with permission).

Daily average wind speeds varied considerably with no general trend observed throughout the study period (Figure 3.3c). Daily average wind speeds were greater than 7.7 m/s, the threshold velocity required to initiate drifting of dry snow (Li and Pomeroy, 1997) for a number of time periods, including February 7 to 11, February 21 to 22, March 1 to 6, March 29 to April 4, and April 28 to May 4 (Figure 3.3c). Wind direction also varied considerably throughout the sampling period (Figure 3.3d). During periods with wind speeds greater than the threshold velocity for dry snow, daily average wind direction was consistently from the east or west (Figure 3.3d).

Daily precipitation recorded at the CASES location show that a number of snowfall events occurred over multiple days. During the winter season, 5.6 cm of snowfall occurred between February 3 and 9, and 4.2 cm fell between March 18 and 24, 2004 (Figure 3.3e). During the spring season, as expected, the frequency of precipitation events increased, with more days recording snowfall (Figure 3.3e). A minor snowfall event of 2.1 cm occurred between April 5 and 7, 2004, while between April 29 and May 6, 4.8 cm of snowfall occurred within the sampling area. Another major depositional event of 5.5 cm occurred between May 13 and 25.

3.2.2 Evolution and meteorological forcing of snow distribution

Between January 24 and March 16, 2004, the average and standard deviation in snow depth was fairly consistent with small increases (i.e. on February 9) and decreases (i.e. on January 28) within this time period (Figure 3.4a). After March 16,

large increases in the snow depth were measured on March 20, April 5, April 10, and May 5, 2004 (Figure 3.4a). The snowfall events that occurred during this period (Figure 3.3e) would explain the large increases in average snow depth on these days. The increases in standard deviation observed on these three days were due to the strong wind events that occurred prior to sampling (Figure 3.3c).

A comparison of the probability density functions (PDF) of the snow depth suggests slight differences in the snow distributions between consecutive sampling days. However patterns in the PDFs are evident that may suggest grouping of the distributions. Between January 24 and March 16, 2004, the PDFs indicated that the snow distribution was unimodal (mode at 4 cm), and positively skewed (tail in the distribution with deep snow depths; Figure 3.4b). Between March 16 and 23, the snow distributions change slightly to a more positively skewed distribution with a lower fraction of observations at the mode of 4 cm (Figure 3.4b). The PDFs also show a longer tail, indicating the presence of deeper snowdrifts. After March 23, the PDFs shift to multimodal distributions, with modes centered at snow depths greater than 4 cm (Figure 3.4b). In addition, the PDFs are further positively skewed during this period and exhibit a longer tail suggesting the presence of even deeper snow depths over smooth land-fast ice. This shift in the PDFs suggests some readjustment of the snow depth distribution to larger depths, primarily due to the snow depositional and drifting snow events that occurred after March 16, 2004. These patterns of PDFs for snow depth distribution and the relationship to the meteorological forcing suggests that the PDF is able to capture the variability in

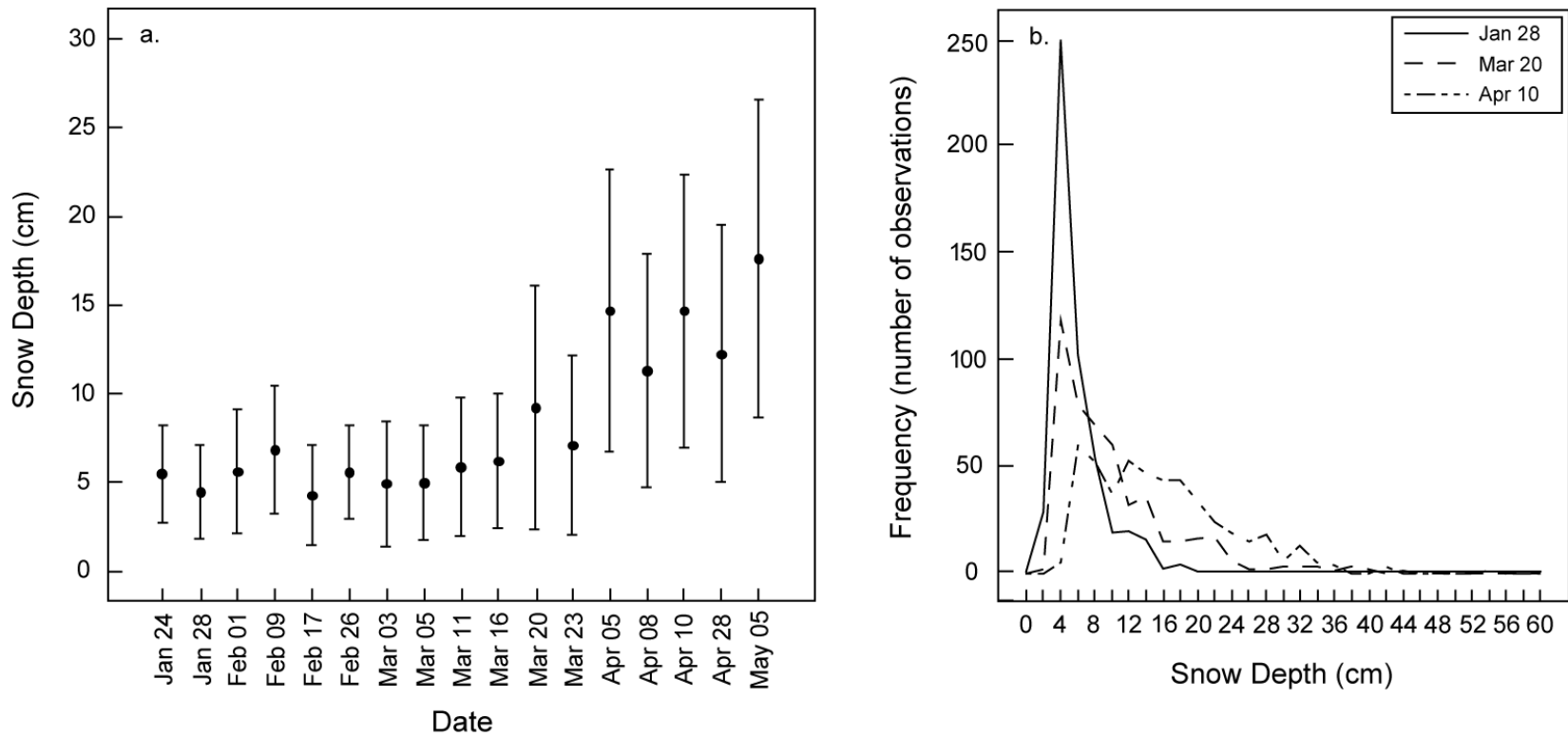


Figure 3.4: (a.) Plot of the mean (closed circles) and one standard deviation (bars) for snow depth measured at the smooth ice sites between January 24 and May 5 2004. (b.) Three probability density functions representing different snow depth distribution sampled over smooth land-fast sea ice in 2004. The bin size is 2 cm. (From Iacozza and Barber, 2010. © Wiley-Blackwell. Reprinted with permission).

snow depth distribution at the sampling sites and thus may be useful to estimate snow depth distributions in models.

For snow distribution over smooth ice, the nugget values are significantly low for most of the sampling days (less than 0.10 or 10% for 13 of the 18 sampling days). This would suggest that a significant portion of the variability in snow depth could be modeled using this geostatistical technique. During the beginning of the sampling period (January 24), the nugget value was large (0.20) indicating that approximately 20% of the variability in snow depth could not be accounted for by the separation distance. The larger nugget value during this sampling period was probably due to the low snow depth and high variability in distribution not captured at the sampling interval used (i.e. 1 m).

The correlation length varied throughout the study period (Figure 3.5a). The variability in correlation lengths suggests that the snow distribution was constantly readjusting due to meteorological factors. Correlation lengths were significantly larger for three dates, January 28, March 3 and May 5, 2004 (Figure 3.5a). These larger values suggest an increase in the periodicity in the snowdrifts (and longer snowdrifts), which corresponds to the timing of snow depositional and drifting snow events prior to or during these dates.

The anisotropy values calculated for each site were significantly greater than 1 for most of the sampling dates (Figure 3.5b). This indicates the presence of geometric anisotropy for most of the sites and thus clearly defined and oriented snowdrifts were located in the area. Between March 3 and 11 and for January 28,

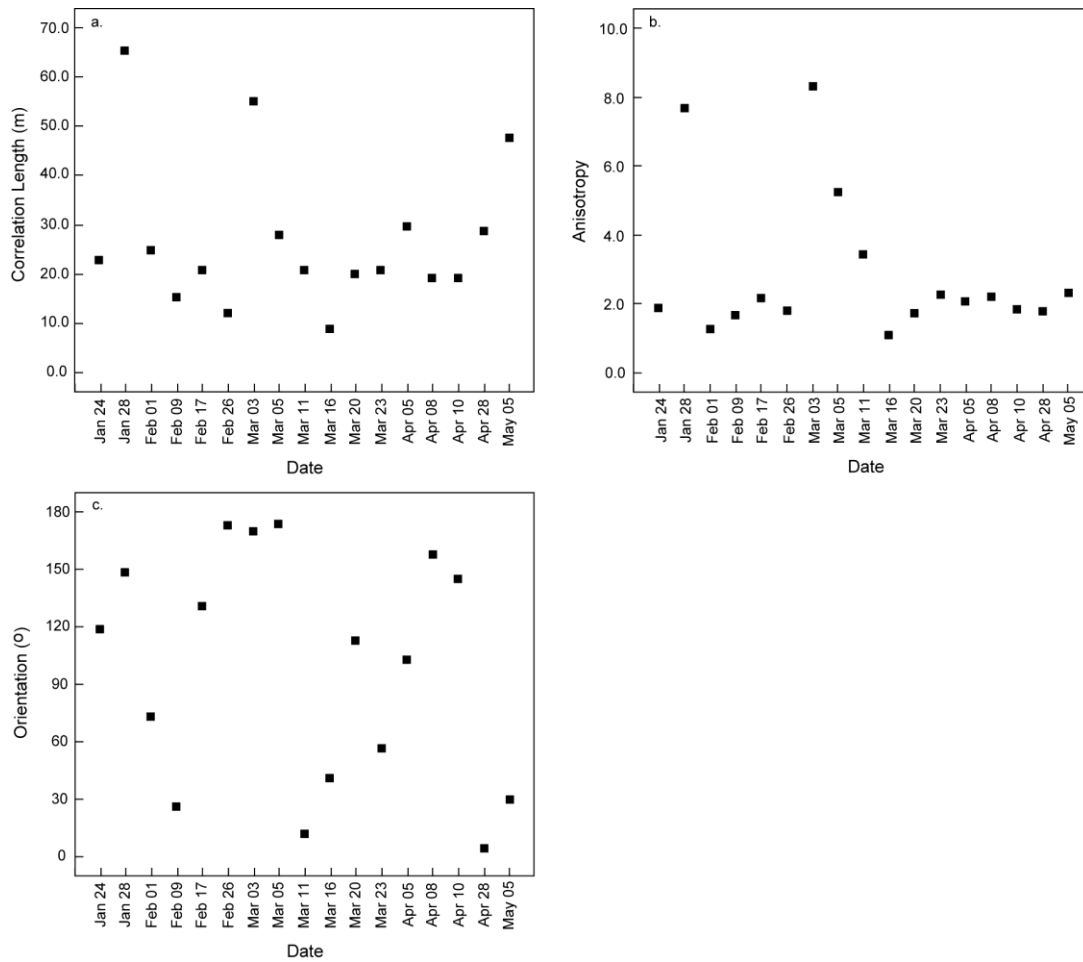


Figure 3.5: Correlation length (a.), anisotropy (b.) and orientation (c.) derived from the variogram analysis for snow depth distributions measured over smooth land-fast sea ice in 2004. Note: For orientation 0° denotes east orientation of snowdrifts, while 90° denotes north orientation. (From Iacozza and Barber, 2010. © Wiley-Blackwell. Reprinted with permission).

the geometric anisotropy was significantly large (values greater than 3 for all the sampling days). The correlation length of long axis of these snowdrifts was much larger than that for the short axis, suggesting that these drifts were larger, more defined and oriented in a particular direction. Calculated orientation from the

anisotropy analysis for each study area indicates that the snowdrift orientation varied greatly throughout the first part of the study area (Figure 3.5c). The orientation of the snowdrifts alternated from east-west, to north-south and then back to east-west from January 24 to February 17, 2004. The snowdrifts were orientated in the east-west direction between February 26 and March 16 and between April 8 and May 5 (Figure 3.5c), corresponding to the predominant wind direction during snow drifting events.

To understand the mechanism responsible for the temporal evolution in snow distribution, a microscale examination of changes in snowdrift was used. Analyses of the snow depth suggest that depth along both the parallel and perpendicular transects was statistically greater for May 28 compared to before May 28 ($z = -20.4$, $p < 0.01$, $n = 1512$ for the parallel transect; $z = -5.2$, $p < 0.01$, $n = 1512$ for the perpendicular transect). For the parallel transect, this large increase on May 28 occurred along most of the transect, with the valleys between snowdrifts being infilled with snow (Figure 3.6a.), while the change observed along the perpendicular transect was primarily due to infilling of the large valley at the beginning of the sampling transect (Figure 3.6b.). These changes corresponded to the large snowfall event with strong winds that occurred between May 25 and 27 (Figure 3.6c). The snowfall event and wind event persisted over a couple of days, with wind direction predominantly from the east, then changing to the south by the end of the event. The strong winds during this period (greater than 7.7 m/s) would have blown the fallen snow (due to its lower density) into the valleys between dunes, filling in these areas (Figure 3.6a. and b.). A result of this infilling is that the snow surface is

“smoothed” out, modifying the drag coefficient, and thus influencing further drifting snow events (Andreas, 1995). This also resulted in an increase in the correlation length, suggesting the lengthening of the snowdrifts in this particular direction.

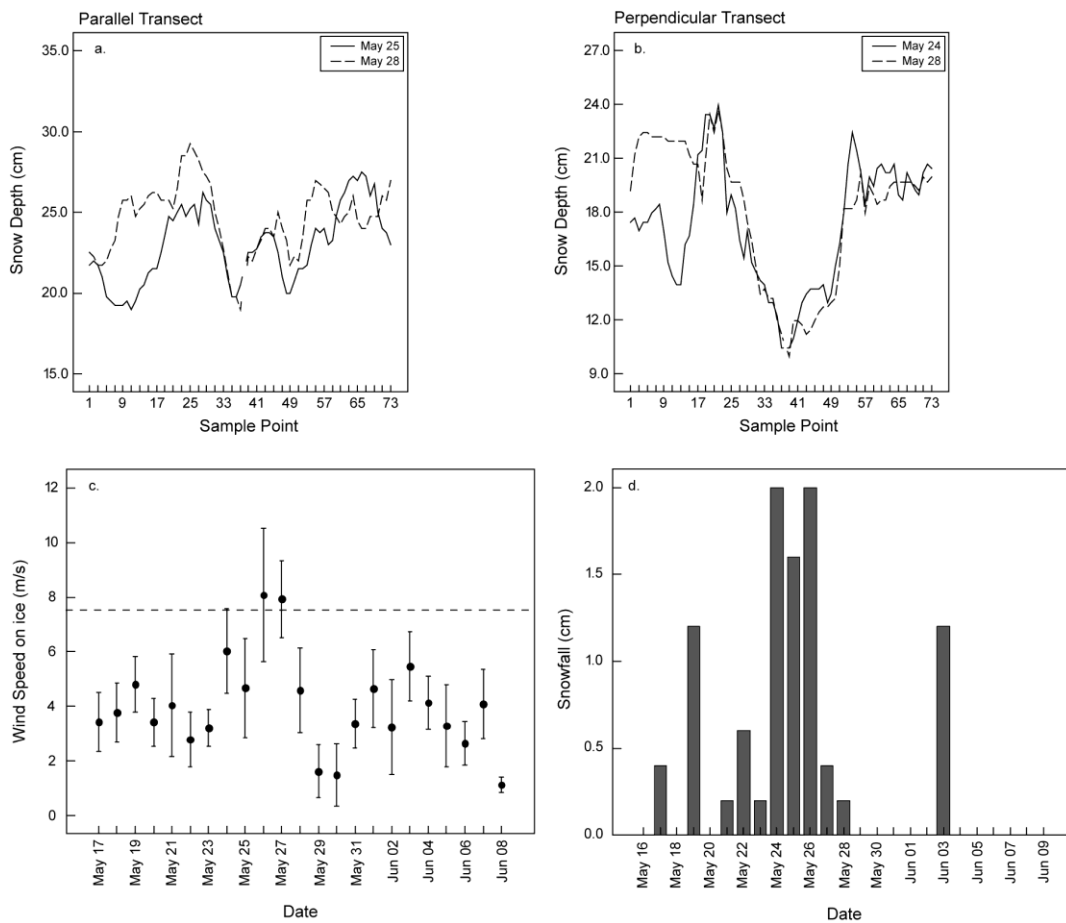


Figure 3.6: The spatial change in snow depth along the parallel (a.) and perpendicular (b.) transects sampled in 2000. The bottom graphs show the time series of daily wind speed on ice (c.) and precipitation frequency (d.) for 2000. Dashed line on the graph of wind speed indicates the threshold wind speed for saltation. (From Iacozza and Barber, 2010. © Wiley-Blackwell. Reprinted with permission).

3.3 COMPARISON OF LAND-BASED VERSUS ON-ICE METEOROLOGICAL DATA

Results suggest that the ability to represent the conditions on sea ice is dependent on the meteorological variable. Regression analysis indicate that a large percentage of the variability in air temperature above the ice in 2004 could be accounted for by the variability of land-based air temperature measured at either weather station during the winter and spring seasons. The equation predicting daily air temperature on the ice from air temperature measured at the Tuktoyuktuk weather station is [3.3]:

$$T_i = -6.8 + 0.8 T_{TS}, \quad [3.3]$$

where T_i is the air temperature ($^{\circ}\text{C}$) above the ice and T_{TS} is the air temperature ($^{\circ}\text{C}$) recorded at the Tuktoyuktuk weather station. This equation is able to account for 85.1% of the variability (Figure 3.7a). The equation predicting daily on-ice air temperature from the air temperature recorded at the Paulatuk weather station is [3.4]:

$$T_i = -6.9 + 0.8 T_{PS}, \quad [3.4]$$

where T_i is the air temperature ($^{\circ}\text{C}$) above the ice and T_{PS} is the air temperature ($^{\circ}\text{C}$) recorded at the Paulatuk weather station. This equation accounts for a similar amount of the variability in temperature on the sea ice (coefficient of determination or $R^2 = 85.4\%$; Figure 3.7b). Both models suggest that the air temperature above ice is approximately 7°C colder than that reported at either land-based station. The slopes in both regression models suggest less than a 1% bias in temperature at the land-based station. The similarity in equations, as well as the large R^2 indicates that

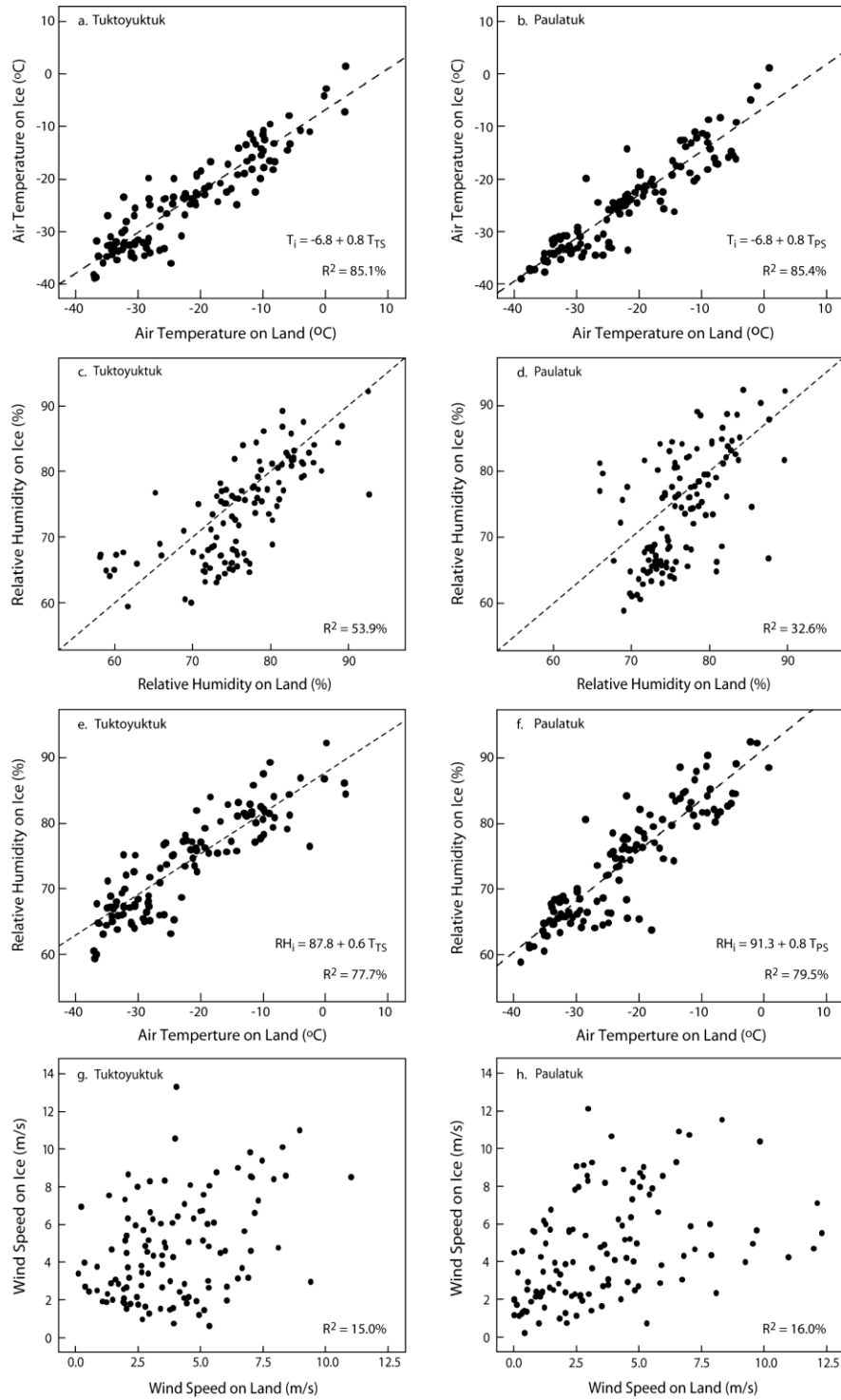


Figure 3.7: Scatterplots of daily averaged temperature (a. and b.), relative humidity (c. through f.) and wind speed (g. and h.) measured at the ice meteorological station versus the weather station at Tuktoyuktuk and Paulatuk. The dashed lines represent the lines of best fit through the scatterplots. Included are the regression equations and R^2 values. (From Iacozza and Barber, 2010. © Wiley-Blackwell. Reprinted with permission).

data collected at either location is suitable as an approximation for on-ice conditions.

Modeling the relationship between the relative humidity recorded at the ice station and at either land-based station failed to produce significant results ($R^2 = 53.9\%$ using relative humidity measured at the Tuktoyuktuk weather station, $R^2 = 32.6\%$ using relative humidity measured at the Paulatuk weather station; Figure 3.7c. and d. respectively). This lack of agreement may be a result of the spatial distance between these locations, and differences between environmental conditions that may influence the relative humidity (i.e. areas of open water).

Further exploratory data analysis suggests that the temperature recorded at either weather station on land may be used to predict relative humidity on the ice. Regression analysis suggests that the land-based temperature can be used as a proxy for relative humidity. Using the Tuktoyuktuk temperature, the relationship between the variables can be estimated using the following equation [3.5]:

$$RH_i = 87.8 + 0.6 T_{TS} \quad [3.5]$$

where RH_i is the relative humidity (%) on the sea ice and T_{TS} is the daily average temperature ($^{\circ}\text{C}$) recorded at the Tuktoyuktuk weather station. This equation is able to account for 77.7% of the variability in the relative humidity on the sea ice. The linear nature of this model indicates that with warmer temperatures, the relative humidity tends to increase (Figure 3.7e). This is to be expected given the fact that as temperature increases, the saturated vapour pressure of air also increases and the air can hold more water vapour.

The accountability of the relationship improves slightly when using the daily average recorded temperature from the Paulatuk weather station ($R^2 = 79.5\%$). The resultant equation is [3.6]:

$$RH_i = 91.3 + 0.8 T_{PS}, \quad [3.6]$$

where RH_i is the relative humidity (%) on the sea ice and T_{PS} is the daily average temperature ($^{\circ}C$) recorded at the Paulatuk weather station. This relationship is linear, suggesting a constant increase over the range of the temperature (Figure 3.7f). It is unclear whether this relationship is an artifact of the locations selected or is valid for a longer temporal period. To examine if this relationship between land-based temperatures and ice-based relative humidity is valid, a comparison using data for other locations and a longer time period should be conducted.

Relatively weak associations were found between wind speed measured above the sea ice and the wind speed measured at the Tuktoyuktuk weather station (Figure 3.7g) or the Paulatuk weather station (Figure 3.7h). The Tuktoyuktuk weather station wind speed was only able to account for 15.0% of the variability in wind speed on the ice, while the wind speed at Paulatuk was only able to account for 16.0% of the variability of wind speed on sea ice. This lack of significant agreement is not surprising since the on-ice meteorological station was located on smooth ice within a relatively open area, while this is generally not the case for the land-based meteorological stations. As well, the land-based meteorological stations were between 100 and 300 km from the meteorological station on the sea ice. This

significant distance would potentially have a greater impact on this meteorological variable, compared to temperature and relative humidity.

Comparing the on-ice to the Tuktoyuktuk weather station, wind direction was the same only 29% of the time (i.e. 34 of the 117 sampling days) (Figure 3.8a). During 58% of the sampling period (67 of the 117 sampling days), wind direction recorded at the Tuktoyuktuk station and wind direction on-ice was different by one directional class (offset by 45°; Figure 3.8a). Using the wind direction recorded at the Paulatuk weather station did not improve these results. 10 of the 124 sampling days (or 8%) recorded the same wind direction, while only 51% of the sampling days (63 of the 124 sampling days) were within one directional class or 45° (Figure 3.8a). As with wind speed, distances between locations and topographic features would influence the local wind direction, thus making it difficult to estimate the on-ice conditions from land-based meteorological station data.

Comparing the daily precipitation measurements made at the land-based weather stations to the measurements on the ice did not produce statistically significant associations (Figure 3.8b). Examination of the daily cumulative precipitation suggests that the land-based precipitation (either Tuktoyuktuk or Paulatuk) was greater than that on the ice for most days. These results suggest that the precipitation on the ice cannot be estimated using the precipitation measured at the land weather stations. Examine of synoptic weather systems may explain these differences, however this will not allow for the prediction of on-ice precipitation from land-based weather stations.

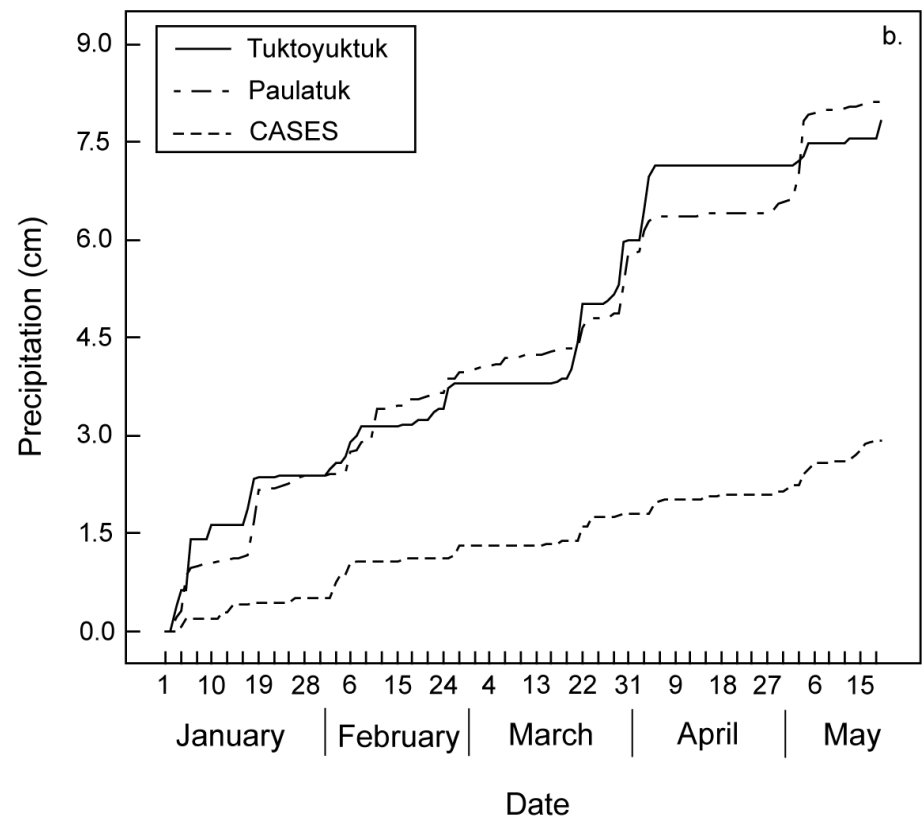
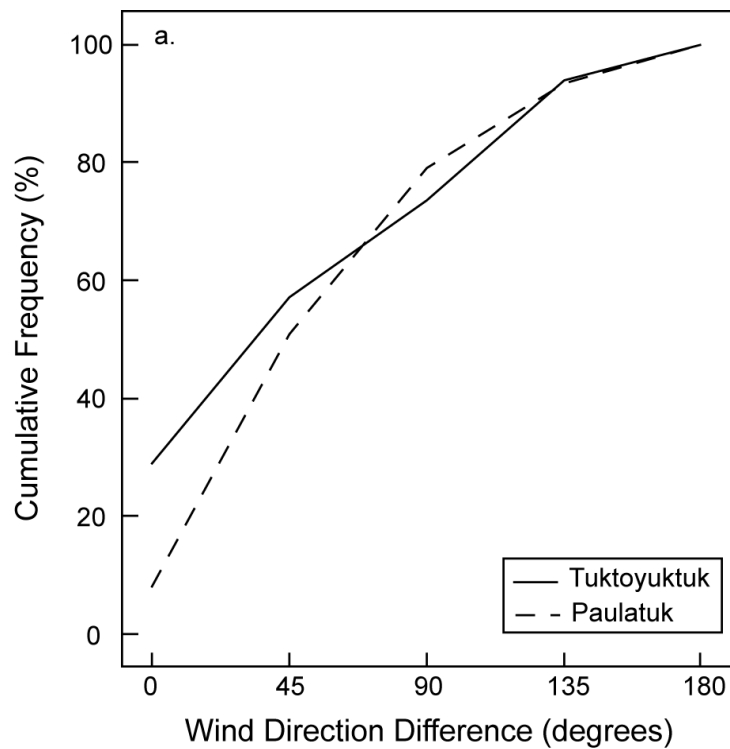


Figure 3.8: (a.) Cumulative frequencies in differences in classes of daily wind direction for Tuktoyuktuk (solid line) and Paulatuk (dashed line), compared to the wind direction measured on the sea ice. A difference of 1 would indicate a 45° difference in daily wind direction. (b.) Comparison of cumulative precipitation recorded on the sea ice at the CASES site, and at the Tuktoyuktuk and Paulatuk weather stations. (From Iacoza and Barber, 2010. © Wiley-Blackwell. Reprinted with permission).

3.4 SNOW REDISTRIBUTION MODELING USING SNOWMODEL

The general trends in the observed total SWE were captured by the four model runs (Figure 3.9). There is a general increase in SWE during the early winter period, with a fairly constant SWE for February and March. In the early spring, both the models and the observed SWE demonstrate another increase in SWE. However, the individual *SnowModel* runs are unable to capture the magnitude of the observed SWE. The total SWE estimated from the modeled runs were significantly lower than the observed SWE for the beginning (January to early February) and the end of the sampling period (April to May; Figure 3.9). This underestimation of the SWE may be due to the density of snow that was used to model the SWE using *SnowModel* (a typical value instead of the actual which was used in the estimation of the observed data) and the inability to capture the larger snowdrifts that formed during the early winter period. During the period from the middle of February to the end of March, the results for the model runs were similar to those observed in the field (Figure 3.9). Run 1, forced using the meteorological variables collected on the sea ice, was the closest to the observed data, as expected.

Due to the fact that snow distribution sampling was done at different locations throughout the sampling period, daily model outputs from *SnowModel* were compared statistically to the sampled distributions using probability density functions. Results from run 1 (using meteorological data from the sea ice station) indicate a lack of correspondence between the modeled SWE distribution and the observed distributions. Both observed and modeled distributions are non-normal

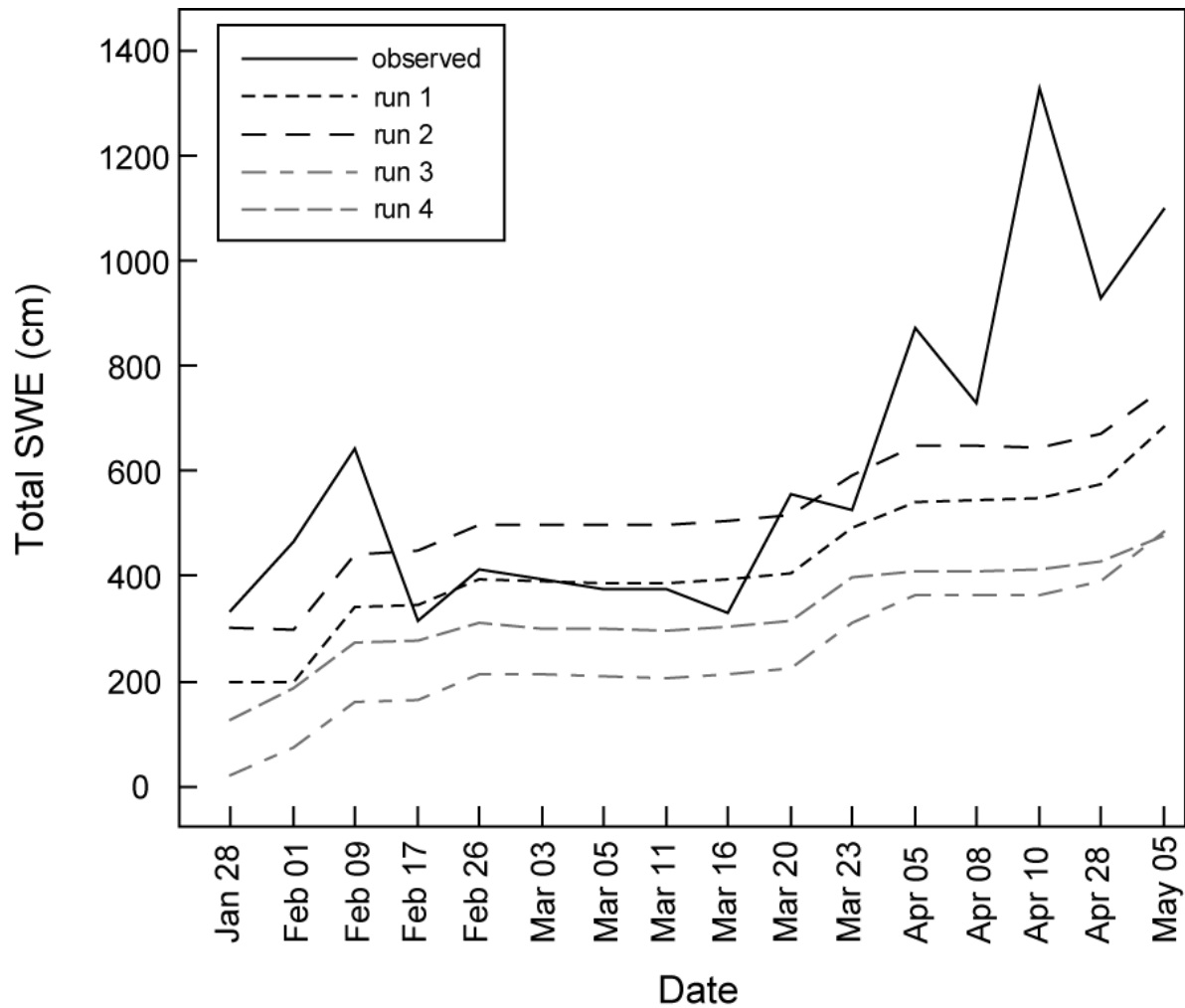


Figure 3.9: Comparison between the magnitude of SWE measured at the sampling sites (observed, solid line) and the four model runs using *SnowModel* (dashed lines). (From Iacoza and Barber, 2010. © Wiley-Blackwell. Reprinted with permission).

and thus a non-parametric test (Mann-Whitney test) was run to compare the two distributions for each sampling date. Results suggest that the two distributions are statistically independent ($p > 0.05$ for each sampling date). An examination of the PDFs suggest that *SnowModel* is not able to estimate the entire range of SWE distribution measured on smooth land-fast sea ice using the inputs for this run. For most sampling days, *SnowModel* output peaks between SWE values of 1.0 and 2.5 cm, with few sampling points greater than 3.0 cm for any sampling date (Figure 3.10a). Between January 28 and March 11, 2004, the distribution in SWE from the model output was unimodal with a peak centered on 1.0 to 1.5 cm (Figure 3.10a). On March 11, the peak in SWE values shifted toward 2.5 cm, with a second peak at lower SWE values, suggesting that with the additional snowfall that occurred around that date, a greater amount of snow was being caught within the study area. This pattern continues throughout the rest of the sampling period, with the development of a more pronounced peak in frequency of SWE. This again would suggest that the model was able to capture a redistribution of snow with the additional snowfall or drifting snow. However, this redistribution does not resemble the pattern measured directly on the sea ice.

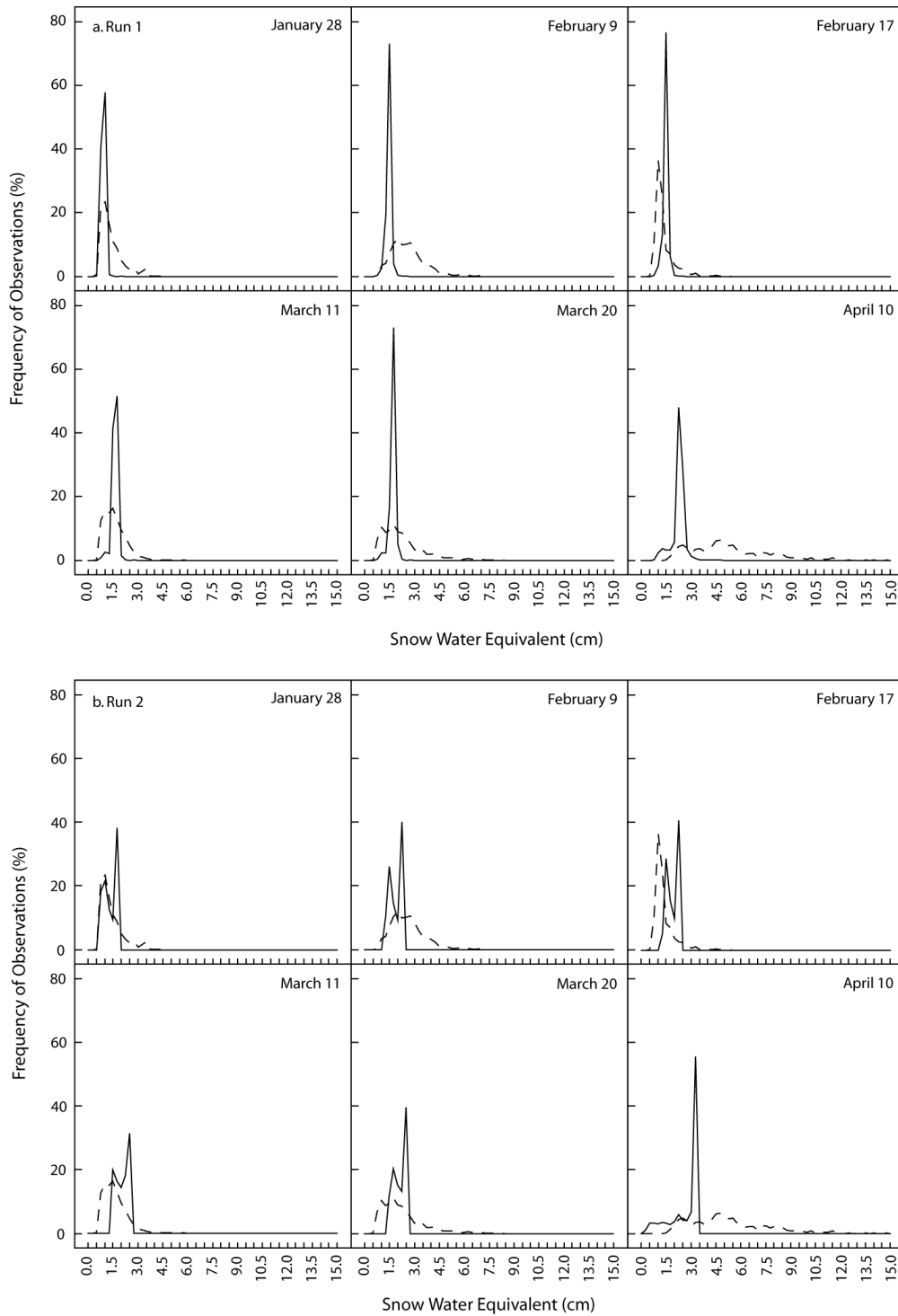


Figure 3.10: Probability density functions of observed SWE (dashed line) and modeled SWE (solid line) from SnowModel, for run 1 (a.), run 2 (b.), run 3 (c.) and run 4 (d). Only eight sampling days are shown to compare sampled and modeled SWE distributions. Bin size is 0.025 cm. (From Iacozza and Barber, 2010. © Wiley-Blackwell. Reprinted with permission).

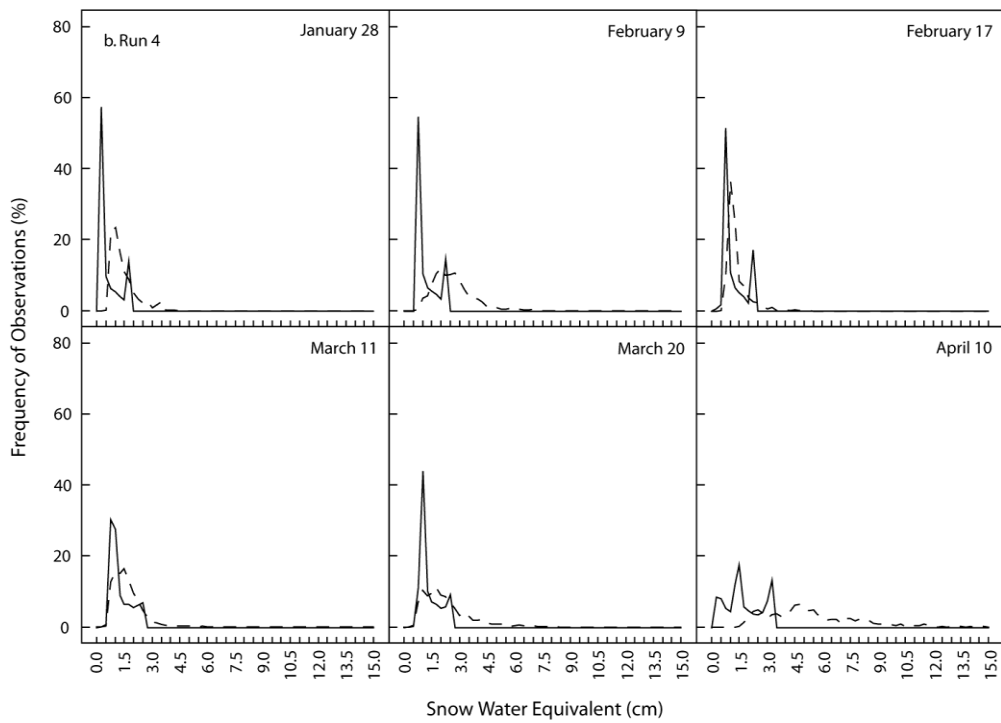
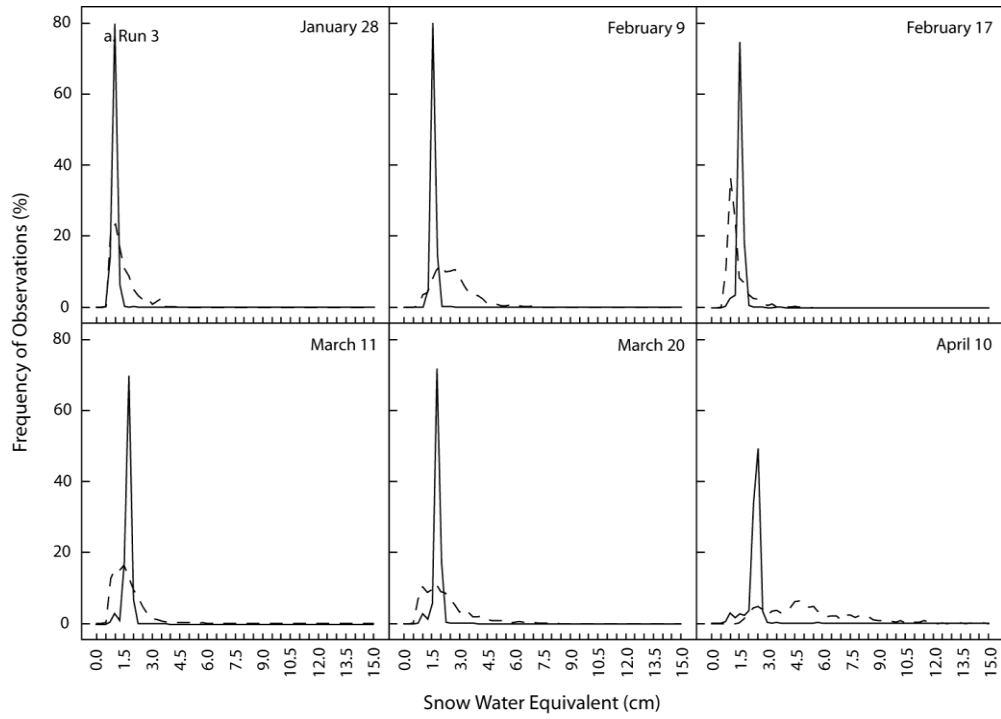


Figure 3.11 con't: (From Iacozza and Barber, 2010. © Wiley-Blackwell. Reprinted with permission).

Comparison between observed SWE distribution and the outputs from run 2 also suggest a failure to capture the range of SWE values. Statistical comparisons between the distributions again suggest that the observed and modeled distributions of SWE are independent ($p > 0.05$ for each sampling day). As with the first model run, the frequency of observations for run 2 was centered around the range 1.0 to 2.5 cm for most of the sampling period (Figure 3.10b). This again does not correspond to the observed PDF for estimated SWE distribution, with *SnowModel* not being able to model the smaller or larger SWE values present in the sampled area. A major difference between model runs is that for run 2 the outputs suggest a bimodal distribution in SWE that is present throughout most of the sampling period (Figure 3.10b). This bimodal distribution is also absent from the observed data, again limiting the ability of this model to estimate the snow redistribution for the given inputs. Another major difference between model runs is that the frequency of observations is less peaked for run 2, suggesting a better approximation of the observed SWE distribution. However, both model runs fail to capture the areas with greater SWE values and thus fail to capture the pattern of observed SWE distribution.

Run 3 used the relationship developed in objective 2 to estimate temperature and relative humidity on the sea ice using the Paulatuk weather station temperature. There was no significant improvement in the estimation of snow redistribution over sea ice using this model run (Figure 3.10c). The modeled outputs resembled the outputs for run 1, suggesting that the timing of the estimation is important to the comparison between observation and *SnowModel*. This also indicates that the

climate variables need to be estimated for the entire year, along with better representations of wind and precipitation data.

Like run 2, the results from run 4 are able to capture (in part) the larger SWE values seen in the observed data (Figure 3.10d). One major difference between run 4 and the observed SWE is that there is a bimodal distribution in SWE for this model run, which is absent in the observed data (yet similar to the results for run 2). Another discrepancy is that there exists a large disagreement between the modeled and observed data, especially during the spring period. This again suggests that the model is unable to capture the large snow drifts (and thus greater SWE values) that are observed over smooth sea ice. Statistical comparison with the observed SWE distribution using the Mann-Whitney test again indicates that run 4 is not statistically similar for each sampling day ($p > 0.05$).

The inputs used in the model runs may explain in part the discrepancies between the observed distributions and the model outputs. For runs 1 and 3, the snow distribution observed on January 21, 2004 was used as the surface topography to drive the model. Outputs from subsequent days were added to this surface topography. Since the model ran from the middle of the sampling period, this may have limited the snow drifting that could occur prior to any snow deposition after January 21. The improved modeling results for run 2 and 4 also indicate that forcing the model from the beginning of the season is required to get a better estimate of the observed SWE. Also, while it is ideal to use the meteorological data measured on the sea ice as an input for the model, these data were only available

from January 2004, while ice consolidation and thus snow distribution over sea ice occurred approximately 3 months prior. Meteorological data from the land-based weather station needs to be employed as an input into the model to represent the distribution from October 2003, however the meteorology used in the input (especially wind speed and direction) may not necessarily correspond to the observed meteorological conditions on the sea ice. A relationship between land-based and ice-based meteorological variables over an annual cycle is required to estimate the on-ice conditions and thus used as an input into *SnowModel*. A common feature for all model runs is the inability to capture the large snow drifts that develop over the smooth sea ice. This may be a result of the initial topography that was used to force the model. This may suggest that small-scale (less than 1 m) topography differences may be important for the evolution of snow over smooth sea ice.

3.5 CONCLUSION

The temporal evolution of snow on sea ice is controlled by the meteorological conditions over the sea ice and the characteristics of the roughness of sea ice. *In situ* data were used to examine the evolution of snow distribution over smooth land-fast sea ice and describe the meteorological forcing factors that influence this evolution. Changes in the PDFs of the snow depth distribution occurred throughout the study period, and these changes correspond to changes in meteorological factors, namely depositional events and drifting snow. Between January 21 and March 16, the PDFs exhibit a unimodal distributional with a mode of 4cm. Between

March 16 and 23, the PDFs shifted to contain a longer tail, suggesting the presence of deep snowdrifts, while retaining a mode at 4 cm. After March 23, the PDFs shifted again to an even longer tail (again suggesting even deeper snowdrifts) and a multimodal distribution at deeper snow depths. These patterns suggest that the PDF is able to capture the variability in snow depth distribution and thus could be used to model snow depth over smooth land-fast sea ice.

Geostatistical spatial analysis of the temporal evolution of the snow distribution indicates a consistency in the model parameters. The low nugget values observed for most of the sampling period indicates that a significant portion of the variability in snow depth can be accounted for using the theoretical model. The other variogram parameters (i.e. correlation length, anisotropy and orientation) provide information on the evolution of the snowdrifts. Over the study period, the correlation length generally increases suggesting an increase in snowdrift size. The large anisotropy for most of the sampling period indicates the presence of clearly defined and oriented snowdrifts. After February 17, 2004 the snowdrifts were oriented primarily in an east-west direction and this is related to the meteorological setting during this period.

A microscale examination of the temporal evolution of the snow over sea ice was conducted to understand the observed changes in the snowdrifts. Results suggest that during periods of significant snowfall or drifting snow, the valleys between dunes would fill-in causing the increase in snowdrifts found with the geostatistical

analysis. This infilling would significantly change the overall pattern of the snow depth distribution, thus modifying further changes due to drifting snow events.

Due to the lack of consistent measurement of meteorological variables over the sea ice, measurements from Paulatuk and Tuktoyuktuk weather stations were compared to the conditions on the sea ice for the winter and spring periods. Results suggest that the ability of land-based meteorological measurements to estimate on-ice condition is dependent on the variable. Land-based air temperature can be used as a proxy measure for on-ice air temperature and relative humidity. For daily wind speed and wind direction, the regression model was not able to account for a significant amount of variability in the on-ice condition. Less than 60% of the daily modes for wind direction on-ice are within 45° of the daily mode recorded at the weather stations on land. This lack of agreement was probably due to local effects (i.e. topographic effects). A similar lack of agreement between precipitation recorded on-land and that recorded on-ice exists during the 2004 study period. Due to the fact that snow redistribution is dependent on the precipitation and wind events, further research needs to be conducted to determine if these meteorological variables can be estimated for locations on the ice.

An additional objective of this research was to model the evolution of snow depth distribution over smooth land-fast sea ice using a spatially distributed snow-evolution model (*SnowModel*). Four independent model runs were done with run 1 using data collected on the ice, run 2 using meteorological inputs from land-based stations, run 3 using the relationship developed in objective 1 to estimate on-ice

temperature and relative humidity, and run 4 using meteorological inputs from NCEP reanalysis modeled meteorological variables. Results from all model runs indicate that the model was not able to adequately reproduce the SWE distribution and thus the snow redistribution. The model fails to capture the range of SWE observations that are measured in the observed distribution. The lack of spatially adequate surface topography, as well as the use of land-based meteorological inputs or on-ice inputs that do not extend over the entire snow cover period may in part contribute to the lack of agreement between observed and modeled outputs.

In future work, this model will need to be adapted to address the issue of snow evolution over sea ice, and better representation of both sea ice surface topography and meteorological condition over sea ice is required. Remote sensing imagery with a fine spatial resolution can be used to estimate the sea ice surface topography subsequent to ice freeze-up and prior to any significant snowfall. In terms of meteorological condition, a complete annual cycle is required to compare on-ice with on-land conditions. These two datasets can then be used in combination with *SnowModel* to better estimate snow evolution. In addition, changes to *SnowModel* may be required to accommodate the differences between a terrestrial landscape (in which the model was designed) and an icescape.

One limitation of this paper is that topographic influences on snow depth evolution are not considered in this paper. The following chapter focuses on investigating snow evolution over rough and ridged sea ice, thus including the surface topography into the forcing of the temporal evolution of the snow

distribution. Another limitation of this study is the spatial distribution of the sampling area. *SnowModel* was run for a small spatial area throughout the sampling period. A more accurate representation of snow redistribution should be done on a regional or basin scale. Regional surface topography over sea ice will provide a more accurate representation of the topography for the input into the model. At present, manual measurements of surface topography are made over sea ice, however this method is not logistically feasible for a regional scale. A method based on remote sensing is thus required to estimate surface topography over sea ice To adequately model the snow distribution and redistribution.

CHAPTER 4: SPATIAL PATTERN OF SNOW DISTRIBUTION VERSUS SEA ICE ROUGHNESS IN THE CANADIAN ARCTIC

The aim of this chapter is to investigate the spatial pattern of snow distribution over rough sea ice. More specifically the objectives are to: (i) define the relationship between mean snow depth and sea ice surface roughness for rubble sea ice and ridges, (ii) describe the spatial pattern (variability about the mean) of snow distribution as function of sea ice roughness, and (iii) examine how the observed spatial pattern evolves over rubble sea ice and ridges through the winter period. These objectives form an important first-step in understanding not only the physical processes operating within the ocean-sea ice-atmosphere (OSA) interface but also in understanding associated physical-biological coupling within the marine cryosphere and modeling snow distributions over sea ice.

4.1 METHODS

4.1.1 Snow depth and surface roughness

In situ snow depth distribution and ice surface roughness over rough ice were collected in the in the winter and spring of 2004 as part of the Canadian Arctic Shelf Exchange Study (CASES). For the purposes of this study, rubble ice consisted of sea ice that was deformed over a large area by collision of sea ice due to atmospheric and/or oceanic forcing. Ridge ice is defined as a linear deformation, again produced by atmospheric and/or oceanic forced ice convergence. The difference between these two classes is one of direction; rubble ice occurs over large areas, while ridge

ice is linear and oriented in a particular direction. Due to the nature of the close proximity of sampling sites, snow depth over each ice type did not vary as a function of age of the sea ice. For all ice types, the approximate location of each site was determined from a satellite image of the area acquired prior to sampling.

In 2004, sampling sites within the two ice types were selected randomly. The only requirement for the selection of sites was that each site be located at least 150 m from another ice type to reduce the influence of the adjacent ice type on the snow distribution patterns within the sampling site. Snow depth sampling within the rubble ice sites was similar to that conducted for smooth ice (Section 3.1) and involved systematic measurements taken at 1 m sampling intervals along eight straight transects radiating from a central point, for 50 m or 71 m (Figure 4.1a). Snow depth measurements were collected at the sampling interval of 1 m using an automated snow probe with a precision of 2 mm. Due to the destructive nature of the sampling technique, each rubble ice site was sampled once during the sampling period.

Surface topography measurements for rubble ice involved surveying the snow-plus-ice surface using a level located in the center of the sampling area. At the center point of each rubble ice site, the height of the level above the ice surface (including the snow depth) and ice thickness were recorded. Using the level and stadia (ruler), the surface topography was surveyed by recording height measurements at a 1m sampling interval (using the same locations as snow depth; Figure 4.1c). Ice thickness at each sampling point was then calculated using the following equation

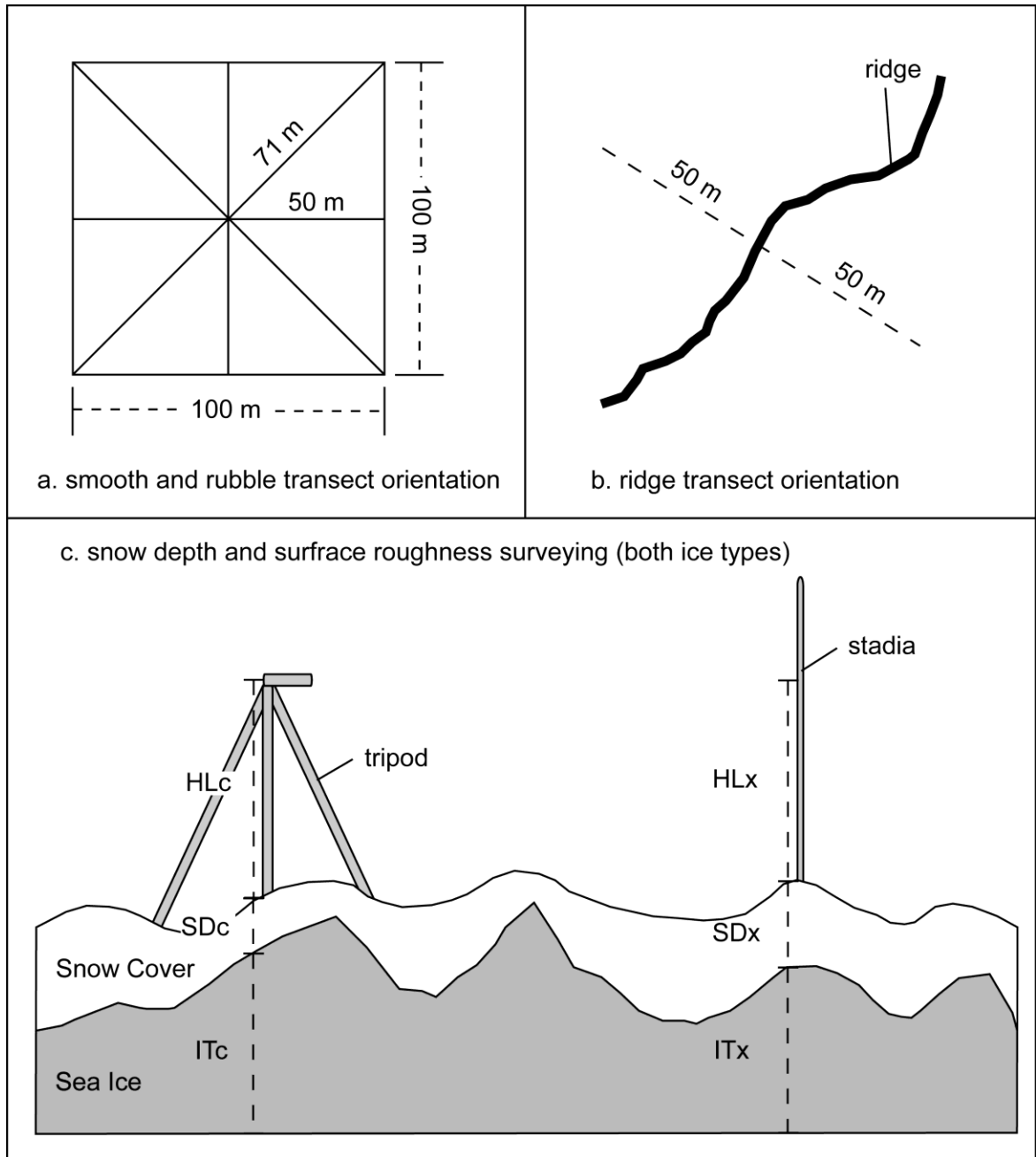


Figure 4.1: Schematic of sampling for a. smooth and rubble ice and b. ridge sites. A diagram illustrating the measurements made at each location is provided in c.

[4.1]:

$$IT_x = (HL_c + SD_c + IT_c) - (HL_x + SD_x) \quad [4.1]$$

where IT_x is the ice thickness at each sampling point, HL_c is the measured height of the level at the centre point, SD_c is the snow depth at the centre point, IT_c is the ice thickness at the centre point, HL_x is the height measured at the sampling point, and SD_x is the snow depth measured at the sampling point. This produces an ice thickness at each sampling point that is relative to the datum at the centre location. Ice surface roughness was calculated as the difference between the minimum ice thickness within the sampling area and the ice thickness estimated at each sampling location. This methodology produced a 2-D grid of ice surface roughness measurements. Similar methodology was used to estimate surface roughness at each ridged ice site. The transit was located on the smooth ice adjacent to the ridge. Sea ice thickness was again estimated for each point perpendicular to the orientation of the ridge using [4.1]. This produced a 1-D profile of ice surface roughness through the ridge. At both ice types, this methodology produced a dataset of coincident snow and ice surface topography measurements. To compare sites, snow depth at each sampling point was standardized. Standardization was accomplished by dividing the measured snow depth at each point by the snowfall that occurred between 1 January 2004 and the sampling date of each site.

Once a ridge was found, the starting point along the ridge was randomly chosen. Measurements were made perpendicular to the orientation of the ridge, beginning on the smooth ice located on one side of the ridge, extending through the ridge to

the smooth ice on the other side of the ridge. Snow depth and ice surface roughness measurements were made at a sampling interval of 1 m for a maximum distance of 100 m (Figure 4.1b). Sampling methodology was similar to that utilized for rubble ice. As with the previous ice types, ridge sites were only visited once during the sampling period due to the destructive nature of the data collection method. The orientation of each ridge sampled varied, however for this research, the ridges were classified as either north-south (N-S) or east-west (E-W) ridges.

During the winter and spring of 2004, 6 sites were sampled on rubble ice (denoted by RB-) and 19 sites along ridges (denoted by RD-; Figure 4.2). These sites were in close proximity to the location of the ship in Franklin Bay due to logistics of transportation to the sites and the time required completing the surveys. The sampling commenced on January 19 and concluded on May 5, 2004 (Table 4.1).

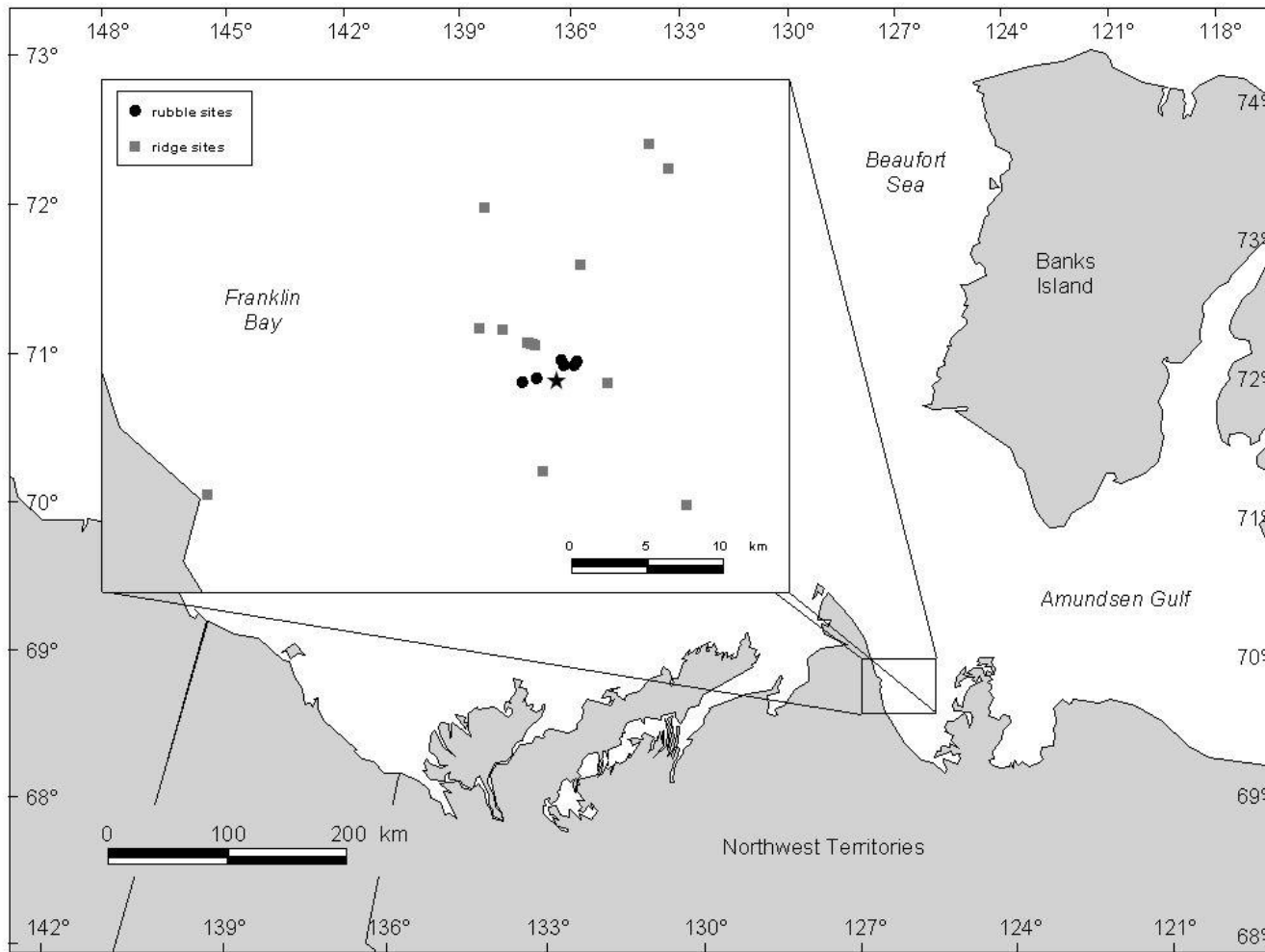


Figure 4.2: Locations of ridge and rubble ice sites sampled in 2004. The star indicates the location of the meteorological site.

Table 4.1: Sampling dates of the rubble and ridge ice sites in 2004. The rubble sites are denoted by the prefix RB-, while the ridge sites have the prefix RD-.

Rubble Ice Sites		Ridge Sites	
Site #	Sampling Date	Site #	Sampling Date
RB-1	February 5	RD-1	January 19
RB-2	February 23	RD-2	January 25
RB-3	March 7	RD-3	January 27
RB-4	March 15	RD-4	January 30
RB-5	March 19	RD-5	January 31
RB-6	April 6	RD-6	February 3
		RD-7	February 4
		RD-8	February 7
		RD-9	February 10
		RD-10	February 17
		RD-11	February 24
		RD-12	March 4
		RD-13	March 9
		RD-14	March 12
		RD-15	March 12
		RD-16	March 16
		RD-17	March 18
		RD-18	March 24
		RD-19	March 28

4.1.3 Spatial analysis

Variography

The spatial continuity of the snow depth and surface roughness variables was computed using the variogram technique. A general description of this technique is described in Chapter 3.1.

Due to the sampling of the snow depth and ice surface roughness measurements along a single transect oriented in one direction for the ridge sites, the computed

omnidirectional variogram examines the influence of distance on the spatial continuity of the variable. The directional component of variography was based on the orientation of the ridge. For the rubble ice sites, sampling was conducted along eight (8) directions, and thus omnidirectional as well as directional variograms were computed for both snow depth and surface roughness. The directional variograms were constructed at 0°, 45°, 90° and 135°, with an angular tolerance of 22.5° for each direction. 0° represents the east-west direction, while north-south is oriented in the 90° direction. From the variograms, correlation lengths (CL), as well as the geometric anisotropy and orientation were calculated for the rubble and ridge snow depth and ice surface roughness. The calculations and explanation of these parameters are described in Section 3.1.3.

Fractal Dimension

Fractal dimension (D) is a quantity that describes the complexity of a feature or structure or the space that structure occupies, independent of scale. For instance, the fractal dimension of a straight line is 1.0, while for an irregular line (i.e. curve) the fractal dimension will vary between 1.0 and 2.0. One property of fractals is statistical self-similarity. This indicates that at different resolutions, the overall complexity of the feature is similar (not necessarily identical). This difference may be due to randomness in the overall structure or processes creating the structure. This statistical quantity can be used to quantify the tortuosity (or curvy nature) of the snow distribution and sea ice roughness.

The fractal dimension was calculated from the slope of the log-log plot of the variogram parameters (Richardson, 1961; Mandelbrot, 1983; Carr, 1995; Nams, 2005) using equation [4.2]:

$$D = 2 - [m/2] \quad [4.2]$$

where D is the fractal dimension and m is the slope of the plot of the log of lag distance versus the log of the semivariance ($\gamma(h)$). Fractal dimension has been employed in the literature to examine the spatial pattern of various physical features, including animal movements (With, 1994; Mårell, *et al.* 2002; Nams, 2005) and snow depth over terrestrial surfaces (Shook *et al.* 1993; Shook and Gray 1996; 1997; Kuchment and Gelfan 2001; Granger *et al.* 2002; Litaor *et al.* 2002; Deems *et al.* 2006; 2008).

The dividers method can also be used to estimate the fractal dimension. With this method, a set of dividers or rulers of fixed length (δ) is moved along the curve. The length of the curve is estimated as the product of the number of “rulers” required to cover the object, and the scale factor. The length of the dividers is then changed (increased or decreased) with additional iterations of the procedure. The fractal dimension is calculated from the plot of $\log L$ versus $\log \delta$ according to equation [4.3]:

$$\log L\delta = \log K + (1-D) \log \delta \quad [4.3]$$

where L is the measured length, δ is the measurement scale, K is a constant, and D is the fractal dimension. Since the measured length may be dependent on the starting

point, it is recommended that this method be repeated, varying the starting location (Sugihara and May, 1990). Due to the lack of theoretical foundation for this method, it has been argued that the dividers method will only give reliable fractal dimensions for statistically self-similar curves (Normant and Tricot, 1991). This method has been successfully used to determine the fractal dimension of lung section (Rigaut, 1988) and rabbit ganglion cells (Wingate et al., 1992) illustrating the utilization of fractals in the life sciences.

An additional method for estimating the fractal dimension is the box-counting method (also known as the cell-counting method) (Longley and Batty, 1989; Hakanson, 1978). Procedurally, this method involves layering a regular grid of boxes of size δ over the curve. The number of boxes intersecting the curve (C) is then calculated as a function of the box size. This procedure is then repeated for a number of different box sizes (δ). The power-law relationship is defined by [4.4]:

$$C = K\delta^{-D} \quad [4.4]$$

where K is a constant. The log of the number of boxes filled by the curve (C) is plotted against the log of the total number of boxes in the grid. The resulting relationship if linear is defined as D . An advantage of this method is that it is easy to implement and does not require complex or large amounts of computational power. A limitation with this method is that it will only give accurate fractal dimension estimates for self-affine structures under certain conditions (Brown, 1995). The estimation of D may be sensitive to the range of box lengths chosen if the data exhibits limited resolution (Pruess, 1995). Some researchers argue that this method

may be unusable for many conditions and yields inaccurate and imprecise results (Normant and Tricot, 1991).

4.2 ASSOCIATION BETWEEN SNOW DEPTH AND SEA ICE SURFACE ROUGHNESS

Results from a one-sample Kolmogorov-Smirnov (K-S) test indicate that the distribution for both standardized snow depth and sea ice surface roughness for the majority of sites over both rubble ice and ridges do not follow a normal distribution, rather are positively skewed (Table 4.2). A Spearman's correlation was used to examine the association between the standardized snow depth and ice surface roughness. Results for rubble ice sites suggest a moderate positive association between these variables based on the individual sampling points (correlation coefficient $r = 0.76$, $p < 0.05$; Figure 4.3a). A positive association also exists between snow depth and ridged ice surface roughness ($r = 0.70$, $p < 0.05$; Figure 4.3b). This result is expected since as the surface of the sea ice become more irregular, the overall capacity to catch snow increases. Deposition will occur due to a reduction in velocity and the infilling of valleys between the roughness elements. The strength of the relationship is site dependent with values ranging from 44.2% (site RB-5) to 75.4% (site RB-3) for rubble ice. Residual analysis suggests that greater underestimation and overestimation by the models occurs at larger surface roughness. The limited accountability of the models, as well as the significant variability in the standardized snow depth at any ice roughness value (Figure 4.3) may be due to the fact that snow depth at any point with the sampling area is a function of the spatial pattern of the ice roughness elements. For instance, the snow

Table 4.2: Kolmogorov-Smirnov (K-S) test and skewness results for the rubble ice and ridge sites sampled in 2004. K-S test and skewness results that are statistically significant (i.e. not normally distributed) at a 0.05 level are shown in bold and italics.

RUBBLE ICE SITES				
SITE #	ROUGHNESS		SNOW DEPTH	
	K-S Test	Skewness	K-S Test	Skewness
RB-1	$z = 1.69$	0.73	$z = 1.04$	0.29
RB-2	<i>$z = 4.69$</i>	<i>1.89</i>	<i>$z = 4.83$</i>	<i>2.63</i>
RB-3	<i>$z = 3.80$</i>	<i>1.56</i>	<i>$z = 3.53$</i>	<i>1.30</i>
RB-4	<i>$z = 2.80$</i>	<i>1.42</i>	<i>$z = 3.48$</i>	<i>1.29</i>
RB-5	$z = 1.16$	0.60	$z = 1.30$	0.23
RB-6	<i>$z = 2.95$</i>	<i>1.17</i>	<i>$z = 2.76$</i>	<i>1.27</i>

RIDGE SITES				
SITE #	ROUGHNESS		SNOW DEPTH	
	K-S Test	Skewness	K-S Test	Skewness
RD-1	$z = 1.03$	0.66	<i>$z = 1.37$</i>	<i>1.06</i>
RD-2	<i>$z = 2.37$</i>	<i>0.75</i>	<i>$z = 2.33$</i>	<i>2.09</i>
RD-3	<i>$z = 2.55$</i>	<i>2.10</i>	<i>$z = 2.10$</i>	<i>2.10</i>
RD-4	<i>$z = 2.07$</i>	<i>1.75</i>	<i>$z = 1.69$</i>	<i>2.56</i>
RD-5	<i>$z = 1.54$</i>	<i>1.82</i>	<i>$z = 1.81$</i>	<i>2.43</i>
RD-6	$z = 1.19$	1.18	<i>$z = 1.59$</i>	<i>1.18</i>
RD-7	$z = 1.30$	1.23	<i>$z = 1.37$</i>	<i>1.20</i>
RD-8	$z = 1.23$	1.16	<i>$z = 1.41$</i>	<i>1.16</i>
RD-9	$z = 1.09$	1.53	<i>$z = 2.32$</i>	<i>2.83</i>
RD-10	<i>$z = 1.98$</i>	<i>0.84</i>	<i>$z = 1.78$</i>	<i>1.10</i>
RD-11	<i>$z = 1.42$</i>	<i>1.77</i>	<i>$z = 2.81$</i>	<i>2.76</i>
RD-12	<i>$z = 1.80$</i>	<i>1.35</i>	<i>$z = 1.64$</i>	<i>1.30</i>
RD-13	<i>$z = 1.55$</i>	<i>1.17</i>	<i>$z = 1.39$</i>	<i>1.22</i>
RD-14	<i>$z = 1.36$</i>	<i>3.03</i>	$z = 0.82$	0.72
RD-15	<i>$z = 1.88$</i>	<i>2.35</i>	<i>$z = 1.72$</i>	<i>1.32</i>
RD-16	<i>$z = 1.43$</i>	<i>3.00</i>	$z = 1.13$	1.29
RD-17	<i>$z = 1.53$</i>	<i>1.43</i>	$z = 1.04$	0.77
RD-18	<i>$z = 1.75$</i>	<i>1.93</i>	<i>$z = 1.56$</i>	<i>1.43</i>
RD-19	$z = 0.99$	1.32	$z = 0.86$	1.54

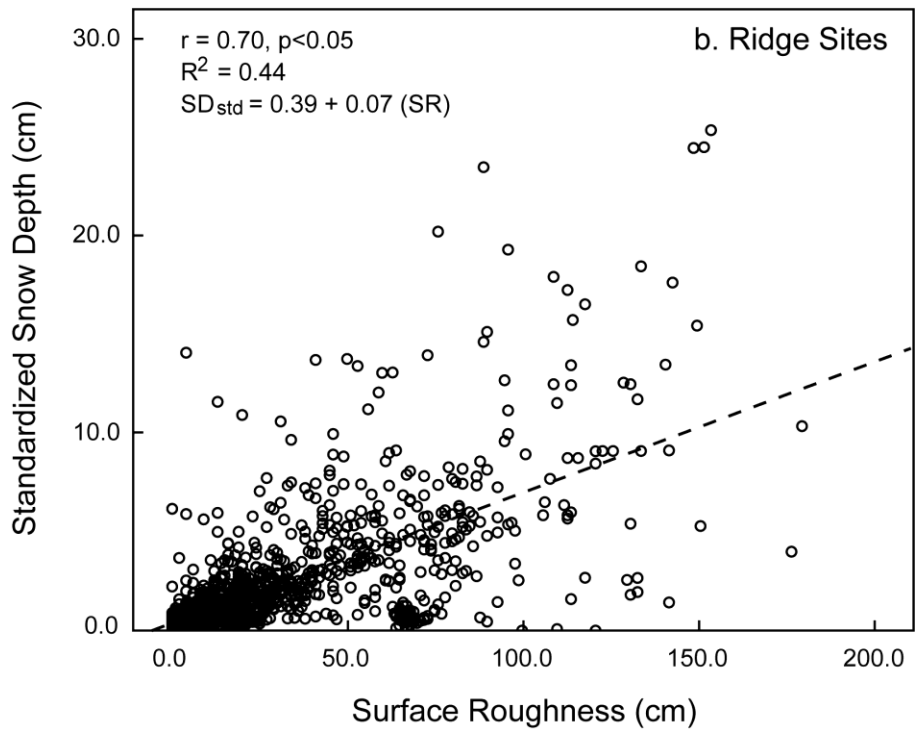
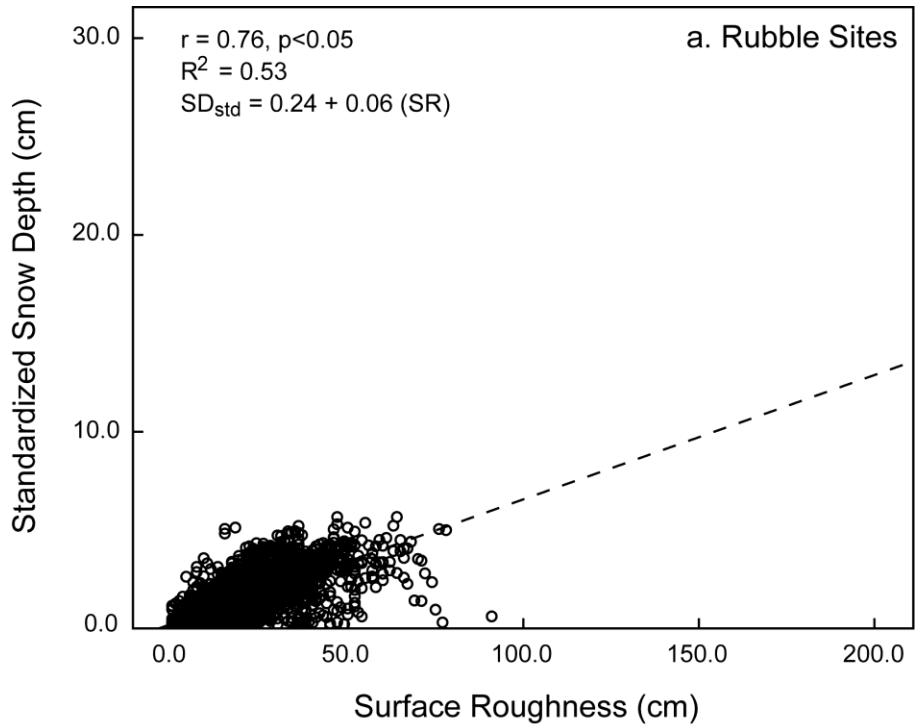


Figure 4.3: Correlation and regression of standardized snow depth versus surface roughness for a. rubble sites and b. ridge sites. The correlation coefficient (r) and coefficient of determination (R^2), as well as the equation of the best-fit line through the scatter of points, for each ice class are included.

depth measured over a ridge that is long with a central peak in surface roughness will be different than a ridge that is composed of many roughness elements.

4.3 SPATIAL PATTERN OF SNOW DEPTH AS A FUNCTION OF SEA ICE ROUGHNESS

The snow depth correlation lengths estimated from the omnidirectional variograms for rubble ice ranged from 8.7 m to 22.4 m (Figure 4.4a.). This value indicates the average length of the snowdrifts (irrespective of direction) measured over this sea ice type. Correlation analysis suggests that the average snowdrift length (based on omnidirectional analysis) does not significantly change over the sampling period ($r = 0.37$, $p = 0.47$). This result indicates that the observed changes in the correlation lengths are probably more a function of sea ice roughness, as well as meteorological forcing, than time. Similar ranges in snow depth correlation length were determined from the directional variograms (Figure 4.4a.). The one exception was for site 6. The correlation length oriented northeast-southwest (45°) for site 6 was 55 m, suggesting that compared to the other three directions longer snowdrifts were oriented in that direction. This is different than the result for the site sampled prior (site RB-5) where the spatial pattern in snow depths was similar in all directions (Figure 4.4a). The correlation lengths were greater for the 45° (northeast-southwest) and 90° (north-south) directions consistently for the first three sites, relative to the other two directions (Figure 4.4a). This indicates that from February 5 to March 7, there was a preferential orientation of snowdrifts. After this period, there was no pattern in the directional correlation lengths.

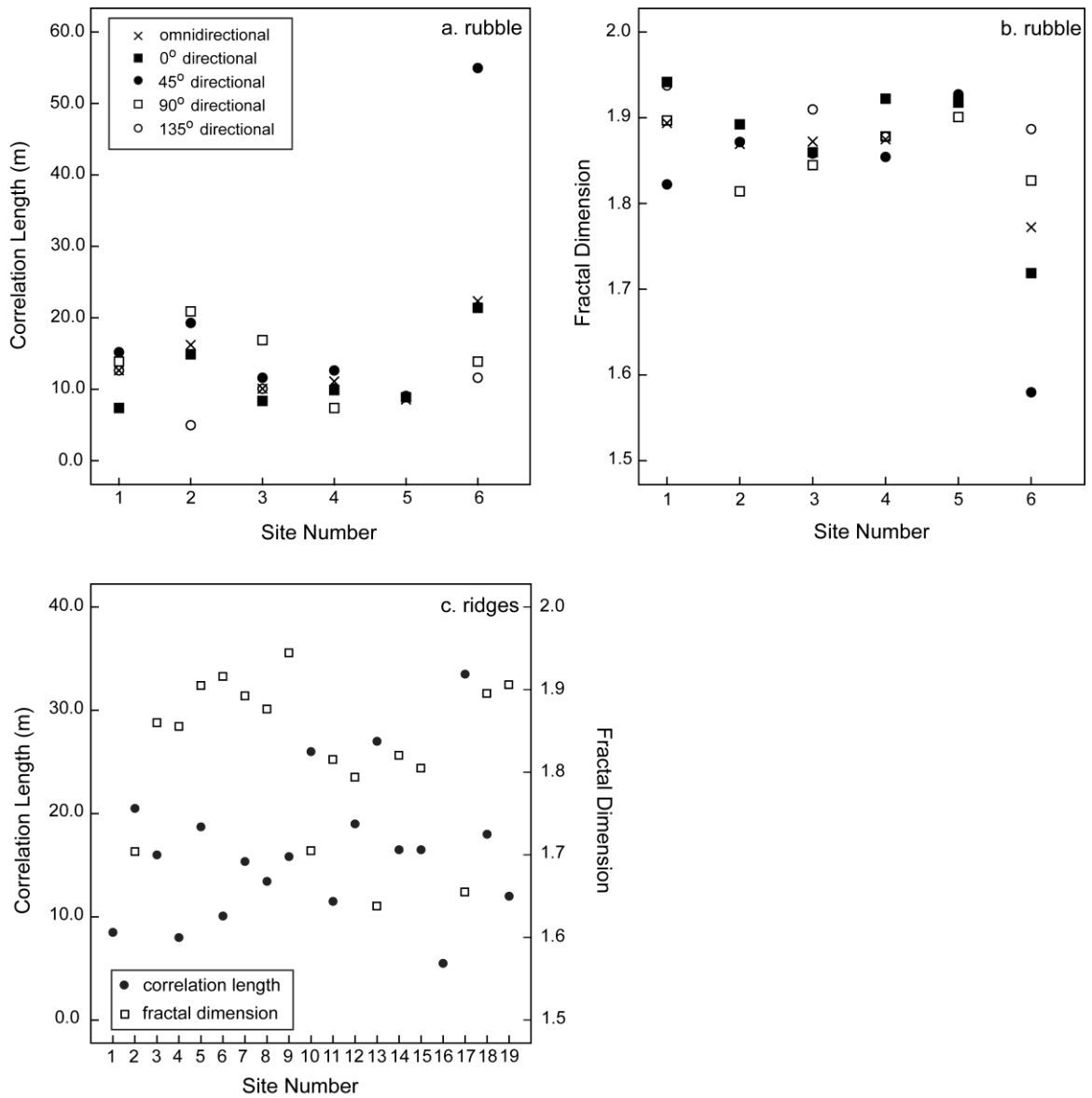


Figure 4.4: Correlation length and fractal dimension for rubble (a. and b. respectively) and ridge sites (c.). For rubble sites, correlation length and fractal dimensions are presented for the omnidirectional and directional data.

The fractal dimensions calculated from the omnidirectional variogram for the snow depth over rubble ice is consistent for the first five sites, with values between

1.85 and 1.9 (Figure 4.4b.). These large values suggest that the snow distribution over rubble ice sites exhibits great tortuosity over the sampling distances (instead of a consistent snow depth), and thus occupies a larger space in cross-section. Similar results were found for the directional analysis, with values ranging from 1.8 to 1.95 for all but one site (Figure 4.4b). The calculated fractal dimension for snow depth is similar to D for snow over forest and steppe (Kuchment and Gelfan, 2001), however slightly larger than that derived for snow depth in an alpine tundra environment (Litaor *et al.*, 2002). These similarities and differences may be related to the underlying surface topography that creates the snowdrifts. For instance, a tundra environment would have relatively low surface roughness, creating smaller snowdrifts and thus a lower fractal dimension. A forest and steppe environment, along with rubble ice, will create a more irregular pattern in snowdrifts and these drifts will contain greater amounts of snow, thus creating a larger fractal dimension. The fractal dimensions for site 6 (omnidirectional and directional) were generally lower than the other sites and exhibited greater directional variability, with values ranging from 1.58 to 1.89 (Figure 4.4b.).

Correlation lengths calculated for snow depth along ridges range from 8 m to 33.5 m (Figure 4.4c.). There is no temporal trend in the correlation lengths over the study period ($p > 0.05$), again suggesting that the ice surface roughness, as well as the orientation of the ridges, may influence the spatial pattern of the snow distribution over this ice type. The fractal dimensions for snow depth calculated for each ridge site were quite large (greater than 1.6; Figure 4.4c.), suggesting great tortuosity in the snowdrifts.

Results using correlation length and fractal dimension suggest that the spatial pattern of snow distribution may be linked to the spatial pattern of ice surface roughness. From the scatterplot of omnidirectional correlation lengths for the rubble sites, two clusters or groups are evident (Figure 4.5a.). One group corresponds to short correlation lengths in surface roughness (approximately 10 m), which produces short snowdrifts, with correlation lengths between 8 and 14 m (Figure 4.5a.). The second group corresponds to the larger class of correlation lengths in surface roughness (greater than 25 m), producing longer snow drifts with correlation lengths greater than 15 m. This result suggests the importance of the spatial pattern of ice surface roughness in creating the snow depth patterns over rubble ice. However, the results suggest that there is a directional component to this relationship. Significant positive associations ($p < 0.05$) between correlation length for snow depth and surface roughness are also evident when direction is considered as a separate variable (Figure 4.5b. to e.). The slope of the relationship is greatest for the northeast-southwest direction (Figure 4.5c.), while smallest for the east-west direction (Figure 4.5b.). This difference suggests a greater change in the correlation length of snow depth with a change in correlation length of surface roughness in the northeast-southwest direction.

The results comparing the fractal dimension of snow depth and surface roughness for rubble sea ice sites are similar to those for correlation length. Generally, as the tortuosity of the surface roughness increases, the fractal dimension of the snow depth also increases (Figure 4.6a.). This result is also true for the east-west direction (Figure 4.6b.), however is not evident for the other directions (Figure

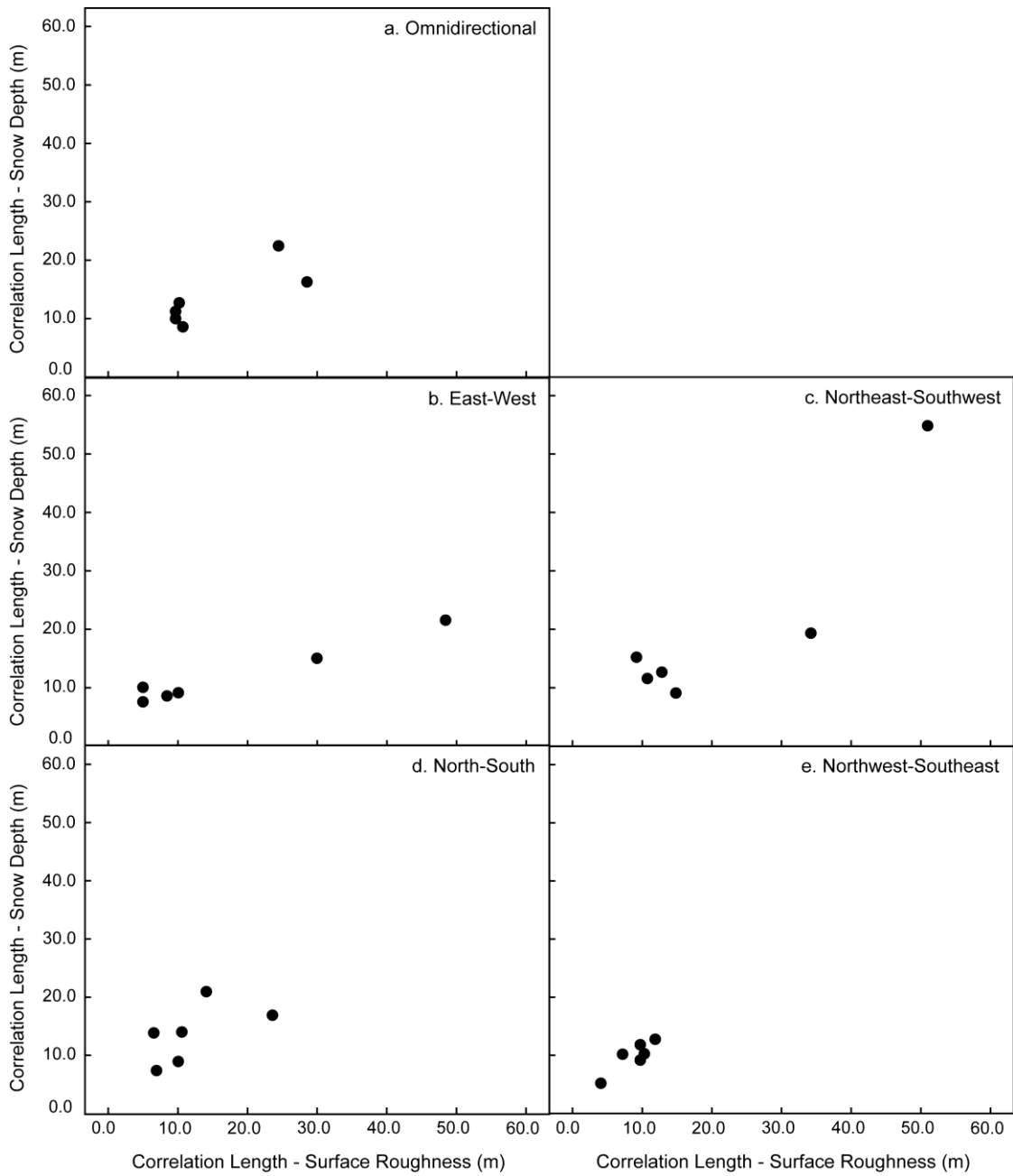


Figure 4.5: Scatterplots of the correlation length of snow depth versus correlation length of surface roughness for rubble sites.

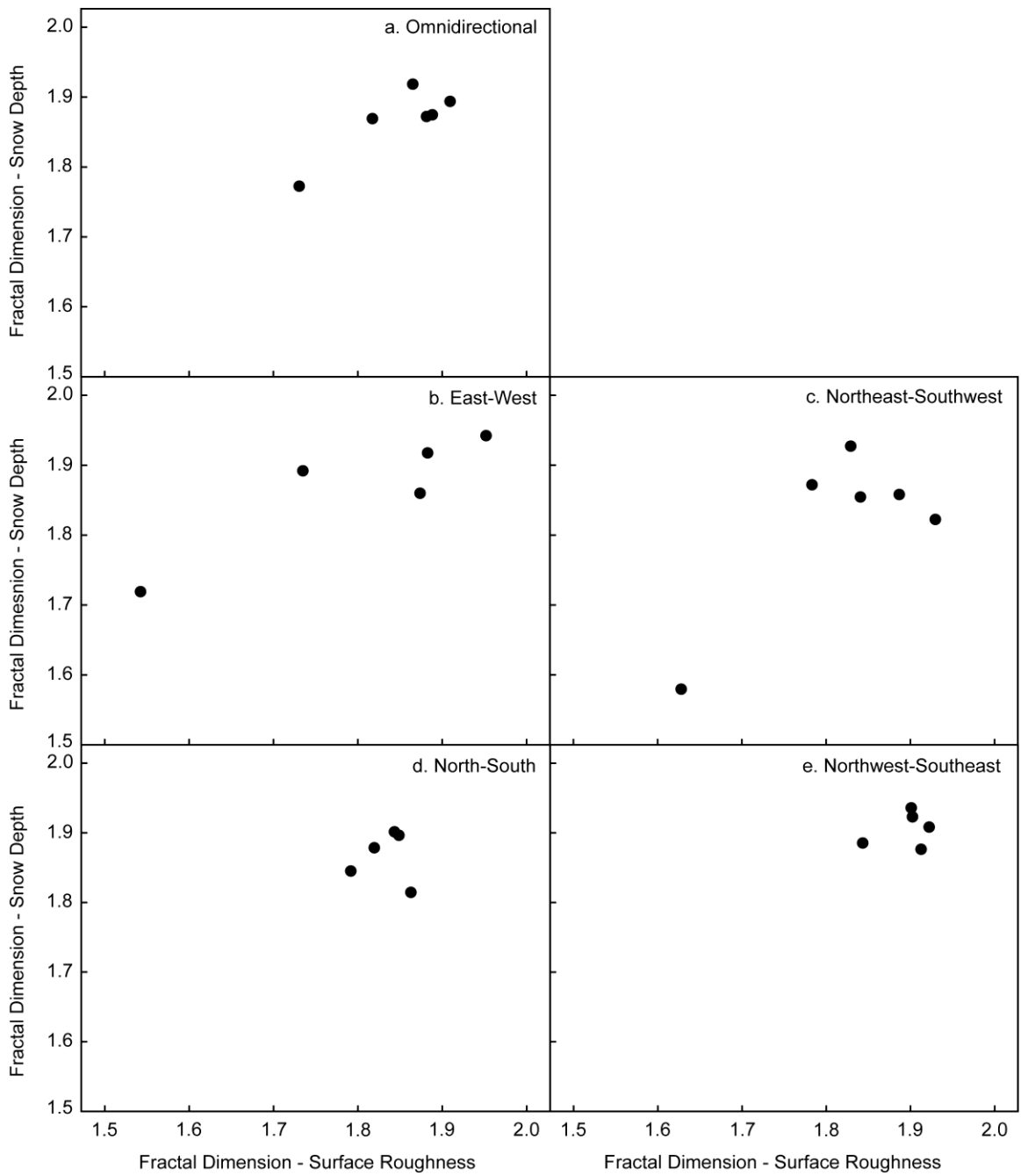


Figure 4.6: Scatterplots of the fractal dimension of snow depth versus fractal dimension of surface roughness for rubble sites.

4.6c. through e.). It is unclear why this relationship is not consistent for the other directions, however it may be due to the small sample size.

The estimated correlation length of snow depth measured over ridges is positively associated with the ice surface roughness correlation length for ridges (Figure 4.7a.). Further examination of the data suggests that the orientation of the ridges plays a role in the relationship between the surface roughness spatial pattern and that for snow depth. The slope of the relationship is greater for ridges aligned in the north-south direction, compared to ridges aligned in the east-west direction (Figure 4.7a.). This suggests that the orientation of the ridge, along with the spatial pattern of the ice surface roughness plays a role in the spatial pattern of the overlying snow depth distribution.

The results for the fractal dimension calculated for the ridge sites suggest a non-linear association (Figure 4.7b.). The association between snow depth fractal dimension and surface roughness fractal dimension is positive until D is approximately 1.76 ($r = 0.86$, $p < 0.05$). Beyond this fractal dimension in surface roughness, the association is level with no significant change in the fractal dimension of snow depth observed ($r = 0.22$, $p = 0.57$). This suggests that the tortuosity in the snow depth reaches a saturation point at approximately 1.86 for ridges. If the tortuosity or variability in the spatial pattern of surface roughness increases beyond 1.76, the spatial pattern of snow depth will not change significantly.

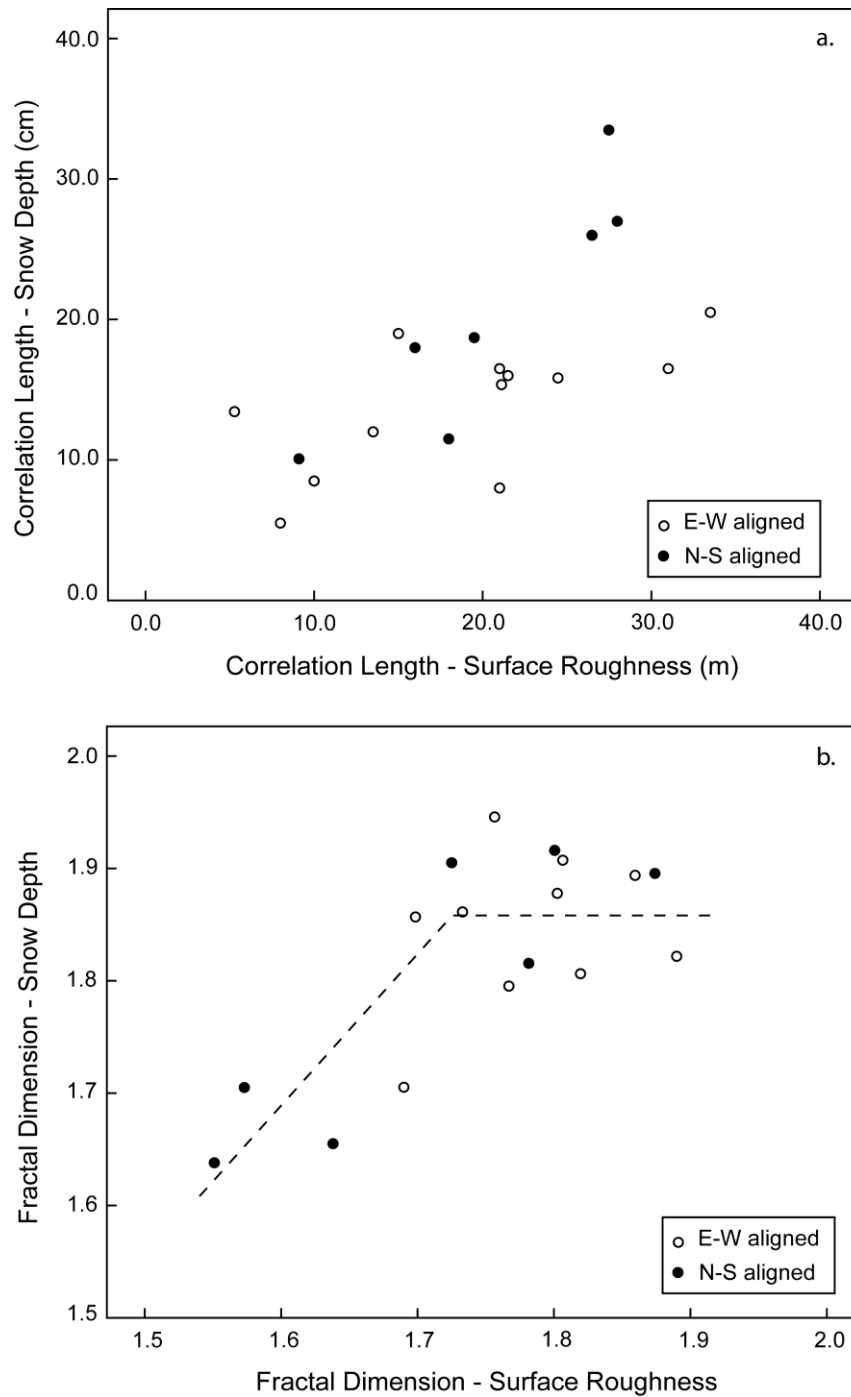


Figure 4.7: Scatterplots of a. correlation length for snow depth versus correlation length of surface roughness and b. fractal dimension of snow depth versus fractal dimension of surface roughness for ridge sites. Open circles represent the values for ridges aligned in the east-west direction and closed circles represent the values for ridges aligned in the north-south direction.

4.4 EVOLUTION OF SPATIAL PATTERN

The evolution of the spatial pattern of snow depth over sea ice is due to the meteorological conditions depositing and drifting snow, as well as the surface roughness features on the sea ice. As indicated previously, the correlation lengths of snow depth were greater in particular directions for the first three sites sampled between February 5 and March 7, 2004 (Figure 4.4a.). Meteorological measurements suggest that during a major snow deposition and blowing snow event that occurred between 5 and 12 February (Figure 3.3a. and b.), the winds shifted from the west to the south and finally to the southwest directions (closed circles; Figure 3.3c.). This would have caused the movement and deposition of snow in that direction, resulting in greater snowdrifts oriented in the northeast-southwest and north-south directions, as observed in the correlation lengths (Figure 4.4a.).

Anisotropy, or the degree of directionality in the correlation length, can also be used to examine the evolution of the spatial pattern in snow depth. The anisotropy for the six sites sampled in 2004 ranged from 1.3 to 5.0 (Table 4.3) suggesting that the maximum range in snow depth was less than or equal to 5 times larger than the minimum range. The degree of anisotropy is primarily associated with the ice surface roughness and increases as the anisotropy in the ice surface roughness increases (Table 4.3).

Table 4.3: Magnitude and direction of anisotropy for snow depth and sea ice surface roughness derived for the 6 sites sampled on rubble sea ice.

Site #	Magnitude		Direction	
	Snow Depth	Roughness	Snow Depth	Roughness
RB-1	3.0	2.5	111	72
RB-2	3.9	7.1	113	154
RB-3	2.4	3.3	95	94
RB-4	5.0	12.0	78	103
RB-5	1.3	1.1	58	132
RB-6	2.2	3.45	120	155

An additional parameter that defines the changes in the spatial pattern is the direction of anisotropy. The direction of anisotropy provides an indication of the predominant orientation of the snowdrifts at each site and is related to the meteorological conditions. For instance, sites 3 and 4 have similar direction of anisotropy for snow depth, as well as similar directions for ice surface roughness (Table 4.3). These sites were sampled during a period with little or no snowfall and light winds (less than the threshold to initiate snow drifting) (Figure 3.3a. and b.), suggesting very little change in the spatial pattern of the snowdrifts. This result is further supported by the similar correlation lengths (omnidirectional; Figure 4.4a.) and fractal dimensions (Figure 4.4b.) for these two sites. Sites RB-5 and RB-6 had similar direction of anisotropy for ice surface roughness (both oriented northwest-southeast), yet dissimilar directions for snow depth (site RB-5 oriented in the north-east direction, while site RB-6 oriented in the northwest-southeast direction; Table 4.3). Between the sampling dates, a snow depositional/blowing snow event occurred (Figure 3.3a. and b.) and the wind direction associated with this event

(Figure 3.3c.) would have caused a re-orientation of the snowdrifts and thus causing the change in the anisotropy direction. These results suggest that the temporal evolution of the spatial pattern of snow over rubble sea ice is dependent on the meteorological conditions, primarily wind direction during snow depositional and blowing snow events.

The evolution of the spatial patterns of snow depth over ridges is also related to the meteorological conditions. The variability in correlation length measured during the first part of the sampling period is lower than the variability for the remaining sites, while large values in the fractal dimension and less variability were observed for the same period (Figure 4.4c.). The lower variability suggests a more consistent spatial pattern from January 19 to February 10. This may be due to the fact that during the period from January 23 to February 4, 2004, there were no major snow depositional and blowing snow events (one small event occurred during the late part of January; however it deposited less than 1 cm of snow; Figure 3.3a. and b.). This lack of any meteorological event would have resulted in no significant changes in the spatial pattern of snow depth (with the variability in spatial pattern determined by the ice surface roughness). After this period, a major depositional/blowing snow event occurred (Figure 3.3a. and b.), resulting in a re-organization of the snow drifts over the ridges and thus changes in the both the variability in correlation length and magnitude of fractal dimension (Figure 4.4c.).

The impact of meteorological events on the spatial pattern of snow over ridges can also be examined when comparing ridges with similar spatial pattern in ice

surface roughness. A major precipitation event occurred late in February, with a snowfall event occurring around February 24 (2.0 cm of snowfall; Figure 3.3a.) and a blowing snow event occurring a few days later (Figure 3.3b.). During this blowing snow event, the average daily wind blew from the east (Figure 3.3c.). Site RD-10 was sampled on February 17, prior to the precipitation event. The surface roughness of this ridge is similar to that sampled on March 9 (site RD-13). The spatial pattern of the ice surface roughness measured at this site was similar to that measured at site RD-13. The correlation length was 26.5 m and 28 m for site RD-10 and RD-13, respectively, with a fractal dimension associated with the surface roughness of 1.57 and 1.55 respectively. In addition, both ridges were oriented in the north-south direction. The spatial pattern of the snow depth between these two sites was only slightly different, with a correlation length of 26 m and 27 m and a fractal dimension of 1.70 and 1.64 (site RD-10 and RD-14, respectively). Due to the close proximity of sites, this result suggests that surface roughness may play a more important role than the meteorological conditions in the evolution of the spatial pattern of snow depth over ridges when wind direction is orthogonal to the orientation of the ridge. The spatial pattern remains constant when the wind is blowing snow perpendicular to the ridge.

The implication of changes in orientation and ice surface roughness were also examined with respect to the evolution of the spatial pattern of snow depth. Site RD-7 (sampled on February 4) and site RD-13 (sampled on March 9) are oriented in the east-west direction. However, these two sites have different configurations of sea ice roughness. Site RD-7 was composed of smaller and more frequent ridge pieces

compared to site RD-13 which was composed of one large ridge. In addition, the spatial pattern of surface roughness is different between sites, with correlation length and fractal dimension of 21.1 m and 1.86 respectively for site RD-7 and 28.0 m and 1.55 for site RD-13. The spatial pattern of snow distribution at the ridge on the later sampling data suggested a more uniform distribution of snow depth (larger correlation length – 28.0 m compared to 21.1 m) and lower tortuosity (1.55 compared to 1.86). The snow redistribution that occurred as a consequence of the snow drifting events that occurred between February 9 and 26 (Figure 3.3) resulted in much larger drifts, both vertically and horizontally as reflected in the differences in correlation length and fractal dimension. The low areas of the drifts would infill with saltating snow, similar to the evolution observed over smooth first-year sea ice (Chapter 3; Iacozza and Barber, 2010). Because the ridge sampled on March 9 was oriented perpendicular to the wind direction during the drifting event, a greater amount of saltating snow would have been deposited along the ridge, causing a greater change in the observed snow distribution.

4.5 CONCLUSION

In terms of snow over sea ice, both the mean and spatial variability have significant implications for the ecology of the Arctic system. Current modeling/remote sensing techniques are able to quantify the mean snow depth over a spatial scale, however the spatial pattern is lacking. It is expected that the spatial pattern of snow, more than the mean snow depth, would be related to the sea ice surface roughness. The objectives of this research were to examine the

spatial pattern of snow distribution over rough sea ice and the relationship between this spatial pattern and ice surface roughness and meteorological conditions. This work is a preliminary step in understanding not only the spatial pattern, but also the dynamic processes responsible for the creation of the snow characteristics over rubble ice and ridges. This examination would improve our understanding of the ecological, oceanographic and climatological aspects of the Arctic marine system and allow for the improvement of snow depth distribution parameterization in sea ice models.

Results from this study suggest that for both rubble ice and ridges, the magnitude in the roughness of the ice surface does not adequately account for the variability in snow depth. Less than 54% of the variability in snow depth can be accounted for by the variability in ice surface roughness. The models are similar for both rubble ice and ridges. This result suggests that the spatial pattern and not the magnitude of ice surface roughness may be more important in creating the snow distribution over rough sea ice.

Correlation length and fractal dimensions were used to quantify the spatial pattern for both snow and ice surface roughness. The correlation lengths suggest that the average snowdrifts over the rubble ice sites sampled in 2004 varied between 8.7 m to 22.4 m (irrespective of direction). Examining correlation lengths based on direction produced similar results for the majority of sites. This difference may be related to differences in the ice surface roughness and/or meteorological conditions. The fractal dimensions estimated for these sites were consistent with

values between 1.85 and 1.9. These large fractal dimensions suggest great tortuosity in the snowdrifts. The fractal dimension for site RD-6 was generally lower than other sites, indicating a more uniform pattern in snowdrifts. For the ridge sites the correlation lengths were estimated to be between 8.0 m and 33.5 m and fractal dimensions between 1.55 and 1.96.

The spatial pattern of snow over both ridges and rubble ice were compared to the spatial pattern of the ice surface topography. For rubble ice, a statistically significant positive association exists between the correlation lengths for ice roughness and snow. There is however evidence that this relationship is directionally dependent, with a greater slope for snowdrifts oriented in the northeast-southwest direction, compared to the other directions. Regression analysis for ridges indicates that a greater slope was observed for ridges oriented in the north-south direction, compared to the east-west direction. This finding suggests that the direction of the correlation length in surface roughness also influences the spatial pattern of the overlying snow for rough ice. For fractal dimension, the relationship between ice roughness and snowdrift is not as clear. Irrespective of direction, there seems to be a positive relationship between the fractal dimension of ice surface roughness and snow over rubble ice, however this association is not true when direction is included. Over ridges, the relationship appears to be non-linear. After a maximum fractal dimension in ice surface roughness is obtained (1.76 for this study), the fractal dimension of snow remains statistically unchanged.

The evolution of the spatial pattern of snow depth was also examined by comparing the patterns in both correlation length and fractal dimension to meteorological conditions that occurred throughout the study period. Results suggest that wind direction during periods of snow deposition and/or blowing snow will impact the pattern in the spatial pattern of snow. However this is also controlled by the spatial pattern of the ice surface roughness. This is a first attempt at examining the evolution of snow depth over rough sea ice. Previous study has shown that the meteorological conditions do play a role in snow evolution over smooth ice (Chapter 3; Iacozza and Barber, 2010), however it remains unclear as to the magnitude wind direction impacts the evolution, in relation to the surface roughness. Further investigation will be conducted that primarily focuses on the evolution of snow over similar ice roughness conditions.

A limitation of this study is the scale at which the measurements were conducted. Due to the fine resolution of the instrumentation, as well as the logistical costs involved in the sampling techniques, it is not practical to sample surface roughness over large areas of the Arctic using the methodology in this research. A more practical technique would be to use satellite based data to estimate the ice surface roughness. Current research is attempting to link helicopter-based surface roughness to satellite based measurements (either synthetic aperture radar (SAR) or spaceborne scatterometry). The associations for the spatial pattern of snow using fractals and/or variography developed in this paper can then be applied to the derived surface roughness to estimate snow distribution over larger spatial scales.

This can then be used to further understand the habitat relationships of polar bears and ringed seals in the Arctic.

CHAPTER 5: DERIVING LAND-FAST SURFACE ROUGHNESS FROM ASAR IMAGES USING SECOND-ORDER TEXTURE MEASURES

This chapter describes the method to determine the estimation of the surface roughness of snow covered sea ice using second-order texture analysis of Advanced Synthetic Aperture Radar (ASAR) images. First it will be determined if the texture technique GLCM can be used to estimate surface roughness and what are the optimal texture statistics(s) and window size. Then the effect of various satellite processing techniques (i.e. speckle reduction) and imagery characteristics (i.e. polarization, incidence angle and path) on the estimation of surface roughness using this texture technique will be presented. The results indicate that second-order texture measures of a speckle-reduced cross-polarized image can estimate the surface roughness.

5.1 Methods

5.1.1 Helicopter-borne surface roughness

Snow-plus-sea ice roughness (referred to as surface roughness) was measured remotely with a fixed-mounted laser within the helicopter-borne electromagnetic induction (EMI) system, called the 'IcePic'. This instrument was mounted directly onto the nose of a BO-105 Canadian Coast Guard helicopter. The EM sensor emits a primary electromagnetic field, which interacts with the seawater producing a secondary field. The amplitude and phase of this secondary field is used in the estimation the distance from the sensor to the ice-water interface and the laser is used to determine the distance to the surface of the ice, together they provided the

snow-plus-sea ice thickness (referred to as ice thickness; Haas *et al.*, 2010). A laser altimeter included in the instrument package of the IcePic is used to estimate the surface roughness at each sampling location. Surface roughness is defined as the difference between the snow-plus-ice surface measured at a point and the surrounding minimum level snow-plus-ice surface surrounding (Peterson *et al.*, 2008). Surface roughness measurements were obtained by subtracting the helicopter altitude variations from the laser altimeter measurements through a three-step high-pass filtering procedure (Hibler, 1972; Holladay and Moucha, 1998). The IcePic is typically flown at low altitudes, between 4 m and 6 m over the ice surface.

Between April 20 and 23, 2004, seven (7) separate transects were sampled using the IcePic (Figure 5.1). Each transect was composed of a number of surface roughness classes and primarily located over land-fast sea ice. The length of each transect ranged from 15.1 km (transect FEM04062) to 109.8 (transect FEM04057; Table 5.1). GPS coordinates were recorded along the length of each transect. Transects FEM04047 and FEM04058 sampled approximately the same sea ice on two separate dates (Figure 5.1). The average spatial resolution of measurements was approximately 4.3 m. During the sampling period, daily air temperatures were consistently below -15C (see Iacozza and Barber, 2010) and thus the snow was considered dry.

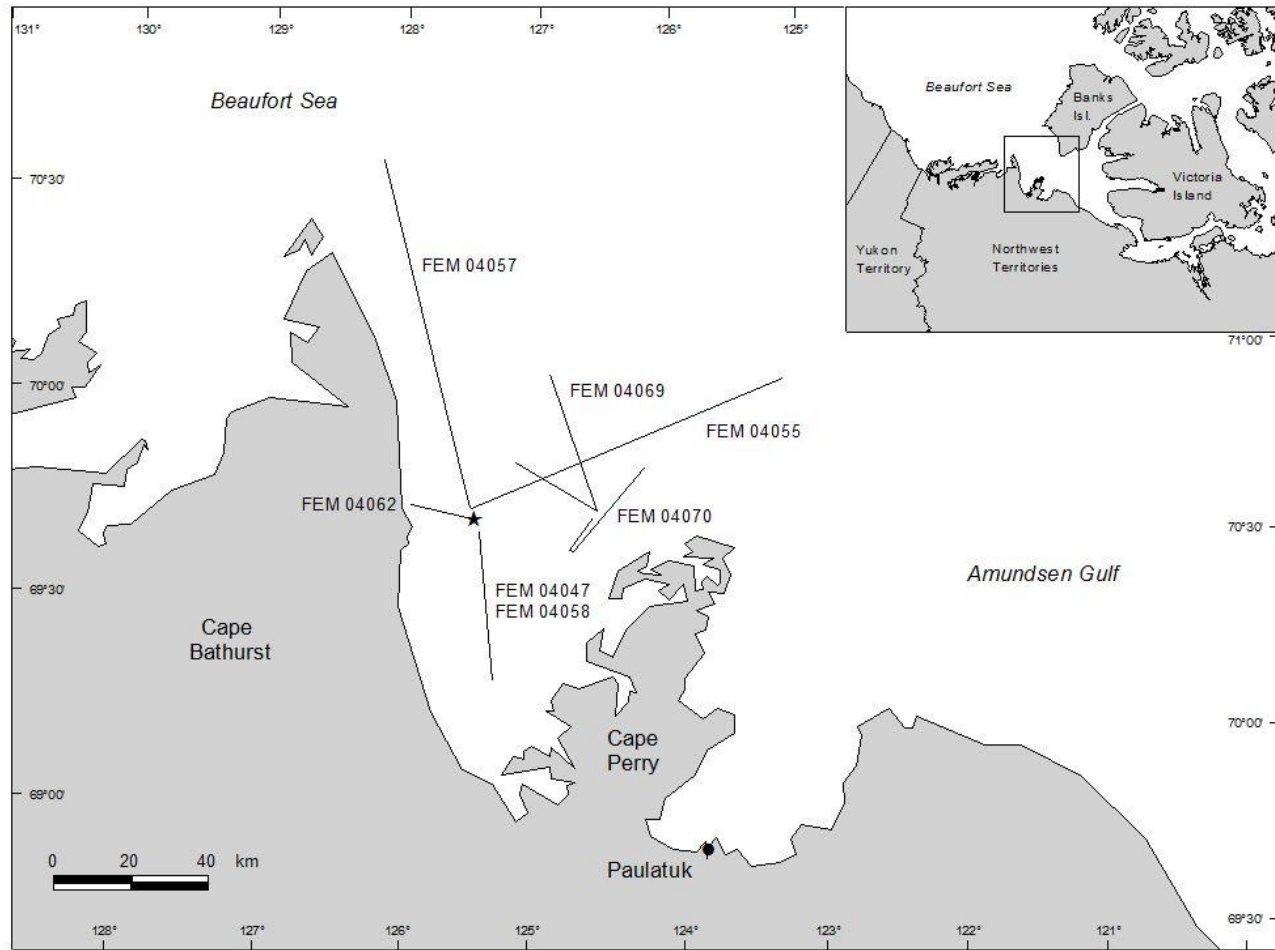


Figure 5.1: Map of the IcePic transects sampled between 20 and 23 April. The star denotes the overwintering location of the icebreaker *CCGS Amundsen*.

Table 5.1: Names, collection date and time, and length (km) of IcePic transects collected during 2004.

Name	Date of Collection	Start Time (UTC)	Length of Transect (km)
FEM04047	20 April	16:19	38.5
FEM04055	21 April	19:37	93.5
FEM04057	21 April	21:20	109.8
FEM04058	22 April	15:29	41.5
FEM04062	22 April	16:31	15.1
FEM04069	23 April	20:02	70.5
FEM04070	23 April	20:53	75.3

5.1.2 Satellite-based remote sensing of sea ice

Three pairs of Advanced Synthetic Aperture Radar (ASAR) imagery were available for the study area between 20 and 22 April 2004. The ASAR sensor is located on the ENVISAT satellite and is an imaging microwave radar, operating at C-band (5.3 GHz). ASAR imagery was provided in Alternating Polarization (AP) mode with a spatial resolution of 30 m and scans between two polarizations, either co-polarization (i.e. VV or HH) or cross-polarization (VH or HV). The first term signifies the transmitted polarization and the second signifies the received polarization. The AP mode gives two co-registered images per acquisition, resulting in five (5) polarization modes (VV, HH, VV/HH, HV/HH, or VH/VV). Table 5.2 lists the image dates and polarizations for the ASAR imagery used in this research. The April 19 image was acquired using different polarizations and incidence angles, compared to the other two images and allows for the comparison between images characteristics. The images acquired on 21 April and 22 April were similar except for the time of

acquisition, with 21 April acquired on the ascending pass, while the 22 April image was acquired on the descending pass (similar to 19 April image). IcePic transects were linked to the satellite imagery that were acquired at the closest date and time. To reduce errors associated with any temporal difference between IcePic sampling and acquisition of satellite imagery, only those locations over landfast sea ice were used in this analysis. No major snow depositional or wind event occurred between the sampling and acquisition dates, thus it can be assumed that surface roughness did not change between the two times.

Table 5.2: Characteristics of the ASAR imagery used in this study. In addition, the IcePic sampling transect(s) corresponding to each image is also listed.

Acquisition Date	Time (UTC)	Polarization Mode	Swath (incidence angle range)	EMI Transect
19 April	18:48:59 (descending)	VV/VH	IS7 (42.5 – 45.2)	FEM04047
21 April	05:50:15 (ascending)	VV/HH	IS6 (39.1 – 42.8)	FEM04055 FEM04057
22 April	18:54:58 (descending)	VV/HH	IS6 (39.1 – 42.8)	FEM04058 FEM04062 FEM04069 FEM04070

5.1.3 Image processing and texture analysis

A common radiometric inaccuracy within radar images is speckle or noise. Speckle is a random pattern of brighter and darker pixels, resulting in a grainy appearance to the image (Lillesand *et al.*, 2008). This appearance is due to constructive and deconstructive interference within the image. Speckle has a negative impact on the contrast within the image and thus can hamper the accuracy

of the texture measures in the analysis of satellite imagery. Therefore prior to the calculation of texture measures, a speckle reduction should be first performed on the image. Three common speckle reduction techniques include Frost, Gamma and Lee adaptive filters. All three filters apply a mathematical calculation within a moving kernel over the image, replacing the central pixel with the new calculated value. For this study, a 3x3 pixels window was utilized for each adaptive filter To minimize the 'smoothing' effect of the technique and thus the reduction in resolution. The main difference between these three filters is the way the new value within the central pixel is calculated. For a Frost filter, the new value for the central pixel is calculated using a weighted sum within the moving kernel (Frost *et al.*, 1982). The weighting factors decrease with increasing distance from the central pixel, while increase as the variance with the kernel increases. The Gamma filter assumes that the original pixel value lies between the digital number of the pixel of interest and the average digital number of the moving kernel (Lopes *et al.*, 1993). Unlike the Gamma filter, the Lee filter assumes that the new value for the central pixel is equal to the mean and variance of all pixels with the moving kernel (Lee, 1981). This filter eliminates the speckle noise and preserves the edges and point features in the imagery. The Frost and Lee filters assume a Gaussian distribution of the speckle noise, while a Gamma filter assumes a Gamma distribution (Lopes *et al.* 1990). While other filtering techniques may be more robust at reducing the speckle within polarimetric SAR images (i.e. Novak and Burl, 1990; Xie *et al.*, 2002), these three filters are the most readily available for radiometric processing of ASAR images in most remote sensing software. No agreement as to the filter that best

eliminates the speckle within a SAR image exists in the literature (i.e. Shi and Fung, 1994; Kushwaha *et al.*, 2000).

After speckle reduction, a second-order texture technique known as a grey-level co-occurrence matrix (GLCM) was applied to the images (i.e. original image, as well as the speckle reduced images referred to as Frost image, Gamma image and Lee image). GLCM measures the texture of the image based on the spatial distribution of the grey-levels for pixels within the image (Haralick *et al.*, 1973). This is accomplished by examining the relation between two pixels at a time, which are offset from one another by both orientation (α) and sampling distance (δ). Based on this, a conditional joint probability (C_{ij}) of all pairwise combinations of pixels within a computational window is calculated based on equation [5.1]:

$$C_{ij} = \frac{P_{ij}}{\sum_{i,j=1}^N P_{ij}} \quad [5.1]$$

where P is the frequency of occurrence of grey levels of pixel i (reference pixel) and pixel j (neighbor pixel) and N refers to the total number of pixel pairs. The conditional probability is used to calculate a number of metrics that describe different aspects of texture of the image. Mean (MEAN) and Variance (VAR) quantify the average and variance in grey level within the local window. These statistics are similar to the descriptive statistical parameters, however are calculated for a smaller set and in combination with a certain neighbor pixel value. Within MEAN, the pixel value is weighted by its frequency of occurrence in

combination with a particular neighbor pixel value and is calculated using [5.2]:

$$\mu_i = \sum_{i,j=0}^{N-1} i(P_{i,j}) \quad \mu_j = \sum_{i,j=0}^{N-1} j(P_{i,j}) \quad [5.2]$$

where μ_i is the mean for the reference pixel (pixel i) and μ_j is the mean for the neighbor pixel (pixel j). VAR uses the GLCM and deals with the combinations of reference and neighbor pixels and is calculated using [5.3]:

$$\sigma_i^2 = \sum_{i,j=0}^{N-1} P_{i,j} (i - \mu_i)^2 \quad \sigma_j^2 = \sum_{i,j=0}^{N-1} P_{i,j} (j - \mu_j)^2 \quad [5.3]$$

where σ_i^2 is the variance for the reference pixel (pixel i) and σ_j^2 is the mean for the neighbor pixel (pixel j). Contrast (CON) and Homogeneity (HOMO) measure the amount of local variation within the image calculated using [5.4] and [5.5] respectively:

$$\sum_{i,j=0}^{N-1} P_{i,j} (i - j)^2 \quad [5.4]$$

and

$$\sum_{i,j=0}^{N-1} \frac{P_{i,j}}{1 + (i - j)^2} \quad [5.5]$$

CON is high when the difference between pixels within the local window is high. The weights used in the calculation increase exponentially as the difference between the reference pixel and neighbor pixel increases. HOMO measures the overall smoothness of the image. It is high when the image within the local window is

relatively smooth, resulting in a concentration of the GLCM along the diagonal. It examines the relationship between spacing of pixels and their relative values (Honeycutt and Plotnick, 2008). The weight values used in this calculation are inverse to those used in the Contrast calculation. Entropy (ENT) and Angular Second Moment (ASM) are metrics focusing on the disorder or complexity of textural homogeneity within the local window calculated using [5.6] and [5.7] respectively:

$$\sum_{i,j=0}^{N-1} P_{i,j} (-\ln P_{i,j}) \quad [5.6]$$

and

$$\sum_{i,j=0}^{N-1} P_{i,j}^2 \quad [5.7]$$

ENT is high when the image is texturally not uniform and thus the GLCM elements have relatively low values. ASM is opposite to ENT and is high when the GLCM has entries of large magnitude. This statistic or metric measures the textural uniformity and highlights geometry and continuity within the image. All six measures were used in this study. Further information on these statistics can be found at Haralick *et al.* (1973) and Barber and LeDrew *et al.* (1991).

For this study, GLCM images were computed in ENVI® for each ASAR image (original, Frost, Gamma and Lee image). The GLCM images were constructed using local windows of 3x3, 5x5, 9x9 and 15x15 pixels. This was done to examine the effect of increasing window size of the ability to estimate surface roughness based

on texture measures. A sampling distance of 1 pixel and orientation of 0° was used in this study. These parameters were selected due to the nature of the roughness elements (i.e. no particular orientation of the roughness features) and relatively small window size (i.e. 3x3 pixels). Once the image was derived, the surface roughness data from the IcePic was overlaid and the GLCM statistics that correspond to each sampling point was extracted. Due to differences in spatial resolution, the EMI sampling points within an ASAR pixel were averaged. This averaged value of surface roughness was then statistically compared to the satellite imagery. The surface roughness values were then binned into 0.05 m bins, and averages for each GLCM statistic were calculated for each bin.

5.2 Individual pixel comparison

Regression analysis was completed comparing the surface roughness for each pixel to each GLCM statistic and parameters for the original image, as well as the other speckle reduction methods (i.e. Frost, Gamma and Lee). Results suggest that overall the Gamma reduction method produced the greatest coefficients of determination (R^2). In addition, results also suggest that HOMO using a window size of 15x15 pixels and a cross- polarized image (VH) was able to account for the greatest amount of variability in the surface roughness ($R^2 = 0.07$, $p < 0.05$). HOMO quantifies the smoothness of the image and the conditional joint probabilities will be centered on the diagonal indicating similar texture within the processing window. As the surface texture increases within the window, the probabilities will be more varied within the matrix, decreasing the HOMO measure. Correlation

analysis ($r = 0.27$, $p < 0.05$) suggests this positive association between the texture measure and surface roughness (Figure 5.2). The relatively large window in which the GLCM measure is calculated suggests the improvement of the relationship between the variables with increased spatial averaging used in computing the texture measure. This is consistent with results from Peterson et al. (2006). Unfortunately the result suggests that only a small fraction of the variability in smoothness can be accounted for by the variability in the texture measures using individual pixels. Changing the window size used in the calculation of the texture measure or the speckle reduction technique does not improve the result.

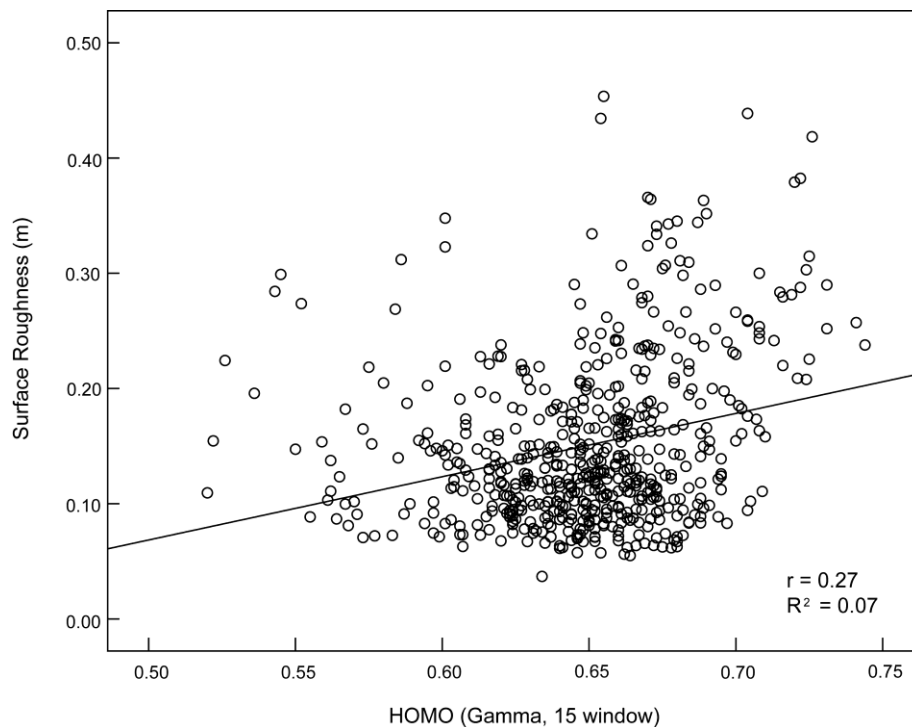


Figure 5.2: Scatterplot of surface roughness (m) versus HOMO texture statistic based on a window size of 15x15 pixels. The texture measure was calculated for the April 19 VH ASAR image. The correlation coefficient (r) and the coefficient of determination (R^2) are provided.

5.3 Binned surface roughness comparison

5.3.1 Effect of ASAR characteristics

In an attempt to improve the relationship between surface roughness and texture measures, the surface roughness measurements were binned into 0.05 m groups and the texture measures were averaged for each bin. Regression analysis using texture measures based on the original grey-level pixel values (i.e. without any speckle reduction) would account for a maximum of 74.7% of the variability in the surface roughness (Figure 5.3). Using a speckle reduction technique on the image prior to the calculation of the texture measures, improved the linear relationship between surface roughness and GLCM measure. As with the non-binned results, the Gamma speckle reduction technique produced the greatest R^2 values, accounting for up to 90% of the variability in surface roughness (Figures 5.4 through 5.6). This result agrees with previous research (i.e. Xiao et al., 2003), which found that the Gamma filter has higher speckle-smoothing capabilities, as well as texture preservation, when applied to C-band synthetic aperture imagery (SAR).

The maximum R^2 was achieved for the VH image (April 19), consistent with the results using un-binned surface roughness. The other polarizations were able to account for a maximum of 68.4% (VV) and 48.0% (HH) for the original image and 81.9% (VV) and 75.0% (HH) for the speckle reduced images (Figures 5.4 through 5.6). This result suggests that the cross-polarized image, combined with the Gamma filter, was better at preserving the textural information in the image that can be used to estimate surface roughness. Previous research has shown that cross-polarized images generally produce a greater difference in backscattering when

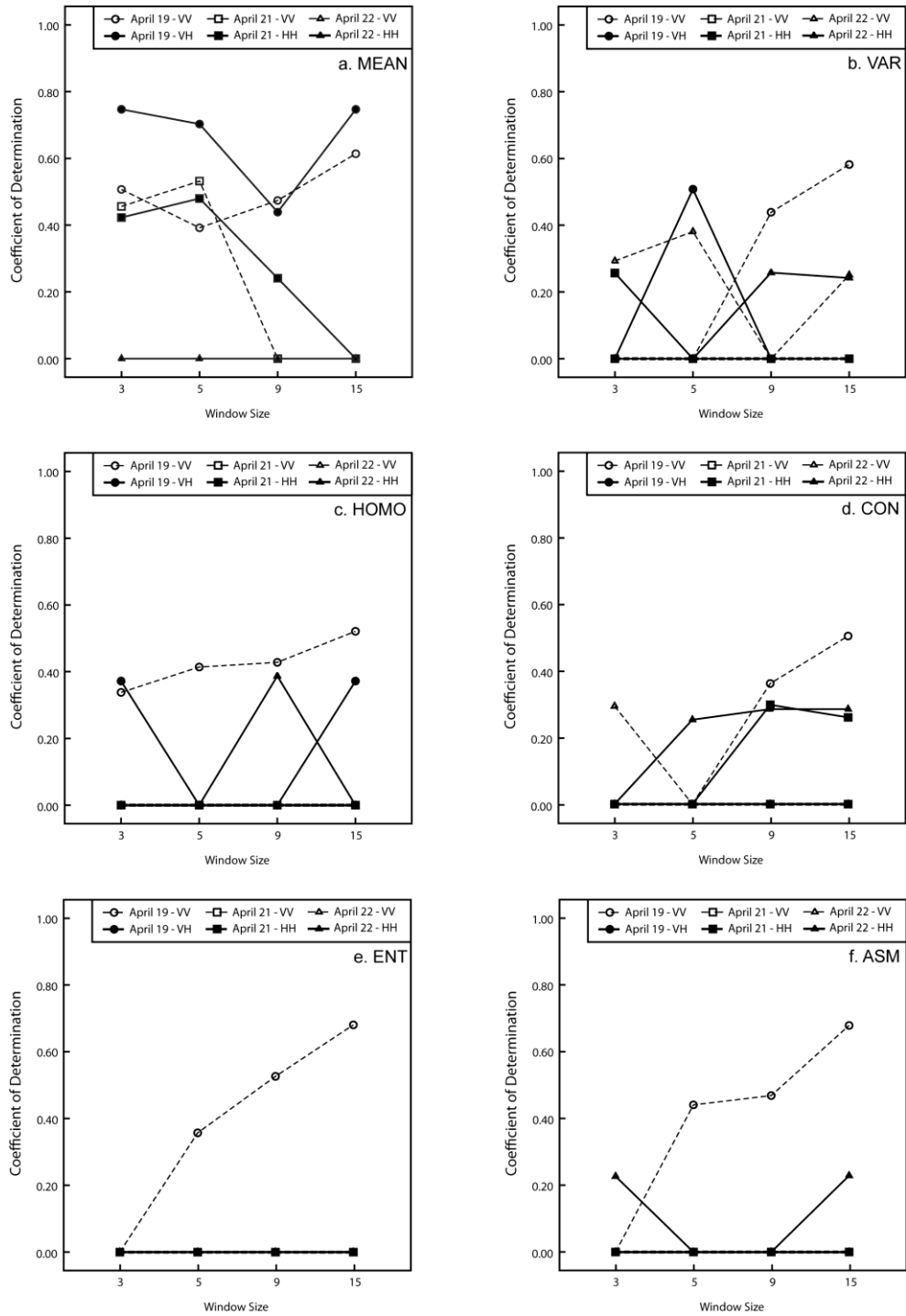


Figure 5.3: Plots of the coefficient of determination (R^2) for the texture measures computed from the original images using four different window sizes. Each line represents the estimated R^2 for each image (different date of acquisition and/or polarization).

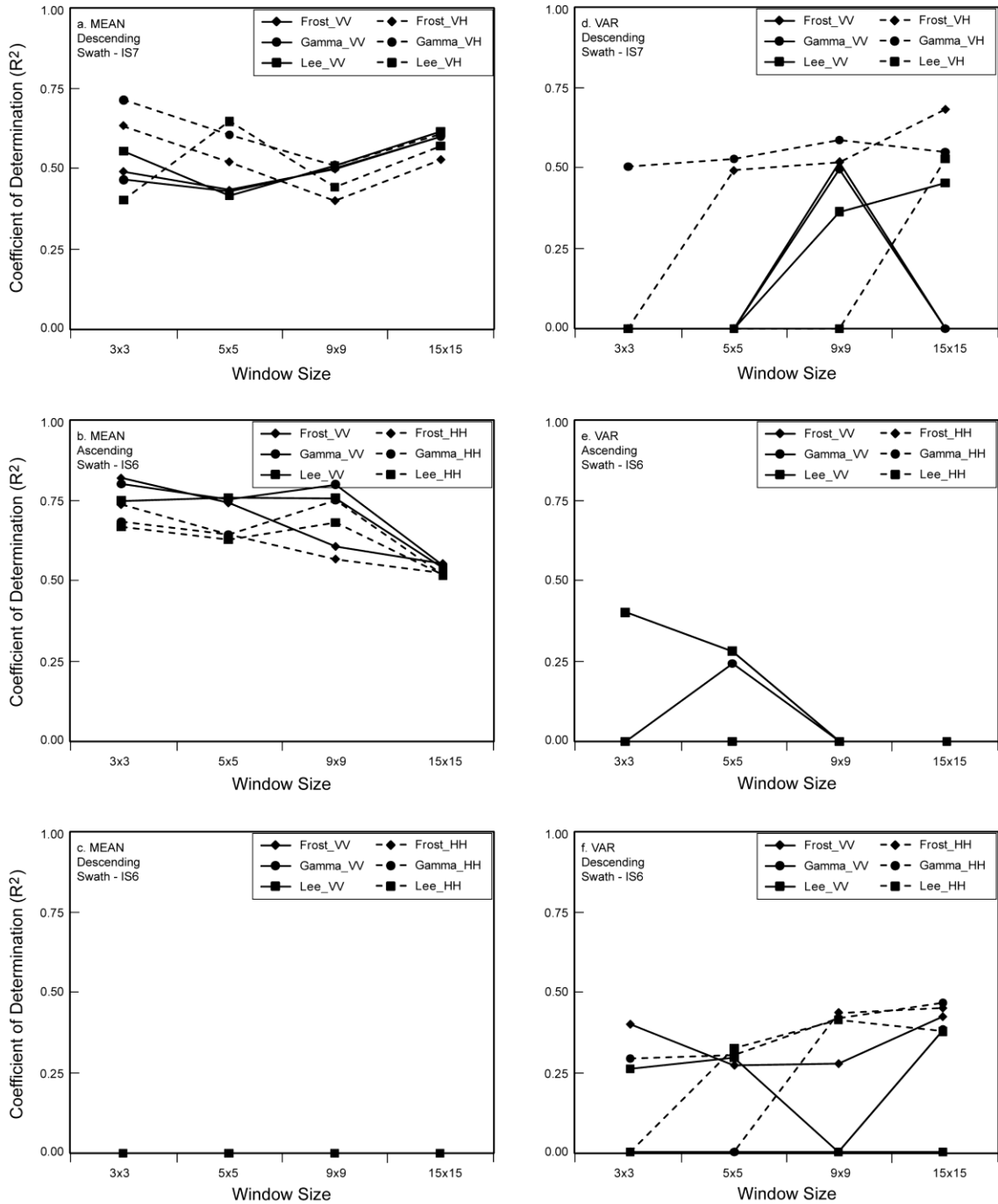


Figure 5.4: Plots of the coefficients of determination (R^2) for the MEAN (a. through c.) and VAR (d. through f.) texture measures computed from the speckle reduced images (frost - diamond, gamma - circle and lee - square) using four different window sizes. Each plot represents an individual image and texture measure. The lines represent the R^2 calculated for the different speckle reduction technique and/or polarization.

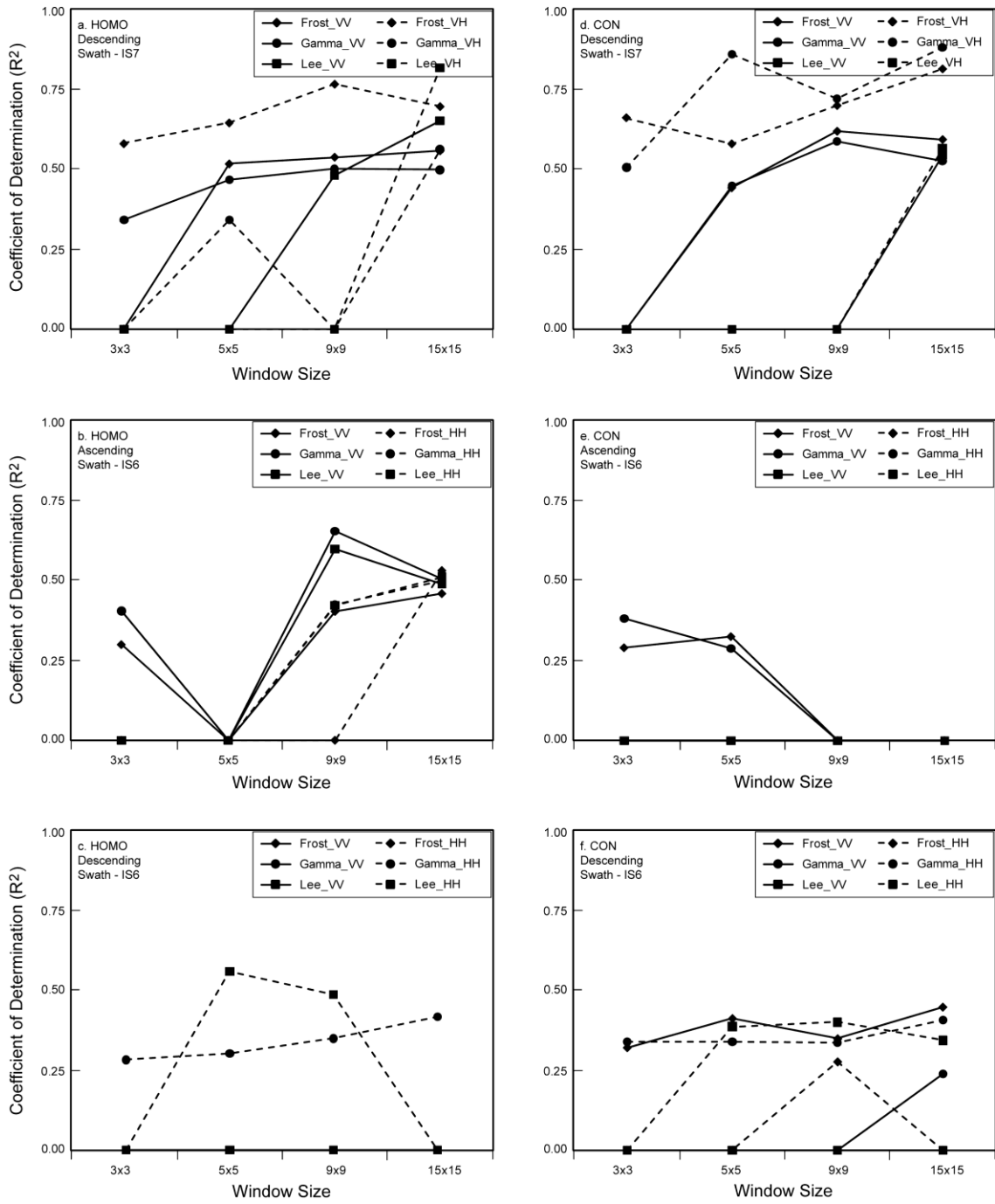


Figure 5.5: Same as Figure 5.4, except showing results for the HOMO (a. through c.) and CON (d. through f.) texture measure.

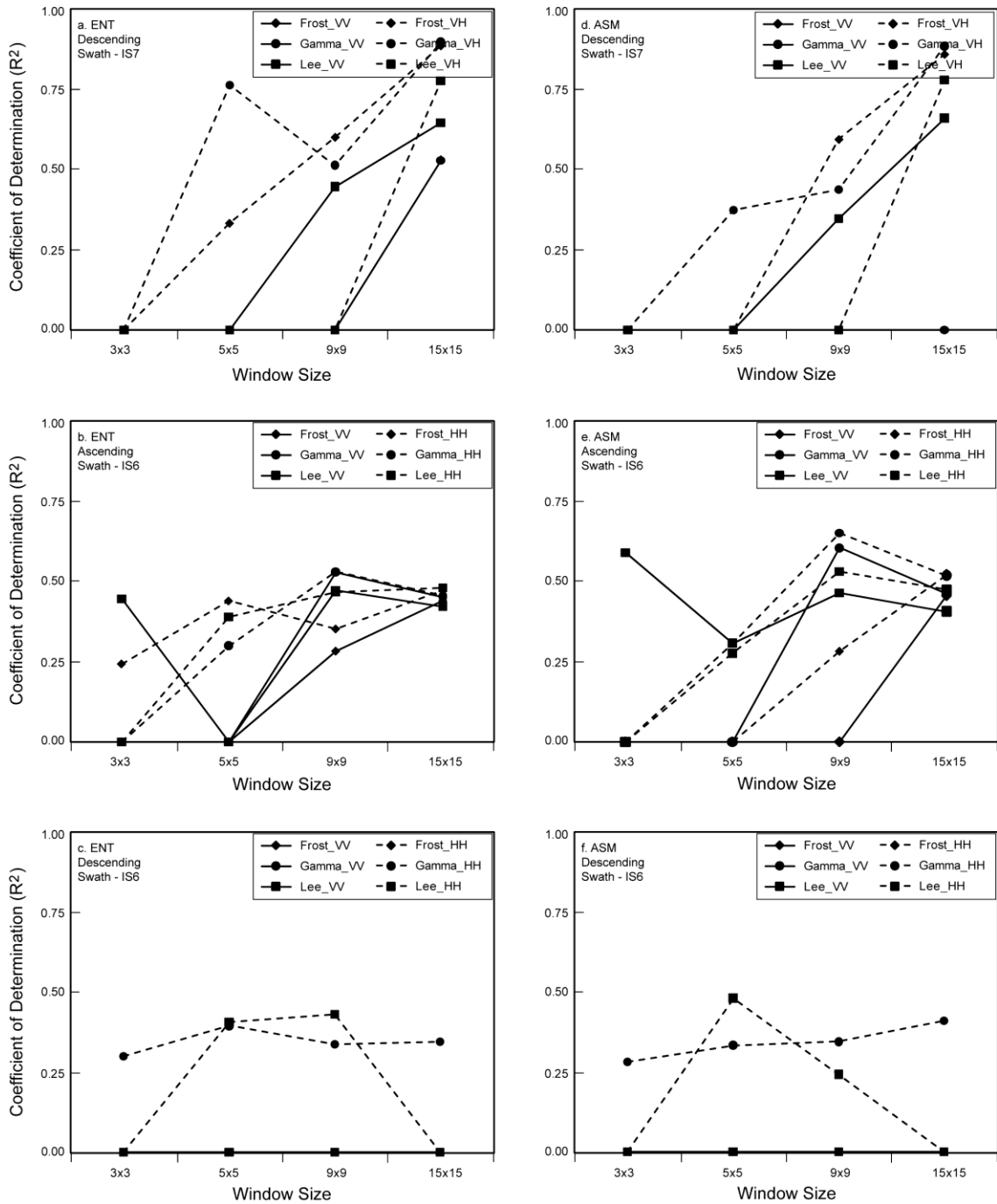


Figure 5.6: Same as Figure 5.4, except showing results for the ENT (a. through c.) and ASM (d. through f.) texture measure.

comparing different ice types (Onstott et al., 1979; Livingstone et al., 1983). Smooth or slightly rough first-year sea ice types will generally have very weak depolarization, while rougher sea ice composed of discrete objects will have a stronger depolarization in cross-polarized imagery (Onstott, 1993).

Differences in accountability were also evident for different incidence angles and paths (i.e. ascending or descending). Comparing regression results for VV polarized images, results suggest that overall images with a greater incidence angle (i.e. April 19) accounted for a greater proportion of the variability in surface roughness (Figures 5.4 through 5.6). Surface scattering becomes more dominant as the incidence angle increases, therefore a greater incidence angle is better to examine the texture information contained in an ASAR image. Results also suggest that images taken during a descending path account for more of the variability in surface roughness than images acquired on the ascending path (keeping other image characteristics constant; Figures 5.4 through 5.6).

5.3.2 Optimal GLCM parameters

Regression results suggest that both ENT and ASM are able to account for the greatest amount of the variability in surface roughness (90.0% and 88.6% respectively). Both of these texture measures quantify the local homogeneity within the image, and thus this finding is consistent with the results using the original image. For ENT, larger values of this texture measure occur for pixels with a smaller average surface roughness ($r = -0.95$, $p < 0.05$; Figure 5.7a.) while the opposite association is evident for ASM ($r = 0.94$, $p < 0.05$; Figure 5.7b.). This difference is

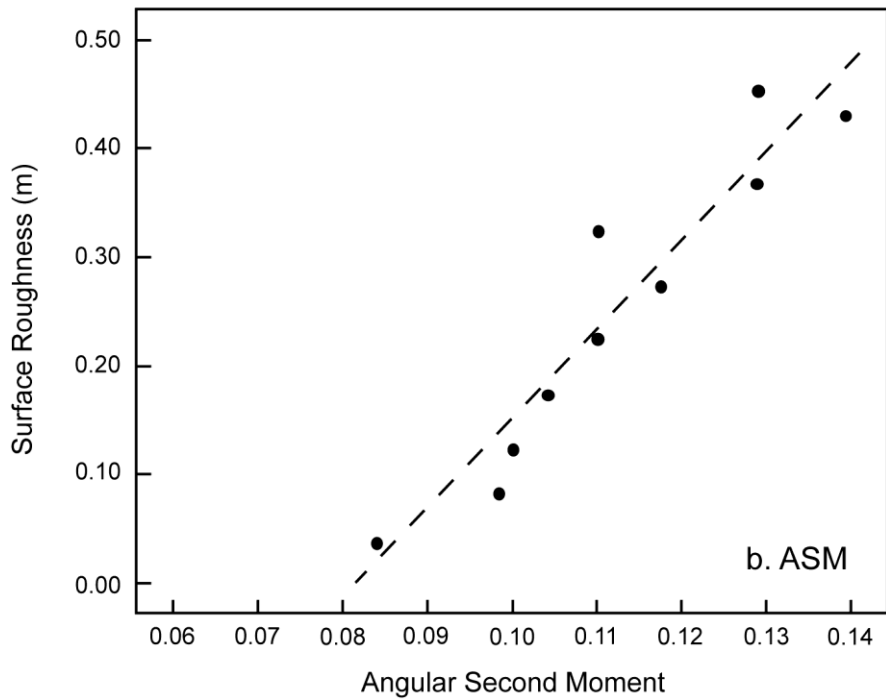
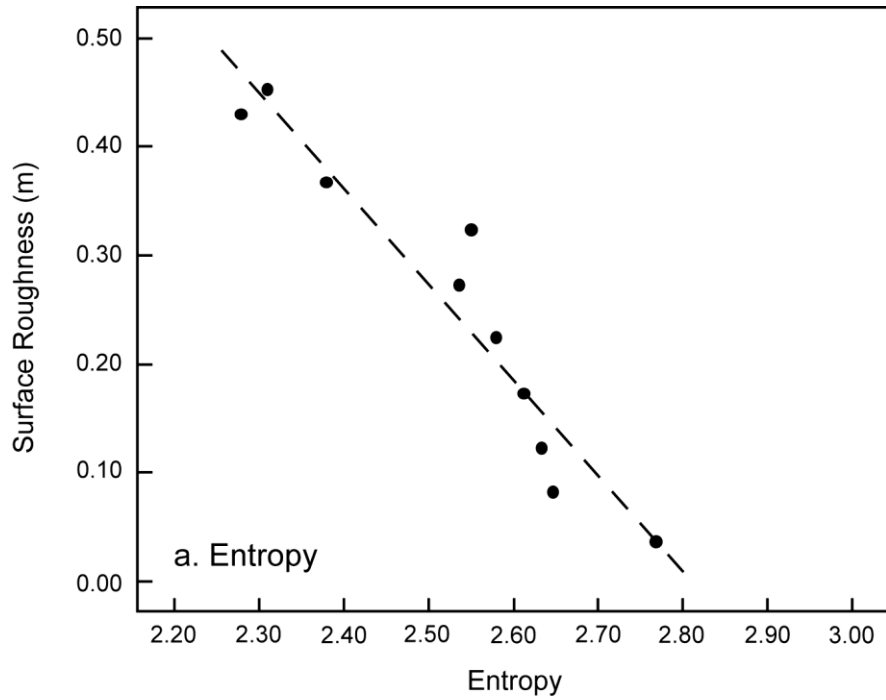


Figure 5.7: Scatterplot of surface roughness versus (a.) ENT or (b.) ASM values calculated from the gamma speckle reduced image and a window size of 15 pixels. The dashed line represents the line of best fit through the scatter.

expected since the computation of these texture measures suggest that when the texture within an image is smooth, ENT will be high and ASM will be low. Consistent with previous results, the greatest variability in surface roughness was accounted for when using a window size of 15x15 pixels for the calculation of the GLCM measure (Figures 5.4 through 5.6). This would again indicate the function of spatial averaging in assessing the relationship.

5.3.3 Case Study

On April 20 and 22, the same transect was sampled using the IcePic (Transects FEM04047 and FEM04058) and correspond to two different ASAR images (Table 5.2). Thus this case study can be used to further examine the differences between image parameters. The distributions of surface roughness for these two transects were statistically similar ($z = -0.35$, $p = 0.72$), therefore any differences observed in the relationship between surface roughness and texture approximation can be attributed mainly to the image characteristics. The two ASAR images that correspond to these transects were acquired on a descending path; however the incidence angles and polarizations were different (Table 5.2). The relationship between surface roughness from the IcePic laser and the ENT or ASM texture measures (using a 15x15 window) is substantially greater for FEM04047 (Figure 5.8). Comparing the results for only these two transects (the results for the April 22 image included other transects), reinforces the results from above, suggesting that cross-polarized images with a larger incidence angle are able to account for a greater proportion of the variability in surface roughness.

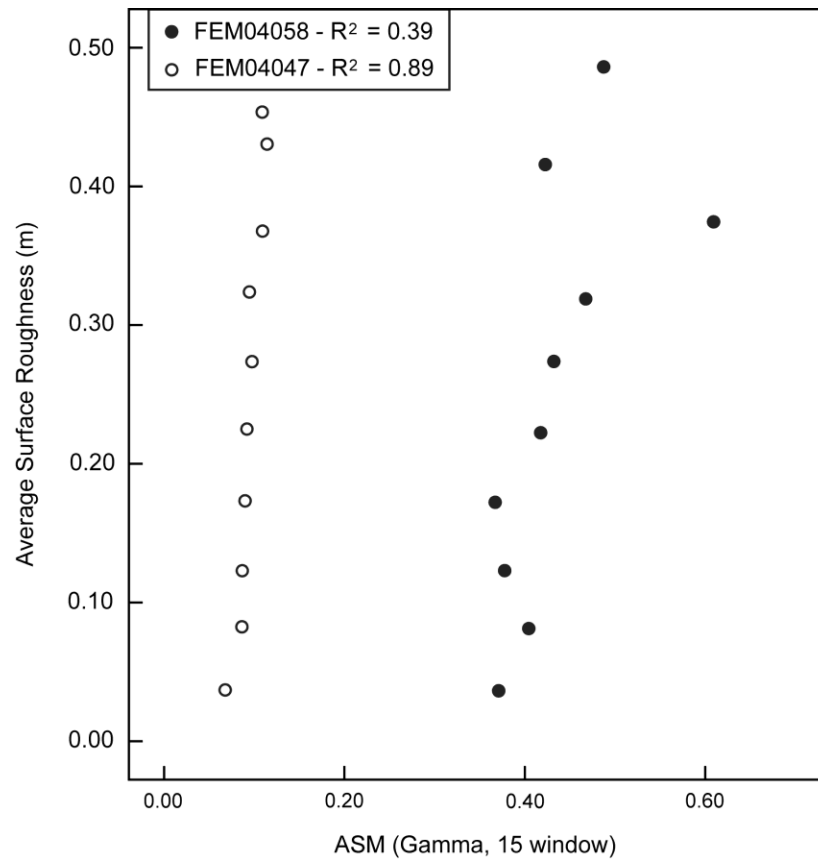
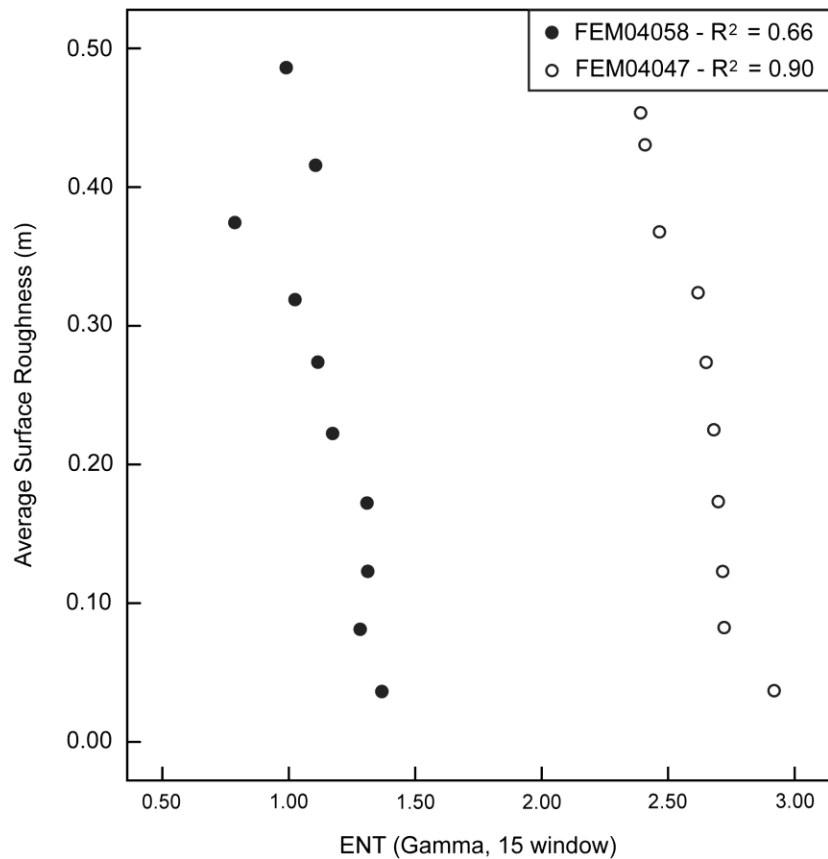


Figure 5.8: Scatterplots of surface roughness and texture measures (ENT and ASM) for transect FEM04047 (open circles) and transect FEM04058 (closed circles). Results for transect FEM04047 were based on the VH image on April 19, while for transect FEM04058, the results were based on the HH image on April 22. A gamma speckle reduction technique was used on the original image and a window size of 15 pixels was used to compute each texture measure.

5.4 Conclusion

Results suggest that second-order texture measures of a speckle-reduced (using a Gamma adaptive filter) cross-polarized ASAR image can be used to estimate the surface roughness. The optimal GLCM texture measures are either ENT or ASM using a 15x15 window. Results also suggest that larger incidence angles associated with the imagery is best due to the fact that surface roughness plays a greater role in the backscatter as the incidence angle increases. Using these image and texture parameters, over 90% of the variability in surface roughness can be estimated using ASAR imagery. This finding can be incorporated into models to examine the snow thickness distribution patterns, as well as habitat or ecological modeling of polar bears and ringed seals.

Due to the nature of the environment and the different orientations of sampling using the helicopter, the present research used a sampling distance of 1 pixel and orientation of 0° to calculate the conditional joint probabilities associated with the GLCM. Future research may investigate the orientation of roughness features such as pressure ridges and the impact of using different orientations within the calculation of the GLCM. This orientation may impact the amount of variability in surface roughness that can be accounted for by the different polarizations (cross- and co-polarized).

One limitation of this research is the pixel size of the satellite imagery (i.e. 30 m). Due to the pixel size, a summary statistic was used within each pixel to approximate the surface roughness values. The averaging smoothed out the surface roughness

eliminating the extremes of surface roughness. Therefore the results are only applicable to surface roughness less than 1.0 m. Often pressure ridges and rubble ice may have surface roughness greater than this limit. Future research may also investigate if finer spatial resolution imagery, such as from CryoSat or IceSat, can be used to estimate surface roughness at a finer spatial scale. Presently, these platforms do not have the temporal resolution as ASAR, and thus may not be considered as operationally ideal for this application. As satellite platforms with finer spatial resolution become more prevalent in acquiring imagery over sea ice, better estimation of surface roughness can be investigated using the un-binned IcePic information.

CHAPTER 6: ASSESSMENT OF SUMMER AND AUTUMN ICE CHARACTERISTICS AS RELATED TO POLAR BEAR SUBPOPULATIONS IN THE CANADIAN ARCTIC

This chapter will examine changes in sea ice presence and timing of any change within the polar bear (*Ursus maritimus*) subpopulations in the Canadian Arctic. Two specific objectives will be addressed: i) describe the spatial and temporal patterns of sea ice characteristics within the polar bear subpopulations between 1978 and 2008; and ii) examine dynamic and thermodynamic factors that have influenced these changes. These changes in sea ice characteristics will also be discussed in the context of known (published) variation in polar bear population condition (i.e. numbers, condition and survival) in the Canadian Arctic.

6.1 Methods

6.1.1 Polar bear subpopulation clusters

To study the large temporal and spatial patterns of sea ice characteristics linked to polar bear habitat, the Canadian Arctic was divided into regions that correspond to the polar bear subpopulations recognized by the International Union for the Conservation of Nature and Natural Resources (IUCN/SSC) Polar Bear Specialist Group (Figure 6.1). Based on similarity of sea ice characteristics, the 13 Canadian polar bear subpopulations (Lunn et al., 2006) were grouped into three clusters (Table 6.1): Eastern Canadian Arctic (ECA), Canadian Arctic Archipelago (CAA) and Beaufort Sea (BS). The ECA cluster is characterized by complete ice retreat in the summer and a minimum concentration of MYI. This cluster contains approximately

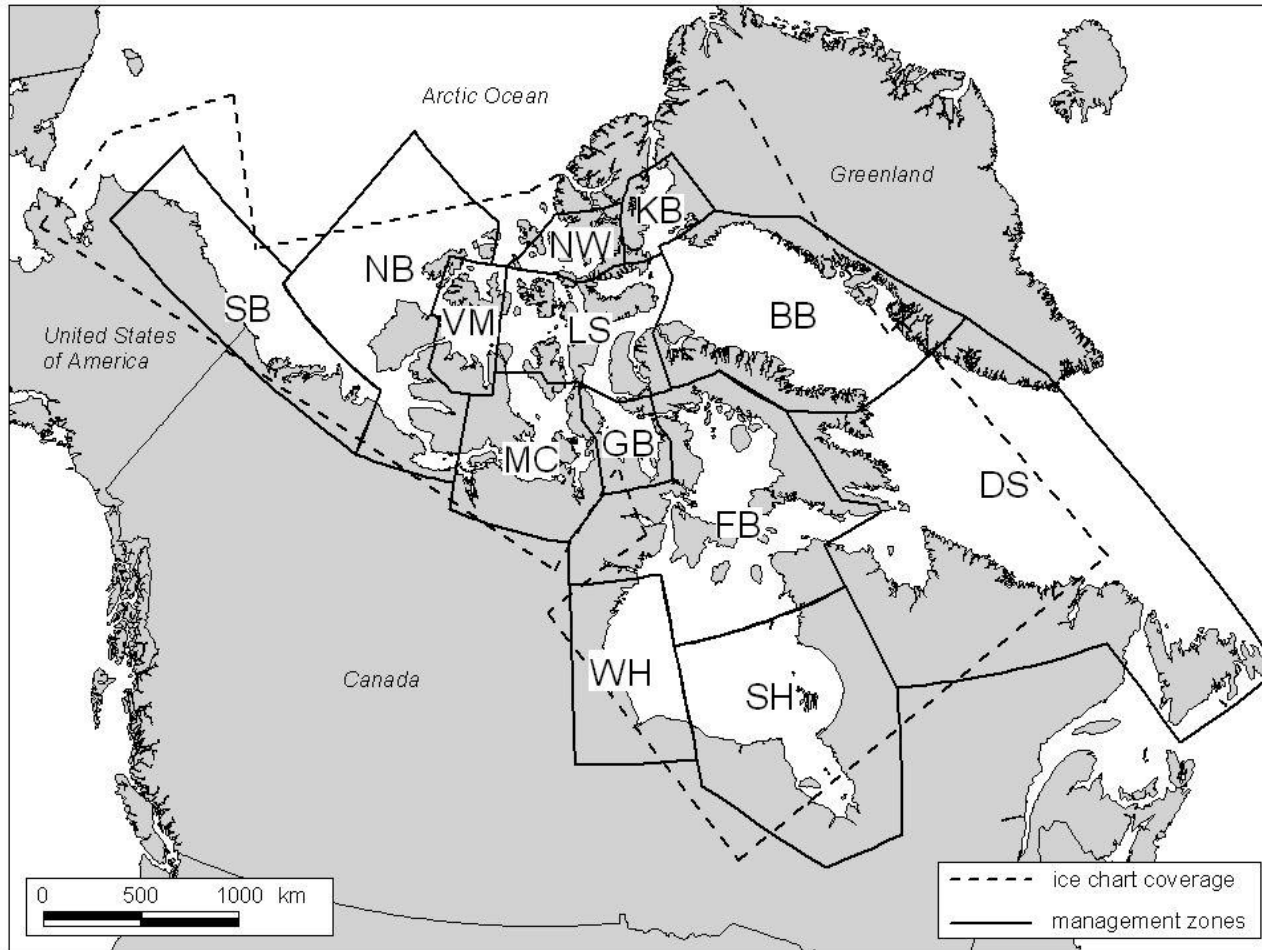


Figure 6.1: Boundaries of the 13 polar bear subpopulations in Canada, and the spatial coverage of the ice charts. The complete names of the subpopulations are listed in Table 6.1.

one half of the Canadian polar bear population (Aars *et al.*, 2006). The sea ice within the CAA cluster does not break-up every year and the polar bears may remain on MYI during the summer period. The BS cluster is located along the western margin of the study area, and is strongly influenced by the oceanic circulation within the Beaufort Sea. Table 6.1 provides a list of the polar bear subpopulations that are included within each cluster.

Table 6.1: The Canadian polar bear subpopulations (Lunn *et al.*, 2006) comprising the three clusters used in this study.

Clusters	Subpopulations
Eastern Canadian Arctic (ECA)	BB - Baffin Bay
	DS - Davis Strait
	FB - Foxe Basin
	SH - Southern Hudson Bay
	WH - Western Hudson Bay
Canadian Arctic Archipelago (CAA)	GB - Gulf of Boothia
	KB - Kane Basin
	LS - Lancaster Sound
	MC - M'Clintock Channel
	NW - Norwegian Bay
	VM - Viscount Melville Sound
Beaufort Sea (BS)	NB - Northern Beaufort Sea
	SB - Southern Beaufort Sea

6.1.2 Canadian Ice Service (CIS) ice charts

Weekly regional ice charts for the Canadian Arctic were obtained from the Canadian Ice Service (CIS) in digital format (<http://www.ec.gc.ca/glaces-ice/>). The charts are produced for tactical planning and operational purposes and represent an estimate of the ice conditions at the time of production (MANICE, 2005). Production of the ice charts integrate all the information available at the time, including but not

limited to weather conditions, visual observations and satellite/aircraft imagery, to characterize the sea ice conditions in the Arctic. Throughout the study period, the quality and quantity of information used to produce the ice charts has improved (i.e. after 1995 with the inclusion of RadarSat-1 data) and thus may impact the quality of the sea ice information. The information on sea ice conditions are charted using the World Meteorological Organization (WMO) egg code, which provides information on the concentration of sea ice, the stage of development or ice type and floe size or form of development (MANICE, 2005). This information is available in a vector format, providing the sea ice information in discrete polygons. These data have been used effectively in previous studies examining the spatial and temporal sea ice characteristics in the Arctic (i.e. Stirling *et al.*, 1999; Barber and Iacozza, 2004; Gagnon and Gough, 2005; Howell *et al.*, 2008).

Ice charts were obtained over a 31-year period, from 1978 to 2008. Ice charts produced prior to 1978 used a different method of coding information, which limits the number of ice characteristics available for analysis. To maintain consistency between years, only ice charts produced between June 11 (week 24) and December 2 (week 48) of each year were acquired and analyzed. Prior to 2007, ice charts were produced monthly or semimonthly from January to May, and thus winter and spring periods were excluded from this research. The ice charts were georeferenced and projected to a Lambert Equal-Area Azimuthal projection. The polar bear subpopulation boundaries were overlaid onto the ice charts (using the same projection) in order to extract information on the sea ice characteristics for each zone. The ice chart coverage did not provide sea ice information for the entire area

of the BB, DS, SH and NB subpopulations (Figure 6.1). In the calculation of the sea ice anomalies, the area of coverage by ice charts for these four subpopulations was used in place of the total area of the zone, and thus the analysis of changes in the ice characteristics is limited to the coverage of the ice charts and not the total area of the subpopulation.

The sea ice characteristics extracted from the weekly regional ice charts included the percentage of open water, sea ice types and floe size. The percentage of the open water within each subpopulation was calculated using the equation [6.1]:

$$\{\sum[(1- IC)/10 * area]\}/ total area \quad [6.1]$$

where *IC* is the ice concentration (expressed as a tenth) for each polygon within a particular subpopulation; *area* is the area of the individual polygon (measured in km²) and *total area* is the area of the subpopulation excluding land (measured in km²). To obtain the open water concentration, the ice concentration was subtracted from 1.

Similar calculations were done for the individual ice types and floe sizes. For this analysis, two ice type classes were considered. The FYI class was made up of first-year, thin, medium and thick first-year ice stages of development (MANICE, 2005). The second class was MYI class and it consisted of old, second and multiyear ice stages of development. The floe sizes were grouped into three (3) classes, and used to give an approximation of the occurrence of ice edges within the ice cover. The first class was called small floe class (0-500 m) and consisted of pancake, brash, ice cakes, small floe and medium floe forms of ice. This class represents an area with a

high number of ice edges and excessive concentration of open water/leads between ice floes. Large floe class (500 m – 10 km) was the second floe size class and consisted of big floe, vast floe and giant floe forms of ice. It was assumed that a lower number of ice edges and minimum concentration of open water/leads is present between floes. The third class was composed of only land-fast ice, and thus named fast ice class.

Within each polygon for the weekly ice charts, the percentage of the total area of each subpopulation covered by the ice type/floe size was calculated using the equation [6.2]:

$$\{\sum[IT_FS/10 * area]\} / total\ area \quad [6.2]$$

where *IT_FS* is the concentration of each ice type or floe size (expressed as a tenth) for each polygon in a particular subpopulation; *area* is the area of the individual polygon (measured in km²) and *total area* is the area of the subpopulation excluding land (measured in km²).

Seasonally summed anomalies were computed by first averaging the percentage for each ice characteristic over the 31-year period for each week. Weekly anomalies or deviations were then calculated by subtracting the averages from the weekly percentages for each ice characteristic. The anomalies were then summed for the summer season (extending from week 24 to 35 or June 11 to September 2) and the autumn season (extending from week 36 to 48 or September 3 to December 2) in order to obtain the seasonally summed anomalies. Negative anomalies would

indicate less percentage of the ice characteristic compared to the 31-year average, while positive anomalies suggest a greater percentage compared to the same period.

6.1.3 Modeled dynamic and thermodynamic parameters

For this study, mean daily air temperature from modeled National Centres for Environmental Prediction (NCEP) reanalysis data (Kanamitsu *et al.*, 2002) was used to examine the thermodynamic influence on the spatial and temporal patterns of the various sea ice characteristics; as well as to force *SnowModel*. Daily air temperature values (modeled at 2 m) were obtained through the NCEP reanalysis for an area that incorporated all thirteen (13) subpopulations

(<http://www.esrl.noaa.gov/psd/data/gridded/data.ncep.reanalysis2.html>). Data were not available for the 1970s, thus these data extended from 1980 to 2008.

Seasonal averages, along with the average over the 29-year period, were then computed for each subpopulation. Seasons were defined as follows: winter – December 1 through February 28/29, spring – March 1 through May 31, summer – June 1 through August 31 and autumn – September 1 through November 30. These definitions were based on the orbital geometry of the Earth, with respect to the sun. Therefore the winter and summer seasons as defined above include the winter and summer solstice respectively, while the autumn and spring seasons include the corresponding equinoxes. Winter and spring seasons were included to investigate the seasonal lags between anomalies in sea ice characteristics and deviations in air temperatures. Deviations (anomalies) were derived by subtracting the seasonal average over the entire study period from the seasonal average for each year.

Positive anomalies in temperature would indicate an overall warming with the subpopulation, while negative anomalies would indicate an overall cooling. One limitation of the NCEP reanalysis data for this study is the spatial resolution. Only a few modeled sampled points of air temperature are available for the smaller subpopulations (i.e. KB).

Dynamic factors can be characterized by large-scale atmospheric and oceanic circulation patterns. The Arctic Oscillation (AO) has been shown to influence sea ice motion and oscillation on large spatial scales (Wang and Ikeda, 2000; Rigor et al., 2002) and thus was used to characterize the atmospheric circulation patterns related to sea ice characteristics within the 13 polar bear subpopulations. Monthly values for the AO index were obtained from the National Weather Service Climate Prediction Center website http://www.cpc.noaa.gov/products/precip/CWlink/daily_ao_index/ao_index.html from January 1978 to December 2008. A 12-month running average was computed from the monthly values in order to visualize the annual trends in the index, while reducing the monthly variability (Figure 6.2). In addition, seasonal averages were computed for the AO values. Seasons consisted of the same months as defined for the NCEP temperature analysis. Other dynamic factors, which may play a role in the spatial and temporal trends in sea ice characteristics such as atmospheric pressure and winds, are not accurately modeled at this spatial scale, limiting the inclusion in this study.

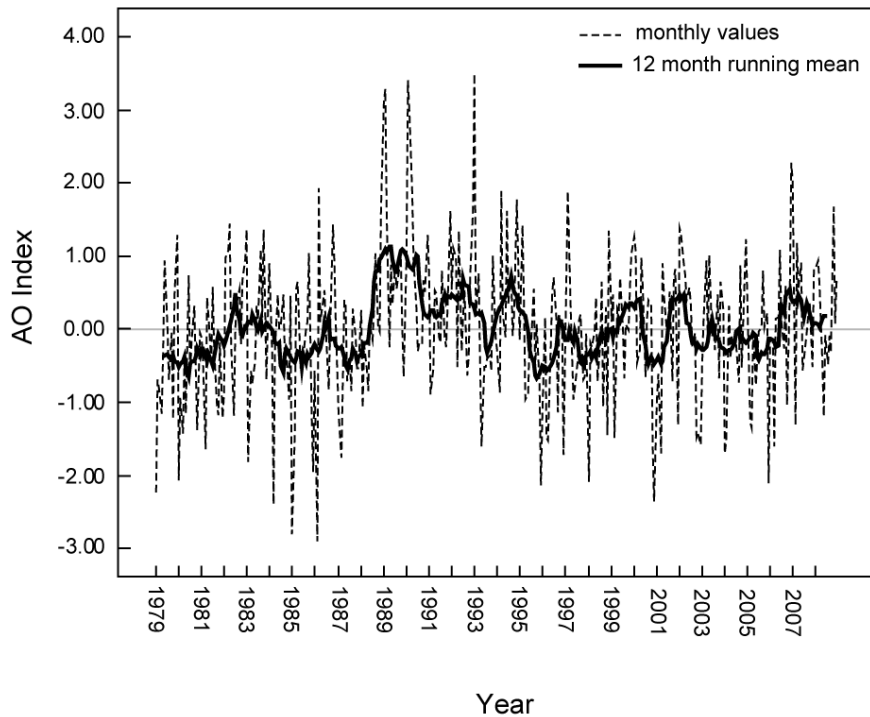


Figure 6.2: Plot of monthly and 12-month running average of the Arctic Oscillation index (data from the National Weather Service Climate Prediction Center).

6.1.4 Spectral analysis

Spectral analysis was used to determine if any periodicity or ‘seasonality’ exists in the time series of the anomalies for each sea ice characteristic. It decomposes the time series into a spectrum of cycles of different lengths that can be interpreted as the temporal autocorrelation of the sea ice characteristic anomalies. This was accomplished by using a periodogram, which plots the amplitude of the time series against the frequency (Brillinger, 1981). To compute the periodicity in the time series, a smoothing function needs to be applied to the periodogram. For this application, a Tukey-Hamming window with a span of 5 was used. This smoothing

technique calculates a weighted moving average transformation of the periodogram values (Blackman and Tukey, 1958). The weight function is greatest for the observations in the centre of the window, and decreases with distance away from the centre. The frequency with the largest peak of the periodogram was determined as the dominant cycle. For this study, the periodicity (ranging from 0 to 1) is defined as frequency of the peak multiplied by 31 years (the length of the time series). Smooth time series tend to generate periodograms with most of the variance in the ice characteristic in the low frequencies (therefore low periodicity), while rapidly oscillating time series tend to generate periodograms with the majority of the variance in ice characteristic in the high frequency (therefore high periodicity). Such a techniques has been used in previous studies to examine biological rhythmicity (i.e. Begum et al., 2006), time series of multispecies microfossil data (Hammer, 2007) and interannual fluctuation of wet and dry periods (Pekarova and Pekar, 2007).

6.2 Spatial and temporal trends in sea ice characteristics

6.2.1 Eastern Canadian Arctic (ECA) cluster

For most subpopulations within the Eastern Canadian Arctic (ECA) cluster, trend analysis suggests an overall increase in open water during both summer and autumn seasons over the 31-year sampling period (Figure 6.3). The slopes (ϕ) of the significant trends indicate a 14% (WH) to a 28% (DS) per decade increase in summer open water concentration (Table 6.2). This is consistent with the reduction observed for this area using passive microwave remote sensing (Comiso, 2003;

Parkinson and Cavalieri, 2008). The trend toward more open water with the DS subpopulation over the study period may be due to the southern location of this zone, as well as the general movement pattern of ice from the BB zone into the DS zone. As for the WH subpopulation, the relatively low increase in open water may be due to the counter-clockwise circulation in this region, and thus ice is usually present in this zone longer than the other zones within this cluster. During autumn, the trends were generally lower for most of the subpopulations, from between 6% (SH) to 24% (FB) per decade (Table 6.2). Spectral analysis of the open water anomalies indicates a periodicity of 14 years for the SH subpopulation in summer only (Table 6.3). This suggests that for other subpopulations no statistically significant periodicity could be detected for open water anomalies in either season. The lack of any periodicity would indicate that open water anomalies are random within the subpopulations.

The subpopulations within this cluster contain low concentrations and thus small anomalies of MYI for both summer and autumn season (Figure 6.4a. and b. – top graphs). Correlation analysis indicates that no significant overall trends occur in the summer and autumn anomalies in this ice type over the 31-year period (Table 6.2). The one exception is FB, which shows an overall trend toward less MYI during the autumn season (2% per decade reduction; Table 6.2). The MYI which populates the FB subpopulation typically enters this area from the Gulf of Boothia through Fury and Hecla Strait. Periodicity in the order of 2-5 years for the summer exists for the three subpopulations within this cluster that contained multiyear sea ice (Table

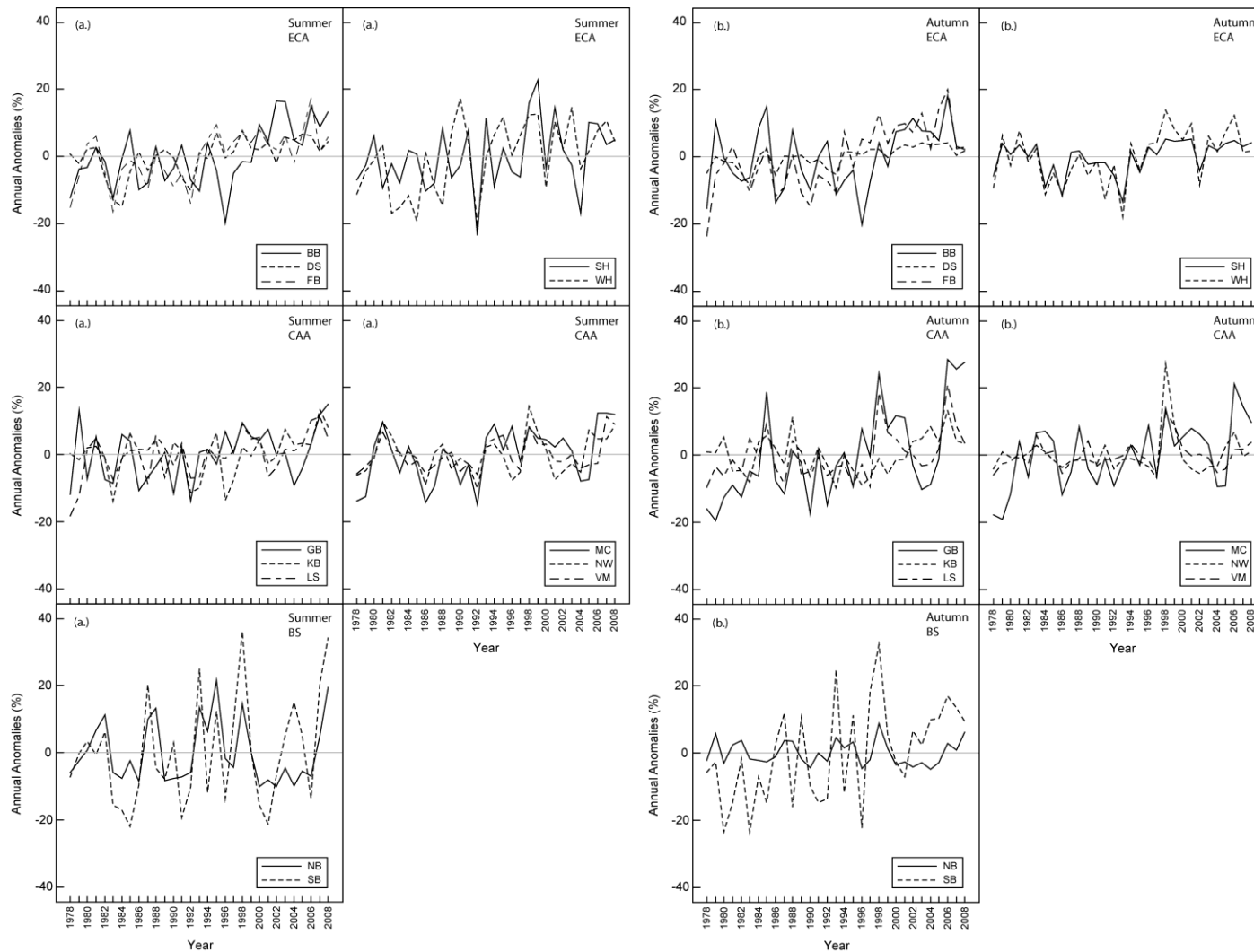


Figure 6.3: Summer (a) and autumn (b) open water anomalies calculated for the subpopulations within the Eastern Canadian Arctic (ECA) cluster (top), Canadian Arctic Archipelago (CAA) cluster (middle) and Beaufort Sea (BS) cluster (bottom).

Table 6.2: 31-year trend analysis (r) and associated slopes (ϕ , % per decade) of open water, multiyear and first-year sea ice concentration, large and small floe sizes and fast ice concentration in the polar bear subpopulations within the three clusters. Statistically significant trends ($p < 0.05$) are highlighted in bold and italics. S = Summer season, A = Autumn season, NA = no multiyear sea ice, NS = non-significant slopes. Summer season is between June 11 and September 2, while autumn season is between September 3 to December 2).

Cluster		Open Water		Multiyear Ice		First-year Ice		Fast Ice		Large Floe Size		Small Floe	
		S	A	S	A	S	A	S	A	S	A	S	A
ECA	BB	<i>$r = 0.57$</i> <i>$\phi = 19$</i>	$r = 0.35$ $\phi = \text{NS}$	$r = 0.07$ $\phi = \text{NS}$	$r = -0.12$ $\phi = \text{NS}$	<i>$r = -0.61$</i> <i>$\phi = 21$</i>	$r = -0.15$ $\phi = \text{NS}$	<i>$r = -0.53$</i> <i>$\phi = 3$</i>	<i>$r = -0.48$</i> <i>$\phi = 2$</i>	$r = -0.35$ $\phi = \text{NS}$	$r = -0.15$ $\phi = \text{NS}$	<i>$r = -0.69$</i> <i>$\phi = 5$</i>	$r = -0.28$ $\phi = \text{NS}$
	DS	<i>$r = 0.54$</i> <i>$\phi = 28$</i>	<i>$r = 0.66$</i> <i>$\phi = 8$</i>	$r = -0.25$ $\phi = \text{NS}$	$r = -0.27$ $\phi = \text{NS}$	<i>$r = -0.53$</i> <i>$\phi = 32$</i>	<i>$r = -0.51$</i> <i>$\phi = 1$</i>	<i>$r = -0.56$</i> <i>$\phi = 1$</i>	<i>$r = -0.51$</i> <i>$\phi = 1$</i>	<i>$r = -0.47$</i> <i>$\phi = 5$</i>	$r = -0.30$ $\phi = \text{NS}$	<i>$r = -0.43$</i> <i>$\phi = 4$</i>	<i>$r = -0.52$</i> <i>$\phi = 3$</i>
	FB	<i>$r = 0.60$</i> <i>$\phi = 23$</i>	<i>$r = 0.69$</i> <i>$\phi = 24$</i>	$r = -0.25$ $\phi = \text{NS}$	<i>$r = -0.50$</i> <i>$\phi = 2$</i>	<i>$r = -0.57$</i> <i>$\phi = 23$</i>	<i>$r = -0.54$</i> <i>$\phi = 7$</i>	$r = -0.35$ $\phi = \text{NS}$	<i>$r = -0.38$</i> <i>$\phi = 1$</i>	$r = -0.31$ $\phi = \text{NS}$	<i>$r = -0.41$</i> <i>$\phi = 7$</i>	<i>$r = -0.37$</i> <i>$\phi = 6$</i>	<i>$r = -0.62$</i> <i>$\phi = 10$</i>
	SH	$r = 0.30$ $\phi = \text{NS}$	<i>$r = 0.36$</i> <i>$\phi = 6$</i>	$r = -0.09$ $\phi = \text{NS}$	NA	$r = -0.30$ $\phi = \text{NS}$	$r = -0.12$ $\phi = \text{NS}$	$r = -0.15$ $\phi = \text{NS}$	$r = -0.21$ $\phi = \text{NS}$	$r = -0.12$ $\phi = \text{NS}$	$r = -0.24$ $\phi = \text{NS}$	<i>$r = -0.39$</i> <i>$\phi = 4$</i>	$r = -0.34$ $\phi = \text{NS}$
	WH	<i>$r = 0.52$</i> <i>$\phi = 14$</i>	<i>$r = 0.40$</i> <i>$\phi = 11$</i>	$r = -0.14$ $\phi = \text{NS}$	$r = -0.35$ $\phi = \text{NS}$	<i>$r = -0.51$</i> <i>$\phi = 15$</i>	<i>$r = -0.44$</i> <i>$\phi = 2$</i>	$r = 0.05$ $\phi = \text{NS}$	$r = 0.08$ $\phi = \text{NS}$	<i>$r = -0.42$</i> <i>$\phi = 12$</i>	$r = -0.34$ $\phi = \text{NS}$	<i>$r = -0.43$</i> <i>$\phi = 6$</i>	$r = -0.28$ $\phi = \text{NS}$
CAA	GB	<i>$r = 0.36$</i> <i>$\phi = 13$</i>	<i>$r = 0.62$</i> <i>$\phi = 30$</i>	<i>$r = -0.61$</i> <i>$\phi = 43$</i>	<i>$r = -0.69$</i> <i>$\phi = 41$</i>	<i>$r = 0.50$</i> <i>$\phi = 8$</i>	$r = 0.00$ $\phi = \text{NS}$	$r = 0.35$ $\phi = \text{NS}$	$r = -0.18$ $\phi = \text{NS}$	$r = -0.32$ $\phi = \text{NS}$	<i>$r = -0.63$</i> <i>$\phi = 38$</i>	$r = -0.07$ $\phi = \text{NS}$	$r = 0.05$ $\phi = \text{NS}$
	KB	$r = 0.32$ $\phi = \text{NS}$	$r = 0.24$ $\phi = \text{NS}$	$r = 0.14$ $\phi = \text{NS}$	$r = -0.09$ $\phi = \text{NS}$	<i>$r = -0.43$</i> <i>$\phi = 15$</i>	<i>$r = -0.48$</i> <i>$\phi = 10$</i>	<i>$r = -0.48$</i> <i>$\phi = 16$</i>	$r = -0.22$ $\phi = \text{NS}$	$r = 0.09$ $\phi = \text{NS}$	$r = -0.06$ $\phi = \text{NS}$	$r = 0.12$ $\phi = \text{NS}$	$r = -0.17$ $\phi = \text{NS}$
	LS	<i>$r = 0.49$</i> <i>$\phi = 22$</i>	<i>$r = 0.41$</i> <i>$\phi = 11$</i>	$r = -0.31$ $\phi = \text{NS}$	$r = -0.20$ $\phi = \text{NS}$	$r = -0.16$ $\phi = \text{NS}$	$r = -0.27$ $\phi = \text{NS}$	$r = 0.23$ $\phi = \text{NS}$	$r = -0.33$ $\phi = \text{NS}$	<i>$r = -0.37$</i> <i>$\phi = 13$</i>	$r = -0.22$ $\phi = \text{NS}$	$r = -0.30$ $\phi = \text{NS}$	$r = -0.20$ $\phi = \text{NS}$
	MC	<i>$r = 0.46$</i> <i>$\phi = 17$</i>	<i>$r = 0.51$</i> <i>$\phi = 18$</i>	<i>$r = -0.48$</i> <i>$\phi = 21$</i>	<i>$r = -0.47$</i> <i>$\phi = 20$</i>	$r = 0.21$ $\phi = \text{NS}$	$r = -0.15$ $\phi = \text{NS}$	<i>$r = 0.38$</i> <i>$\phi = 15$</i>	$r = -0.25$ $\phi = \text{NS}$	<i>$r = -0.54$</i> <i>$\phi = 25$</i>	$r = -0.26$ $\phi = \text{NS}$	$r = -0.07$ $\phi = \text{NS}$	$r = -0.18$ $\phi = \text{NS}$
	NW	$r = 0.20$ $\phi = \text{NS}$	$r = 0.13$ $\phi = \text{NS}$	$r = -0.27$ $\phi = \text{NS}$	$r = -0.31$ $\phi = \text{NS}$	$r = 0.18$ $\phi = \text{NS}$	$r = 0.20$ $\phi = \text{NS}$	$r = 0.15$ $\phi = \text{NS}$	$r = -0.08$ $\phi = \text{NS}$	$r = -0.21$ $\phi = \text{NS}$	$r = -0.13$ $\phi = \text{NS}$	$r = 0.10$ $\phi = \text{NS}$	$r = -0.10$ $\phi = \text{NS}$
	VM	$r = 0.31$ $\phi = \text{NS}$	$r = 0.22$ $\phi = \text{NS}$	$r = -0.16$ $\phi = \text{NS}$	$r = -0.13$ $\phi = \text{NS}$	$r = 0.05$ $\phi = \text{NS}$	$r = -0.11$ $\phi = \text{NS}$	$r = 0.18$ $\phi = \text{NS}$	$r = -0.15$ $\phi = \text{NS}$	$r = -0.21$ $\phi = \text{NS}$	$r = 0.18$ $\phi = \text{NS}$	$r = 0.17$ $\phi = \text{NS}$	$r = -0.09$ $\phi = \text{NS}$
BS	NB	$r = 0.00$ $\phi = \text{NS}$	$r = -0.05$ $\phi = \text{NS}$	$r = 0.26$ $\phi = \text{NS}$	$r = 0.02$ $\phi = \text{NS}$	<i>$r = -0.44$</i> <i>$\phi = 20$</i>	$r = 0.05$ $\phi = \text{NS}$	<i>$r = -0.48$</i> <i>$\phi = 4$</i>	<i>$r = -0.57$</i> <i>$\phi = 3$</i>	$r = 0.23$ $\phi = \text{NS}$	$r = 0.34$ $\phi = \text{NS}$	$r = -0.25$ $\phi = \text{NS}$	$r = -0.26$ $\phi = \text{NS}$
	SB	$r = 0.30$ $\phi = \text{NS}$	<i>$r = 0.52$</i> <i>$\phi = 27$</i>	$r = 0.14$ $\phi = \text{NS}$	$r = -0.34$ $\phi = \text{NS}$	<i>$r = -0.46$</i> <i>$\phi = 11$</i>	$r = -0.26$ $\phi = \text{NS}$	$r = -0.23$ $\phi = \text{NS}$	<i>$r = -0.49$</i> <i>$\phi = 2$</i>	$r = -0.11$ $\phi = \text{NS}$	$r = -0.23$ $\phi = \text{NS}$	<i>$r = -0.55$</i> <i>$\phi = 8$</i>	<i>$r = -0.41$</i> <i>$\phi = 10$</i>

Table 6.3: Periodicity (in years) of open water, multiyear and first-year sea ice concentration, large and small floe sizes and fast ice concentration in the polar bear subpopulations within the three clusters. Statistically significant results ($p < 0.05$) are presented in the table. S = Summer season, A = Autumn season, NA = no significant periodicity beyond 1 year. Summer season is between June 11 and September 2, while autumn season is between September 3 to December 2). *Note: multiyear sea ice within WH and SH subpopulations was lacking and therefore no periodicity in the trends were calculated.

Cluster		Open Water		Multiyear Ice		First-year Ice		Fast Ice		Large Floe Size		Small Floe	
		S	A	S	A	S	A	S	A	S	A	S	A
ECA	BB	NA	NA	2	NA	NA	NA	NA	NA	2	NA	NA	2
	DS	NA	NA	5	2	NA	NA	NA	9	NA	9	5	NA
	FB	NA	NA	2	NA	NA	NA	NA	8	13	NA	13	NA
	SH	14	NA	*	*	14	NA	3	10	13	NA	13	NA
	WH	NA	NA	*	*	NA	NA	7	13	NA	NA	NA	14
CAA	GB	NA	4	NA	NA	2	3	3	NA	5	4	NA	3
	KB	7	2	NA	2	2	9	2	NA	2	2	4	2
	LS	7	4	2	4	2	8	2	8	2	4	NA	2
	MC	5	5	5	5	7	3	7	12	5	5	5	13
	NW	5	4	4	4	6	6	3	9	5	2	4	2
	VM	7	6	5	2	5	2	7	8	4	2	4	2
BS	NB	2	6	2	2	NA	2	NA	NA	2	NA	15	6
	SB	6	NA	6	NA	2	2	NA	NA	6	6	NA	NA

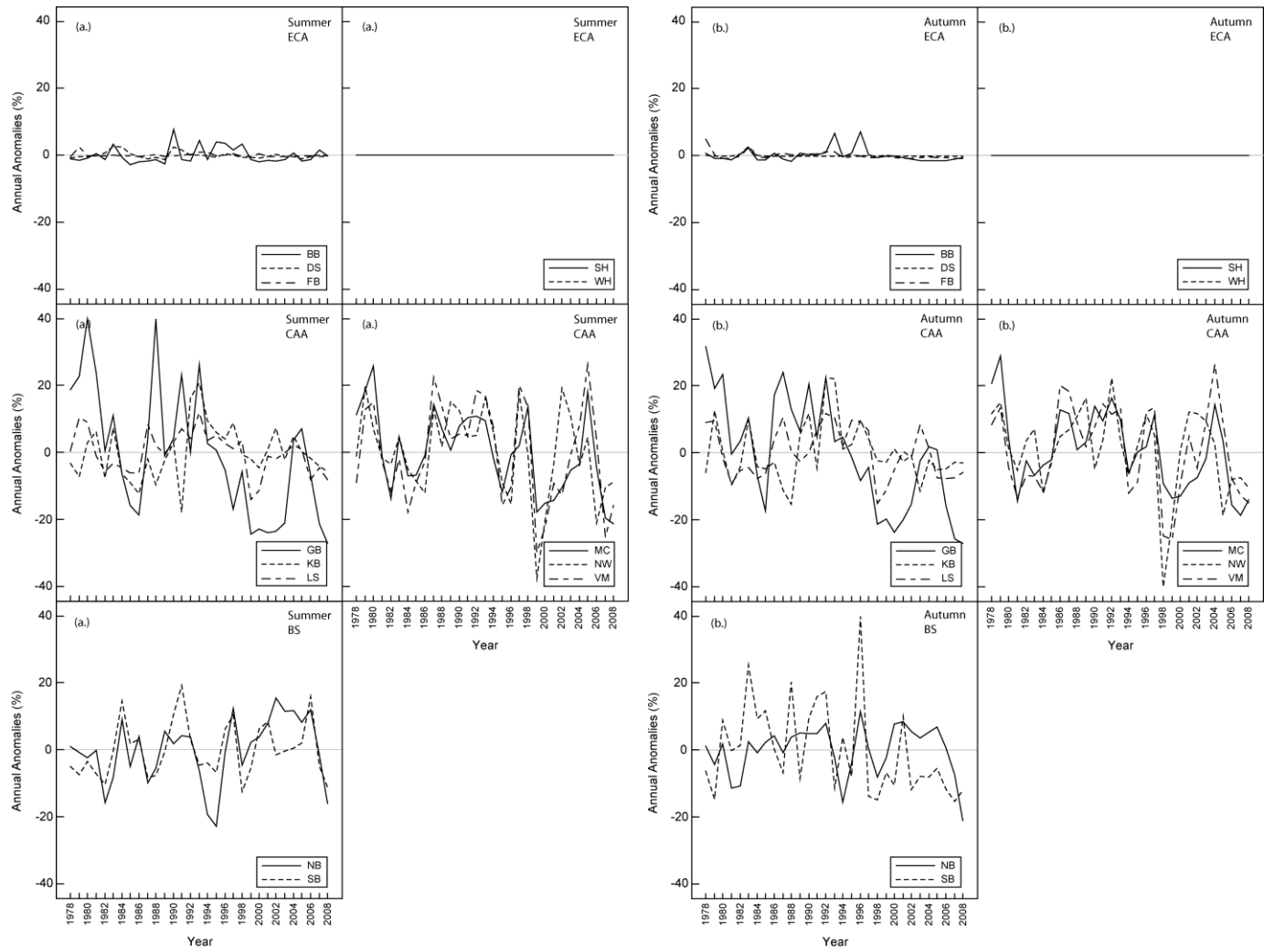


Figure 6.4: Summer (a) and autumn (b) multiyear sea ice anomalies calculated for the subpopulations within the Eastern Canadian Arctic (ECA) cluster (top), Canadian Arctic Archipelago (CAA) cluster (middle) and Beaufort Sea (BS) cluster (bottom).

6.3). A similar result was found for the autumn anomalies within the DS subpopulation only (Table 6.3).

With regards to FYI, trend analyses of anomalies suggest a decrease in this ice type for most subpopulations over the 31-year period (Table 6.2). During summer, the trends in anomalies demonstrate a similar pattern to that for the open water anomalies (Figure 6.5a. – top graphs), with slopes ranging from 15% per decade to 32% reduction per decade (Table 6.2). This result is consistent with previous studies that demonstrated an earlier sea ice break-up (and thus less FYI) in the WH subpopulation during summer (Stirling *et al.*, 1999; Gagnon and Gough, 2005), and is the primary contributing factor to the observed trends in the open water anomalies for this cluster. The summer anomalies were generally positive in the first part of the sampling period for most of the subpopulations (Figure 6.5a. – top graph). For the same season, the SH subpopulation did not exhibit temporal patterns in FYI anomalies (Figure 6.5b. – top graphs). In autumn, the slopes suggest a decrease as well; however the rate is substantially reduced for the subpopulations (Table 6.2). This finding of a slower rate of decrease in autumn relative to summer is consistent to previous studies that have used passive microwave data for the ECA cluster as a whole (Parkinson and Cavalieri, 2008). Spectral analysis indicates that the time series in FYI anomalies for both summer and autumn contain no periodicity beyond a single year, except for the SH subpopulation (summer anomalies; Table 6.3). As with open water, these anomalies are therefore random and influenced by other random factors (i.e. air temperature and/or Arctic Oscillation).

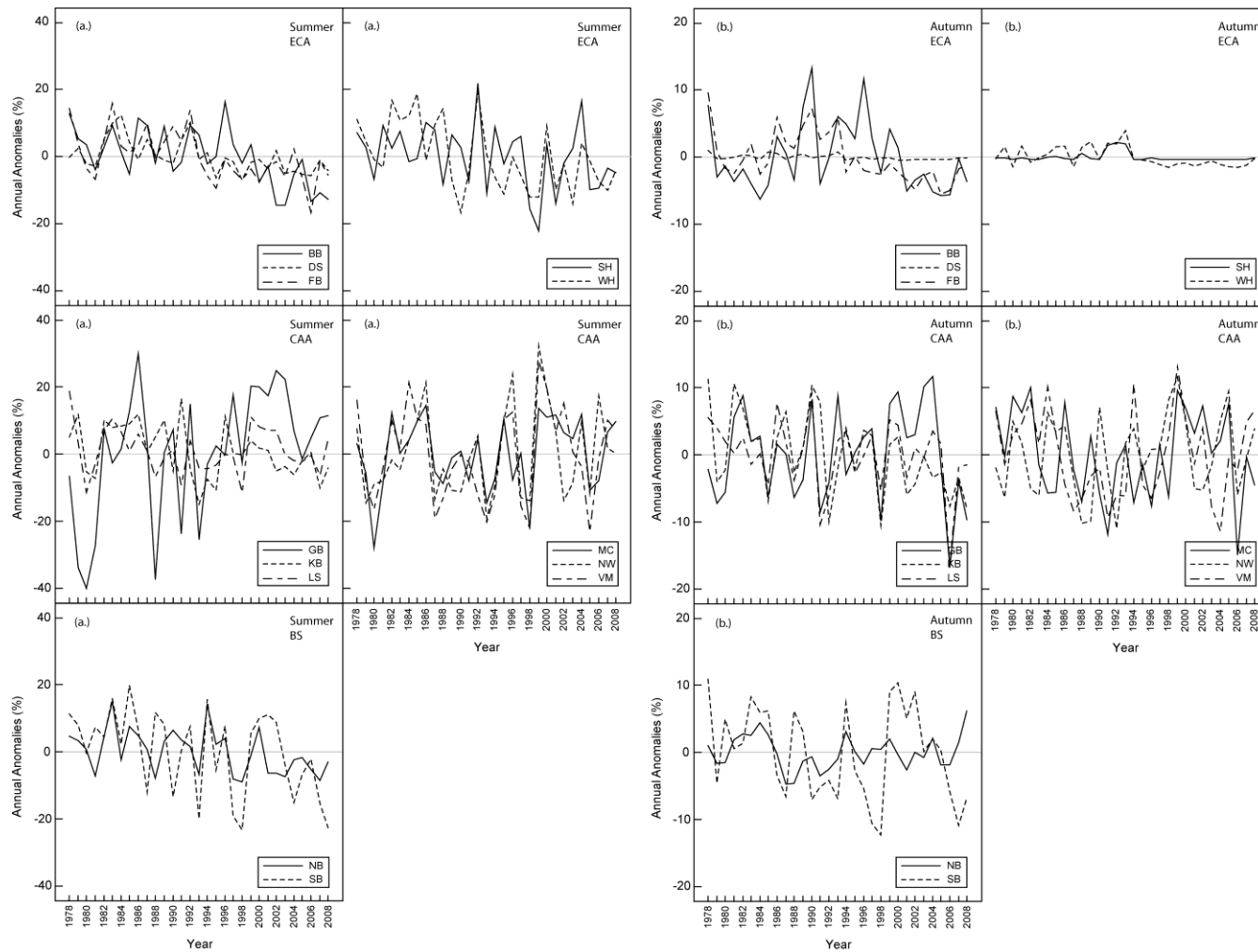


Figure 6.5: Summer (a) and autumn (b) first-year sea ice anomalies calculated for the subpopulations within the Eastern Canadian Arctic (ECA) cluster (top), Canadian Arctic Archipelago (CAA) cluster (middle) and Beaufort Sea (BS) cluster (bottom).

Trends in fast ice anomalies suggest an overall decrease over the sampling period for the BB and DS subpopulations during the summer and autumn seasons, as well as for the FB zone during the autumn season only (Table 6.2). The slopes of the trends suggest a slight decrease per decade (2% per decade) for both seasons (Table 6.2). This small decrease is due to the overall low concentrations of this floe size in these zones (Figure 6.6a. and b. – top graphs) and suggests a relatively consistent formation of this floe size. No trends were evident for the WH and SH subpopulations over the 31-year study period. Examination of the shorter temporal pattern of anomalies indicates that there is no significant deviation from 0, suggesting minimal interannual variability in both summer and autumn seasons for these subpopulations (Figure 6.6a. and b. – top graphs). Periodicity in the trend in fast ice anomalies was evident for the SH and WH subpopulations (both seasons), as well as the DS and FB (autumn season only; Table 6.3). The periodicities were larger for the autumn season compared to the summer season, suggesting a longer temporal ‘seasonality’ or cycle in this sea ice characteristic.

As with fast ice, the trends in large floe anomalies are limited to only a few subpopulations within this cluster. The summer anomalies in large ice floes showed a general negative trend in the DS and WH subpopulations only, while in the autumn season, a similar trend was evident for the FB subpopulation (Table 6.2). The slopes of the trends suggest that during the summer and autumn seasons, the decrease in large floe sizes was between 5% per decade and 12% per decade (Table 6.2). On shorter temporal periods, the summer large floe anomalies for the FB subpopulation were generally positive during the late 1970s to early 1990s and negative from the

mid-1990s through to the 2000s (Figure 6.7a. and b. – top graphs). Similar patterns were not evident for the other subpopulations. Positive anomalies tend to be dominant in the 1980s and 1990s, with negative anomalies dominating again in the later part of the sampling period (Figure 6.7a. and b. – top graphs). As with the other sea ice characteristics, the periodicity varied between subpopulations and seasons (Table 6.3), suggesting that correlations in the large floe anomalies exist at shorter temporal cycles for a few subpopulations.

The trends in small floe size summer anomalies suggest a decrease in the concentration over the 31-year period for all subpopulations within this cluster (Table 6.2). The rate of decrease was similar for all 5 zones, varying between 4% per decade and 6% per decade (Table 6.2). For three of the five subpopulations, the periodicity suggests that small floe size anomalies during the summer also occurred at intervals between 5 and 13 years (Table 6.3). For the autumn season, significant trends occur within the DS and FB subpopulations only. The slopes suggest a greater range in the rate of decrease of the small floe size (between 3% and 10% per decade; Table 6.2). For the remaining subpopulations, positive anomalies dominate the first two decades of the sampling period during both the summer and autumn seasons (Figure 6.8a. and b. – top graphs), suggesting a greater than average concentration of small ice floes in all five subpopulations and thus greater prevalence for ice edges. After the mid- to late-1990s, small negative anomalies dominate all subpopulations for both seasons (Figure 6.8a. and b. – top graphs), suggesting a lower than average concentration of small floe sizes. Within the WH subpopulation, small floe size anomalies varied with a periodicity of 14 years during

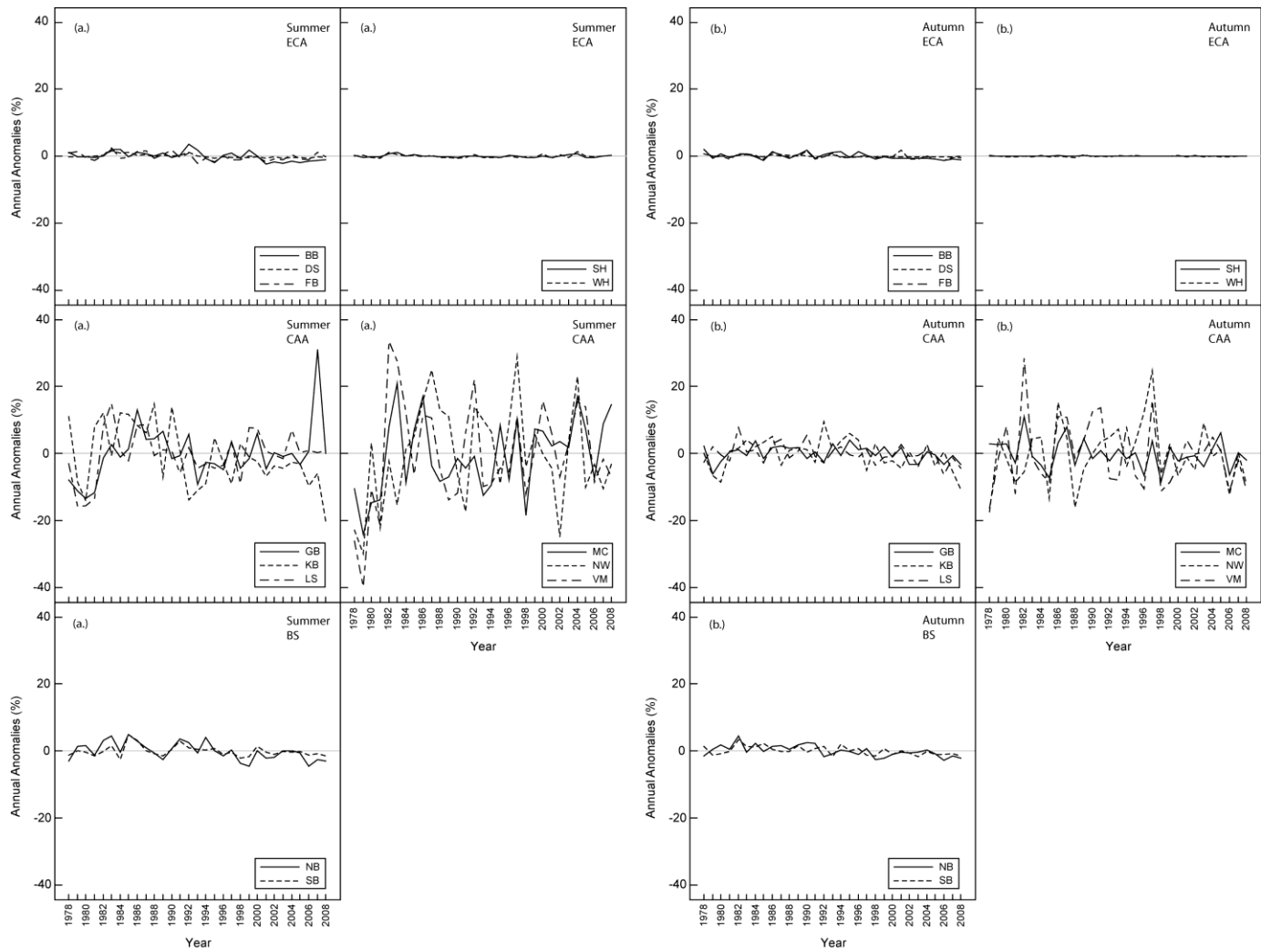


Figure 6.6: Summer (a) and autumn (b) fast sea ice anomalies calculated for the subpopulations within the Eastern Canadian Arctic (ECA) cluster (top), Canadian Arctic Archipelago (CAA) cluster (middle) and Beaufort Sea (BS) cluster (bottom).

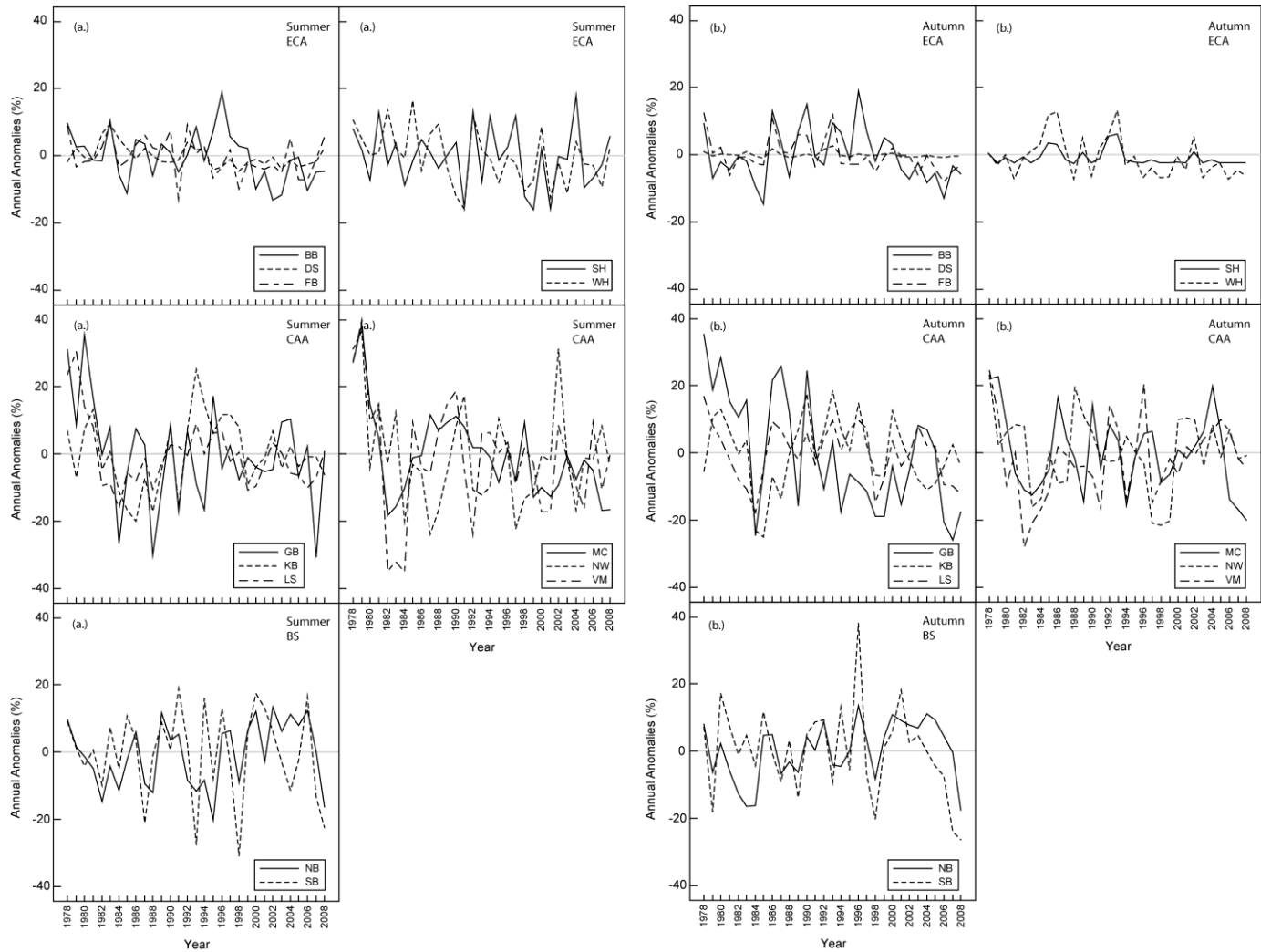


Figure 6.7: Summer (a) and autumn (b) large floe size anomalies calculated for the subpopulations within the Eastern Canadian Arctic (ECA) cluster (top), Canadian Arctic Archipelago (CAA) cluster (middle) and Beaufort Sea (BS) cluster (bottom).

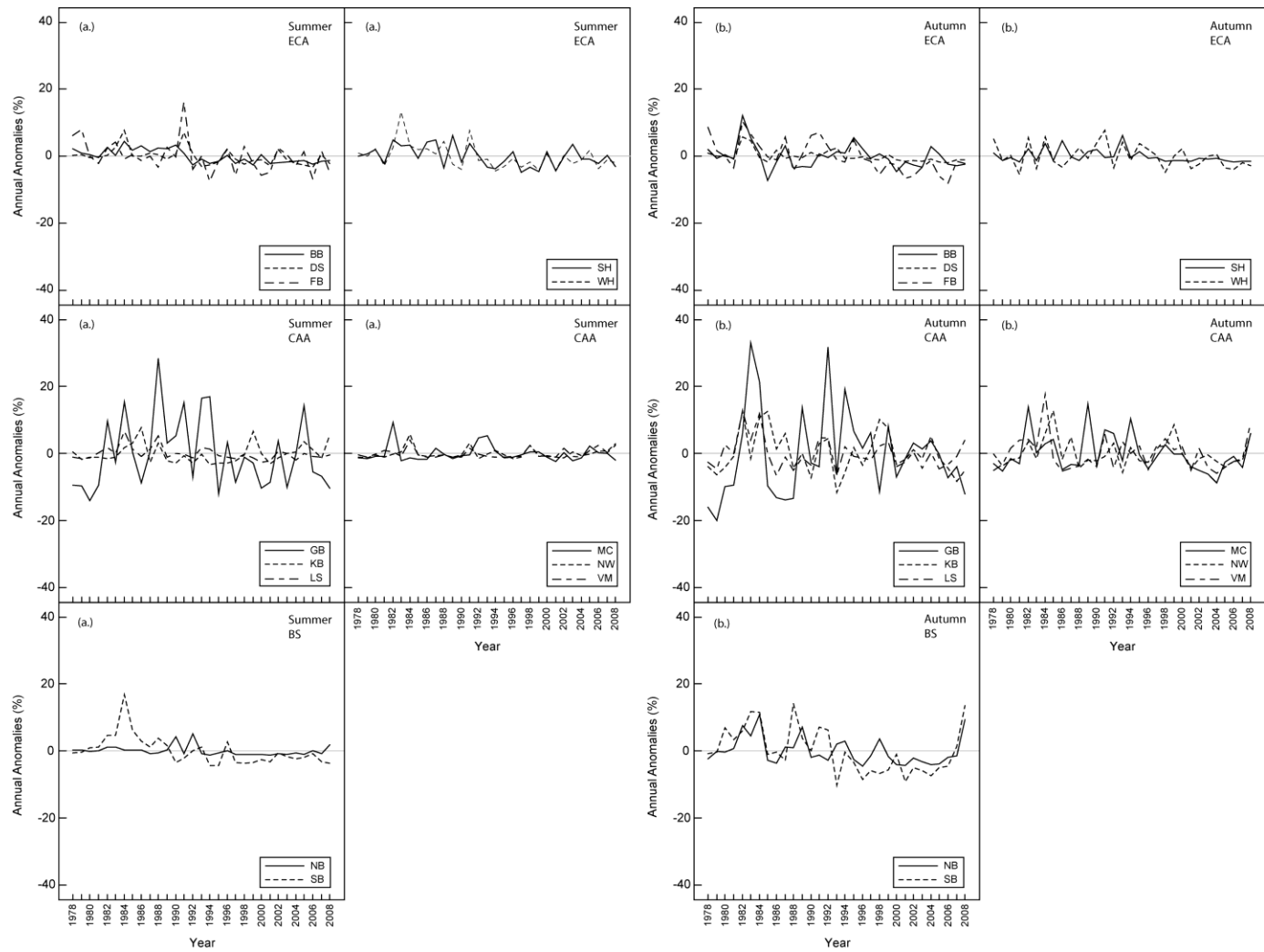


Figure 6.8: Summer (a) and autumn (b) small floe size anomalies calculated for the subpopulations within the Eastern Canadian Arctic (ECA) cluster (top), Canadian Arctic Archipelago (CAA) cluster (middle) and Beaufort Sea (BS) cluster (bottom).

the autumn season, while a much lower cycle is evident for the BB subpopulation (Table 6.3).

6.2.2 Canadian Arctic Archipelago (CAA) cluster

As with the Eastern Canadian Arctic cluster, spatial and temporal trends in open water anomalies are evident during the study period for the subpopulations within the Canadian Arctic Archipelago (CAA) cluster. In both summer and autumn, positive trends in open water anomalies occur for GB, LS and MC subpopulations over the 31-year study period (Figure 6.3). These trends suggest an increase in open water between 13% per decade and 22% per decade in the summer, and an increase between 11% per decade and 30% per decade in the autumn (Table 6.2). Similar trends are not evident for the KB, NW and VM subpopulations. This result may be due to the fact that the NW and KB subpopulations are smaller areas close to the Arctic Ocean, while the Beaufort Sea may influence the ice movement into and hence the open water concentration within the VM subpopulation.

Shorter temporal patterns exist in the open water anomalies for the KB, NW and VM subpopulations. In summer, lower open water concentrations (i.e. negative anomalies) generally occur during the first half of the sampling period, after which positive anomalies dominate the pattern (Figure 6.3a. and b. – middle graphs). The timing of this reversal occurs between 1994 and 1995 for the NW and VM subpopulations in both summer and autumn. The timing of the change from negative to positive anomalies within these subpopulations is similar to patterns

found within the Arctic Sea region (Lindsay and Zhang, 2005). For KB, the timing of this reversal in anomalies is later, occurring in 1999 (summer) and 2000 (autumn) (Figure 6.3 a. and b.). During summer, spectral analysis suggests a 5 to 7 year periodicity in the open water anomalies for most subpopulations within this cluster, while the periodicity in autumn exhibits a greater range between 2 and 6 years (Table 6.3). This suggests that the open water anomalies exhibit larger temporal cycles in the summer season, compared to the winter season within this cluster.

Statistically significant trends in summer and autumn MYI anomalies only occur within the GB and MC subpopulations (Table 6.2). The slope of the trends suggest a relatively large decrease in MYI within these two zones, approximately 20% per decade for MC in both seasons and 40% per decade for GB in both seasons (Table 6.2). On a shorter time-scale, large negative anomalies tend to dominate the KB, LS, NW and VM subpopulations in the mid- to late-1980s, as well as in the late-1990s and early 2000s for both seasons (Figure 4a. and b. – middle graphs). Another interesting result is that these subpopulations exhibit large interannual variability in the MYI anomalies, with deviations from the 31-year average in excess of 20% (Figure 4a. and b. – middle graphs). The timing of this pattern is consistent with the timing of positive anomalies in the BB subpopulation (ECA cluster), suggesting the occurrence of large-scale factor(s) that would control these patterns. Spectral analysis suggests similar periodicity of 2 to 5 years in summer and autumn MYI anomalies within these subpopulations (Table 6.3).

A positive trend in summer FYI anomalies is evident for the GB subpopulation, suggesting an overall increase of approximately 8% per decade over the 31-year study period (Table 6.2). Opposite trends in FYI anomalies are estimated for the KB subpopulation (Table 6.2). It is unclear why these two subpopulations exhibit opposite trends in FYI anomalies. It may be due to their location; GB located in the southern part of the cluster, while KB is close to the Arctic Ocean in the northern part of the cluster. A possible explanation is that due to a trend towards less FYI in both the BB and DS subpopulations (located to the south of KB subpopulation; Table 6.2), more FYI may be moving from the KB subpopulation and melting further south, resulting in the observed negative trend. As with the other sea ice characteristics, temporal patterns in summer FYI anomalies for the other subpopulations are evident at scales less than the 31-year study period. For the LS, MC, NW and VM subpopulations, positive anomalies dominate during the early and mid-1980s, followed by negative anomalies during the late-1980s to mid-1990s and again a predominance of positive anomalies during the second part of the study period (Figure 6.5a. – middle graph). During autumn, there is considerable interannual variability for the subpopulations (except KB) within the CAA cluster, and thus no pattern in these anomalies (Figure 6.5b. – middle graph). For each of the subpopulations, FYI anomalies exhibit temporal cycles at scales ranging from 2 to 7 years in the summer and 3 to 9 years in the autumn season (Table 6.3).

Similar to the FYI anomalies, the KB and MC subpopulations exhibit opposite trends in fast ice anomalies during the summer season (Table 6.2). Fast ice concentration within the KB subpopulation decreased by 16% per decade, while the

concentration of fast ice within the MC subpopulation increased by 15% per decade over the 31-year study period (Table 6.2). No statistically significant trends are evident for any subpopulations during the autumn season. During summer and autumn, positive anomalies in fast sea ice are observed for the LS subpopulation from the mid-1980s to the mid-1990s followed by negative anomalies for the remainder of the sampling period (Figure 6.6a. – middle graph). Significant interannual variability in fast ice anomalies are present for the NW and VM subpopulations, with no clear trends in summer or autumn fast ice concentration over the study period (Figure 6.6b. – middle graph). Spatial variability is also evident in the periodicity or ‘seasonality’ in the fast ice anomalies. The periodicity in the fast ice anomalies for the LS, MC, NW and VM subpopulations were greater during the autumn season compared to the summer season (Table 6.3). It is unclear why this seasonal variability occurs with regards to the periodicity in fast ice anomalies. For the other two subpopulations, the fast ice anomalies exhibit a temporal cycle at scales of 2 to 3 years; however this is only statistically significant for the summer season (Table 6.3).

Spatial variability also exists in the overall trends with regards to large floe anomalies. The MC and LS subpopulations exhibit a negative trend in summer large floe anomalies, while a similar trend is evident within the GB subpopulation during the autumn season. In summer, the large floe sizes decrease by 13% per decade (LS) and 25% per decade (MC; Table 6.2). In autumn, a significantly greater decrease in large floe sizes occurs within the GB subpopulation (Table 6.2). For the remaining subpopulations, large positive anomalies dominate the early part of the sampling

period, followed by negative anomalies in the early 1980s to early 1990s and again in the late 1990s through to 2000s, (Figure 6.7a. – middle graph). This pattern occurs for the summer season in the various subpopulations (excluding NW). Large interannual variability dominates the large floe size anomalies within the NW subpopulation during that season (Figure 6.7a. – middle graph). During autumn, the positive anomalies dominate the KB and LS subpopulations for the first part of the study period, followed by negative anomalies (Figure 6.7b. – middle graph). No clear trends in the autumn large floe size anomalies were evident for the remaining subpopulation, with large interannual variability thorough the study period (Figure 6.7b. – middle graph). In addition, spectral analysis suggests that for both seasons, the large floe anomalies exhibit a periodicity of between 2 and 5 years.

No subpopulation within this cluster exhibits a statistically significant trend in small floe size anomalies over the 31-year study period. An examination at a shorter scale suggests some temporal patterns in the anomalies for this ice floe class. The pattern in summer and autumn anomalies within the KB and LS subpopulations show similar patterns to those for the ECA cluster. Positive anomalies dominate the 1980s, followed by negative anomalies during the 1990s and early 2000s (Figure 6.8a. and b. – middle graph). Within the GB subpopulation, the anomalies (both positive and negative) were larger compared to the KB and LS zones (Figure 6.8a. and b. – middle graphs), suggesting greater yearly differences in the small floe size concentration compared to the 31-year average. This result, coupled with the anomalies for the other ice characteristics, suggest that significant interannual variability exists within the GB subpopulation, and therefore the lack of any

temporal pattern in any of the ice characteristics studied. Within the other three subpopulations, no patterns in the summer small floe size anomalies were observed over the 31-year period (Figure 6.8a. – middle graph). During autumn, the small floe size anomalies tended to be positive in the 1980s and negative after 1996 within the MC, NW and VM subpopulations (Figure 6.8b. – middle graph). No clear patterns in the autumn anomalies are evident for the other subpopulations. Spectral analysis suggests that small floe anomalies exhibit similar temporal patterns for either season, with periodicities of between 4 and 5 years in the summer and between 2 and 3 years in the autumn (Table 6.3). The exception is the MC subpopulation which had a periodicity of 13 years for the autumn anomalies (Table 6.3).

6.2.3 Beaufort Sea (BS) cluster

As opposed to the other clusters, the subpopulations within the Beaufort Sea (BS) cluster do not exhibit a temporal trend in the summer open water anomalies (Table 6.2). A statistically significant trend in autumn open water anomalies is only evident for the SB subpopulation, with a 27% per decade increase over the sampling period (Table 6.2). The summer (both subpopulations) and autumn (NB subpopulation only) open water anomalies within this cluster exhibit greater interannual variability, with anomalies greater than 20% occurring frequently throughout the sampling period (Figure 6.3a. – bottom graphs). The open water anomalies exhibit a periodicity of 2 years (summer) and 6 years (autumn) for the NB subpopulation, while a 6-year periodicity in anomalies occurs only during the summer season for the SB subpopulation (Table 6.3).

Over the 31-year study period, the analysis of the anomalies for summer and autumn suggests that there is no overall trend in MYI anomalies within the NB and SB subpopulations (Table 6.2). In summer, negative anomalies dominate the mid- to late-1980s and mid-1990s, with a prevalence of positive anomalies from the late 1980s to early 1990s and during the 2000s (Figure 6.4a. – bottom graph). The periodicity in these anomalies is between 2 and 6 years (Table 6.3), consistent with the periodicity in the other clusters. During autumn, positive anomalies tend to dominate the SB subpopulation from 1980 to the mid-1990s, followed by negative anomalies until 2008 (Figure 6.4b. – bottom graph). The pattern in autumn anomalies for the NB subpopulation resembles the summer pattern for the same subpopulation (Figure 6.4b. – bottom graph).

FYI anomalies within this cluster exhibit a general decreasing trend for the summer period, while no trend is evident in the anomalies for this ice type during the autumn period (Table 6.2). Over the 31-year study period, summer FYI decreased by 20% per decade for the NB subpopulation and 11% per decade for the SB subpopulation (Table 6.2). Temporal patterns over short time scales are evident for this cluster. During autumn, the FYI anomalies are generally positive during the early to mid-1980s, followed by negative anomalies from the late 1980s to mid- or late 1990s, and concluding with generally positive anomalies (Figure 6.5b. – bottom graph). A periodicity of 2 years was estimated for the FYI anomalies within both subpopulations (Table 6.3).

Anomalies in fast ice generally decreased over the study period for the NB (both

seasons) and SB (only autumn) subpopulations (Table 6.2). In summer, a 4% per decade reduction is estimated for the NB subpopulation, while similar reductions occur in the autumn for NB and SB subpopulations (Table 6.2). In summer, the anomalies for SB subpopulation suggest that fast ice concentration was slightly greater than the 31-year norm in the late-1970s until the mid-1990s (Figure 6.6a. and b. - bottom graphs). After this period, negative anomalies tend to dominate, however these anomalies were small. No significant periodicities in fast ice anomalies were found within these subpopulations (Table 6.3). This suggests that over the study period, the anomalies in this ice characteristic were random.

No significant trends in large floe size anomalies are evident for either subpopulation in both summer and autumn (Table 6.2). Large interannual variability is evident in both seasons for the SB subpopulation, with no shorter-term pattern in anomalies (Figure 6.7a. and b. – bottom graphs). One interesting point is that the variability for both seasons is greater in the mid- to late 1990s compared to any other time period. This result suggests increased variability in floe size occurrence within this subpopulation. Within the NB subpopulation, negative anomalies dominate the early half of the sampling period for both seasons, followed by a predominance of positive anomalies (Figure 6.7a. and b. – bottom graphs). Large floe size anomalies illustrate a longer temporal periodicity in the SB subpopulation, compared to the NB subpopulation for both seasons (Table 6.3).

Trend analysis of small floe size anomalies suggests spatial differences within this cluster. For the SB subpopulation, the analysis suggests a negative trend in the

small floe size anomalies over the 31-year study period for both summer and autumn (Table 6.2). Results indicate that the anomalies decreased by 8% per decade and 10% per decade in summer and autumn, respectively (Table 6.2). Similar trends were not observed for the NB subpopulation, with no trends evident for the two seasons (Table 6.2). As with fast ice anomalies, the summer anomalies in small floe size within the NB and SB subpopulations were relatively small throughout the 31-year study period (Figure 6.8a. – bottom graph). During both seasons, the NB subpopulation had a greater occurrence of positive anomalies (and thus greater than the 31-year average) prior to the early 1990s (Figure 6.8b – bottom graph). After this period, the concentration of small floe sizes decreased to values less than the 31-year average. The small floe size anomalies exhibit a 15 year (summer) and 6 year (autumn) periodicity in the NB subpopulation (Table 6.3), suggesting that the anomalies are correlated over longer time periods in the summer season within this area. No statistically significant periodicities were found for the SB subpopulation.

6.3 Dynamic and thermodynamic forcing

Open water anomalies in numerous subpopulations are positively correlated with the anomalies in NCEP modeled temperature for both seasons (Figure 6.9). Lindsay and Zhang (2005) also note similar sensitivity of open water to thermodynamic factors. The association between these variables however is not evident in all of the subpopulations. For instance, statistically significant correlations were not observed for the DS, KB and BB subpopulations in one or both

seasons (Figure 6.9). The AO index is negatively associated with the open water trends in SB (both seasons) and KB and VM (autumn only; Figure 6.9). For the autumn season, the associations suggest a lag of one season (SB and VM) or a lag from the previous winter (KB). With regards to KB, BB and DS subpopulations, the duration of the North Water polynya and the winds within this area may have a greater control on open water concentration than thermodynamic influences. For instance, in years when the North Water polynya bridge was present later into the summer season (Barber *et al.*, 2001; Mundy and Barber, 2001), less sea ice and thus greater open water would be present in the BB subpopulation.

Thermodynamically, the trends in MYI anomalies within various subpopulations within the CAA and BS clusters are statistically negatively correlated with temperature trends in summer and/or autumn (Figure 6.10). The observed trends in MYI anomalies are also associated with the timing of the AO index. Positive associations are observed with the summer anomalies, while negative associations occur in the autumn (Figure 6.10). The AO index results in a cyclonic pattern in the wind velocity within the Arctic region between 1989 and 1995 (Zhang *et al.*, 2000). This pattern causes greater ice being advected into the Archipelago (Rigor *et al.*, 2002) and thus influencing the formation of the positive anomalies in MYI during the late 1980s to late 1990s. The timing of negative MYI anomalies within the subpopulations in close proximity to the Beaufort Sea is also concurrent with the fall reversal in the Beaufort Gyre (Proshutinsky *et al.*, 2002; Zhang *et al.*, 2004; Lukovich and Barber, 2006). The reversal in the gyre would lead to MYI being pushed out of the area (Lukovich and Barber, 2006), and thus resulting in lower than normal (or

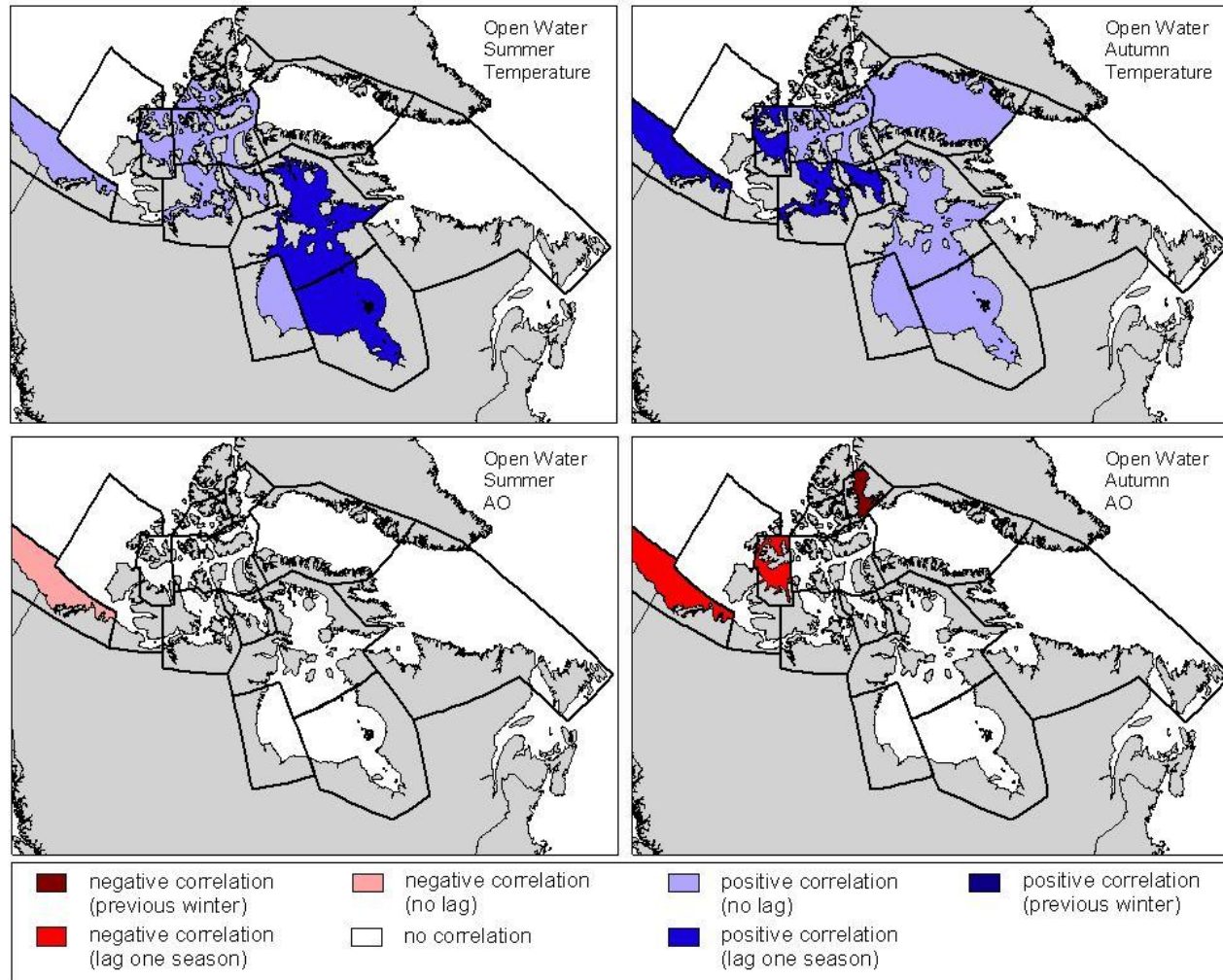


Figure 6.9: Correlation between open water anomalies and temperature anomalies calculated from NCEP (National Centres for Environmental Prediction) data (top graphs) or AO (Arctic Oscillation) seasonal averages (bottom graphs). Statistically significant correlations ($p < 0.05$) are shown for the individual polar bear subpopulations. Negative (positive) correlations are shown in red (blue).

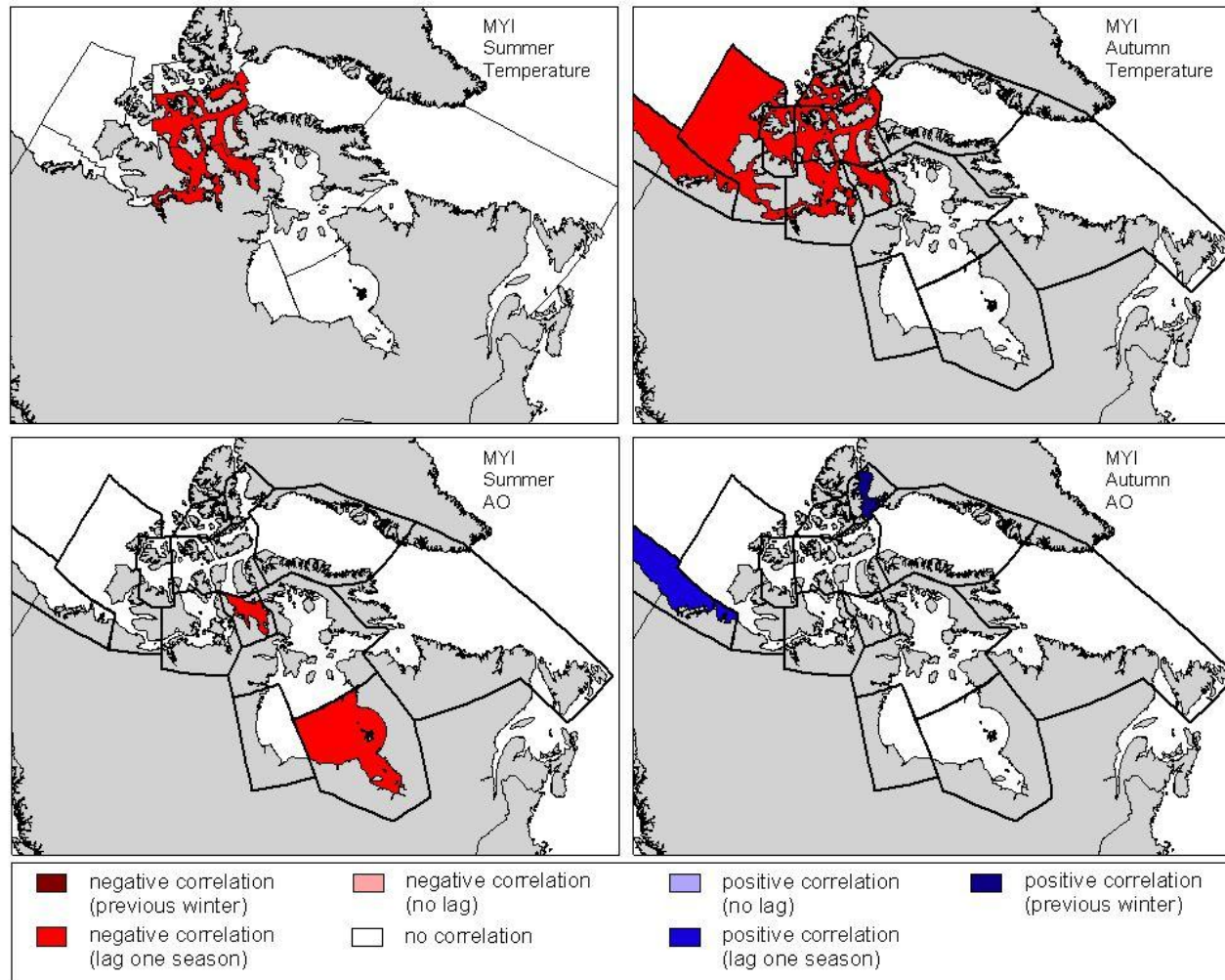


Figure 6.10: Correlation between multiyear sea ice anomalies and temperature anomalies calculated from NCEP (National Centres for Environmental Prediction) data (top graphs) or AO (Arctic Oscillation) seasonal averages (bottom graphs). Statistically significant correlations ($p < 0.05$) are shown for the individual polar bear subpopulations. Negative (positive) correlations are shown in red (blue).

31-year average) concentration in this ice type.

The trends in FYI anomalies for numerous subpopulations within the three clusters are negatively correlated with temperature anomalies (Figure 6.11). For FB and SH, the summer correlations indicate a lag, suggesting that the summer anomalies are correlated with the temperature of the spring season. The lack of any significant correlations for the other subpopulations may be due to the fact that sea ice motion plays a more important role in the concentration of FYI. The FYI anomalies for the ECA cluster are not associated with the AO index, while summer FYI anomalies in the GB and MC subpopulations, as well as the subpopulations within the BS cluster are positively associated with AO index (Figure 6.11). The Beaufort Gyre may also be a dynamic factor influencing the FYI anomalies. The reversal of the Gyre to anticyclonic circulation between 1990 and 1996 would result in greater MYI and thus less FYI present in some subpopulations.

Summer and autumn fast ice anomalies are negatively correlated with modeled temperature anomalies for numerous subpopulations within the three clusters (Figure 6.12). The associations vary between subpopulations. For instance, in the NB, WH and FB subpopulations, the summer fast ice anomalies are correlated with the summer temperature anomalies, while for the SH and VM subpopulations, the fast ice anomalies are correlated with the spring temperature anomalies (Figure 6.12). The lack of significant correlations during the autumn season for the subpopulations in the ECA cluster is probably due to the low concentration of fast ice during the study period. In summer, only fast ice anomalies within the GB

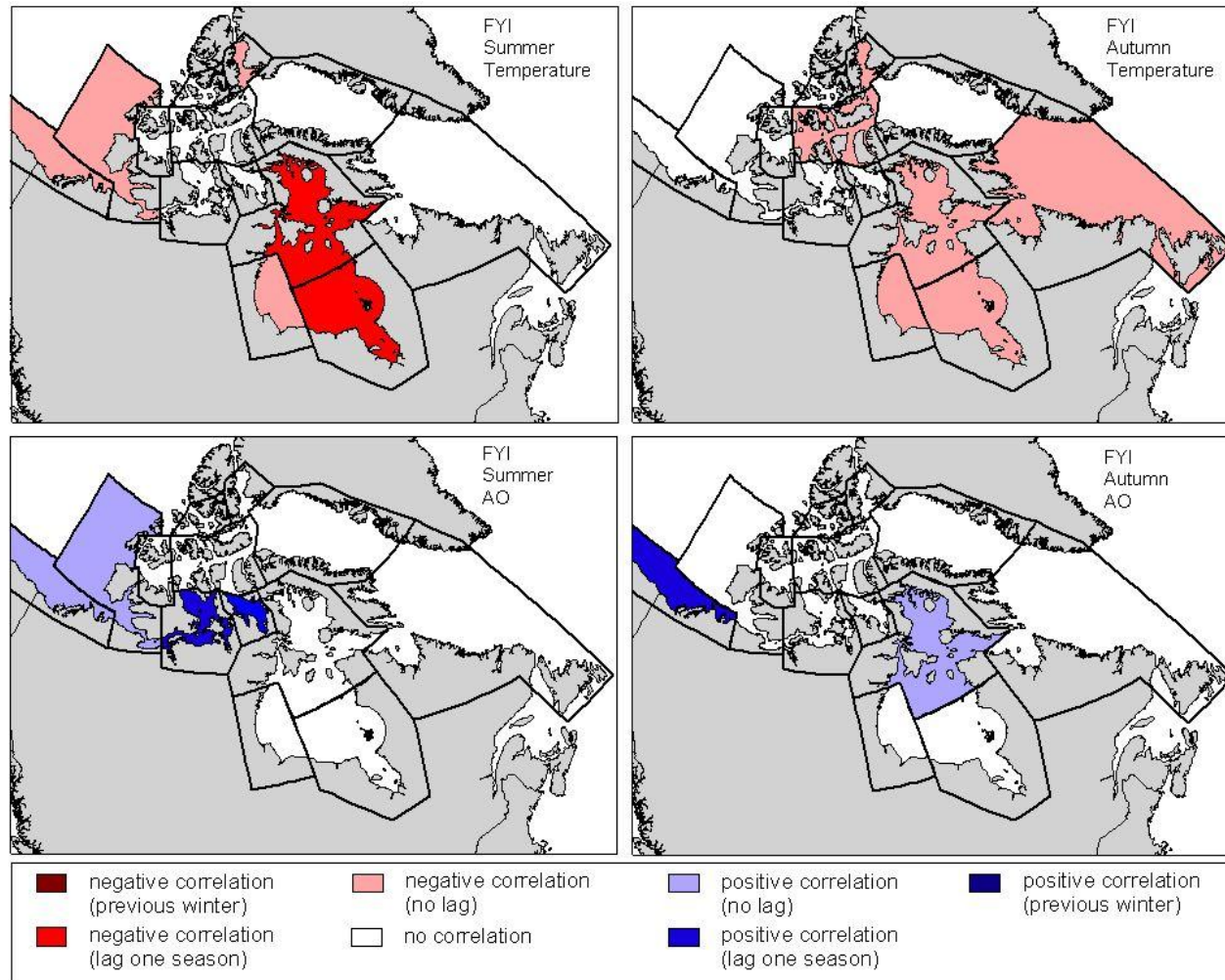


Figure 6.11: Correlation between first-year sea ice anomalies and temperature anomalies calculated from NCEP (National Centres for Environmental Prediction) data (top graphs) or AO (Arctic Oscillation) seasonal averages (bottom graphs). The correlations are shown for the individual polar bear subpopulations. Negative (positive) correlations are shown in red (blue).

subpopulation is correlated with AO index. This correlation is positive with a lag of one season (Figure 6.12), suggesting that the summer fast ice anomalies are associated with the spring AO index. For the autumn season, the statistical correlations are positive, however some subpopulations are correlated with a lag of one season (i.e. SB and KB) or correlated with the AO index of the previous winter season (i.e. WH; Figure 6.12). There is no clear spatial pattern in the correlations of this ice characteristic with the AO index.

The summer anomalies in large floe sizes within parts of the ECA and CAA clusters are correlated with the modeled temperature anomalies either for the summer season or for the previous season (Figure 6.13). The lag of one month for SH and no lag for WH is evident in the summer season is consistent with the results for the other sea ice characteristics (except for MYI). During the autumn season, spatial pattern in the association with temperature anomalies seems to exist. For the subpopulations with the CAA and BS clusters, the statistically significant correlations suggest that the autumn large floe size anomalies are associated with the summer temperature anomalies (Figure 6.13). Increased temperatures in the summer may weaken the sea ice, causing earlier breakup, increased mobility of the ice, and a reduction in the concentration of large floes. The statistically significant correlations for the subpopulations within the ECA clusters suggest that the autumn large floe size anomalies are associated with the autumn temperature anomalies (Figure 6.13). The anomalies for this floe size within the SB (both seasons) and KB zones (autumn only) are also significantly correlated (positive) with the AO index (Figure 6.13). However similar results are not found for the other subpopulations.

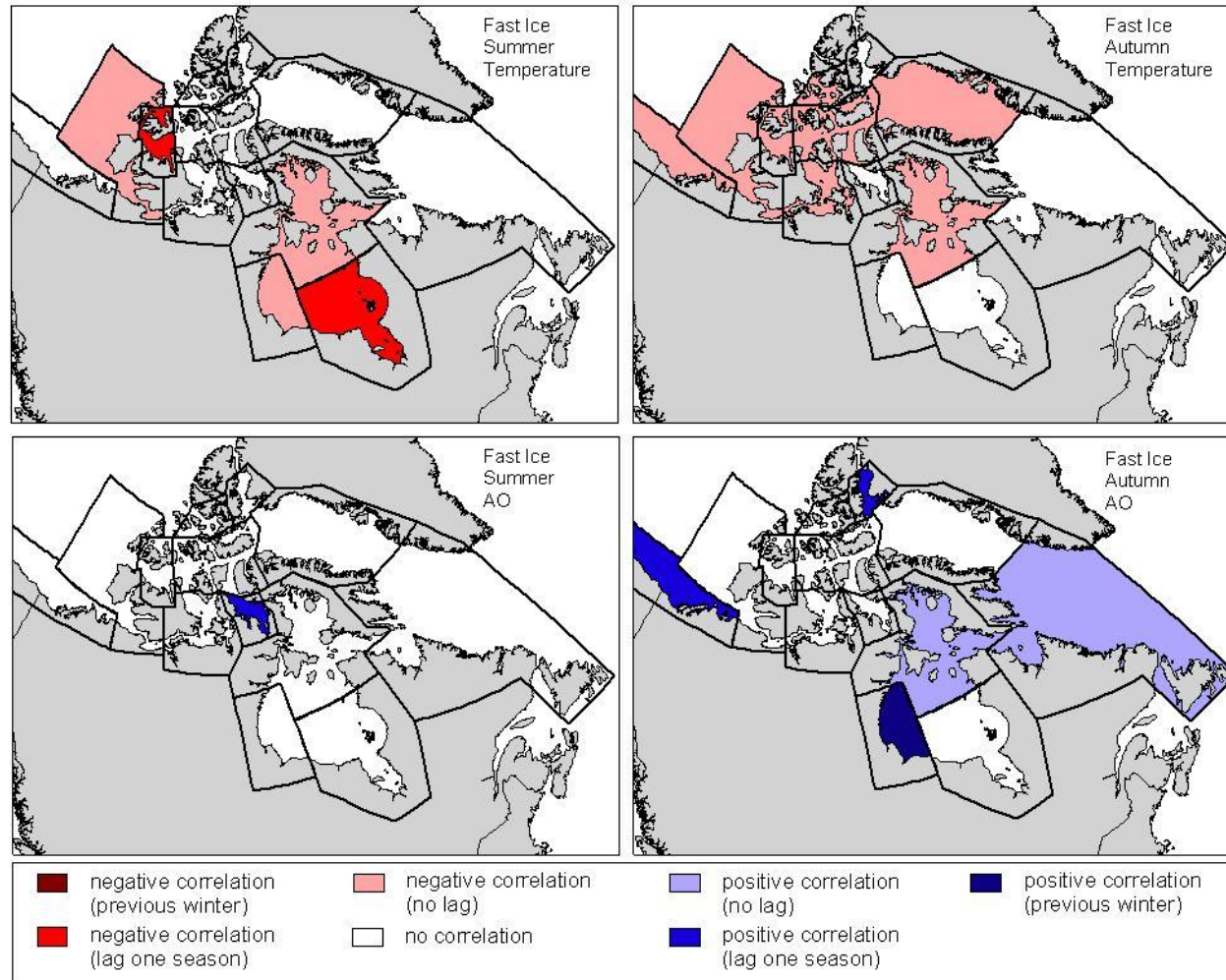


Figure 6.12: Correlation between fast sea ice anomalies and temperature anomalies calculated from NCEP (National Centres for Environmental Prediction) data (top graphs) or AO (Arctic Oscillation) seasonal averages (bottom graphs). Statistically significant correlations ($p < 0.05$) are shown for the individual polar bear subpopulations. Negative (positive) correlations are shown in red (blue).

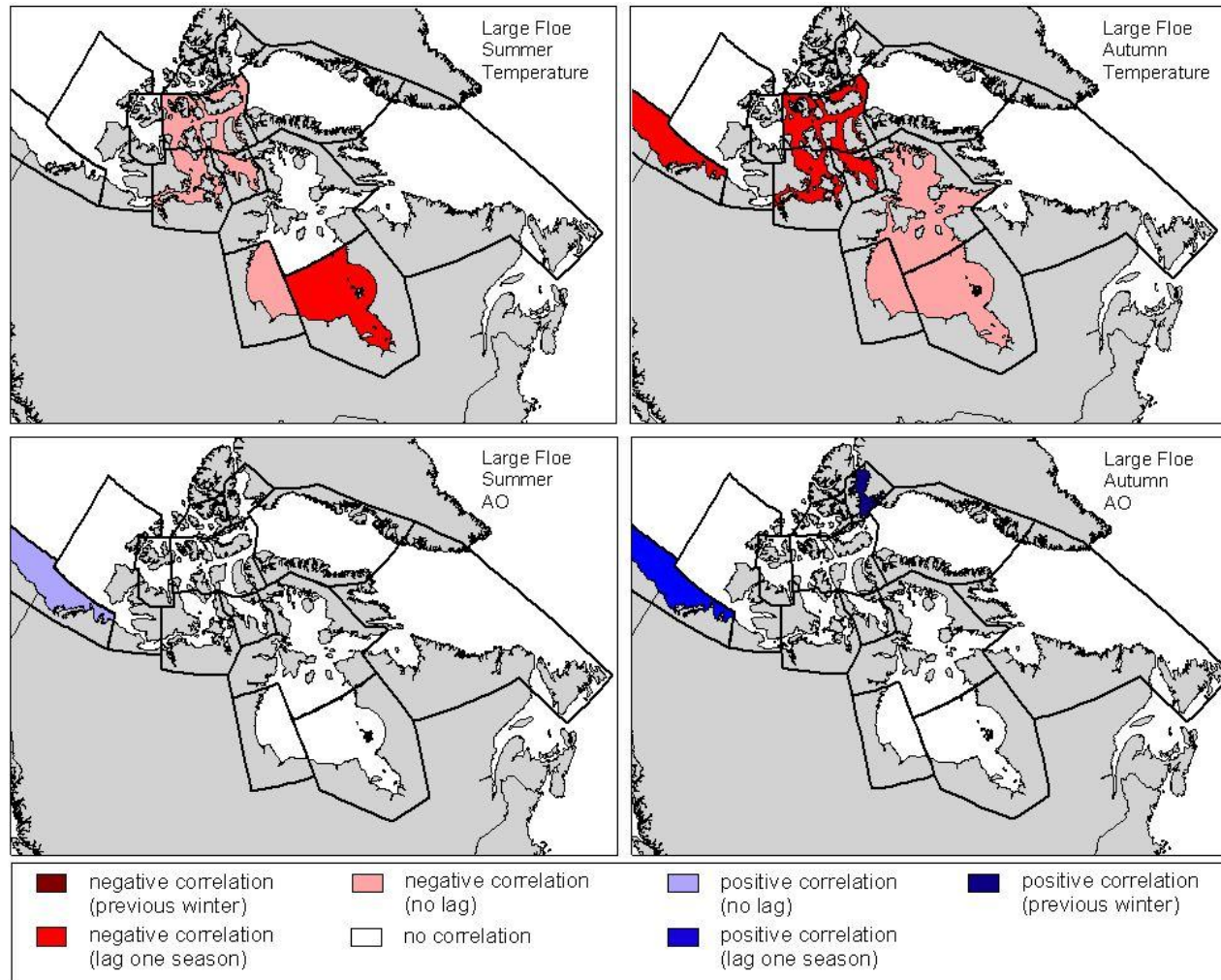


Figure 6.13: Correlation between large floe size anomalies and temperature anomalies calculated from NCEP (National Centres for Environmental Prediction) data (top graphs) or AO (Arctic Oscillation) seasonal averages (bottom graphs). Statistically significant correlations ($p < 0.05$) are shown for the individual polar bear subpopulations. Negative (positive) correlations are shown in red (blue).

Results for the third floe size class (small floe) indicate negative correlations in VM and NW subpopulations for the summer period (Figure 6.14). During the autumn season, positive associations occur between the anomalies for this floe size class and temperature for the SH and FB subpopulations (Figure 6.14). Only one subpopulation exhibits a statistically significant correlation with AO index (GB subpopulation; Figure 6.14).

The generally weak results between the dynamic factor (i.e. AO index) and the various sea ice characteristic anomalies for the majority of subpopulations suggest that other dynamic factors may also play a role in the trends. For instance, the floe size distribution within the BB and DS subpopulations may be related to the amount of ice advected through these zones from the Archipelago and Arctic Basin. As well, small temporal scales may play a significant role in the occurrence of the anomalies. For instance, the positive open water anomalies in NW subpopulation in the mid-1990s may be a result of the strong positive AO index (Figure 6.2) and a weaker Beaufort high-pressure system during the same period (Zhang *et al.*, 2000), which causes thinner sea ice to be pushed into the Beaufort Sea region, and thus earlier breakup and greater open water concentrations within most subpopulations. The negative AO index (Figure 6.2) and anti-cyclonic circulation in the Beaufort Sea during the 1980s may cause the ice to move into the Beaufort Sea and causing relatively weak ice to breakup into small floes, thus explaining the positive anomalies in this floe size during the same period within the BS and CAA clusters (Figure 6.8).

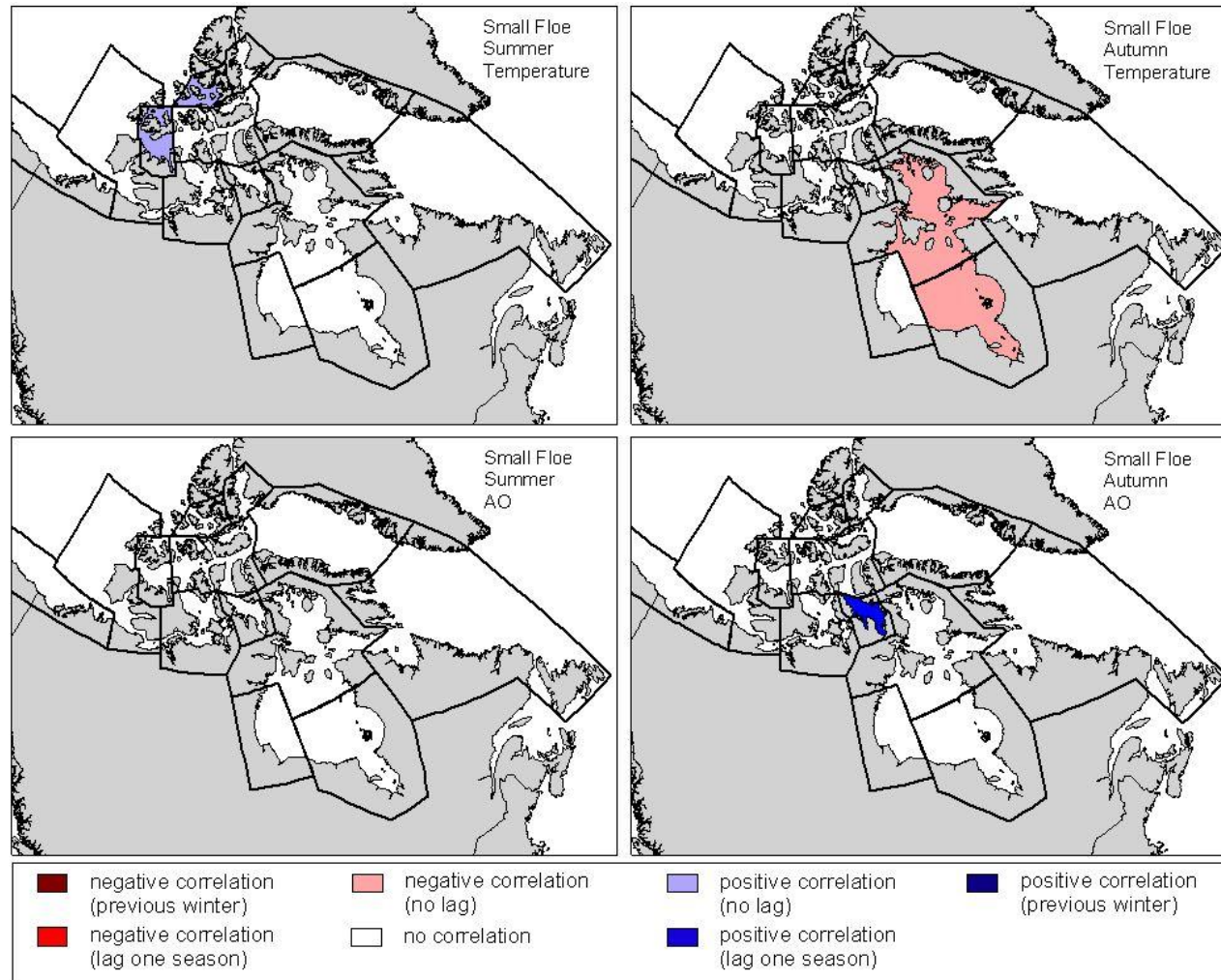


Figure 6.14: Correlation between small floe size anomalies and temperature anomalies calculated from NCEP (National Centres for Environmental Prediction) data (top graphs) or AO (Arctic Oscillation) seasonal averages (bottom graphs). Statistically significant correlations ($p < 0.05$) are shown for the individual polar bear subpopulations. Negative (positive) correlations are shown in red (blue).

6.4 Trends in polar bear condition related to sea ice trends

Changes in polar bear condition and survival within the WH and SH subpopulations correspond to the observed trends in sea ice characteristics. Regehr *et al.* (2007) and Stirling *et al.* (1999) found that in the WH population, the survival and condition of polar bears were generally higher in the 1980s compared to the late 1990s and 2000s. Research has also suggested that similar trends in polar bear condition have occurred in the SH subpopulation, with average body conditions significantly poorer in 2000-2005 compared to 1984-1986 (Obbard *et al.*, 2006; 2007). As described above, these subpopulations experienced a decrease in ice concentration (positive open water anomalies and negative FYI anomalies) in the late 1990s and 2000s, resulting in a decrease in the availability of sea ice and thus recruitment and reproductive rates of prey during the summer and autumn seasons (Ferguson *et al.*, 2005; Stirling, 2005). Similar relationship between sea ice condition and polar bear and ringed seal population has been found for other areas of the Arctic region (i.e. Rosing-Asvid, 2006). In addition, the temporal variability in large floe size anomalies may vary the concentration of traditional prey species (i.e. ringed seals) thus impacting habitat availability and potentially resulting in greater energy expenditure to locate preferred habitat. This may have also contributed to the poorer condition of polar bears in the late 1990s and 2000s within the WH and SH subpopulations.

Polar bear condition and survival has not been quantified for the other subpopulations within the ECA cluster. Assuming a similar relationship between polar bear condition and sea ice characteristics, it may be anticipated that polar

bears within these subpopulations may be experiencing similar reduction in condition since the ice conditions (FYI and large floe size concentration) have been decreasing below the 31-year average. In summer (autumn), polar bears within these subpopulations select large (small) floe sizes (Ferguson *et al.*, 2000), and the observed reduction in the concentration of this floe size during this period may have a negative impact on the condition of polar bears. However, polar bears are able to adapt their feeding from traditional ringed seals to available prey such as harp seals (Thiemann *et al.*, 2008). Therefore bears in this cluster may be able to adapt to changes in environmental conditions by varying their choice of prey, suggesting a lower association of population changes with ice characteristics variability.

The FYI anomalies, along with the trends in the open water anomalies correspond to a reduction in survival and breeding of polar bears and cub of the year (COY) litter survival in the SB subpopulation during the 2000s reported by Regehr *et al.* (2007; 2010). Polar bear population estimates within the SB subpopulation increased from the mid-1980s into the 1990s and then decreased in the 2000s (Amstrup *et al.*, 1986; Regehr *et al.*, 2006; Hunter *et al.*, 2007; Rode *et al.*, 2007). During this period, anomaly trends indicate that open water was lower, while FYI coverage was greater during the mid-1980s to mid-1990s, compared to the 31-year average. This would result in a potential increase in the prey population, as well as greater access to the prey. MYI is typically not favorable habitat due to the low concentrations of prey. During the 1980s to 1990s, the concentration of MYI was lower than the 31-year average, decreasing the favorable habitat for polar bears in the SB and NB subpopulations and thus reducing the denning of polar bears on

the sea ice in the Beaufort Sea (Fischbach *et al.*, 2007). Between 1979 and 2005, polar bear sightings within the SB subpopulation suggest an eastward and landward shift in location (Gleason and Rode, 2009), related to changes in sea ice conditions during the same period.

6.5 Conclusion

This research has investigated the spatial and temporal trends in various sea ice characteristics (including open water, ice type and floe size) within the polar bear subpopulations in the Canadian Arctic. The second objective was to examine how these changes were affected by temperature anomalies and large-scale atmospheric and oceanic circulation. In addition, the published changes in polar bear population and condition within the various clusters were discussed in context with these changes in sea ice condition.

Trend analysis of the sea ice characteristics for the three clusters illustrates significant temporal and spatial patterns. For example, most subpopulations in the Eastern Canadian Arctic cluster experienced negative trends in open water, FYI and small floe sizes. On the other hand, there was greater spatial and interannual variability in the fast and large ice floe size characteristics, with a few subpopulations experiencing a significant trend. Greater spatial variability in the trends in sea ice characteristics was evident for the CAA cluster. Only three of the six subpopulations within this cluster exhibit significant trends in open water, ice type and ice floe classes over the 31-year study period for both seasons. For the BS

cluster, seasonal and spatial variability occurred for the ice type and ice floe size classes, with no significant trends for large floe sizes, and at least one subpopulation exhibiting a significant trend in either season for the other floe size classes. This spatial variability in the rate of change for the ice characteristics indicates that some subpopulations may become more suitable for polar bear habitat and may provide refuges.

Possible thermodynamic and dynamic factors that may explain the spatial and temporal patterns in the sea ice characteristics were also investigated. Air temperature was used to represent the thermodynamic factors, while the Arctic Oscillation (AO) represented the dynamic processes. Results suggest that the trends in open water for the ECA and CAA cluster are thermodynamically driven, with statistically significant correlations between air temperature and open water anomalies. For the BS cluster, the open water anomalies are most likely associated with large-scale atmospheric and oceanic circulation. The trends in FYI anomalies are probably due to a combination of both thermodynamic and dynamic forcing. For instance, cooler temperatures and calm wind conditions would result in earlier freeze-up and thus more FYI, compared to time periods with warmer temperatures and/or stronger winds. As with the ice type, the trends in the ice floe anomalies are related to both thermodynamic and dynamic factors, and are specific to the subpopulation. For instance, the trend in fast ice anomalies with the NB subpopulation is associated with the temperature anomalies over the study period, however a statistical association is observed between fast ice and AO in the SB subpopulation.

One limitation of this study is that only one thermodynamic and dynamic factor were included in the examination of the potential factors contributing to the observed trends in sea ice characteristics. Other atmospheric factors such as wind speed and direction and ocean circulation may partially contribute to the trends in a number of sea ice characteristics, however these variables are not routinely collected over the sea ice for the 31-year study period. In addition, these variables are not as accurately reproduced using spatial models for the Arctic region, thus limiting their application in this study. Land-based measurements of a number of thermodynamic and dynamic factors are routinely collected; however these measurements cannot be used to accurately estimate on-ice conditions (Iacozza and Barber, 2010).

Published changes in polar bear condition and survival within the Eastern Canadian Arctic and Beaufort Sea cluster were related to the trends in sea ice condition. Results suggest that the reduction in polar bear population and condition co-occur with the observed changes in the various sea ice characteristics. These associations are valid for the two clusters, however due to a lack of research on changes in polar bears within the CAA cluster, changes in sea ice conditions can only be used to speculate on the potential changes within these subpopulations. However not all populations may react similarly to changes in environmental conditions, and in some subpopulations within the CAA cluster, environmental changes may be 'improving' habitat for polar bears (i.e. changing MYI to FYI).

Polar bear habitat is also related to sea ice deformation and the associated snow distributions (Stirling *et al.*, 1993; Ferguson *et al.*, 2001). At present, sea ice deformation and snow evolution over sea ice are not adequately defined on a large scale. Future research will attempt to investigate methods to use remote sensing to acquire sea ice surface roughness and modeling of snow evolution over sea ice. These factors can then be used to further explain the observed changes in polar bear condition and population, as well as modeling potential future increases or decreases in polar bear habitat.

CHAPTER 7: CONCLUSION

7.1 Summary of results

An understanding of the spatial distribution and temporal evolution of snow on sea ice at different scales is essential for the improvement of snow parameterization in sea ice models and for a complete understanding of the physical-biological habitat relationships in the Arctic. In the first objective, the temporal evolution of snow over smooth land-fast first year sea ice was examined using both observational and modeled data. Changes in probability density functions indicate that depositional and drifting events control the evolution of snow distribution. Geostatistical analysis suggests that snowdrifts increased over the study period, and the orientation was related to the meteorological conditions. One of the problems we face however is that long-term climate data are not routinely collected over sea ice. Results using two land-based climate reporting stations (Paulatuk and Tuktoyuktuk, NWT) suggest that only on-ice air temperature and relative humidity can be estimated using air temperature recorded at either station. Other variables such as wind speed, direction and precipitation on ice cannot be accurately estimated. The temporal evolution of snow distribution over smooth land-fast sea ice was modeled using *SnowModel* and four different forcing regimes. The results from these model runs indicate a lack of agreement between observed distribution and model outputs.

The second objective of this dissertation was to examine the spatial pattern of snow distribution over rough sea ice and ridges and the relationship between the spatial patterns and ice roughness and meteorological conditions. Results from this

study indicate that the ice roughness accounts for less than 54% of the variability in snow depth, suggesting that the spatial pattern of ice roughness may be important in creating the snow distribution. The correlation lengths indicate that the average snowdrifts over the ridges varied between 8.0 m to 33.5 m. For rubble sites, the correlation lengths of snow ranged from 8.7 m to 22.4 m. The fractal dimensions estimated for rubble ice varied between 1.8 and 1.95 for the first five sites and between 1.58 and 1.89 for site 6. For ridges, the fractal dimension was greater than 1.7. The correlation length (fractal dimension) for snow is associated with the correlation length (fractal dimension) for ice roughness for rubble ice and ridges and direction. The evolution of the spatial pattern of snow depth was also examined by comparing the patterns in both correlation length and fractal dimension to meteorological conditions that occurred throughout the study period. Results suggest that wind direction during periods of snow deposition and/or blowing snow will impact the pattern in the spatial pattern of snow.

The next objective of this dissertation describes the methods to estimate land-fast snow-plus-sea ice surface roughness from Advanced Synthetic Aperture Radar (ASAR) images. Surface roughness data was obtained with a helicopter-borne electromagnetic induction system known as the 'IcePic'. Various image processing techniques were tested against ASAR images with different polarizations, incidence angles and orbital paths to determine the optimal parameters for estimating surface roughness. Results suggest that using a Gamma filter for speckle reduction on a cross-polarized (VH) image acquired for a larger incidence angle on a descending path is able to account for a significant amount of variability in surface roughness.

The optimal grey-level co-occurrence matrix texture measures are entropy (ENT) or angular second moment (ASM) calculated using a 15x15 window. Each texture measure is able to account for more than 88% of the variability in sampled surface roughness.

The final objective investigates the spatial and temporal trends in sea ice characteristics within the polar bear subpopulations in the Canadian Arctic and to relate the observed changes to dynamic and thermodynamic factors. The published changes in polar bear population and condition within the various subpopulations are also discussed in context with these trends in ice characteristics. Spatial and temporal variability in the trends for the sea ice characteristics from 1978 to 2008 occur in the various subpopulations within the three clusters. Thermodynamic (i.e. temperature) and dynamic (i.e. Arctic Oscillation index) factors are able to explain the anomalies for a limited number of sea ice characteristics within only a few subpopulations, suggesting the role of other factors in producing the seasonal trends. The trends in sea ice characteristics are related to previously published changes in polar bear condition and survival. Results suggest that the reduction in polar bear population and condition within two clusters (ECA and BS) co-occur with observed changes in the sea ice characteristics.

7.2 Climate change implications

7.2.1 Projected changes in sea ice and snow

A number of research studies have focused on recent changes and projections to Arctic precipitation and snowfall. Records indicate that since the 1950s precipitation in the Arctic region has increased (Groisman and Easterling, 1994; Georgiyevskii, 1998; Kattsov and Walsh, 2000). Models using climate change scenarios estimate that this trend in precipitation will continue due to an increase in air temperature (and associated increase in moisture holding capacity) and changes in storm tracks (Carter *et al.*, 2000; Rinke and Dethloff, 2008). Over the Arctic Basin, an increase in snowfall of 1 - 2 cm is predicted by the middle of this century (Walsh, 2008), while doubling of winter precipitation expected over a longer time period (Rinke and Dethloff, 2008). The greatest change in precipitation is estimated to occur during the autumn and winter seasons (period of maximum snowfall) in the Arctic Basin (Walsh 2008; Rinke and Dethloff, 2008). If the temperatures remain below zero during these periods, this projected increase in precipitation occurs as snowfall, potentially increasing the snow depth on the sea ice. Interannual variability is also expected to increase, with more variability in the winter precipitation compared to the summer season (Rinke and Dethloff, 2008).

Projections of sea ice surface topography under a climate change scenario are complicated by the changes in sea ice extent, thickness and type, as well as possible changes to synoptic-scale atmospheric pressure. Changes to sea ice extent and abundance of both first-year and multiyear sea ice have already begun and are projected to continue over the next 100 years. The Northern Hemisphere is

experiencing a dramatic change in sea ice characteristics. Between 1979 and 2006, sea ice extent has decreased by approximately 3.7% per decade, which corresponds to a $45.1 \times 10^3 \text{ km}^2$ loss in sea ice area per year (Cavalieri *et al.*, 1997; Parkinson and Cavalieri, 2008). Seasonally, the greatest loss in sea ice extent is occurring during the summer period (Stroeve *et al.*, 2007; 2008) with a loss of approximately 6.2% per decade in summer compared to 2.6% per decade in winter (Parkinson and Cavalieri, 2008). This reduction is also spatially dependent, with areas such as the Barents and Greenland Seas experiencing a greater loss in sea ice extent (as large as 50% in winter) compared to other areas in the Northern Hemisphere (Parkinson, 2000; Parkinson and Cavalieri, 2008). Hudson Bay has experienced a 5.3%/decade reduction in sea ice extent between 1979 and 2006, with the largest negative anomalies in monthly ice extent recorded in the later years of the 1990s/early 2000s (Comiso, 2003; Parkinson and Cavalieri, 2008). Multiyear sea ice has decreased by approximately 9% per decade over the last two decades (Johannessen *et al.*, 1999; Comiso, 2002), with a 23% loss between March 2005 and 2007 (Nghiem *et al.*, 2007). These changes in sea ice characteristics are partly attributed to the dynamics of sea ice in the region, including sea ice drift through the Transpolar Drift and wind anomalies during the study period (Nghiem *et al.*, 2007).

Sea ice thickness has also changed over the last century. In the central Arctic region, the mean sea ice thickness has decreased by 0.13 to 1.3 m, corresponding to a 40% reduction in thickness since 1958 (Nagurduy, 1995; Rothrock *et al.*, 1999; Makshtas *et al.*, 2003). Similarly, decreases in sea ice thickness in the Eurasian Basin have also been measured during the 1990s (Zhang *et al.*, 2000; Maslanik *et al.*,

2000). This decrease in sea ice is primarily a result of a reduction in the dynamic process operating in the area (i.e. less deformation of the sea ice and ridge concentration due to winds), as opposed to thermodynamic causes (i.e. due to an increase air temperature and advanced melt) (Makshtas *et al.*, 2003; Zhang *et al.*, 2000).

Sea ice coverage is expected to continue to decrease significantly over this century (Overland and Wang, 2007). Most of the change in sea ice extent will come during the sea ice minimum period (September) when sea ice extent will be reduced by approximately 50% by the middle of this century, compared to the coverage during the last two decades of the last century (Walsh, 2008). The sea ice maximum occurring in March will only be reduced by 10-15% during the same period. The disparity in the rates of ice retreat indicates that there will be an increase in the area of first-year sea ice, relative to multiyear sea ice. Some climate models predict a completely ice-free Arctic by the middle of this century (Holland *et al.*, 2006; Stroeve *et al.*, 2007; Walsh, 2008). This reduction in sea ice may be due to abrupt changes, rather than a steady decrease (Holland *et al.*, 2006). Some years will see a drastic reduction in sea ice extent, while in other years the ice extent may not change significantly. Due to ice-albedo feedbacks and thermodynamic processes, sea ice reduction and open water may be accelerated once melt has begun. Global climate models predict that landfast FYI will decrease both in thickness and extent over the next 100 years. The thickness of landfast first-year sea ice in the Canadian Arctic will decrease by 50 cm by the end of this century, while ice cover duration will decrease by 2 months over the same period (Dumas *et al.*, 2005; 2006).

Changes in multiyear sea ice are also predicted to occur under a climate change scenario. Using three different climate change scenarios, Zhang and Walsh (2006) found that multiyear sea ice would decrease by 46%-65% over the last twenty years of this century. Multiyear sea ice forms relatively stable ice bridges across channels in the Canadian Arctic. These ice bridges control the drifting of sea ice and in part the extent of deformation in the Canadian Archipelago. Without these ice bridges, sea ice conditions in the area will decline significantly with more mobile ice and less fast ice (Derocher *et al.*, 2004).

Decrease in thickness of sea ice will influence the breakup and freeze-up dates for sea ice. In the Canadian Archipelago, climate models are predicting that the season of open water will increase by approximately 75 days or 2.5 months (Walsh, 2008) or approximately 7.5 days per °C (Flato and Brown, 1996). With a thinner ice cover due to less deformation and ridging, sea ice may be easier to break-up, increasing the timing of open water. This increase in the open water season will result in greater absorption of incoming solar radiation, warming the oceans and causing a later freeze-up. Results suggest that for the eastern Canadian Arctic, the difference between present day freeze-up dates and those estimated for the end of this century is greater than the difference in break-up dates (Dumas *et al.*, 2006). This suggests that the date at which sea ice forms will be significantly later by the end of this century, reducing ice cover duration. A later freeze-up will affect the snow catchment. Without the sea ice, there will be no substrate to catch the snowfall during the autumn/early winter period when the largest influx of snowfall occurs. This snow will fall into the ocean and thus will not be available for the

formation of drifts around ridges and can have implications on ringed seals and polar bear habitats (see Section 8.2.2 for more discussion). In areas around Hudson Bay, break-up dates were changing at a greater rate, compared to the freeze-up dates, suggesting spatial variability in the factors contributing to the loss of sea ice duration (Stirling *et al.*, 1999; Gagnon and Gough, 2005).

With the projected decrease in sea ice concentration and increase in open water, sea ice floes may actually be able to move more freely due to wind and water stresses creating increase ridging in limited areas in the short-term. As sea ice concentration further decreases though, this convergence and ridging of sea ice will occur less frequently. Therefore, in the short-term, dynamic processes and the related local thickening of the sea ice associated with deformation of sea ice may be able to offset some of the thinning that is predicted with climate change. With a projected increase in snowfall, this may result in deeper and greater prevalence of snowdrifts in the short-term.

Changes in synoptic scale atmospheric circulation under global warming scenarios will impact the dynamic forces controlling sea ice roughness. Most climate change models are predicting that the AO index will remain in the positive phase over the next 100 years as a response to greenhouse gas forcing (Shindell *et al.*, 1999; Nazarenko *et al.*, 2006). Under a 2xCO₂ scenario, winter sea ice concentration is negatively correlated with AO index in most of the Arctic Basin (Nazarenko *et al.*, 2006), suggesting that sea ice concentration will decrease further if the AO remains in a positive phase during this century. A continuation of the

positive phase of the AO may cause the Beaufort Gyre to remain in a weakened state, causing more advection and divergence of sea ice. This will result in less deformation and ridging of sea ice, greatly reducing the volume of sea ice, as well as changing the snow catchment hydrology over first-year sea ice, with implications to habitat selection by polar bears and ringed seals.

7.2.2 Implications for marine mammal habitat

Research has suggested that changes in the environmental conditions of the Arctic system (i.e. sea ice and snow catchment changes) are capable of producing significant consequences on ringed seal and polar bear populations. The polar bear has been classified as one of the most sensitive species to climate change, while the ringed seal was classified as the least sensitive (Laidre et al, 2008). The reason for the 'top place' finish for polar bears is that this "species (is) principally reliant on annual sea ice over the continental shelf and areas toward the southern extent of the edge of foraging" (Laidre *et al.*, 2008). The ringed seals have a more varied diet and more importantly variable habitat requirements thus making it less sensitive to changes in the environment. However, these rankings do not suggest that the ringed seal will not be adversely affected by or vulnerable to climate change.

Snowfall and snow distribution have been shown to affect the population of ringed seals in the Arctic. In the 1970s, snowfall in Hudson Bay decreased, while evidence of a decrease in seal recruitment was evident during the same period (Ferguson *et al.*, 2005). A similar pattern was evident for the 1990s, while an increase in snowfall and recruitment was observed during the 1980s. During

periods of decreased snowfall, the snow drifts formed over the deformation structures on the sea ice would be considerably shallower, thus providing less protection for the seal pups from predation (Ferguson *et al.*, 2005).

Projected changes to snowfall will impact the habitat of ringed seals and polar bears. As indicated in Section 8.2.1, snowfall is expected to increase in the Arctic through this century. This increase in snowfall will result in thicker snowdrifts (assuming no change or an increase in deformation over the short-term). This change will improve breeding and nursing habitats for ringed seals, allowing female seals greater opportunity to produce lairs with potentially thicker snow over the lair and thus greater protection against predation (positive impact). Related to this is a negative impact for polar bears since an increase snow depth will reduce the success of hunting by polar bears, as well as the ability of the polar bear to transverse through the environment. These impacts will only occur if the sea ice is present to catch the snowfall. Without significant sea ice extent, snowfall will not accumulate and drift forming the required snow thicknesses for ringed seal lair construction. This will result in a negative impact in the birthing and nursing of ringed seals.

The interannual variability in snowfall is also expected to increase. This variability will cause snowdrifts to greatly vary over the next century, potentially causing years with less snowfall and thinner drifts. This would reduce the success of ringed seals in producing suitable lairs for birthing and nursing, increasing the vulnerability of the pups to the colder temperatures and predation (negative

impact), while increasing the success of hunting by polar bears (positive impact). This decrease in ringed seal population would have impacts for a number of years.

In addition, the timing of precipitation events will also influence the subnivean lairs created for seal pups. With a milder spring season in the Arctic, precipitation will fall as rain instead of snow. These early rainfall events would result in softer snow conditions over the lairs or melting of the snow cover, causing an increase in polar bear hunting success and/or forcing seals out of the lairs (Ferguson *et al.*, 2005). Stirling and Smith (2004) found that during years with rain events that caused softening of the snow cover, hunting success by polar bears was three times higher than previously recorded. Sea ice changes have also been shown to influence ringed seal population. In the Beaufort Sea area, failure in the reproduction of ringed seals observed during the 1960s to 1980s was associated with severe (or heavy) ice conditions (Stirling and Archibald, 1977; Smith and Stirling 1978; Stirling *et al.*, 1982; Stirling 2002).

Changes in the sea ice characteristics of the Arctic may benefit the ringed seal in the short term (Kingsley and Byers, 1998, Ferguson *et al.*, 2005). It has been documented that sea ice concentration has been decreasing in the Arctic (Cavalieri *et al.*, 1997; Parkinson and Cavalieri, 2008), which may result in greater ridging and deeper snowdrifts in the short term, increasing the survival of pups. In addition, climate models are suggesting that multiyear sea ice will be replaced with first-year sea ice (Walsh, 2008). This replacement may increase productivity of the Arctic due to increase light penetrating into the water column, increasing the prey of the ringed

seals (Laidre *et al.*, 2008).

Over the long term however, a milder climate and less thin sea ice (as predicted by climate models and with a positive phase of the AO index) will reduce the habitat for ringed seals. Landfast first-year sea ice is projected to decrease (Dumas *et al.*, 2005), concentrating their lairs, and allowing for greater predation (Rosing-Asvid, 2006). This may also result in young pups being forced out of the lairs at an earlier date, exposing them to polar bears and to the colder environment (Smith and Harwood, 2001), as well as causing distress by requiring pups to expend higher amounts of energy due to more swimming (Smith *et al.*, 1991). This negative impact has already been documented in the growth and survival of pups in eastern Beaufort Sea (Harwood *et al.*, 2000). In the Baffin Bay region, the occurrence of ringed seals decreased during periods with light ice coverage (Woolett *et al.*, 2000). The instability of the first-year sea ice would have a negative impact on the ringed seal pups since the early break-up may cause an earlier separation between mother and pup (Laidre *et al.*, 2008).

The condition of polar bears (including reproductive status, natality and weight) is closely linked to the sea ice conditions, especially the length of the sea ice cover (Stirling and Derocher, 1993; Stirling *et al.*, 1993; Stirling *et al.*, 1999). For instance, break-up in Hudson Bay has been shown to be occurring 7-8 days earlier per decade for the past two decades (Stirling *et al.*, 1999). This earlier breakup reduced the reproductive success and poorer body condition of polar bears in this subpopulation (Stirling *et al.*, 1999; Stirling and Parkinson, 2006). Bears are forced

to move ashore at an earlier date and have less time to feed on ringed seals in Hudson Bay, therefore fasting for a longer period. Based on average mass of polar bears and current decreases in sea ice extent for Hudson Bay, female polar bears will not reach the necessary weight of reproductive success within the next 100 years, causing a crash in the population within that management zone (Derocher *et al.*, 2004). Similar trends in sea ice break-up have occurred in Foxe Basin, Baffin Bay and Davis Strait (Stirling and Parkinson, 2006).

A reduction in landfast sea ice will have negative impacts on female polar bears. Females with COY prefer stable landfast sea ice habitat, and avoid other ice types due to the presence of more dominant classes of bears. With a reduction in stable landfast ice, these polar bears will be required to move into other ice types, resulting in a potential increase of predation on COY by adult and subadult males.

More dynamic sea ice may cause significant increases in the width of leads and thus polar bears will be required to expend more energy while transversing these leads or walking around them to get to suitable habitat for hunting or mating (Derocher *et al.*, 2004). If dynamic processes increase due to increased wind speed and thinner sea ice, this may cause the fracturing and transportation of sea ice out of the area. Polar bears located on the ice edge off the southwest Greenland have already been trapped on sea ice as it was pushed away from the main pack and transported to unfavourable habitats (Derocher *et al.*, 2004). With a decrease in extent of sea ice, density of polar bears will increase, causing greater competition for the available prey in the area and ultimately having a negative impact on the

condition of non-dominant polar bears (Derocher *et al.*, 2004). A more dynamic sea ice environment may also result in lower pregnancy rates for polar bears due to the fact that the tracking of females by male polar bears may be significantly reduced on smaller traveling floes (Derocher *et al.*, 2004). This projection is based on the assumption that polar bears within these environments will maintain ringed seals as their main prey. If the selection of prey by polar bears changes to other seals (i.e. harp seals – Theimann *et al.*, 2008), then the negative impacts over the short-term as described above may be incorrect.

In the short-term, a milder climate and less sea ice may benefit polar bears in the Arctic. As indicated above, less sea ice may result in a higher density of seals in certain areas of the Arctic, allowing for greater hunting success by the polar bear (Rosing-Asvid, 2006). This will result in high polar bear cub survival. In the long-term, an increase in amount of open water will cause ringed seals to be less restrictive in the location of breathing holes and less predictable in their habitat, thus significantly reducing the hunting efficiency of the polar bear (Derocher *et al.*, 2004). In addition, an ice-free Arctic will result in polar bears coming ashore and having to fast for longer periods, worsening the condition and success of polar bears.

In the long-term, projections using forecasted minimal ice levels suggest a substantial reduction in polar bears within this century (Amstrup *et al.*, 2007). Polar bear habitat is expected to decrease globally by between 15% and 25% (depending on model inputs). This decrease is projected to result in a decline in

polar bear carrying capacity of between 22% and 32% by the end of this century for areas that undergo seasonal sea ice changes (i.e. Hudson Bay; Amstrup et al., 2007). Within the Archipelago region, the carrying capacity is expected to be reduced by 23-48% by the end of this century (Amstrup et al., 2007). An uncertainty associated with these projections is a lack of complete understanding in the physical system and thus the statistical modeling of the physical system within the models. In addition the improved understanding of the polar bear-prey relationship with regard to seal species has improved and are typically not included in this projection. This current research can be used to improve the models for better predictions in habitat changes within the Canadian Arctic. Future research may also investigate the response of other potential prey species (i.e. harp seals) to changes in ice conditions.

REFERENCES

- Aars, J., N.J. Lunn, and A.E. Derocher. 2006. *Polar bears*. Occasional paper No. 32. Proceedings of the 14th Working Meeting of the IUCN/SSC Polar Bear Specialist Group, IUCH, Gland, Switzerland and Cambridge, UK.
- Adolphs, U. 1999. Roughness variability of sea ice and snow cover thickness profiles in the Ross, Amundsen and Bellingshausen Seas. *Journal of Geophysical Research*, 104(C6): 13577-13591.
- Amstrup, S.C., G.M. Durner, I. Stirling, N.J. Lunn and F. Messier. 2000. Movements and distribution of polar bears in the Beaufort Sea. *Canadian Journal of Zoology*, 78: 948-966.
- Amstrup, S.C. and C. Gardner. 1994. Polar bear maternity denning in the Beaufort Sea. *Journal of Wildlife Management*, 58: 1-10.
- Amstrup S.C., B.G. Marcot and D.C. Douglas. 2007. *Forecasting the range-wide status of polar bears at selected times in the 21st century*. USGS Alaska Science Center, Anchorage, Administrative Report.
- Amstrup, S.C., I. Stirling and J.W. Lentfer. 1986. Past and present status of polar bears in Alaska. *Wildlife Society Bulletin*, 14:241-254.
- Andreas, E.L. 1995. Air-sea drag coefficients in the western Weddell Sea: 2. A model based on form drag and drifting snow. *Journal of Geophysical Research*, 100: 4833-4843.
- Andreas, E.L., M.A. Lange, S.F. Ackley and P. Wadhams. 1993. Roughness of Weddell Sea ice and estimates of the air-ice drag coefficient. *Journal of Geophysical Research*, 98(C7): 12439-12452.
- Bagnold, R.A. 1941. *The Physics of Blown Sand and Desert Dunes*. Chapman and Hill, London, UK. 255 pp.
- Banke, E.G., S.D. Smith and R.J. Anderson. 1980. Drag coefficients at AIDJEX. In: R.S. Pritchard (ed.), *Sea Ice Processes and Models*. University of Washington Press, Seattle, Washington, pp. 430-442.
- Barber, D.G., J.M. Hanesiak, W. Chan and J. Piwowar. 2001. Sea-ice and meteorological conditions in Northern Baffin Bay and the North Water Polynya between 1979 and 1996. *Atmosphere-Ocean*, 39:343-359.
- Barber, D.G. and J.M. Hanesiak. 2004. Meteorological forcing of sea ice concentrations in the southern Beaufort Sea over the period 1979 to 2000. *Journal of Geophysical Research*, 109, doi:10.1029/2006JC002027.
- Barber, D.G., and J. Iacozza. 2004. Historical analysis of sea ice conditions in M'Clintock Channel and the Gulf of Boothia, Nunavut: Implications for ringed seal and polar bear habitat. *Arctic*, 57:1-14. 705
- Barber, D.G. and E.F. LeDrew. 1991. SAR sea ice discrimination using texture statistics: A multivariate approach. *Photogrammetric Engineering and Remote Sensing*, 57(4):385-395.

- Begum, E., M. Bonno, M. Obata, H. Yamamoto, M. Kawai and Y. Komada. 2006. Emergence of physiological rhythmicity in term and preterm neonatal intensive care unit. *Journal of Circadian Rhythms*, 4:11, doi: 10.1186/1740-3391-4-11.
- Berkes, F. 1998. Indigenous knowledge and resource management systems in the Canadian sub-Arctic. In: Berkes, F., C. Folke, and J. Colding (eds.) *Linking Social and Ecological Systems*. Cambridge University Press, New York, NY, USA, pp. 98-128.
- Blackman, R.B., and Tukey, J.,W., 1958: *The measurement of power spectra from the point of view of communication engineering*. Dover Publications, 190 pp.
- Brillinger, D.R. 1981. *Time Series: Data Analysis and Theory*. San Francisco: Holden-Day. 540 pp.
- Brown, S.R. 1995. Measuring the dimension of self-affine fractals: examples of rough surfaces. In: C.C. Barton and P.R. LaPointe (eds.) *Fractals in the Earth Sciences*. New York: Plenum Press. pp. 77-87.
- Budd, W.R., R. Dingle and U. Radok. 1966. The Byrd snowdrift project: Outline and basic results. *Studies in Antarctic Meteorology*, American Geophysical Union, *Antarctica Research Service*, 9: 71-134.
- Carr, J.R. 1995. *Numerical analysis for the geological sciences*. New York, NY: Prentice Hall.
- Carter, T.R., M. Hulme, J.F. Crossley, S. Malyshev, M.G. New, M.E. Schlesinger and H. Tuomenvirta. 2000. *Climate Change in the 21st Century - Interim Characterizations based on the New IPCC Emissions Scenarios*. The Finnish Environment 433, Finnish Environment Institute, Helsinki, 148 pp.
- Cavaleri, D.J., P. Gloersen, C. Parkinson, J.C. Comiso and H.J. Zwally. 1997. Observed hemispheric asymmetry in global sea ice changes. *Science*, 278: 1104-1106.
- Clausi, D.A. 2002. An analysis of co-occurrence texture statistics as a function of grey level quantization. *Canadian Journal of Remote Sensing*, 28(1):45-62.
- Comiso, J.C. 2002. A rapidly declining perennial sea ice cover in the Arctic. *Geophysical Research Letters*, 29, doi:1029/2002GL015650.
- Comiso, J.C. 2003. Chapter 4: Large-scale characteristics and variability of the global sea ice cover. In: D. Thomas and G. Diekmann (eds.), *Sea Ice: An Introduction to Its Physics, Chemistry, Biology and Geology*, Blackwell Scientific, Oxford, UK, pp. 112-142.
- Cooke, A. 1984. Historical evidence of Inuit use of sea ice. In Cook, A. and E. Van Alstine (eds.) *Sikumuit: The People Who Use the Sea Ice*. Ottawa: Canadian Arctic Resources Committee, pp. 61-72.
- Deems, J.S., S.R. Fassnacht, and K.J. Elder. 2008. Interannual consistence in fractal snow depth patterns at two Colorado mountain sites. *Journal of Hydrometeorology*, 9: 977-988, doi:10.1175/2008JHM901.1.
- Deems, J.S., S.R. Fassnacht, and K.J. Elder. 2006. Fractal distribution of snow depth from lidar data. *Journal of Hydrometeorology*, 7: 285-297.

- Derocher, A.E., N.J. Lunn and I. Stirling. 2004. Polar bears in a warming climate. *Integrative and Comparative Biology*, 44: 163-176.
- Derocher, A.E. and I. Stirling. 1990. Distribution of polar bears (*Ursus maritimus*) during the ice-free period in western Hudson Bay. *Canadian Journal of Zoology*, 68: 1395-1403.
- Dery S.J. and M.K. Yau. 2002. Land-scale mass balance effects of blowing snow and surface sublimation. *Journal of Geophysical Research*, 107, doi:10.1029/2001JD001251.
- Dumas, J.A., E. Carmack and H. Melling. 2005. Climate change impacts on the Beaufort shelf landfast ice. *Cold Regions Science and Technology*, 42: 41-51.
- Dumas, J.A., G.M. Flato and R.D. Brown. 2006. Future projections of landfast ice thickness and distribution in the Canadian Arctic. *Journal of Climate*, 19:5175-5189.
- Durner, G.M., S.C. Amstrup, R. Nielson and T.L. McDonald. 2004. Using discrete choice modeling to generate resource selection functions for female polar bears in the Beaufort Sea. In S. Huzurbazar, (ed.) *Resource Selection Methods and Applications, Proceedings of the 1st Conference on Resource Selection Modeling*. January 2003, Laramie, Wyoming, pp.107-120,
- Durner, G.M., D.C. Douglas, R.M. Nielson, S.C. Amstrup, and T.L. McDonald. 2007. *Predicting the Future Distribution of Polar Bear Habitat in the Polar Basin from Resource Selection Functions Applied to General Circulation Model Projections of Sea Ice*. USGS Alaska Science Center, Anchorage, Administrative Report.
- Durner, G. M., D.C. Douglas, R.M. Nielson, S.C. Amstrup, T.L. McDonald, I. Stirling, M. Mauritzen, E.W. Born, Ø. Wiig, E. DeWeaver, M.C. Serreze, S.E. Belikov, M.M. Holland, J. Maslanik, J. Aars, D.A. Bailey, and A.E. Derocher. 2009. Predicting 21st-century polar bear habitat distribution from global climate models. *Ecological Monographs*, 79:25-58, doi:10.1890/07-2089.1
- Eicken, H. 2003. Chapter 2: From the microscopic to the macroscopic to the regional scale: Growth, microstructure and properties of sea ice. In: Thomas, D.N. and G.S. Dieckmann (eds.) *Sea Ice: An Introduction to its Physics, Biology, Chemistry and Geology*. London: Blackwell Scientific Ltd, pp. 22-81.
- Eicken, H., H. Fischer and P. Lemke. 1995. Effects of the snow cover on Antarctic sea ice and potential modulation of its response to climate change. *Annals of Glaciology*, 21: 369-376.
- Eicken, H., M.A. Lange, H.-W. Hubberten and P. Wadhams. 1994. Characteristics and distribution patterns of snow and meteoric ice in the Weddell Sea and their contribution to the mass balance of sea ice. *Annales Geophysicae*, 12(1): 80-93.
- Ferguson, S.H., I. Stirling and P. McLoughlin. 2005. Climate change and ringed seal (*Phoca hispida*) recruitment in western Hudson Bay. *Marine Mammal Science*, 21(1): 121-135.
- Ferguson, S.H., M.K. Taylor, E.W. Born and F. Messier. 1998. Fractals, sea-ice landscape and spatial patterns of polar bears. *Journal of Biogeography*, 25: 1081-1092.
- Ferguson, S.H., M. Taylor, E. Born, A. Rosing-Asvid and F. Messier. 2001. Activity and movement patterns of polar bears inhabiting consolidated versus active pack ice. *Arctic*, 54(1): 49-54.

Ferguson, S.H., M. Taylor and F. Messier. 2000. Influence of sea ice dynamics on habitat selection by polar bears. *Ecology*, 81(3): 761-772.

Finley, K.J., G.W. Miller, R.A. Davis and W.R. Koski. 1983. A distinctive large breeding population of ringed seals (*Phoca hispida*) inhabiting the Baffin Bay pack ice. *Arctic*, 36: 162-173.

Fischbach, A.S., S.C. Amstrup and D.C. Douglas. 2007. Landward and eastward shift of Alaskan polar bear denning associated with recent sea ice changes. *Polar Biology*, 30:1395-1405.

Flato, G.M. and R.D. Brown, 1996. Variability and climate sensitivity of landfast Arctic sea ice. *Journal of Geophysical Research*, 101: 25767-25777.

Flato, G.M. and W.D. Hibler III. 1995. Ridging and strength in modeling the thickness distribution of Arctic sea ice. *Journal of Geophysical Research*, 100(C9): 18,611-18,626.

Frost, K.J. and L.F. Lowry. 1981. Ringed, Baikal and Caspian seals. In: S.H. Ridgway and R.J. Harrison (eds.) *Handbook of Marine Mammals, Volume 2*. Academic Press, New York, New York, pp. 29-53.

Frost, K.J., L.F. Lowry, J.R. Gilbert and J.J. Bums. 1988. *Ringed seal monitoring: relationships of distribution and abundance to habitat attributes and industrial activities*. Unpublished final report RU No. 667 to Outer Continental Shelf Environmental Assessment Program, Anchorage, AK.

Frost, V.S., J. Stiles, K. Shanmugan and J. Holtzmann. 1982. A model for radar images and its application to adaptive digital filtering of multiplicative noise. *IEEE Transactions on Pattern Analysis and Machine Intelligence*, 4:157-166.

Furgal, C.M., S. Innes and K.M. Kovacs. 1996. Characteristics of ringed seal, *Phoca hispida*, subnivian structures and breeding habitat and their effects on predation. *Canadian Journal of Zoology*, 74: 858-874.

Gagnon, A.S. and W.A. Gough. 2005. Trends in the dates of ice freeze-up and breakup over Hudson Bay, Canada. *Arctic*, 58(4): 370-382.

Georgievskii, V.Y. 1998. On global climate warming effects on water resources. In: *Water: a looming crisis?* Technical Documents in Hydrology, No. 18, UNESCO, Paris, pp. 37-46.

Giles, K.A., S.W. Laxon, D.J. Wingham, D.W. Wallis, W.B. Krabill, C.J. Leuschen, D. McAdoo, S.S. Manizade, and R.K. Raney. 2007. Combined airborne laser and radar altimeter measurements over the Fram Strait in May 2002. *Remote Sensing of the Environment*, 111:182-194, doi:10.1016/j.rse.2007.02.037.

Gleason, J.S. and K.D. Rode. 2009. Polar bear distribution and habitat association reflect long-term changes in fall sea ice conditions in the Alaskan Beaufort Sea. *Arctic*, 62:405-417.

Granberg, H.B. 1998. Snow cover on sea ice, In: M. Leppäranta (ed.) *Physics of Ice Covered Seas, Volume 2*. University of Helsinki, Helsinki, Finland, pp. 605-649.

Granger, R.J., J.W. Pomeroy and J. Parviainen. 2002: Boundary-layer integration approach to advection of sensible heat to a patchy snow cover. *Hydrological Processes*, 16:3559-3569.

- Groisman, P.Y. and D.R. Easterling. 1994. Variability and trends of precipitation and snowfall over the United States and Canada. *Journal of Climate*, 7:184-205.
- Haas, C. 2003. Chapter 3: Dynamics versus thermodynamics: The sea ice thickness distribution. In: Thomas, D.N. and G.S. Dieckmann (eds.) *Sea Ice: An Introduction to its Physics, Biology, Chemistry and Geology*. London: Blackwell Scientific Ltd, pp. 82-111.
- Haas, C., S. Hendricks and M. Doble. 2006. Comparison of the sea ice thickness distribution in the Lincoln Sea and adjacent Arctic Ocean in 2004 and 2005. *Annals of Glaciology*, 44:44A121.
- Haas, C., S. Hendricks, H. Eicken, and A. Herber. 2010. Synoptic airborne thickness surveys reveal state of Arctic sea ice cover. *Geophysical Research Letters*, 37, doi:10.1029/2010GL042652.
- Hakanson, L. 1978. The length of closed geomorphic lines. *Mathematical Geology*, 10:141-167.
- Hammer, O. 2007. Spectral analysis of a Plio-Pleistocene multispecies time series using the Mantel periodogram. *Palaeogeography, Palaeoclimatology, Palaeoecology* 243:373-377, doi:10.1016/j.palaeo.2006.08.009
- Hammill, M.O. and T.G. Smith. 1989. Factors affecting the distribution and abundance of ringed seal structures in Barrow Strait, NWT. *Canadian Journal of Zoology*, 67: 2212-2219.
- Hansen, D.J. 2004. Observations of habitat use by polar bears, *Ursus maritimus*, in the Alaskan Beaufort, Chukchi and northern Bering Seas. *Canadian Field-Naturalist*, 118(3): 395-399.
- Haralick, R.M., K. Shanmugam, I. Dinstein. 1973. Textural features for image classification. *IEEE Transactions on Systems, Man, and Cybernetics*, SMC-3 (6): 610-621.
- Harwood, L.A., T.G. Smith and H. Melling. 2000. Variation in reproduction and body condition of the ringed seal (*Phoca hispida*) in western Prince Albert Sound, NT, Canada as assessed through a harvest-based sampling program. *Arctic*, 53: 422-431.
- Heil, P., V.I. Lytle and I. Allison. 1998. Enhanced thermodynamic ice growth by sea-ice deformation. *Annals of Glaciology*, 27: 433-437.
- Herzfeld, U.C. 2002. Vario functions of higher order – definition and application to characterization of snow surface roughness. *Computers and Geosciences*, 28: 641-660.
- Hibler, W.D. 1972. Removal of aircraft altitude variation from laser profiles of the Arctic pack. *Journal of Geophysical Research*, 77:7190-7195.
- Holladay, J. S. and R. Moucha. 1998. *Electromagnetic/Laser Ice Thickness Data from the Labrador Shelf, 1994*. Can. Contract. Rep. Hydrogr. Ocean Sci. No. 49: vii+340 p.
- Holland, M.M., C.M. Bitz and B. Tremblay. 2006. Future abrupt reductions in the summer Arctic sea ice. *Geophysical Research Letters*, 33, doi:10.1026/2006GL028024.

- Holland M., M. Serreze, and J. Stroeve. 2010. The sea ice mass budget of the Arctic and its future change as simulated by coupled climate models. *Climate Dynamics*, 34:185-200, DOI: 10.1007/s00382-008-0493-4.
- Honeycutt, C.E. and R. Plotnick. 2008. Image analysis techniques and gray-level co-occurrence matrices (GLCM) for calculating bioturbation indices and characterizing biogenic sedimentary structures. *Computers & Geosciences*, 34(11):1461-1472, doi:10.1016/j.cageo.2008.01.006.
- Howell, S.E.L., A. Tivy, J.J. Yackel, and S. McCourt. 2008. Multi-Year Sea-Ice Conditions in 746 the Western Canadian Arctic Archipelago Region of the Northwest Passage: 1968–2006. *Atmosphere-Ocean*, 46: 229-242.
- Hunter, C.M., H. Caswell, M.C. Runge, E.V. Regehr, S.C. Amstrup and I. Stirling. 2007. *Polar bears in the southern Beaufort Sea III: Demography and population growth in relation to sea ice conditions*. USGS Alaska Science Center, Anchorage, Administrative Report.
- Hurrell, J.W., Y. Kushnir, G. Ottersen, and M. Visbeck (eds.). 2003. *The North Atlantic Oscillation: Climate Significance and Environmental Impact*. American Geophysical Union, Geophysical Monograph Series, 134, 279 pp.
- Hvidegaard, S. M. and R. Forsberg. 2002. Sea-ice thickness from airborne laser altimetry over the Arctic Ocean north of Greenland. *Geophysical Research Letters*, 29(20), doi:10.1029/2001GL014474.
- Iacozza, J. and D.G. Barber. 1999. An examination of the distribution of snow on sea ice. *Atmosphere-Ocean*, 37(1): 21-51.
- Iacozza, J. and D.G. Barber. 2001. Ablation patterns of snow cover over smooth first-year sea ice in the Canadian Arctic. *Hydrological Processes*, 15:3559-3569.
- Iacozza J. and D.G. Barber. 2010. An examination of snow redistribution over smooth land-fast sea ice. *Hydrological Processes*, 24:850–865, doi: 10.1002/hyp.7526
- Isaaks E.H. and R.M. Srivastava. 1989. *An Introduction to Applied Geostatistics*, Oxford University Press: New York; 552 pp.
- IUCN/SSC Polar Bear Specialist Group 2002. In: N.J. Lunn, S. Schliebe and E.W. Born (eds.), *Polar bears: Proceedings of the 13th Working Meeting of the IUCN Polar Bear Specialist Group*, IUCN, Gland, Switzerland and Cambridge, UK. pp. 21-35.
- Jeffries, M.O., R. Jana, S. Li and S. McCullars. 1995. Sea-ice-and snow-thickness distributions in late winter 1993 and 1994 in the Ross, Amundsen and Bellingshausen Seas. *Antarctic Journal*, 30(1-4):18-21.
- Johannessen, O.M., E.V. Shalina and M.W. Miles. 1999. Satellite evidence for an Arctic sea ice cover in transformation. *Science*, 286:1937-1939.
- Kanamitsu, M., W. Ebisuzaki, J. Woollen, S-K Yang, J.J. Hnilo, M. Fiorino, and G. L. Potter. 2002. NCEP-DOE AMIP-II Reanalysis (R-2). *Bulletin of the Atmospheric Meteorological Society*, 83(11):1631-1643, doi:10.1175/bams-83-11-1631.

- Karvonen, J. A. 2004. Baltic sea ice SAR segmentation and classification using modified pulse-coupled neural networks. *IEEE Transactions on Geoscience Remote Sensing*, 42(7):1566–1574.
- Kattsov, V.M. and J.E. Walsh. 2000. Twentieth-century trends in Arctic precipitation from observational data and a climate model simulation. *Journal of Climate*, 13: 1362-1370.
- Kikuchi, T. 1981. A wind tunnel study of the aerodynamic roughness associated with drifting snow. *Cold Regions Science and Technology*, 5: 107-118.
- Kind, R.J. 1981. Chapter 8: Snow Drifting. In: D.M. Gray and D.H. Male (eds.) *Handbook of Snow – Principles, Processes, Management and Use*. Pergamon Press Canada Ltd., Toronto, Ontario, pp.338-359.
- Kingsley, M.C.S. and T.J. Byers. 1998. Failure of reproduction in ringed seals (*Phoca hispida*) in Amundsen Gulf, Northwest Territories in 1984-87. *NAMMCO Scientific Publications*, 1: 197-210.
- Kingsley, M.C.S., I. Stirling and W. Calvert. 1985. The distribution and abundance of seals in the Canadian high Arctic, 1980-82. *Canadian Journal of Fisheries and Aquatic Sciences*, 42: 1189-1210.
- Kobayashi, D. 1972. Studies of snow transport in low-level drifting snow. *Contributions from the Institute for Low Temperature Science Series A*, 24: 1-58.
- Kotlyakov, V.M. and M.G. Grosswald. 1990. Interaction of sea ice, snow and glaciers with the atmosphere and ocean. *Polar Geography and Geology*, 14(1): 3-248.
- Kuchment, L.S. and A.N. Gelfan. 2001. Statistical self-similarity of spatial snow accumulation variations and its application to snowmelt runoff models. *Hydrological Processes*, 15:3343-3355.
- Kurtz N.T., M. Thorsten, D.J. Cavalieri, W. Krabill, J.G. Sonntag and J. Miller. 2008. Comparison of ICESat data with airborne laser altimeter measurements over Arctic sea ice. *IEEE Transactions on Geoscience and Remote Sensing*, 46(7):1913-1924.
- Kushwaha, S.P.S., R.S. Dwivedi and B.R.M. Rao. 2000. Evaluation of various digital image processing techniques for detection of coastal wetlands using ERS-1 SAR data. *International Journal of Remote Sensing*, 21(3):565-579.
- Kwok, R. and G.F. Cunningham. 2008. ICESat over Arctic sea ice: Estimation of snow depth and ice thickness. *Journal of Geophysical Research*, 113, doi:10.1029/2008JC004753.
- Laidre, K.L., I. Stirling, L.F. Lowry, Ø. Wiig, M.P. Heide-Jørgenson and S.H. Ferguson. 2008. *Ecological Applications*, 18(2) Supplement: S97-S125.
- Lang, R.M., B.R. Leo and R.L. Brown. 1984. Observations on the growth process and strength characteristics of surface hoar. *Proceedings of the International Snow Science Workshop*, International Snow Science Workshop Committee, Aspen, Colorado, pp. 188-195
- Langlois, A., D.G. Barber, and B.J. Hwang. 2007. Development of a winter snow water equivalent algorithm using *in situ* passive microwave radiometry over snow-covered first-year sea ice. *Remote Sensing of Environment*, 106:75-88.

- Ledley, T.S. 1991. Snow on sea ice: competing effects in shaping climate. *Journal of Geophysical Research*, 96(D9): 17,195-17,208.
- LeDrew, E.F., D. Johnson, and J.A. Maslanik. 1991. An examination of atmospheric mechanisms that may be responsible for the annual reversal of the Beaufort Sea ice field. *International Journal of Climatology*, 11:841-859.
- Lee, J.S. 1981. Speckle analysis and smoothing of synthetic aperture radar images. *Computer Graphics and Image Processing*, 17: 24- 31.
- Lemke, P., M. Harder and M. Hilmer. 2000. The response of Arctic sea ice to global change. *Climatic Change*, 46:277-287.
- Lentfer, J.W. 1975. Polar bear denning on drifting sea ice. *Journal of Mammalogy*, 56:716.
- Li, L. and J.W. Pomeroy. 1997. Estimates of threshold wind speeds for snow transport using meteorological data. *Journal of Applied Meteorology*, 36:205-213.
- Lillesand, M.T., R.W. Keifer and J.W. Chipman. 2008. *Remote Sensing and Image Interpretation*. Sixth Edition. John Wiley & Sons, New York, NY.
- Lindsay, R.W. and J. Zhang. 2005. The thinning of Arctic sea ice, 1988-2003: Having we passed a tipping point? *Journal of Climate*, 18:4879-4894.
- Liston, G.E., and K. Elder. 2006. A distributed snow-evolution modeling system (SnowModel). *Journal of Hydrometeorology*, 7:1259-1276.
- Liston, G.E. and M. Sturm. 2002. Winter Precipitation Patterns in Arctic Alaska Determined from a Blowing-Snow Model and Snow-Depth Observations. *Journal of Hydrometeorology*, 3:646-659.
- Litaor, M.I., T.R. Seastedt, and D.A. Walker. 2002. Spatial analysis of selected soil attributes across an alpine topographic/snow gradient. *Landscape Ecology*, 17:71-85.
- Liu, P., C. Zhao, X. Li, M. He and W. Pichel. 2010. Identification of ocean oil spills in SAR imagery based on fuzzy logic algorithm, *International Journal of Remote Sensing*, 31: 17,4819-4833.
- Livingstone, C.E., R.K. Hawkins, A.L. Gray, L. Drapier, L.D. Arsenault, K. Okamoto, T.L. Wilkinson and D. Person. 1983. *The CCRS/Sursat Active-Passive Experiment 1978-1980: the Microwave Signatures of Sea Ice*, Canada Centre for Remote Sensing, Ottawa.
- Longley, P.A. and M. Batty. 1989. On the fractal measurement of geographical boundaries. *Geographical Analysis*, 21(1): 47-67.
- Lopes, A., E. Nezry, R. Touzi and H. Lauri. 1990. Maximum a posteriori speckle filtering and first order texture models in SAR images. *Proceedings of Geoscience and Remote Sensing Symposium (IGARSS' 90)*, May 1990, Maryland, 3:2409-2412.
- Lopes, A., E. Nezry, R. Touzi and H. Laur. 1993. Structure detection and statistical adaptive speckle filtering in SAR Images. *International Journal of Remote Sensing*, 14:1735-1758.
- Lubin, D. and R. Massom. 2006. *Polar Remote Sensing; Volume 1: Atmosphere and Oceans*.

Springer-Verlag, Berlin, Germany.

Lukin, L.R. and V.A. Potelov. 1978. Living conditions and distributions of ringed seals in the White Sea in winter. *Biol. Morya (Vladivost.)*, 3: 62-69.

Lukovich, J.V. and D.G. Barber. 2006. Atmospheric controls on sea ice motion in the southern Beaufort Sea. *Journal of Geophysical Research*, 111, doi:10.1029/2005JD006408

Lunn, N.J., I. Stirling and S.N. Nowicki. 1997. Distribution and abundance of ringed (*Phoca hispida*) and bearded seals (*Erignathus barbatus*) in western Hudson Bay. *Canadian Journal of Fisheries and Aquatic Science*, 54:914-921.

Lunn, N.J., M. Branigan, L. Carpenter, K. Chaulk, B. Doige, J. Galipeau, D. Hedman, M. Huot, R. Maraj, M. Obbard, R. Otto, I. Stirling, M. Taylor and S. Woodley. 2006. Polar bear management in Canada 2001-2004. In: Aars, J., N.J. Lunn and A.E. Derocher. *Polar Bears*. Occasional Paper No. 32. Proceedings of the Fourteenth Working Meeting of the IUCN/SSC Polar Bear Specialist Group. IUCH, Gland, Switzerland and Cambridge, UK. pp. 41-52.

Maeno, N., R. Naruse, K. Nishimura, I. Takei, T. Ebinuma, S. Kobayashi, N. Nishimura, Y. Kaneda and T. Ishida. 1985. Wind-tunnel experiments on blowing snow. *Annals of Glaciology*, 6:63-67.

Makshtas, A., S. Shoutilin and E. Andreas. 2003. Possible dynamic and thermal causes for the recent decrease in sea ice in the Arctic. *Journal of Geophysical Research*, 108: 25-1-25-13.

Mandelbrot, B.B. 1983. *The Fractal Geometry Of Nature*. San Francisco, CA: Freeman.

MANICE (Manual of Standard Procedures for Observing and Reporting Ice Conditions). 2005. Canadian Ice Service, <http://www.ec.gc.ca/glaces-ice/default.asp?lang=En&n=4FF82CBD-1>, date accessed: July 29, 2010.

Mårell, A., J.P. Ball and A. Hofgaard. 2002: Foraging and movement paths of female reindeer: insights from fractal analysis, correlated random walks, and Lévy flights. *Canadian Journal of Zoology*, 80:854-865.

Maslanik, J.A., A.H. Lynch, M.C. Serreze and W. Wu. 2000. A case study of regional climate anomalies in the Arctic: Performance requirements for a coupled model. *Journal of Climate*, 13(2):383-401.

Massom, R.A., M.R. Drinkwater and C. Haas. 1997. Winter snow cover on sea ice in the Weddell Sea. *Journal of Geophysical Research*, 102(C1): 1101-1117.

Massom, R.A., H. Eicken, C. Haas, M.O. Jeffries, M.R. Drinkwater, M. Sturm, A.P. Worby, X. Wu, V.I. Lytle, S. Ushio, K. Morris, P.A. Reid, S.G. Warren and I. Allison. 2001. Snow on Antarctic sea ice. *Review of Geophysics*, 39(3):413-445.

Mauritzen, M., S. Belikov, A. Boltunov, A. Derocher, E. Hansen, R.A. Ims, Ø. Wiig and N. Yoccoz. 2003. Functional responses in polar bear habitat selection. *Oikos*, 100:112-124.

Maykut, G.A. 1986. The surface heat and mass balance. In Untersteiner, N. (ed.) *The Geophysics of Sea Ice*. Dordrecht: Martinus Nijhoff Publ., pp. 395-463.

McLaren, I.A. 1958. The biology of the ringed seal (*Phoca hispida*, Schreber) in the eastern

- Canadian Arctic. *Bulletin of the Fisheries Research Board of Canada*, no. 118.
- McNutt, S.L. and J.E. Overland. 2003. Spatial hierarchy in Arctic sea ice dynamics. *Tellus*, 55A:181-191.
- Melling, H. and D.A. Riedel. 1995. The underside topography of sea ice over the continental shelf of the Beaufort Sea in the winter of 1990. *Journal of Geophysical Research*, 100: 13,641-13,653.
- Mernild, S.H., G.E. Liston and B. Hasholt. 2007. Snow-distribution and melt modeling for glaciers in Zachenberg river drainage basin, north-eastern Greenland. *Hydrological Processes*, 21:3249-3263.
- Mernild, S.H., G.E. Liston, D.L. Kane, N.T. Knudsen and B. Hasholt. 2008. Snow, runoff, and mass balance modeling for the entire Mittivakkat Glacier (1998-2006), Ammassalik Island, SE Greenland. *Geografisk Tidsskrift-Danish Journal of Geography*, 108:121-136.
- Messier, F., M.K. Taylor and M.A. Ramsay. 1992. Seasonal activity patterns of female polar bears (*Ursus maritimus*) in the Canadian Arctic as revealed by satellite telemetry. *Journal of Zoology*, 226:219-229.
- Messier, F., M.K. Taylor and M.A. Ramsay. 1994. Denning ecology of polar bears in the Canadian Arctic Archipelago. *Journal of Mammalogy*, 75:420-430.
- Molotch, N.P., M.T. Colee, R.C. Bales and J. Dozier. 2005. Estimating the spatial distribution of snow water equivalent in an alpine basin using binary regression tree models: the impact of digital elevation data and independent variable selection. *Hydrological Processes*, 19:1459-1479.
- Moore, S.E. and H.P. Huntington. 2008. Arctic marine mammals and climate change: impacts and resilience. *Ecological Applications*, 18(2) Supplement: S157-S165.
- Moritz, R.E. and D.K. Perovich. 1996. *Surface Heat Budget of the Arctic Ocean Science Plan*, ARCHSS/OAII report number 5, University of Washington, Seattle, 64 pp.
- Mundy, C.J. and D.G. Barber. 2001. On the relationship between spatial patterns of sea ice type and the mechanisms which create and maintain the North Water (NOW) polynya. *Atmosphere-Ocean*, 39:327-341.
- Mundy, C.J., D.G. Barber and C. Michel. 2005. Variability of snow and ice thermal, physical and optical properties pertinent to sea ice algae biomass during spring. *Journal of Marine Systems*, 58(3-4):107-120.
- Nagurduy, A.P. 1995. Long standing changes of the ice thickness the Arctic basin. *Meteorology and Hydrology*, 6: 80-83.
- Nams, V.O. 2005. Using animal movement paths to measure response to spatial scale. *Oecologia*, 143:179-188, doi:10.1007/s00442-004-1804-z.
- Nazarenko, L., T. Tausnev and J. Hansen. 2006. Sea-ice and North Atlantic climate response to CO₂-induced warming and cooling conditions. *Journal of Glaciology*, 52(178):433-439.
- Nelson, R.K. 1969. *Hunters of the Northern Ice*. Chicago: The University of Chicago Press.

432 pp.

Nghiem, S.V., I.G. Rigor, D.K. Perovich, P. Clemente-Colón, J.W. Weatherly and G. Neumann. 2007. Rapid reduction of Arctic perennial sea ice. *Geophysical Research Letters*, 34, doi:10.1029/2007GL031138.

Normant, F. and C. Tricot. 1991. Methods for evaluating the fractal dimension of curves using convex hulls. *Phys. Rev. A*, 43:6518-6525.

Novak, L.M. and M.C. Burl. 1990. Optimal speckle reduction in polarimetric SAR imagery. *IEEE Transactions on Aerospace and Electronic Systems*, 26(2):293-305, doi: 10.1109/7.53442

Obbard, M.E., M.R.L. Cattet, T. Moody, L.R. Walton, D. Potter, J. Inglis, and C. Chenier. 2006. *Temporal trends in the body condition of Southern Hudson Bay polar bears*. Ontario Ministry of Natural Resources, Applied Research and Development Branch, Sault Ste. Marie, Canada, Climate Change Research Information Note 3. Available from <http://sit.mnr.gov.on.ca>, accessed 12 December 2008.

Obbard, M.E., T.L. McDonald, E.J. Howe, E.V. Regehr and E.S. Richardson. 2007. *Polar Bear Population Status in Southern Hudson Bay, Canada*. US Geological Survey Administrative Report, Reston, USA. Available from http://www.usgs.gov/newsroom/special/polar_bears/docs/USGS_PolarBear_Obbard_SHudsonBay.pdf, accessed 12 December 2008.

Onstott, R.G. 1993. Chapter 5: SAR and Scatterometer Signatures of Sea Ice. In Carsey, F. (ed.) *Microwave Remote Sensing of Sea Ice*, American Geophysical Union, Washington, D.C., USA.

Onstott, R.G., R.K. Moore and W.F. Weeks. 1979. Surface-Based scatterometer results of Arctic sea ice. *IEEE Transactions on Geoscience Electronics*, 17(3):78-85, doi: 10.1109/TGE.1979.294616

Overland, J.E. 1985. Atmospheric boundary layer structure and drag coefficients over sea ice. *Journal of Geophysical Research*, 95(C5): 9029-9049.

Overland, J.E. and K.L. Davidson. 1992. Geostrophic drag coefficients over sea ice. *Tellus*, 44(A): 54-66.

Overland, J.E. and M. Wang. 2007. Future regional Arctic sea ice declines. *Geophysical Research Letters*, 34, doi:10.1029GL030808.

Pannatier Y. 1996. *VARIOWIN: Software for Spatial Data Analysis in 2D*. Springer-Verlag: New York; 91 pp..

Parkinson, C.L. 2000. Variability of Arctic sea ice: the view from space, an 18-year record. *Arctic*, 53(4): 341-358.

Parkinson, C.L. and D.J. Cavalieri. 2008. Arctic sea ice variability and trends, 1979-2006. *Journal of Geophysical Research*, 113, doi:10.1029/2007JC004558.

Parks, E.K., A.E. Derocher and N.J. Lunn. 2006. Seasonal and annual movement patterns of

- polar bears on the sea ice in Hudson Bay. *Canadian Journal of Zoology*, 84:1281-1294.
- Parmeter, R.R. 1975. A model of simple rafting in sea ice. *Journal of Geophysical Research*, 80: 1948-1952.
- Parmeter, R.R. and M. Coon. 1972. Model of pressure ridge formation in sea ice. *Journal of Geophysical Research*, 77:6565-6575.
- Pekarova, P. and J. Pekar. 2007. Teleconnections of inter-annual streamflow fluctuation in Slovakia with Arctic Oscillation, North Atlantic Oscillation, Southern Oscillation, and Quasi-Biennial Oscillation phenomena. *Advances in Atmospheric Science*, 24(4): 655-663, doi:10.1007/s00376-007-0655-z.
- Peterson, I., S. Prinsenberg and J. Holladay. 2006. Comparison of Helicopter-borne Measurements of Sea-Ice Properties with ENVISAT ASAR APP Data for Amundsen Gulf. *IEEE International Conference on Geoscience and Remote Sensing Symposium*, July 31-Aug. 4 2006, doi: 10.1109/IGARSS.2006.935.
- Peterson, I.K., S.J. Prinsenberg and J.S. Holladay. 2008. Observations of sea ice thickness, surface roughness and ice motion in Amundsen Gulf. *Journal of Geophysical Research*, 113, doi:10.1029/2007JC004456.
- Pomeroy, J.W. and D.M. Gray. 1990. Saltation of Snow. *Water Resources Research*, 26(7): 1583-1594.
- Pomeroy, J.W. and D.M. Gray. 1995. *Snowcover: Accumulation, Relocation and Management*. NHRI Science Report No. 7., National Hydrology Research Institute, Saskatoon, Saskatchewan, 134 pp.
- Prestud, P. and I. Stirling. 1994. The International Polar Bear Agreement and the current status of polar bear conservation. *Aquatic Mammals*, 20(3): 113-124.
- Proshutinsky, A., R.H. Bourke, and F.A. McLaughlin. 2002. The role of the Beaufort Gyre in Arctic climate variability: Seasonal to decadal climate scales. *Geophysical Research Letters*, 29, 2100, doi:10.1029/2002GL015847.
- Pruess, S.A. 1995. Some remarks on the numerical estimation of fractal dimension. In: C.C. Barton and P.R. LaPointe (eds.) *Fractals in the Earth Sciences*. New York: Plenum Press. pp. 65-75.
- Ramsay, M.A. and I. Stirling. 1988. Reproductive biology and ecology of female polar bears (*Ursus maritimus*). *Journal of Zoology*, 214: 601-634.
- Reeves, R. 1996. *World review of distribution, abundance and biology of the ringed seal (Phoca hispida)*. NAMCO Scientific Commission Document SC/4/RS/8. 37 pp. Available from NAMMCO Secretariat, University of Tromso, 9037 Tromso, Norway.
- Regehr, E.V., S.C. Amstrup, and I. Stirling. 2006. *Polar Bear Population Status in the Southern Beaufort Sea*. US Geological Survey Open-File Report 2006-1337, Reston, USA.
- Regehr, E.V., C.M. Hunter, H. Caswell, S.C. Amstrup, and I. Stirling. 2010. Survival and breeding of polar bears in the southern Beaufort Sea in relation to sea ice. *Journal of Animal Ecology*, 79: 117-127, doi: 10.1111/j.1365-2656.2009.01603.x

- Regehr, E.V., N.J. Lunn, S.C. Amstrup, and I. Stirling. 2007. Survival and population size of polar bears in western Hudson Bay in relation to earlier sea ice breakup. *Journal of Wildlife Management*, 71:2673–2683, doi: 10.2193/2006-180.
- Richardson, L.F. 1961. The problem of contiguity: an appendix of statistics of deadly quarrels. *General Systems Yearbook*, 6, 139-88
- Richter-Menge, J.A., S.L. McNutt, J.E. Overland and R. Kwok. 2002. Relating arctic pack ice stress and deformation under winter conditions. *Journal of Geophysical Research*, 107(C10), doi:10.1029/2000JC000477.
- Riewe, R. 1991. Inuit use of the sea ice. *Arctic and Alpine Research*, 23(1): 3-10.
- Rigaut, J.-P. 1988. Automated image segmentation by mathematical morphology and fractal geometry. *Journal of Microscopy*, 150(1):21-30.
- Rigor, I.G., J.M. Wallace and R.L. Colony. 2002. Responses of sea ice to the Arctic Oscillation. *Journal of Climate*, 15:2648-2663.
- Rinke, A. and K. Dethloff. 2008. Simulated circum-Arctic climate changes by the end of the 21st century. *Global and Planetary Change*, 62(1-2):173-186.
- Rode, K.D., S.C. Amstrup and E.V. Regehr. 2007. *Polar bears in the southern Beaufort Sea III: Stature, mass and cub recruitment in relationship to time and sea ice extent between 1982 and 2006*. USGS Alaska Science Center, Anchorage, Administrative Report.
- Rosing-Asvid, A. 2006. The influence of climate variability on polar bear (*Ursus maritimus*) and ringed seals (*Pusa hispida*) population dynamics. *Canadian Journal of Zoology*, 84:357-364.
- Rothrock, D.A., Y. Yu and G.A. Maykut. 1999. Thinning of the Arctic sea-ice cover. *Geophysical Research Letters*, 26:3469-3472.
- Savel'ev, S.A., M. Gordon, J. Hanesiak, T. Papakyriakou and P.A. Taylor. 2006. Blowing snow studies in the Canadian Arctic Shelf Exchange Study, 2003-04. *Hydrological Processes*, 20:817-827.
- Schmidt, R.A. 1980. Threshold wind-speeds and elastic impact in snow transport. *Journal of Glaciology*, 26:453-467.
- Schmidt, R.A. 1982. Properties of blowing snow. *Review of Geophysics and Space Physics*, 20:39-44.
- Shi, Z. and K.B. Fung. 1994. A comparison of digital speckle filters. *International Geoscience and Remote Sensing Symposium (IGARSS '94)*. August, 8-12, 1994, doi: 10.1109/IGARSS.1994.399671
- Shindell, D.T., R.L. Miller, G.A. Schmidt and L. Pandolfo. 1999. Simulation of recent northern winter climate trends by greenhouse-gas forcing. *Nature*, 399(6735): 452-455.
- Shokr, M. E. 1991. Evaluation of second-order texture parameters for sea ice classification from radar images. *Journal of Geophysical Research*, 96(C6): 10,625–10,640, doi:10.1029/91JC00693.

- Shook, K. and D.M. Gray. 1996. Small-scale spatial structure of shallow snowcovers. *Hydrological Processes*, 10:1283–1292.
- Shook, K. and D.M. Gray. 1997. Synthesizing shallow seasonal snow covers. *Water Resources Research*, 33:419–426.
- Shook, K., D.M. Gray and J.W. Pomeroy. 1993. Temporal variation in snow-cover area during melt in prairie and alpine environments. *Nordic Hydrology*, 24:183–198.
- Smith, T.G. 1975. Ringed seals in James Bay and Hudson Bay: population estimates and catch statistics. *Arctic*, 28: 170-182.
- Smith, T.G. 1987. The ringed seal, *Phoca hispida*, of the Canadian western Arctic. *Canadian Bulletin of Fisheries and Aquatic Science*, 216: 1-81.
- Smith, T.G. and M.O. Hammill. 1981. The ecology of the ringed seal (*Phoca hispida*) in its fast ice breeding habitat. *Canadian Journal of Zoology*, 59:966-981.
- Smith, T.G., M.O. Hammill and G. Taugbol. 1991. A review of the developmental, behavioural and physiological adaptations of the ringed seal, *Phoca hispida*, to life in the Arctic winter. *Arctic*, 44:124-141.
- Smith, T.G. and L.A. Harwood. 2001. Observations of neonate ringed seals, *Phoca hispida*, after early break-up of the sea ice in Prince Albert Sound, Northwest Territories, Canada, spring 1998. *Polar Biology*, 24(3):215-219.
- Smith, T.G. and I. Stirling. 1975. The breeding habitat of the ringed seal (*Phoca hispida*): the birth lair and associated structures. *Canadian Journal of Zoology*, 53:1297-1305.
- Smith, T.G. and I. Stirling. 1978. Variation in the density of ringed seal (*Phoca hispida*) birth lairs in the Amundsen Gulf, Northwest Territories. *Canadian Journal of Zoology*, 56:1066-1071.
- Soh, L.-K. and C. Tsatsoulis. 1999. Texture analysis of SAR sea ice imagery using gray level co-occurrence matrices. *IEEE Transactions on Geoscience and Remote Sensing*, 37(2):780-795.
- Steele, M., J. Zhang, D. Rothrock and H. Stern. 1997. The force balance of sea ice in a numerical model of the Arctic Ocean. *Journal of Geophysical Research*, 102(C9):21,061-21,079.
- Stefansson, V. 1945. *Arctic Manual*. New York: The MacMillan Company, 556 pp.
- Stirling, I. 2002. Polar bears and seals in the eastern Beaufort Sea and Amundsen Gulf: A synthesis of population trends and ecological relationships over three decades. *Arctic*, 55(S1):59-76.
- Stirling, I. 2005. Reproductive rates of ringed seals and survival of pups in northwestern Hudson Bay, Canada, 1991-2000. *Polar Biology*, 28:381-387.
- Stirling, I., D. Andriashek and W. Calvert. 1993. Habitat preferences of polar bears in the western Canadian Arctic in late winter and spring. *Polar Record*, 29(168):13-24.

- Stirling, I. and W.R. Archibald. 1977. Aspects of predation of seals by polar bears. *Journal of the Fisheries Research Board of Canada*, 34:1126-1129.
- Stirling, I. and A.E. Derocher. 1993. Possible impacts of climatic warming on polar bears. *Arctic*, 46(3):240-245.
- Stirling, I., M. Kingsley and W. Calvert. 1982. *The distribution and abundance of seals in the eastern Beaufort Sea, 1974-1979*. Canadian Wildlife Service Occasional Paper, 47:1-25.
- Stirling, I., N.J. Lunn and J. Iacozza. 1999. Long-term trends in the population ecology of polar bears in western Hudson Bay in relation to climate change. *Arctic*, 52(3):294-306.
- Stirling, I. and N.A. Øritsland. 1995. Relationships between estimates of ringed seal and polar bear populations in the Canadian Arctic. *Canadian Journal of Fisheries and Aquatic Sciences*, 52:2594-2612.
- Stirling, I., and C.L. Parkinson. 2006. Possible effects of climate warming on selected populations of polar bears (*Ursus maritimus*) in the Canadian Arctic. *Arctic*, 59(3):261-275.
- Stirling, I. and T.G. Smith. 2004. Implications of warm temperatures and an unusual rain event on the survival of ringed seals on the coast of southeastern Baffin Island. *Arctic*, 57: 59-67.
- Stroeve, J.C., M.M. Holland, W. Meier, T. Scambos and M. Serreze. 2007. Arctic sea ice decline: faster than forecast. *Geophysical Research Letters*, 34, doi: 10.1029/2007GL029703.
- Stroeve, J., M. Serreze, S. Drobot, S. Gearheard, M. Holland, J. Maslanik, W. Meier and T. Scambos. 2008. Arctic sea ice extent plummets in 2007. *EOS Trans. AGU*, 89, doi: 10.1029/2008E0020001.
- Sturm, M., K. Morris and R. Massom. 1998. The winter snow cover of the West Antarctic pack ice: its spatial and temporal variability. *Antarctic Sea Ice: Physical Processes, Interactions and Variability*, 74:1-18.
- Sturm, M., J. Holmgren and D.K. Perovich. 2002. Winter snow cover on the sea ice of the Arctic Ocean at the Surface Heat Budget of the Arctic Ocean (SHEBA): temporal evolution and spatial variability. *Journal of Geophysical Research*, 107(C10): 23-1-23-17.
- Sturm, M., J.A. Maslanik, D. Perovich, J.C. Stroeve, J. Richter-Menger, T. Markus, J. Holmgren, J.F. Heinrichs and K. Tape. 2006. Snow depth and ice thickness measurements from the Beaufort and Chukchi Seas collected during the AMSR-Ice03 campaign. *IEEE transactions on Geoscience and Remote Sensing*, 44(1):3009-3020.
- Sugihara, G. and R.M. May. 1990. Applications of fractals in ecology. *Trends in Ecology and Evolution*, 5:79-86.
- Takeuchi, M. 1979. Vertical profile and horizontal increase of drift snow transport. *Journal of the Faculty of Science, Hokkaido University Ser. VII (Geophysics)*, VI(1):143-156.
- Thiemann, G.W., S.J. Iverson, and I. Stirling. 2008. Polar bear diets and arctic marine food webs: insights from fatty acid analysis. *Ecological Monographs*, 78:591-613., doi:10.1890/07-1050.1

- Thorndike, A.S. and R. Colony. 1982. Sea ice motion in response to geostrophic winds. *Journal of Geophysical Research*, 87(C8):5845-5852.
- Uotila, J. 2001. Observed and modeled sea-ice drift response to wind forcing in the northern Baltic Sea. *Tellus*, 53A:112-128.
- Wadhams, P. 2000. *Ice in the Oceans*. Gordon and Breach Science Publishers, London, UK. 351 pp.
- Walsh, J.E. 2008. Climate of the Arctic marine environment. *Ecological Applications*, 18(2): S3-S22.
- Wang, J. and M. Ikeda. 2000. Arctic oscillation and Arctic sea-ice oscillation. *Geophysical Research Letters*, 27(9):1287-1290, doi:10.1029/1999GL002389.
- Wang, M. and J.E. Overland. 2009. A sea ice free summer Arctic within 30 years? *Geophysical Research Letters*, 36, doi:10.1029/2009GL037820.
- Wang, X. and N.D. Georganas. 2009. GLCM texture based fractal method for evaluating fabric surface roughness. *Canadian Conference on Electrical and Computer Engineering, 2009, CCECE '09*. St. John's, Newfoundland, 3-6 May 2009 doi: 10.1109/CCECE.2009.5090100
- Warren, S.G., I.G. Rigor, N. Untersteiner, V.F. Radionov, N.N. Bryazgin, Y.I. Aleksandrov and R. Colony. 1999. Snow depth on Arctic sea ice. *Journal of Climate*, 12:1814-1829.
- Welch, H.E. 1991. Comparisons between lakes and seas during the Arctic winter. *Arctic and Alpine Research*, 23(1):11-23.
- Welch, H.E. and M.A. Bergmann. 1989. Seasonal development of ice algae and its prediction from environmental factors near Resolute, N.W.T., Canada. *Canadian Journal of Fisheries and Aquatic Sciences*, 46:1793-1804.
- Wiig, Ø. 1995. Distribution of polar bears (*Ursus maritimus*) in the Svalbard area. *Journal of Zoology*, 237:515-529.
- Wiig, Ø, A.E. Derocher and S.E. Belikov. 1999. Ringed seal (*Phoca hispida*) breeding in the drifting pack ice of the Barents Sea. *Marine Mammal Science*, 15: 595-598.
- Wingate, R.J., T. Fitzgibbon and I.D. Thompson. 1992. Lucifer yellow, retrograde tracers and fractal analysis characterize adult ferret retinal ganglion cells. *Journal of Comparative Neurology*, 323:449-474.
- With, K.A. 1994. Using fractal analysis to assess how species perceive landscape structure. *Landscape Ecology*, 9:25-36.
- Woo, M-K and K.L. Young. 2004. Modeling arctic snow distribution and melt at the 1 km grid scale. *Nordic Hydrology*, 35:295-307.
- Woolett J.M., A.S. Henshaw and C.P. Wake. 2000. Paleoecological implications of

- archaeological seal bone assemblages: case studies from Labrador and Baffin Island. *Arctic*, 53:395–413
- Xiao, J., J. Li and A. Moody. 2003. A detail-preserving and flexible adaptive filter for speckle suppression in SAR imagery. *International Journal of Remote Sensing*, 24: 12,2451-12,2465.
- Xie, H., L.E. Pierce and F.T. Ulaby. 2002. SAR speckle reduction using wavelet denoising and Markov random field modeling. *IEEE Transactions on Geoscience and Remote Sensing*, 40(10):2196-2212, doi: 10.1109/TGRS.2002.802473.
- Yu, Y., G.A. Maykut and D.A. Rothrock. 2004. Changes in the thickness distribution of Arctic sea ice between 1958-1970 and 1993-1997. *Journal of Geophysical Research*, 109(C8), doi:10.1029/2003JC001982.
- Zhang, J., R. Lindsay, M. Steele, and A. Schweiger. 2008. What drove the dramatic retreat of arctic sea ice during summer 2007? *Geophysical Research Letters*, 35, doi:10.1029/2008GL034005.
- Zhang, J., D. Rothrock and M. Steele. 2000. Recent changes in Arctic sea ice: the interplay between ice dynamics and thermodynamics. *Journal of Climate*, 13:3099-3114.
- Zhang, X.D. and J.E. Walsh. 2006. Toward a seasonally ice-covered Arctic Ocean: scenarios from the IPCC AR4 model simulations. *Journal of Climate*, 19:1730-1747.
- Zhang, X.D., J.E. Walsh, J. Zhang, U.S. Bhatt, and M. Ikeda. 2004. Climatology and interannual variability of arctic cyclone activity: 1948–2002. *Journal of Climate*, 17:2300–2317.
- Zwally, H.J., D. Yi, R. Kwok, and Y. Zhao. 2008. ICESat measurements of sea ice freeboard and estimates of sea ice thickness in the Weddell Sea. *Journal of Geophysical Research*, 113, doi:10.1029/2007JC004284.